UNIVERSITY OF CALIFORNIA, SAN DIEGO

Measurements of the Chemical, Physical, and Optical Properties of Single Aerosol Particles

A Dissertation submitted in partial satisfaction of the requirements for the degree

Doctor of Philosophy

in

Chemistry

by

Ryan Christopher Moffet

Committee in charge:

Professor Kimberly A. Prather, Chair
Professor Robert E. Continetti
Professor John E. Crowell
Professor Stanley J. Opella
Professor Lynn M. Russell

2007

This dissertation of Ryan Christopher Moffet is approved, and it is acceptable in quality and form for publication on microfilm:

_____

_____

_____

_____

_____
Chair

University of California, San Diego
2007

Dedicated to my parents, Janice and John Moffet for inspiring my love of natural science.

Table of Contents

List of Figures

List of Tables

Acknowledgements

During the past five years I have learned to do science as an independent researcher. This would not have been possible without the wonderful support provided by my advisor, Kim Prather. Not only did she provide me with her initial ideas as a place to start, but she funded me the whole way through! For someone who loves to do science this is the best kind of situation: complete freedom to take your own paths. You learn to succeed and fail by your own hand, you learn what works and what doesn't, you learn how to interact with others and learn from their expertise. This, I think, was the most valuable lesson that I learned.

Of course, Kim provided me with a great group of people to learn from. Her postdoc, Hiroshi Furutani, guided me to learn many principles of laboratory work with electronics, flow systems and basic troubleshooting. David Sodeman ("Sody"), who was a senior graduate student while I was starting out, taught me all about how to handle the instrument on a field study. Sody loved to talk in detail about procedures, and it was a good thing that I took notes. Without their help, my laboratory and field studies would have never gotten off the ground.

Lab work is only part of what we do in the Prather lab, and any alumnus will tell you about the long hours spent doing data analysis. Ryan Wenzel was particularly helpful in getting me started. At the time Ryan was supposed to be writing his thesis, he would get bored and come into my office and show off his MATLAB skills on my data. Ryan taught me how to write a loop and how to use various commands in MATLAB to automate my data analysis. Most importantly, he taught me to debug. Those first scripts

Ryan wrote with me got my data analysis started off very quickly. Then we got a new data analysis guru through a data analysis competition and his name was Thomas Rebotlier. Thomas is an exceptional programmer and he has taught me many new tricks that I have used throughout this thesis. One fine Sunday, while Thomas was kitesurfing with “doggie”, he helped save the Milagro campaign by helping me identify a faulty board that was causing the instrument to shut off as soon as I opened the software. If it wasn’t for Thomas’s help I could have been working on that problem for days!

My fellow graduate students were also of great help. I found that they often had different insights to problems I was having, and that always helped me when I was stuck. My office mate, John Holecek, was particularly good at bouncing ideas off of. He was a great listener, and always had very logical and directed advice for me. John was a good friend and roommate I knew I could always talk with him when I was having any sort of problem. He always recommended interesting reading material too. All of my fellow lab mates: Andy Ault, Kerri Denkenberger, Lindsay Hatch, Joe Mayer, Meagan Moore, Laura Shields, Matt Spencer, Yongxuan Su, Ryan Sullivan, Sharon Qin, and Steven Toner were great to work with and provided so much help at different stages of my time in the Prather lab.

Besides the lab, I learned that one cannot be happy without a life beyond the lab. San Diego is a great place to live with many wonderful people. I met the majority of my friends through climbing. Ngoc Tran, who came with me from SFSU, was my best friend during my first year or two here at UCSD. Chris Chan was a good friend during my early years at UCSD, and she taught me how easy it was to get off route. We would often climb together and we met other scientist-climbers. Robert Swartzenbacher and Elke

Zobl together with the rest of the “European Contingency” were so much fun to travel the desert and climb with. I could always talk with Robert for science and he would offer me great advice. Robert also taught me a great deal about climbing.

Through climbing I met my fiancée, Athena and her son, Kenyon. Athena and Kenyon have provided me with a true family here in San Diego, and I love both of them very much. I don’t think I could have made it through the last two years of graduate school without them; I am so happy we will be a family. I look forward to the coming adventures we will have together and surely they will serve to bond us even closer together.

Chapter 2, in full, is a reprint of the material as it appears in:

Moffet, R. C.; Prather, Kimberly A. (2005) Extending ATOFMS Measurements to Include Refractive Index and Density *Analytical Chemistry* 77, 6535-6541. The dissertation author was the primary author of this paper.

Chapter 3, in full, is a reprint of the material as it appears in:

Moffet, R.C., B. de Foy, L.T. Molina, M.J. Molina, and K.A. Prather: Measurement of Ambient Aerosols in Northern Mexico City by Single Particle Mass Spectrometry, *Atmospheric Chemistry and Physics Discussions*, 6413-6457, 2007. The dissertation author was the primary author of this paper.

Chapter 4, in full, is a manuscript to be submitted:

Ryan C. Moffet, Sharon Qin, Thomas Rebotier, Hiroshi Furutani and Kimberly A. Prather: Determining Chemically Segregated Optical and Microphysical Properties of Ambient Aerosols Using Single Particle Mass Spectrometry with Aerodynamic Sizing

and Light Scattering, *In Preparation*. The dissertation author was the primary author of this paper.

Chapter 5, in full, is a manuscript to be submitted:

Ryan C. Moffet, Sharon Qin, Thomas Rebotier, and Kimberly A. Prather: Coupled Optical and Chemical Measurements of Single Elemental Carbon Particles in the Ambient Atmosphere , *In Preparation,*. The dissertation author was the primary author of this paper.

Chapter 6, in full, is a manuscript to be submitted:

Ryan C. Moffet, Yury Desyaterik, Rebecca J. Hopkins, Alexei V Tivanski1, Mary K. Gilles, V. Shutthanandan, Luisa T. Molina, Rodrigo A. Gonzalez, Kirsten S. Johnson, Violeta Mugica, Mario J. Molina, Alexander Laskin and Kimberly A. Prather: Characterization of Aerosols Containing Zn, Pb, and Cl from an Industrial Region of Mexico City, *In Preparation,*. The dissertation author was the primary author of this paper.

Chapter 7, in full, is a reprint of the material as it appears in:

Moffet, R. C.; Shields, L.G.; Berntsen, J.; Devlin, R. B.; Prather, K. A. (2004). Characterization of an Ambient Coarse Particle Concentrator Used for Human Exposure Studies: Aerosol Size Distributions, Chemical Composition and Concentration Enrichment. *Aerosol Science and Technology*. 38(10), 1123-1137. The dissertation author was the primary author of this paper.

Vita

2002	B.S. in Chemistry, San Francisco State University
2002 – 2007	Graduate research assistant, Department of Chemistry and Biochemistry, University of California, San Diego
2002 - 2003	Teaching Assistant, Department of Chemistry and Biochemistry, University of California, San Diego
2004	M.S. in Chemistry, University of California, San Diego
2007	Ph.D. in Chemistry, University of California, San Diego

Publications

Moffet, R.C., B. de Foy, L.T. Molina, M.J. Molina, and K.A. Prather: Measurement of Ambient Aerosols in Northern Mexico City by Single Particle Mass Spectrometry, *Atmospheric Chemistry and Physics Discussions*, 6413-6457, 2007.

Denkenberger, K.A.; Holecek, J. C.; Moffet, R. C.; Prather, K. A. (2007) Real-Time, Single-Particle Measurement of Ambient Aerosol Particles Containing Oligomeric Species, *Environmental Science and Technology*, In Press

Su, Y. S., M. F.; Spencer, M. T.; Qin, X.; Moffet, R. C.; Shields, L. G.; Prather, K. A.; Venkatachari, P.; Jeong, C.; Kim, E.; Hopke, P. K.; Gelein, R. M.; Utell, M. J.; Oberdorster, G.; Berntsen J.; Devlin, R. B.; Chen, L. (2006) Real-Time Characterization of the Composition of Individual Particles Emitted From Ultrafine Particle Concentrators *Aerosol Science and Technology*, 39(5), 437-455.

Moffet, R. C.; Prather, Kimberly A. (2005) Extending ATOFMS Measurements to Include Refractive Index and Density *Analytical Chemistry* 77, 6535-6541.

Moffet, R. C.; Shields, L.G.; Berntsen, J.; Devlin, R. B.; Prather, K. A. (2004). Characterization of an Ambient Coarse Particle Concentrator Used for Human Exposure Studies: Aerosol Size Distributions, Chemical Composition and Concentration Enrichment. *Aerosol Science and Technology*. 38(10), 1123-1137

Fields of Study

Major Field: Chemistry

Studies in Atmospheric Chemistry:
Professor Kimberly A. Prather

Studies in Mass Spectrometry:
Professor Kimberly A. Prather

ABSTRACT OF THE DISSERTATION

Measurements of the Chemical, Physical, and Optical Properties of Single Aerosol Particles

by
Ryan Christopher Moffet

Doctor of Philosophy in Chemistry
University of California, San Diego, 2007
Professor Kimberly A. Prather, Chair

Knowledge of aerosol physical, chemical, optical properties is essential for judging the effect that particulates have on human health, climate and visibility. The aerosol time-of-flight mass spectrometer (ATOFMS) is capable of measuring, in real-time, the size and chemical composition of atmospheric aerosols. This was exemplified by the recent deployments of the ATOFMS to Mexico City and Riverside. The ATOFMS provided rapid information about the major particle types present in the atmosphere. Industrial sources of particles, such as fine mode particles containing lead, zinc and chloride were detected in Mexico City. The rapid time response of the ATOFMS was also exploited to characterize a coarse particle concentrator used in human health effects studies. The ATOFMS showed the ability to detect changes in particle composition with a time resolution of 15 min during short 2 hour human exposure studies.

As a major component of this work, an optical measurement has been added to the ATOFMS. The scattered light intensity was acquired for each sized and chemically

analyzed particle. This scattering information together with the particle aerodynamic diameter, enabled the refractive index and density of the aerosol to be retrieved. This method was validated in the laboratory using different test particles such as oils, aqueous salt solutions and black carbon particles. It was found that the nozzle-type inlet does not evaporate aqueous salt particles as has been observed for aerodynamic lens inlets. These new optical and microphysical measurements were integrated into the ATOFMS for field deployment in Riverside and Mexico City. For both cities, the different mixing states were found to have unique refractive indexes and densities. A fraction of the strongly absorbing elemental carbon particles were observed to have a spherical morphology due to heavy mixing with secondary species. In addition to the quantitative refractive index and effective density measurements, qualitative information on the morphology was obtained, which, together with the refractive index, provided information on the physical state of the particle. This is the first time that the ATOFMS data has been combined with optical measurements.

1

Optical Measurement of Aerosols

1.1 The Big Picture: Visibility, Climate Change and Health Effects

An aerosol is defined as any solid or liquid suspended in a gas. Aerosol particles are ubiquitous in the atmosphere: they are the main visibility-reducing component from large fires, dust storms, sea spray, and urban smog. Although aerosols are ubiquitous, they still remain to be a measurement challenge because their physical and chemical properties are difficult to quantify. Atmospheric aerosols are typically 0.001 – 10 μm in diameter, and their small size is one of the reasons they are so difficult to measure. However, within the last 60 years, researchers in the field of aerosol science have made continual progress in advancing the understanding of these complex particles. In addition, aerosols are a major subject of research in other areas such as drug development, industrial hygiene, and defense. The bulk of this introduction focuses on optical characterization of aerosol particles, mainly from the atmospheric/climate science perspective. We begin by stating some of the major problems in the areas of climate change, visibility and health effects. This is followed by basic theory on the optics of small particles and definitions of the key parameters used in visibility and climate science. Next, a comprehensive survey of analytical techniques used to measure aerosol optical properties is provided. Lastly, future directions for aerosol analytical science are discussed.

Extensive studies show that there are significant associations between the physico-chemical properties of airborne particulate matter and adverse respiratory and cardiovascular health effects [*Davidson et al.*, 2005; *Dockery et al.*, 1993; *Lippmann et al.*, 2003]. However, there is considerable controversy among policy makers over what is the best metric for relating particulate matter to adverse health effects [*Lippmann et al.*, 2003]. Results from these studies indicate that both the chemical and physical properties are needed to explain the deleterious health effects – properties such as chemical composition and size distribution. Deconvoluting size and chemical composition and their relationship to health effects remains an ongoing issue. The problem is that the measurements of aerosol chemical and physical properties are not sufficient to address the needs of health effects experts. Most measurements of size and chemical composition during health effects studies rely on filter measurements to provide a useful but limited description of the aerosol. While filter measurements are quantitative, they have poor time resolution and do not distinguish what chemical species are associated within the particles (mixing state information). Time resolved mixing state is critical to develop effective policy to identify sources of particles that are harmful to human health. For this reason it is imperative that new techniques continue to be developed to accurately measure ambient atmospheric aerosol.

The radiative forcing by aerosols is one of the largest sources of uncertainty in climate prediction [*Andreae et al.*, 2005; *Charlson et al.*, 1992; *Hansen et al.*, 1998; *IPCC*, 2007]. Most aerosols scatter (reflect) solar radiation and thus have a cooling effect on climate. Some aerosols, such as black carbon (BC), are strongly absorbing and have a warming effect. The direct interaction of radiation with aerosols by scattering and

absorption is called the direct effect. It is important to highlight that all aerosols, including black carbon, undergo chemical aging, which is one of the processes that act to remove them from the atmosphere. The aging process typically involves the condensation of gas phase oxidation products (eg SO_2 and HNO_3) that change how the aerosols interact with water. The condensation water and other species leads to larger particles sizes that scatter light more efficiently. Furthermore large number concentrations of anthropogenic pollution aerosols leads to an increased number of cloud droplets and increased cloud brightness (optical depth): this is the first indirect effect [*Twomey*, 1974]. With an increase in the number of cloud droplets, the liquid water is distributed over more sites, and thus smaller droplets form for a given water content. Smaller droplets lead to decreased precipitation efficiency; this is the second indirect effect. Yet another indirect effect of aerosols on clouds is called the semi-direct effect. Here, absorbing aerosol heats the cloud, causing evaporation of water, decreasing droplet radius and precipitation efficiency [*Ackerman et al.*, 2000]. In addition to affecting climate, light scattering and absorption by aerosol particles decrease visibility in our cities and national parks. Several governmental organizations have taken measures to research and mitigate these problems with legislation and the regional haze rule [*EPA*, 1999; *Watson*, 2002]. Developing strategies to improve visibility requires an understanding between chemical composition and extinction [*Malm and Sisler*, 2000]. The current state of knowledge about aerosol optical properties on a regional and global scale is not sufficient to accurately predict the future climate or to accurately apportion atmospheric visibility to sources. Improvement in these areas can only be achieved through measurements.

In all applications, there is a need for real-time measurements of optical properties directly linked with chemical composition and particle size. As we show below, aerosol optical properties are controlled by size and chemical composition. Moreover, the mixing of different chemical components within the same particle is also found to have a strong effect on absorption [*Bond and Bergstrom*, 2006; *Bond et al.*, 2006; *Yu et al.*, 2006]. It has been found that adding a non-absorbing shell over a strongly absorbing particle amplifies the total amount of light absorbed [*Ackerman and Toon*, 1981; *Mikhailov et al.*, 2006; *Schnaiter et al.*, 2005]. Furthermore, particle morphology will have a great influence on particle measurements and models that often assume particles scatter and absorb light like spherical homogenous particles; this assumption may lead to large errors in some cases. Current measurements are usually inadequate to detect this level of detailed morphology. For this reason, we include such detailed optical measurement of aerosols in addition to the more standard measurements. First, we start with describing and defining the key measurable parameters relating to aerosol optical properties. Understanding these fundamental parameters will lead naturally to better insight of the current state of the art in measurement techniques. A sound knowledge of these basic optical parameters not only helps us understand climate change, but leads to advances in other fields of aerosol science such as health effects.

1.2 Fundamental Aerosol Optical Parameters and Principles Governing Climate Change and Visibility

Size and chemical composition are the main factors that determine aerosol optical properties. There are several fine textbooks that give a general [*Finlayson-Pitts and Pitts*,

2000; *Hinds*, 1999; *Sienfeld and Pandis*, 1998] or detailed [*Bohren and Huffman*, 1981; *Mishchenko et al.*, 2000; *van de Hulst*, 1957] account of how size and chemical composition affect particle optical properties. In the following discussion, we show how aerosol size and chemical composition are linked to single particle optical properties. Then, these single particle optical properties are integrated to give bulk optical constants that control the aerosol direct effect, always keeping chemical composition and mixing state explicit. We start with one of the most important parameters: aerosol size.

1.2.1 Aerosol Size Distribution

If we define aerosol number concentration (N) as the number of particles per m^3, then it follows that particle area, volume and mass are defined as:

$$A = \frac{\pi D_p^2}{4} N \quad (\mu m^2 / m^3) \tag{1.1}$$

$$V = \frac{\pi D_p^3}{6} N \quad (\mu m^3 / m^3) \tag{1.2}$$

$$M = \frac{\rho \pi D_p^3}{6} N \quad (\mu g / m^3) \tag{1.3}$$

where D_p is the geometric particle diameter and ρ is the particle density. In these relations we have assumed that the particles are spherical; the explanation will be more complicated for nonspherical particles. Figure 1.1 shows an example of size distributions measured in Mexico City an aerodynamic particle sizer (APS) and scanning mobility particle sizer (SMPS). The size distributions are presented on a logarithmic abscissa with

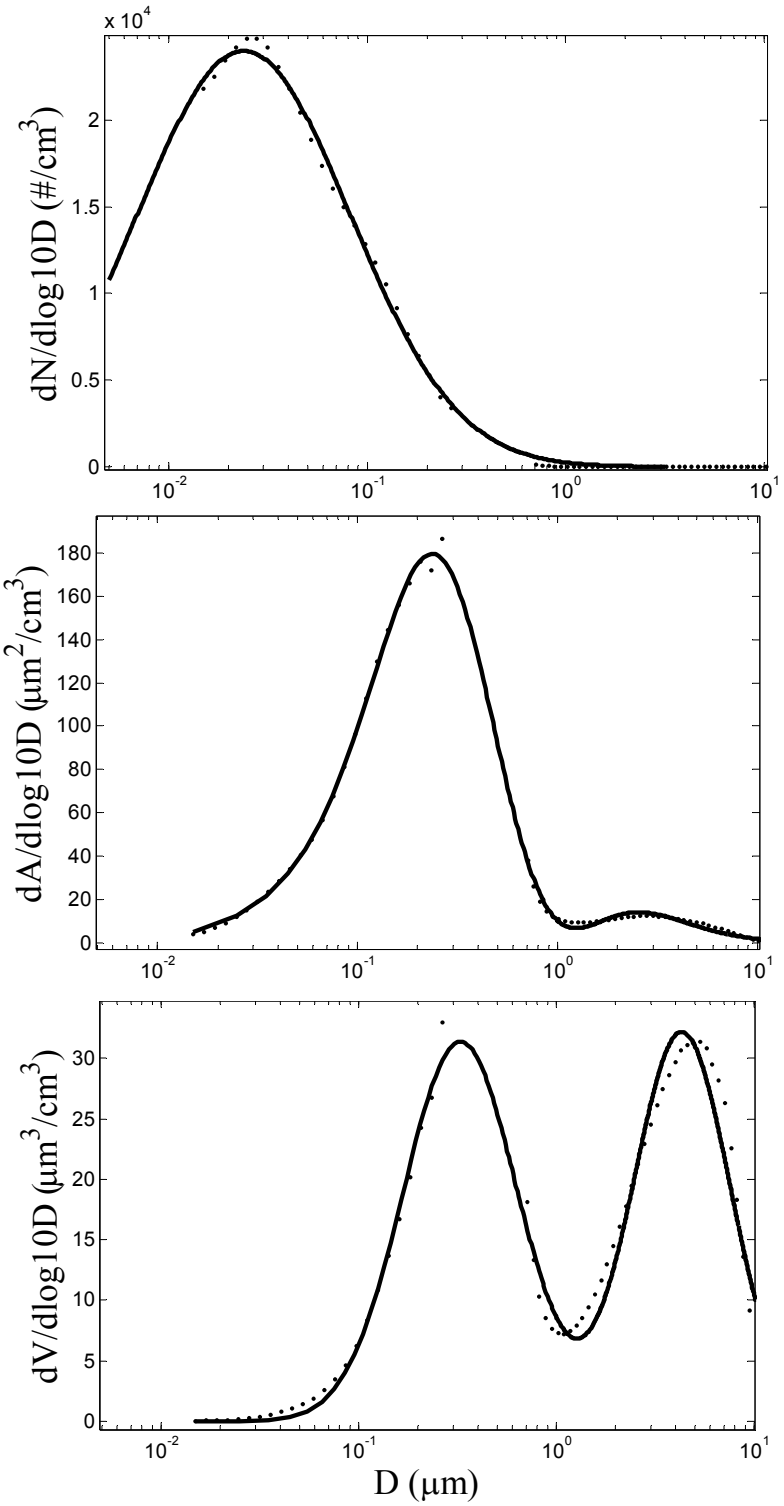

Figure 1.1 Average a) number, b) surface area and c) volume distributions measured in Mexico City during the MILAGRO campaign. Data courtesy of Don Collins and J. Wang.

ordinate units normalized by the logarithmic bin width. Normalizing by the bin width enables easier comparisons with measurements having different size resolution (bin widths). We show from top to bottom of Fig 1.1, aerosol number, surface area and volume distributions. The different weighting factors highlight different features of the distribution. First, for number concentration, sizes from 0.01 – 0.1μm are the most important. This is the size where particles are formed by homogenous nucleation of a supersaturated vapor without the assistance of additional ions or a nucleus. This mode is called the nucleation mode. Once these particles are formed, they will continue to grow by condensation and coagulation. Coagulation for these small sizes occurs very quickly due to their small size and large diffusion coefficient. Coagulation of these small particles moves them from the nucleation mode to the accumulation mode [*Friedlander and Wang*, 1966; *Lai et al.*, 1972], occurring between 0.1 – 0.5μm. From Fig 1.1, we see that particles in the accumulation mode have the most surface area, and therefore, these particles are most important for gas-to-particle conversion processes (with the exception of dust storms). For the volume (or mass) distribution in a polluted environment, there will be two well defined modes: the accumulation mode (below 1 μm) and the coarse mode above 1 μm. Particles in the coarse mode are formed primarily by mechanical generation such as a blowing wind on desert dust.

The compositions in the coarse and fine mode are drastically different. The coarse mode consists primarily of mineral dust, sea salt, pollen and vegetative detritus. The accumulation mode in an urban environment may be composed of a wide variety of species as a result of gas to particle condensation and coagulation: salts of nitrate, sulfate, ammonium, and potassium as well as a large contribution from elemental and organic

carbon. As mentioned earlier, size is the most important parameter affecting how the aerosol scatters or absorbs solar radiation. In the next section we see how both chemical composition and size determine aerosol optical properties by looking at how aerosol particles interact with electromagnetic waves (light).

1.2.2 Basic Optics for Small Particles and the Refractive Index

In Sec 1.2.1, an overview was given of the size range of common aerosol species found in the atmosphere and it was noted that size was the most important factor determining scattering. It was also mentioned that chemical composition has an effect on aerosol optical properties; these two variables are shown here to be connected through the refractive index. Each chemical species can be assigned a refractive index that controls how it interacts with an electromagnetic wave, and therefore, scatters and absorbs light. We define refractive index as

$$\mathrm{m} = n + ik \tag{1.4}$$

where m is the refractive index (an imaginary number), i is $\sqrt{-1}$, and n and k are the real and imaginary parts of the index of refraction. Using this form of the index of refraction leads to a description of a plane wave (E_c) traveling in a medium:

$$E_c = E_0 \exp\left(-\frac{2\pi kz}{\lambda}\right)\exp\left(\frac{i2\pi nz}{\lambda} - i\omega t\right) \tag{1.5}$$

where E_0 is the amplitude, λ is the wavelength, ω is the angular frequency, t is time and z is distance. From this relation it is seen that the real part of the index of refraction gives

Table 1.1. Refractive index and density of several atmospherically relevant substances

Substance	**Refractive Index**	**Wavelength**	**Material Density**	**Reference**
Water	1.333	589	1.0	1
Ice	1.309	589		1
NaCl (aq)	1.33 – 1.38	589	1.035 – 1.189	1
NaCl (s)	1.54	589	2.17	1
$(NH_4)_2SO_4$ (s)			1.77	
KNO_3			2.105	
K_2SO_4	1.494	589	2.66	1
a - pinene	1.47	589	0.858	1
Oleic acid	1.46	589		1
Polystyrene latex	1.59	589	1.01	1
Atmospheric soot (elemental or black carbon)	1.85+0.71i	550	1.8	3
Magnetite (Fe_2O_3)	2.58+0.58i	589		1
SiO_2	1.54	589	2.6	1
Kaolinite	1.493 + 5.25E-5i	533	2.16 – 2.68	2
Montmorillonite	1.525 + 0.0012i	533		2
Illite	1.414 + 8.32E-5i	533		
$Pb(NO_3)_2$	n=1.78	?	4.53	4, 1
$PbCl_2$	n=2.2	589	5.98	1
$Zn(NO_3)_2$				
ZnO	n=2.013	589	5.6	1
Copper	0.62+2.63i	589	8.96	1

1. [*Lide*, 2006] 2. [*Egan and Hilgeman*, 1979], 3. [*Bond and Bergstrom*, 2006]
4. [*Richards and Schumb*, 1918]

the phase velocity (speed of light divided by the refractive index) and the imaginary part gives attenuation (absorption). Table 1.1 shows the refractive index and density for several substances found in atmospheric aerosol particles. These values for refractive indeces are given with a specified wavelength because, although termed optical *constants*, they are a strong function of wavelength. Wavelengths near 500nm are very important because this is the peak of the solar spectrum as well as a common wavelength used in measurements. It is seen from Table 1.1 that the real part of the index of refraction varies from 0.6 for pure copper to 2.6 for Fe_2O_3. However, common values for atmospheric aerosols are expected to be ~1.33-1.7. The imaginary part of the refractive index is expected to vary from ~0 for water to 2.63 for metallic copper. The most common absorbing (nonzero *k*) aerosols in the atmosphere are elemental carbon (EC) particles which have a typical refractive index of 1.85 + 0.71i. We should emphasize that atmospheric particles are rarely observed to be composed of pure substances. Methods of determining "effective" refractive indices have been developed but their use in aerosol physics has been questioned because they assume homogenous mixing. These effective refractive indices frequently give values of k not observed for any physical substances [*Bohren and Huffman*, 1981; *van de Hulst*, 1957]. In fact, mixing within single atmospheric particles is often found to be inhomogeneous, and this has far reaching implications for their optical properties [*Jacobson*, 2001]. In Jacobson, 2001, it was found that such internal mixing for black carbon particles leads to an enhanced warming in a global climate model.

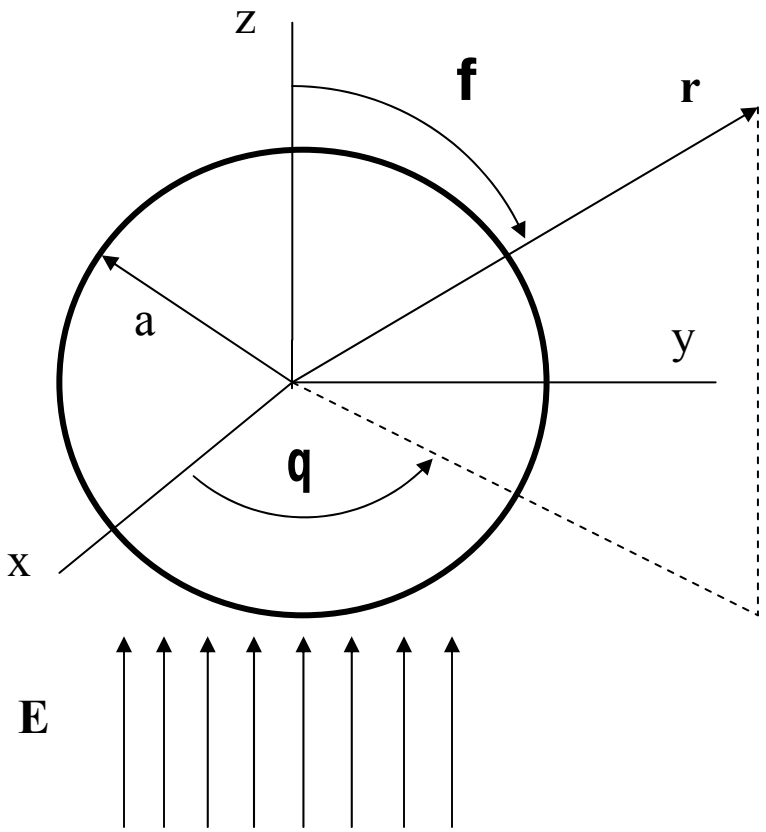

Figure 1.2. Spherical polar coordinate system used to solve the electromagnetic scattering for a sphere of radius a and center at the origin. The incident electric field is denoted by E. Maxwells equations are solved for the internal and scattered fields.

1.2.3 Scattering by an Arbitrary Particle

With an understanding of the general sizes and refractive indices of atmospheric particles, we can look at scattering in general through the coordinate system shown in Figure 1.2. The problem consists of an incident electric field (E_i) onto a spherical particle, where the center of the particle is taken as the center for the spherical polar coordinate system. In this system there is the polar angle **q** and azimuthal angle **f**. Scattering in the forward and backward direction occur at **q** = 0 and 180, respectively. The scattered electric field is given by

$$\begin{pmatrix} E_{\|s} \\ E_{\perp s} \end{pmatrix} = \frac{e^{ik(r-z)}}{-ikr} \begin{pmatrix} S_2 & S_3 \\ S_4 & S_1 \end{pmatrix} \begin{pmatrix} E_{\|i} \\ E_{\perp i} \end{pmatrix} \tag{1.6}$$

where r is the distance at which the field is measured, k is wave number, and the elements of the scattering matrix S. The scattering matrix is very important because it contains all of the information about how the particle interacts with the incident field. The **^** and || symbols represent the perpendicular and parallel polarization with respect to the **f**=0° plane. It is apparent that the crux of the solving Eq 1.6 lies in determining the scattering matrix. There are several methods available for calculating the scattering matrix and we will return to calculating the scattering matrix elements by Mie theory in Sec 1.2.4.

In order to develop the more compact notation given in Bohren (1981), it is convenient to re-write Eq 1.6 as

$$\mathbf{E_s} \sim \frac{e^{ik(r-z)}}{-ikr} \mathbf{X} E \tag{1.7}$$

where

$$\mathbf{X} = (S_2 \cos\phi + S_3 \sin\phi)\hat{\mathbf{e}}_{\|\mathbf{s}} + (S_4 \cos\phi + S_1 \sin\phi)\hat{\mathbf{e}}_{\perp\mathbf{s}} \tag{1.8}$$

X is known as the vector scattering amplitude. We now can define the scattering cross section, which represents the total energy scattered in all directions if it were falling on the area C_{sca}:

$$C_{sca} = \int_0^{2\pi}\int_0^{\pi} \frac{|\mathbf{X}|^2}{k^2} \sin\theta d\theta d\phi \tag{1.9}$$

The term $|X|^2/k^2$ is known as the differential scattering cross section, and C_{sca} is known as the scattering cross section. The differential scattering cross section is a very useful quantity that can be used to calculate instrument response over a defined set of angles (See Chapter 2). Frequently, we encounter the term phase function in atmospheric chemistry and physics, and it is defined as $|\mathbf{X}|^2/k^2C_{sca}$ so that integration of the phase function over all angles yields unity.

The total amount of energy lost that falls on an area C_{ext} is known as the extinction cross section and is defined as

$$C_{ext} = \frac{4\pi}{k^2} \mathrm{Re}\{(\mathbf{X}\cdot\hat{\mathbf{e}}_x)_{\theta=0}\} \tag{1.10}$$

By conservation of energy, the amount of energy absorbed on an area C_{abs} is:

$$C_{abs} = C_{ext} - C_{sca} \tag{1.11}$$

Equations 1.9 – 1.11 are very fundamental equations, and their quantities will be used throughout this work. For more explanation of these quantities, we highly encourage the reader to consult Borhen (1981) and van de Hulst (1957).

1.2.4 Mie's Solution for Spherical Particles

The scattering cross sections and phase functions can be calculated for a variety of particles using different theories (Sec 1.2.5), but perhaps the most convenient way to compute them is using Mie theory. Mie theory is the rigorous solution of Maxwell's equations applied to the scattering problem posed in Eq 1.6 for a homogenous spherical particle. Here we give only the results that were derived by others [*Bohren and Huffman*, 1981; *Mie*, 1908; *van de Hulst*, 1957].

For a sphere we note that $S_3 = S_4 = 0$. The remaining matrix elements are given by:

$$S_1 = \sum_{j=1}^{jcnv} \frac{2j+1}{j(j+1)}(a_j \pi_j + b_j \tau_j) \tag{1.12}$$

$$S_2 = \sum_{j=1}^{jcnv} \frac{2j+1}{j(j+1)}(a_j \tau_j + b_j \pi_j) \tag{1.13}$$

where

$$a_j = \frac{m\psi_j(mx)\psi_j'(x) - \psi_j(x)\psi_j'(mx)}{m\psi_j(mx)\xi_j(x) - \xi_j(x)\psi'_j(mx)} \tag{1.14}$$

$$b_j = \frac{\psi_j(mx)\psi_j'(x) - m\psi_j(x)\psi_j'(mx)}{m\psi_j(mx)\xi_j(x) - m\xi_j(x)\psi'_j(mx)}. \tag{1.15}$$

Note that $x = 2\pi a/\lambda$ is the called the size parameter and the primes in 14 and 15 represent derivatives. The angular functions τ and π are given by

$$\pi_j = \frac{P_j^1(\cos\theta)}{\sin\theta}, \tau_j \frac{dP_j^1(\cos\theta)}{d\theta} \tag{1.16}$$

and

$$\psi_0 = \sin\left(\frac{\omega mx}{c}\right), \psi_1 = \frac{c}{\omega mx}\sin\left(\frac{\omega mx}{c}\right) - \cos\left(\frac{\omega mx}{c}\right), \ldots \psi_{jcnv} \tag{1.17}$$

$$\xi_0 = -\cos\left(\frac{\omega mx}{c}\right), \xi_1 = -\frac{c}{\omega mx}\cos\left(\frac{\omega mx}{c}\right) - \sin\left(\frac{\omega mx}{c}\right), \ldots \xi_{jcnv} \quad (1.18)$$

are the well-known Ricatti-Bessel functions. P_j^1 are the Legendre polynomials. These are all of the necessary elements needed to calculate cross sections and the phase function. As will be shown later (Sec 1.2.6), the scattering cross section and phase function can be used to describe scattering processes in the atmosphere. Note that Eqs 1.12 – 1.13 are calculated via upward recurrence (iteration from $1 \ldots j_{cnv}$ where j_{cnv} is the step at which the series converges) and that this is somewhat time-consuming. Mie calculations were very difficult to obtain prior to ~1980, after which Bohren and Huffman (1981) first used computer programs to calculate 12 and 13.

Now, Mie theory can be used to observe how scattering varies as a function of size and angle. In Fig 1.3, the scattering cross section is plotted as a function of size for several refractive indices. We chose the size range to overlap with both accumulation and coarse mode aerosols. Below 0.1μm, light scattering by particles is negligible in comparison to that of larger particles. Just above 0.1μm, C_{sca} increases approximately as D^6 until it begins to reach a local maximum. The D^6 region is located at a transition between Rayleigh scattering and Mie scattering. Rayleigh scattering is an approximate theory that is sufficient to calculate scattering for particles much smaller than the wavelength of incident light. The broad local maxima occurring about every 1 μm are caused by the interference of transmitted and scattered light. Note that the first broad maximum occurs at a larger size for a smaller refractive index. This is because changing the size and refractive index have the same effect: they both affect the phase lag of light traveling through the particle. Superimposed upon the broad interference structure, there

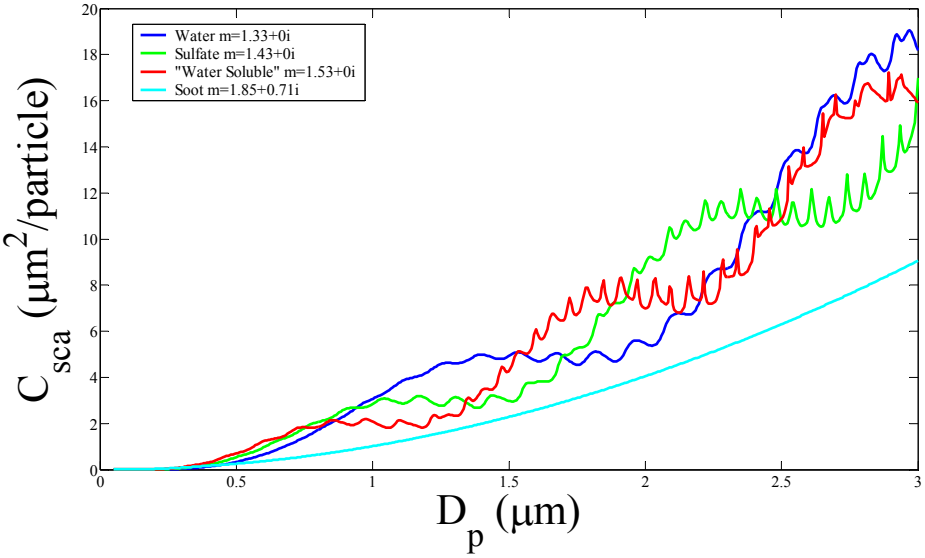

Figure 1.3. Scattering cross sections as a function of size predicted by Mie theory for a wavelength of 532nm.

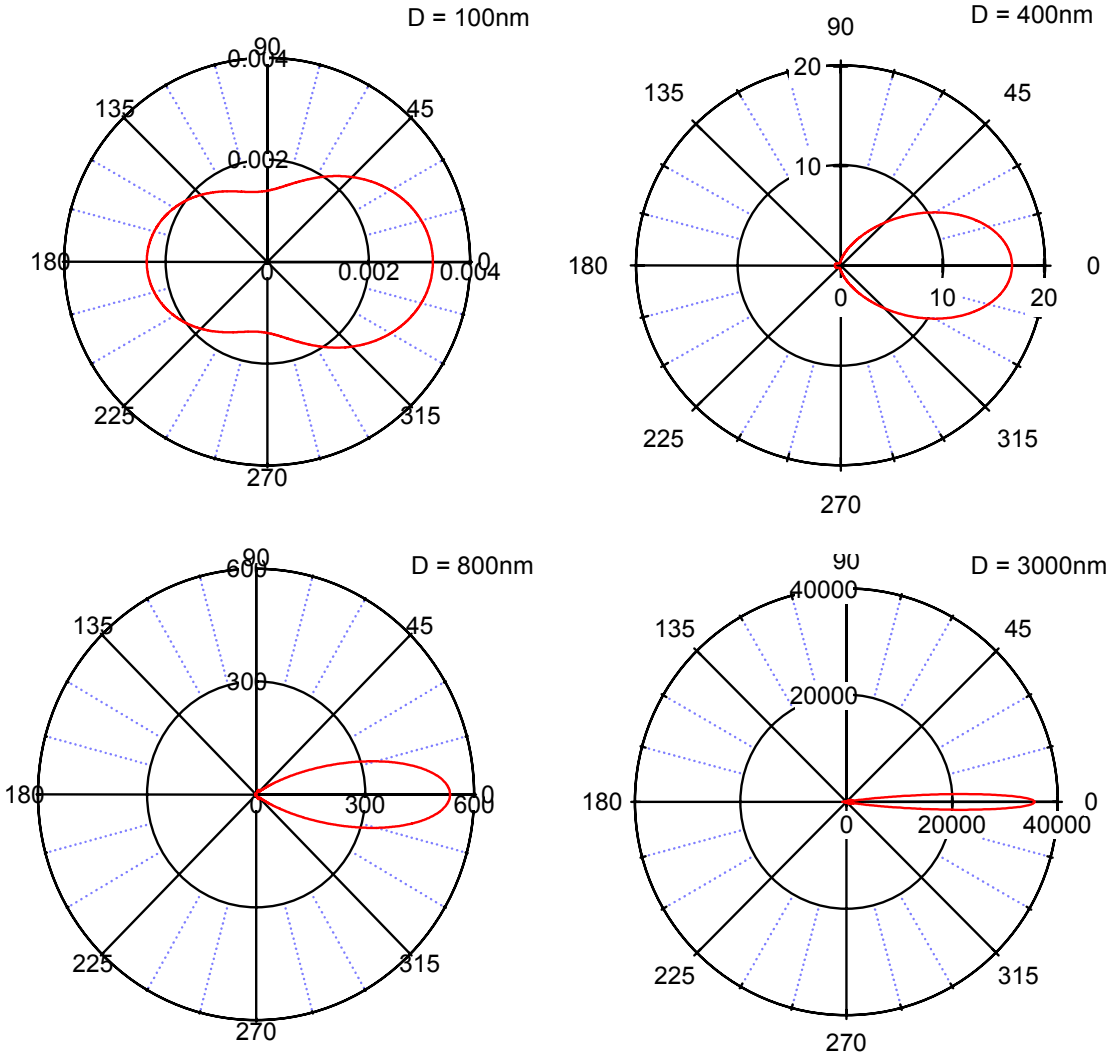

Figure 1.4. Scattering as a function of angle for different sizes predicted by Mie theory.

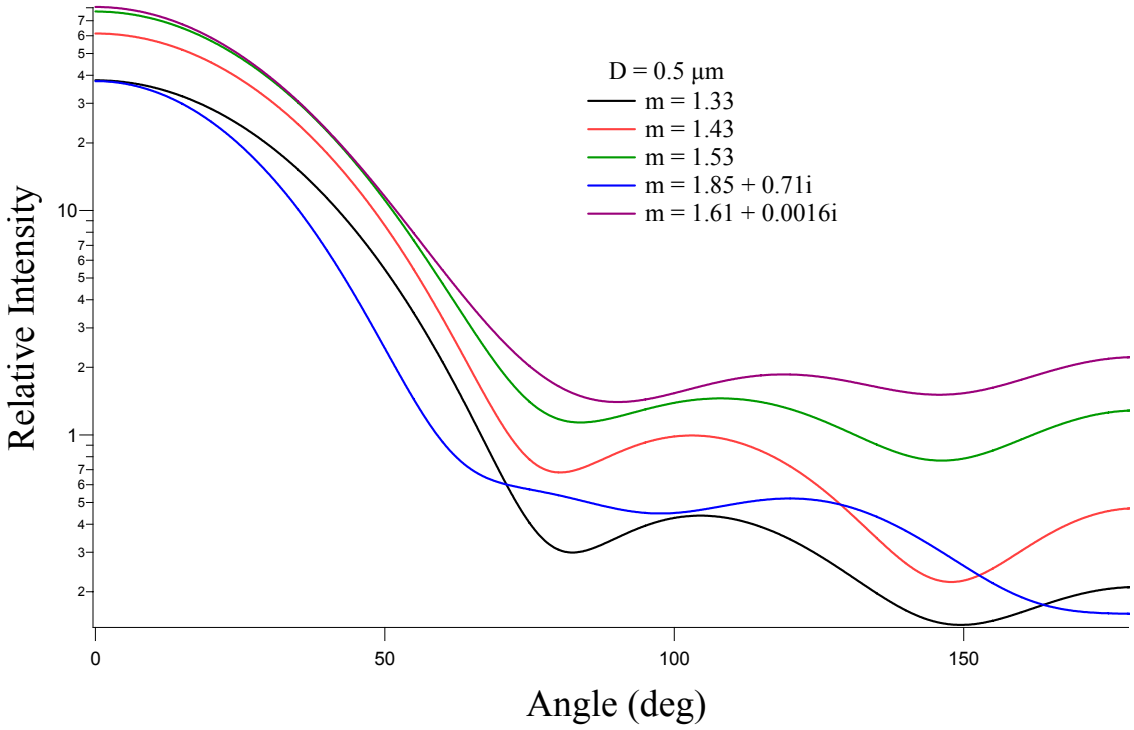

Figure 1.5. Scattering as a function of angle for aerosols for different refractive indices.

are progressively sharper irregularly shaped peaks that are known as “ripple” structure. Ripple structure is caused by electromagnetic surface modes residing on the surface of the sphere that are set up by the incident electric field. Note that as absorption increases (from water to soot), the surface modes disappear since absorption acts to dampen the modes.

In Fig 1.4, scattered intensity as a function of angle (phase function) is plotted on a polar diagram. For the smallest size particle, it is seen that the forward to back scattering ratio is close to 1, but as the size increases, the forward to back scattering ratio also increases. In Fig 1.5, scattering intensity is plotted vs. angle for the same size spheres, but with differing refractive indices. It is apparent that side scattering (~θ = 90º) is fairly sensitive to refractive index. Many instruments utilize both angular and size dependences shown in Figs 1.3-1.5 to give size and refractive index information for ambient aerosol.

1.2.5 Calculating Scattering for Inhomogeneous and Nonspherical Particles

In the ambient atmosphere it is often found that particles are nonspherical and the chemical constituents within them are heterogeneously mixed. Since the basic assumptions of Mie theory are that the particles are homogenous spheres, Mie theory is often unsuitable for calculating the optical properties of real particles. Various different methods are available for calculating the matrix elements and scattering efficiencies for nonspherical and/or heterogeneous particles. Mishchenko (2000) [*Mishchenko et al.*, 2000] gives a good overview of techniques available for these types of particles.

It has been suggested that mixing state plays a large role in determining the radiative properties of absorbing aerosols such as elemental carbon. For instance, it has been shown through modeling that if an elemental carbon particle is surrounded by a non absorbing shell its absorption may be amplified [*Ackerman and Toon*, 1981; *Jacobson*, 2001; *Schnaiter et al.*, 2005]. Methods for calculating core – shell morphology [*Bohren and Huffman*, 1981] predict enhanced absorption relative to a particle that is a homogenous mixture of the two substances. These theories have even been extended to clusters of spheres (several small attached spherical particles) (e.g. [*Fuller et al.*, 1999]). It is not yet proven whether or not these models are sufficient to model the actual optical behavior of atmospheric soot particles.

Perhaps the most flexible method for computing the optical properties of nonspherical and heterogeneously mixed particles is the discrete dipole approximation (DDA) [*Draine and Flatau*, 1994]. DDA represents the particles as a number of discrete dipoles that are allowed to interact with the electromagnetic field. The more dipoles one uses in the calculation, the more accurate the calculation becomes. DDA has the advantage of being able to compute the optical properties of an arbitrary particle. However, for large sizes, the computation becomes very large and infeasible for desktop PCs.

A few other techniques exist for calculating optical properties of homogenous nonspherical particles. The most widely used method is the T-Matrix method, which is a solution of the scattering problem for particles possessing rotational symmetry. The T-matrix method is attractive because it is computationally efficient. The T-matrix method is beginning to see use in both satellite and ground based retrievals of optical properties

from remote sensing (See Sec 1.3.5). For a review of the T-matrix method, see [*Mishchenko et al.*, 1996].

1.2.6 Beer's Law and Scattering and Absorption Coefficients

Given the definitions and tools provided by single particle optics, we are ready to tackle bulk optics. Visibility on a given day is primarily determined by optical depth. Optical depth (**t**) is given by Beer's law to be:

$$\frac{I}{I_0} = e^{-\tau} = e^{-\beta_{ext} x} \tag{19}$$

where I and I_0 are the transmitted and incident intensities, x is the pathlength and $\mathbf{b}_{ext}$ is the extinction coefficient. In the atmosphere there are contributions to extinction from both aerosol particles and gas molecules:

$$\mathbf{b}_{ext} = \mathbf{b}_{ext,p} + \mathbf{b}_{ext,g} \tag{1.20}$$

We can relate the particle extinction chemical composition and size through the following relation which gives the extinction coefficient for l chemical classes:

$$\beta_{ext,p} = \sum_{l} \int_{-\infty}^{\infty} C_{ext}(m_l, D_p) N(D_p) dD_p \tag{1.21}$$

Analogous relations hold for scattering and absorption. Through this equation, we have shown that the aerosol extinction depends on chemical composition through refractive index. Moreover, extinction is directly dependent on size distribution. This equation implies that if we had a measurement that could apportion all l chemical species to sources and determine their size distributions, then we could apportion aerosol extinction, scattering and absorption. We shall find in the next section that no such instrument currently exists.

When evaluating radiative forcing, it is useful to think of a quantity that is known as the single scattering albedo, which is defined as:

$$\omega = \frac{\beta_{scat}}{\beta_{ext}} = \frac{C_{sca}}{C_{ext}} \tag{1.22}$$

It is usually estimated that aerosol above **w** = 0.85 will have a cooling effect on the earth. Note that $\mathbf{b}_{ext} = N*C_{ext}$, where N equals the number concentration of particles. Although there is no implicit dependence on size distribution (an intensive variable), it is dependent on *chemical* size distribution according to the previous relation. This is important as this shows that different aerosol sources and concentrations will affect the single scattering albedo differently.

During early measurements of atmospheric extinction, Angstrom (1929) [*Angstrom*, 1929] noted that there was a relationship between extinction and wavelength:

$$\beta_{ext} \propto \lambda^{\alpha} \tag{1.23}$$

where **a** is the well-known Angstrom exponent. It was later it was found that the angstrom exponent is related to the aerosol size distribution through

$$\alpha = \upsilon * -2 \tag{1.24}$$

$$\frac{dN}{d\log D_p} = const \times D_p^{\upsilon *} \tag{1.25}$$

Thus, if the extinction coefficient is measured as a function of wavelength in the atmosphere, it is possible to obtain some information on size distribution. The Angstrom exponent is widely used by remote sensing instruments such as satellites to obtain the size distribution of atmospheric aerosols.

1.2.7 Relative Humidity

While the work in this thesis is not directly concerned with aerosol thermodynamics, it is important to discuss the strong dependence of optical properties on particle water content. As we saw in Table 1.1, aerosols are commonly made up of water soluble salts. When the relative humidity (RH) is high enough, these salt aerosols will under go deliquescence and uptake water, such that particle size increases with relative humidity. It is estimated that for relative humidities above 70-80%, over half of the aerosol mass is water [*McMurry*, 2000; *Rood et al.*, 1989]. Fig 1.3 shows that scattering depends on $\sim D^6$ for sizes in the middle of the accumulation mode. Therefore when aerosols of this size take up water, scattering will increase by a large extent [*Malm and Kreidenweis*, 1997].

Water uptake by ambient aerosol is strongly affected by mixing state. Mixing a soluble salt with organic material can increase the overall solubility of the organic particle [*Prenni et al.*, 2003]. As mentioned above, this increase in size will result in an increase in scattering (and possibly absorption). However, other measurements indicate that chemical composition may play a secondary role to size when considering the particles ability to form a condensation nucleus [*Dusek et al.*, 2006]. The same argument holds for elemental carbon – salt mixtures. The addition of a soluble salt will cause the black carbon particles to take up water at a decreased RH forming core-shell particles which have an enhanced absorption [*Lesins et al.*, 2002]. Water uptake by particles that have an insoluble core has been modeled by modifying the existing Kohler theory; however the situation is complicated by any heating of the core due to absorption [*Nenes et al.*, 2002].

1.3 Measurement of Key Aerosol Variables

Aerosol optics assessments are carried out through the measurement of the key variables we introduced in Sec 1.2; here we describe these measurements. These chemical and physical measurements will influence models on the lowest, most fundamental level. The development of new real-time aerosol measurement instrumentation has allowed for an increase in our understanding of atmospheric processes [*Sullivan and Prather*, 2005]. The most significant advances in aerosol measurements have been made with the introduction of new techniques to measure angular scattering profiles (Sec 1.3.3.1) and aerosol absorption and extinction using the photoacoustic and cavity ring-down techniques (Sec 1.3.3.3). Furthermore, standard light scattering techniques are being coupled to real time chemical measurements (Sec 1.3.2.1). A comprehensive review of aerosol measurements, excluding remote sensing, has been provided previously by [*McMurry*, 2000]. Here, we follow McMurry (2000) in the description of the more standard *in situ* measurements, but we include sections on remote sensing by both ground and satellite instruments (Sec 1.3.5). These remote sensing sections have been included because there has been an increased effort to understand aerosols using satellite measurements. More detailed reviews of remote sensing and satellite measurements may be found in [*Kaufman et al.*, 2002; *Yu et al.*, 2006]. Overall, this section is organized similarly to the last section, starting with basic aerosol size measurements and moving to more complicated measurements of integrated optical properties on a global scale.

1.3.1 Size distribution

As pointed out in Sec 1.2, size has a very large effect on aerosol optical properties. For particles in the accumulation mode, scattering increases roughly as D^6. While microscopy may be used to obtain direct geometric diameters (D_p), it is not a feasible method for statistical distributions over long periods of time at a high time resolution. For this reason, particles are typically separated by their aerodynamic, electrical or optical properties and then counted at frequencies exceeding 100 Hz. It is important to keep in mind that these measurements have different metrics (e.g. geometric and aerodynamic size) of size and that converting between two types of size can lead to large errors as it requires assumptions to be made regarding shape and material density. Since scattering depends strongly on size, attention must be paid to these errors.

1.3.1.1 Aerodynamic Sizing Methods

The most common method for measuring aerosol sizes from ~0.2 – 20 μm is aerodynamic sizing. The typical aerodynamic particle sizer is based on the early designs by Dahneke (1973) [*Dahneke*, 1973]; a schematic of a typical instrument is shown in Fig 1.6. The aerosol is pulled into the instrument through a nozzle, and the resulting beam of particles is surrounded with sheath air in order to prevent particle divergence. After exiting the nozzle, each particle traverses two continuous wave laser beams where at each beam, the particle scatters a pulse of light. Based on the time difference between the two pulses, a size is determined based on an empirical calibration. The resultant *aerodynamic diameter* (D_a) is related to the geometric diameter by

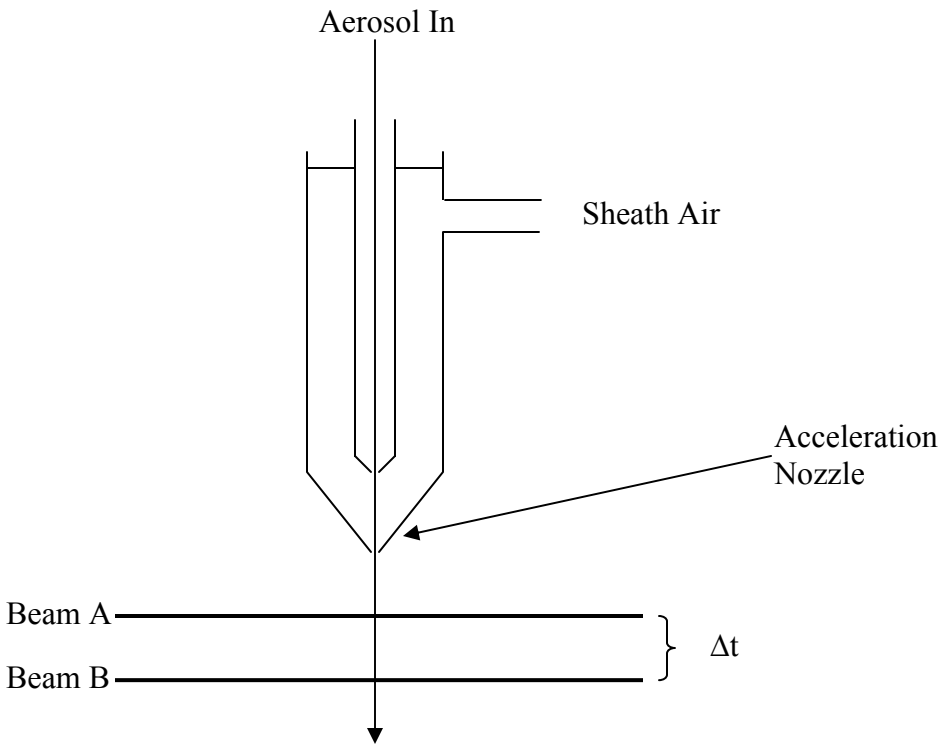

Figure 1.6. Schematic of an aerodynamic particle sizing instrument. Aerosols are pulled through a nozzle where they under go an acceleration that is dependant on their aerodynamic diameter. The aerodynamic diameter of the particle is determined by the particle velocity.

$$D_a = D_p \sqrt{\frac{C(D_p)\,\rho_p}{\chi_d\; C(D_a)\,\rho_0}} \tag{1.26}$$

where ρ_p and ρ_0 are the particle and standard density, C is the Cunningham slip correction factors and χ_d is the dynamic shape factor [*Hinds*, 1999]. The standard density is the density of whatever particles were used to determine the empirical size calibration of the instrument. Typically polystyrene spheres are used which have densities of ~1g/cm^3.

There are two commonly available particle sizers. The TSI (www.tsi.com) aerodynamic particle sizer (APS) measures particles from 0.5 – 20μm in diameter. The other particle sizer is the API AeroSizer [*Oskouie et al.*, 1998]. Although the API AeroSizer is no longer in production, it is instructive to look at its development. It is important to stress that information regarding the transmission efficiency of these commercial instruments has not been provided by the manufacturers. However, recent studies have independently measured transmission efficiencies for the APS [*Peters and Leith*, 2003; *Volckens and Peters*, 2005] and API aerosizer [*Thornburg et al.*, 1999]. These studies of transmission efficiency have indicated losses for large liquid particles. Older versions of the TSI APS were found to give large errors in particle mass due to spurious counts at large particle sizes that gave low scattered intensity [*Stein et al.*, 2002]. These effects were attributed to problems with particle recirculation in the optical cavity of the instrument. This has been corrected in newer versions of the instrument [*Stein et al.*, 2003]. Others have also indicated sizing errors due to the distortion of large liquid droplets in the expansion of the nozzle [*Bartley et al.*, 2000; *Mallina et al.*, 1997; *McMurry*, 2000; *Secker et al.*, 2000; *Secker et al.*, 2001].

1.3.1.2 Optical Sizing Methods

Particles may be detected using light scattering at sizes above ~0.1μm. The basic operating principal of the optical particle counter (OPC) is that the intensity of light scattered by a single particle may be used as a measure of its size. A schematic of an OPC is shown in Fig 1.7. The OPC works by pulling aerosol particles into the center of an ellipsoidal reflector (like those used in flashlights) where it passes through a beam of light. Upon passing through the light beam, the light scattered by the particle is collected by the ellipsoidal reflector and focused onto a photomultiplier tube. The output pulse from the photomultiplier tube is analyzed for height, which is related to size. The relationship between the instrument response and size is complicated, but may be predicted by Mie theory for homogenous spheres.

In order to calibrate the OPC, standard spheres of a known refractive index are sampled. With knowledge of the angular range (Ω) of the instrument, the theoretical instrument response (R) can be calculated with Mie theory:

$$R = \int_{\Omega} \frac{|\mathbf{X}|^2}{\mathbf{k}^2} d\Omega \tag{1.27}$$

Once the calibration is set, it is adjusted for particles spanning a wide range of refractive indices. This is because particles of different refractive indices scatter light in different ways as shown in Fig 1.3. Figure 1.8 shows the results of such a calculation for an instrument having an ellipsoidal reflector similar to the one shown in Fig 1.7. In Fig 1.8, the black curve is taken to be the average response of atmospheric particles. Therefore during sampling, knowledge of intensity equates to knowledge of size via the average curve in Fig 1.8. The curves in Fig 1.7 were calculated using a single wavelength. For

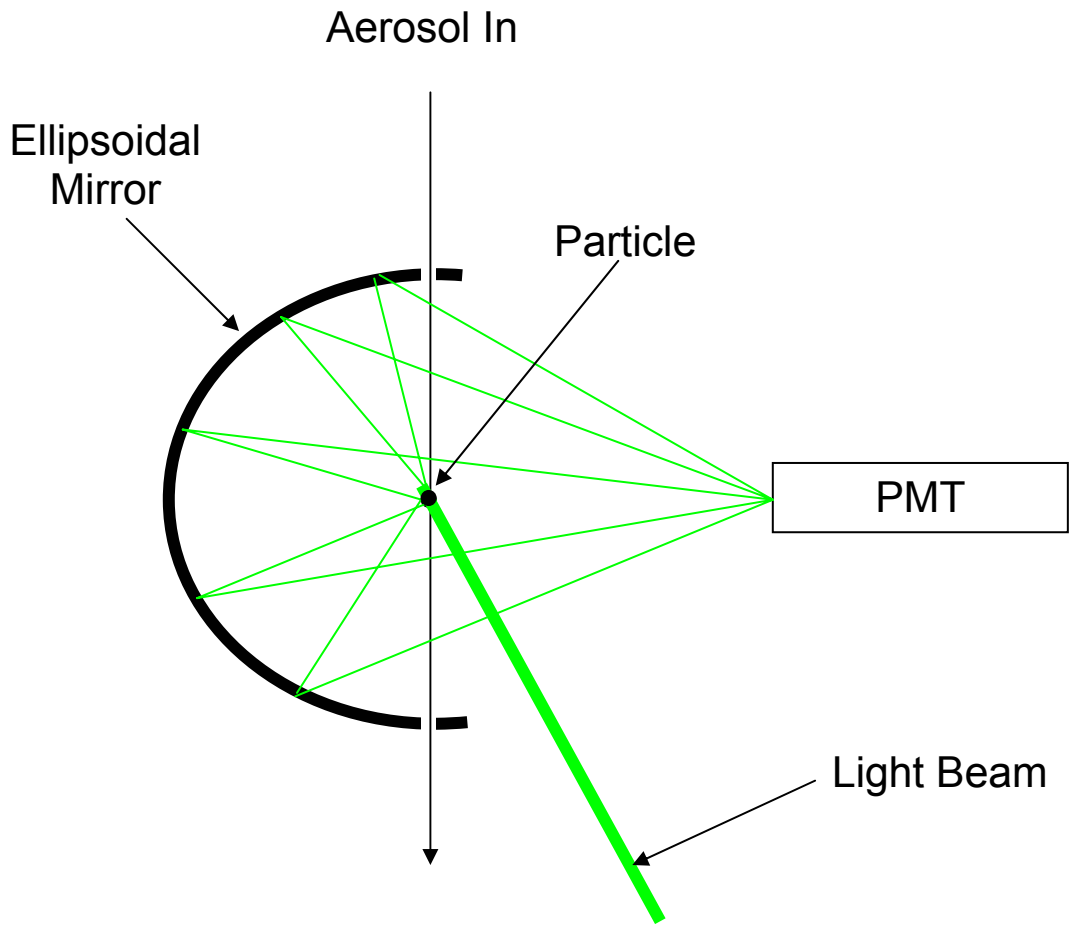

Figure 1.7. Schematic of an optical particle counter.

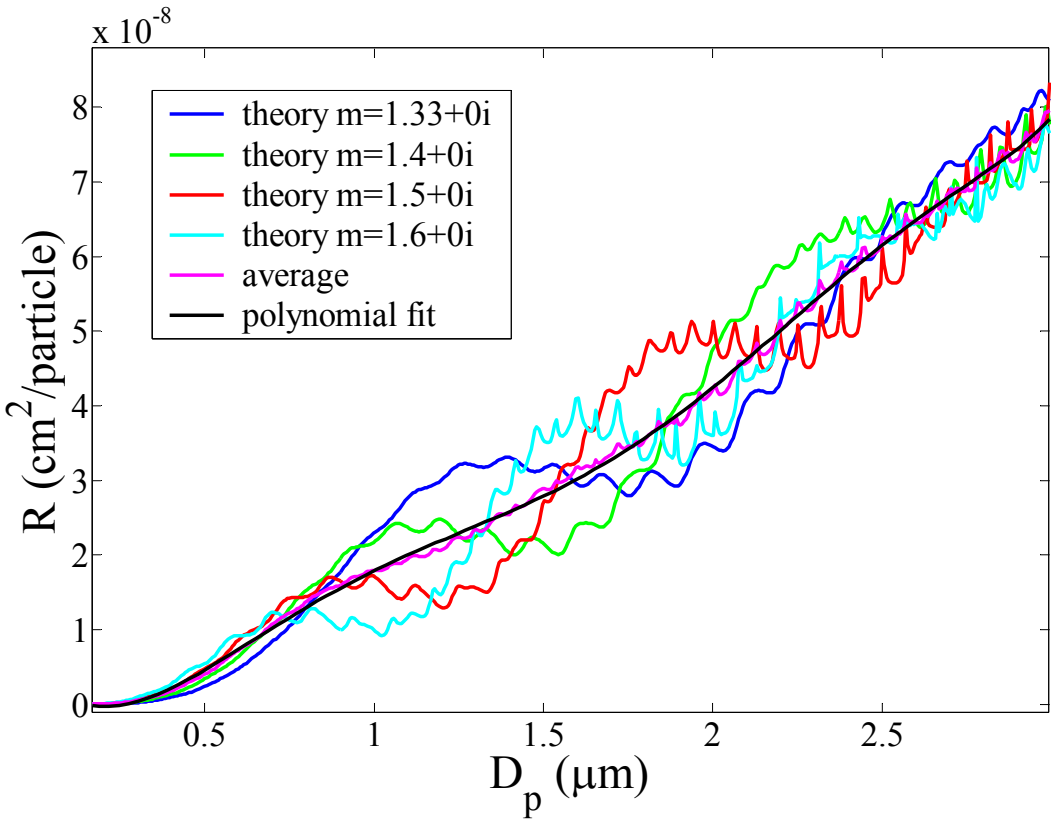

Figure 1.8. OPC response is determined by averaging instrument response for several refractive indices. Errors may be substantial above 1μm for single wavelength instruments. This happens to be the exact response for the OPC used in the ATOFMS instrument described later in Sec 1.3.2.2.

OPCs that use light sources having broad spectrums, the oscillatory nature of the response curves is smoothed out [McMurry, 2000]. Particles having a different refractive index will give have a different response characteristic than response assumed for the OPC. This will be interpreted as the particle having a different size -this factor limits the size resolution of the OPC. OPCs may be prone to other artifacts such as a decrease in particle size due to evaporation [*Biswas et al.*, 1987]. A comprehensive review of the existing OPC instruments is given in McMurry (2000) [*McMurry*, 2000].

1.3.1.3 Electrical Mobility Sizing Methods

For particles too small to be detected optically (<~100nm), electrical sizing methods may be used. This technique relies on the fact that most atmospheric particles carry a nonzero charge on them; therefore they may be deflected in an electric field. Figure 1.9 shows a schematic of the most common instrument used to size aerosol particles on the basis of electrical mobility. Known as the scanning mobility particle sizer (SMPS), this instrument works by first pulling charged aerosol into the space between the two coaxial cylinders. As the aerosols drift down the cylinder, particles having the correct size/charge will be attracted to the cylinder. Particles that have a higher *electrical mobility* (see Hinds, 1999) will move over toward the rod faster. Particles having a lower mobility will tend to stay in closer alignment with the flow streamlines. Particles having just the correct mobility diameter (D_m):

$$D_m = D_p \frac{C(D_m)\chi_d}{C(D_p)} \tag{1.28}$$

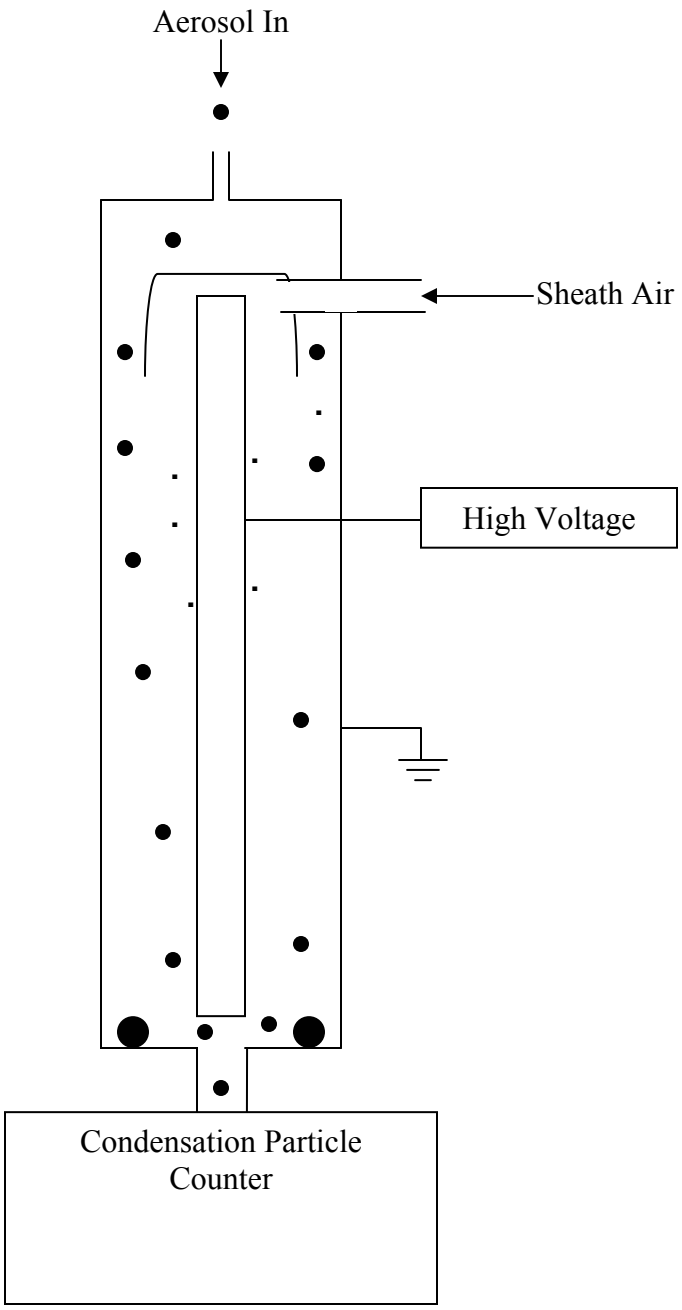

Figure 1.9. Schematic of a differential mobility sizer and a condensation particle counter (CPC). When used together, they are referred to as a scanning mobility particle sizer. The instrument determines electrical mobility size distributions.

will be able to exit a small hole in the bottom of the cylinder, where they can be detected with a device known as a condensation particle counter (CPC). The CPC grows the particles in a supersaturated vapor of butanol and counts them optically. The first part of the instrument is known as a differential mobility analyzer (DMA), and it can be used to select particles having one mobility diameter. The cylindrical geometry is the most common DMA configuration used for atmospheric measurements and was first described by [*Knutson and Whitby*, 1975; *Liu et al.*, 1974].

When the voltage within the DMA is scanned [*Wang and Flagan*, 1989], the entire size distribution may be acquired. The lower size range is approximately 10 nm and limited by diffusion of the small particles and the higher size limit (~600nm) is limited by particles obtaining several charges [*McMurry*, 2000]. The problem of multiple charges for large particles is the main limitation of the DMA. It is unfortunate that the higher size range is around 600nm, which corresponds to the center of the accumulation mode. Because of this, SMPS measurements are commonly combined with APS measurements to provide a description of the entire size distribution. However, difficulties are often encountered when trying to combine the two distributions due to the fact that they do not measure the same physically defined size. This has been exploited to obtain a measure of the particle effective density ($=\rho/\chi_d$) [*Khlystov et al.*, 2004].

1.3.2 Size Resolved Chemical Composition

There are many different techniques that can be used to measure the chemical composition of particulate matter. Perhaps the easiest way to measure chemical composition is to simply collect the particles on a filter, and prepare the sample for the

desired technique. Analysis of aerosols by filter sampling by standard off-line techniques has been around for many decades and many of these will not be covered here. Instead we focus mainly on the size resolved chemical measurements (e.g. real-time mass spectrometry) which are the most useful measurements for the assessment of aerosol optical properties (recall Eq 1.21).

1.3.2.1 Impaction

The impaction of particles on substrates allows for their separation as a function of time and size; after collection, their chemical composition can be measured with a wide variety of offline techniques. The idea stems from the observation that particles may be separated by their inertia (size) as they move around a sharp curve. This basic idea was first applied to atmospheric aerosols by [*May*, 1945]. A micro-orifice uniform deposit impactor (MOUDI), shown in Fig 1.10, is used to collect aerosols on stages according to size [*Marple et al.*, 1986; *Marple et al.*, 1981; *Marple and Willeke*, 1976]. As the particles flow through the MOUDI, they are forced to go around sharper and sharper bends. Therefore, the particles that have the most inertia (largest size, or mass) will be impacted at the top (wider bends) whereas the smaller particles will be impacted on the substrates at the bottom where the bends are sharper. Using a configuration different than that shown in Fig 1.10, the position of the impaction area may be changed continuously over time to extract temporal information with a 6 hr resolution [*Cahill and Wayakabashi*, 1993; *Raabe et al.*, 1988].

The benefit of collecting the particles on a substrate is that they may be analyzed with a number of different analytical techniques including microscopic and spectroscopic

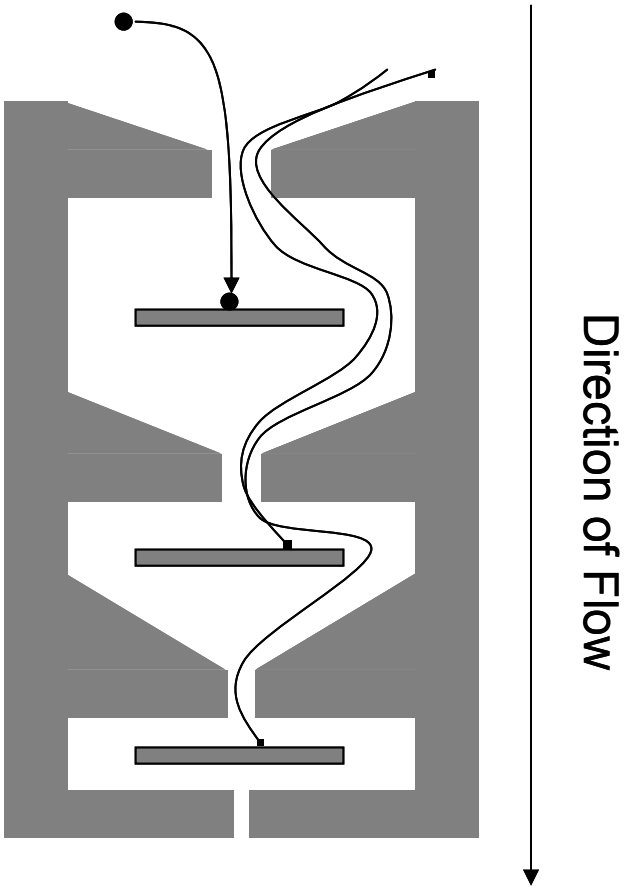

Figure 1.10. Schematic of a micro orifice uniform deposit impactor used to collect particles of different sizes on impaction surfaces.

methods. If the techniques used are non-destructive such as electron microscopy, the same particles may be analyzed several times enabling a more intensive analysis for a particular aerosol sample. Many of the techniques used to analyze impactor samples (e.g.inductively coupled plasma) are quantitative, and therefore accurate information on the concentrations of different chemical species are obtained. With quantitative chemical concentrations and size, a "forward calculation" of scattering and absorption may give an apportionment of scattering and absorption coefficients.

There are several drawbacks to analyzing particles through bulk impactor samples. First there is the issue of particle bounce: where particles bounce from one stage of the impactor to the next, causing errors in the size measurement whereby large particles (such as dust) will end up on impactor stages intended to collect small particles. Second, particles may undergo chemical transformation while they sit on the impactor sample: they may loose volatile species to the gas phase, or they may undergo reactions. If destructive bulk techniques are carried out, no information on the chemical associations within single particles is obtained. Lastly, the time resolution for impactor sampling is typically limited to 6 hours, which is often insufficient for capturing the dynamic nature of many short lived aerosol plumes, or during aircraft sampling.

1.3.2.2 Real-Time Size-Resolved Chemical Measurements

Due to the limitations of bulk impactor and filter sampling, real-time methods are desirable. Figure 1.11 shows a schematic of an aerosol mass spectrometer (AMS) that is used to collect quantitative mass concentrations of non-refractory aerosol material: primarily ammonium, nitrate, sulfate, chloride and organic carbon (OC). Aerosols are

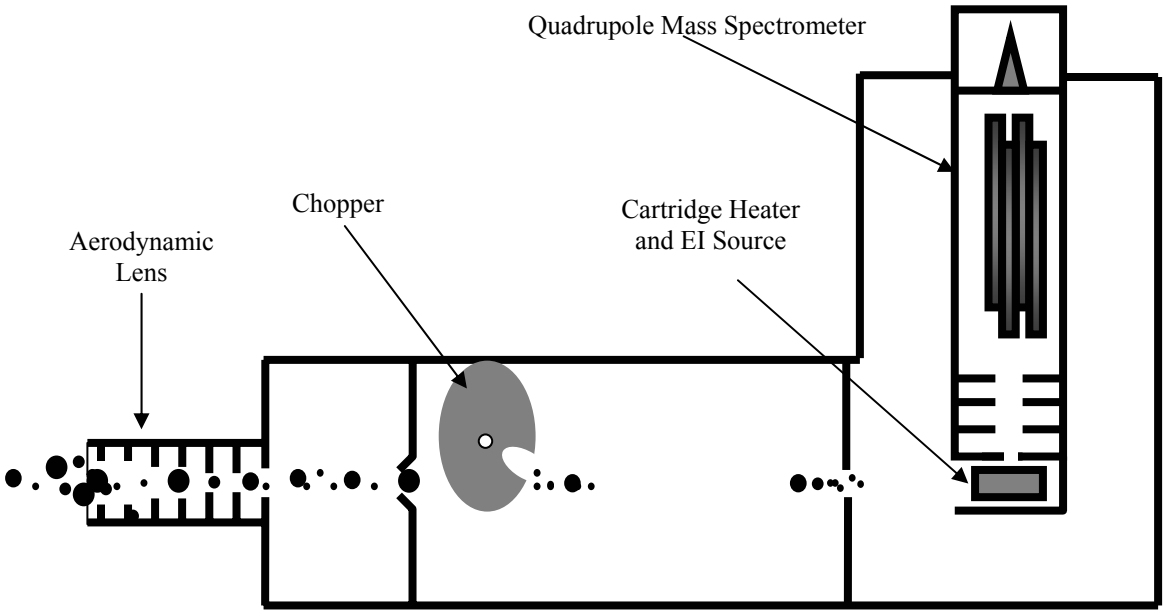

Figure 1.11. Schematic of an aerosol mass spectrometer. This instrument is used to measure bulk quatitative mass concentrations of non-refractory species including nitrate, sulfate, ammonium, chloride and organics.

focused into the vacuum chamber of the AMS using an aerodynamic lens. The aerodynamic lens consists of a series of orifices that get progressively smaller, resulting in a tightly collimated aerosol beam [*Liu et al.*, 1995a; *Liu et al.*, 1995b]. After exiting the aerodynamic lens, the aerosol beam goes through the center of a skimmer that is used to pump away excess gas. The aerosol beam is then chopped into short pulses by a mechanical beam chopper. The particles within each pulse will separate according to aerodynamic diameter. At the end of the vacuum chamber, the particles encounter a cartridge heater and electron impact ionization source. It is in this region that the aerosols are volatilized and ionized. The ions are then directed into a quadrupole mass spectrometer for mass analysis. A comprehensive review of the AMS instrument has recently become available [*Canagaratna et al.*, 2007]. Recent work using a high resolution time-of-flight in place of a quadrupole mass spectrometer has allowed for the determination of the empirical formula of the fragments within the mass spectrum [*DeCarlo et al.*, 2006; *Drewnick et al.*, 2005].

The AMS instrument has several advantages. The AMS determines quantitative concentrations of non-refractory species in real-time. The time resolution of the AMS can be shorter than 1 hr if there is sufficient aerosol mass. Furthermore, the AMS is not limited by optical detection limits and reports mass distributions down to a size of 20nm. Because of its quantitative capabilities, the AMS has proven to be of value measuring fluxes of non refractory aerosol species in the field, source profiles, and laboratory studies of reactive uptake. However, the AMS is limited to measure only the non-refractory aerosol species, which does not include sea salt, dust, elemental carbon, and many metals. Furthermore, because the transmission efficiency of the aerodynamic lens

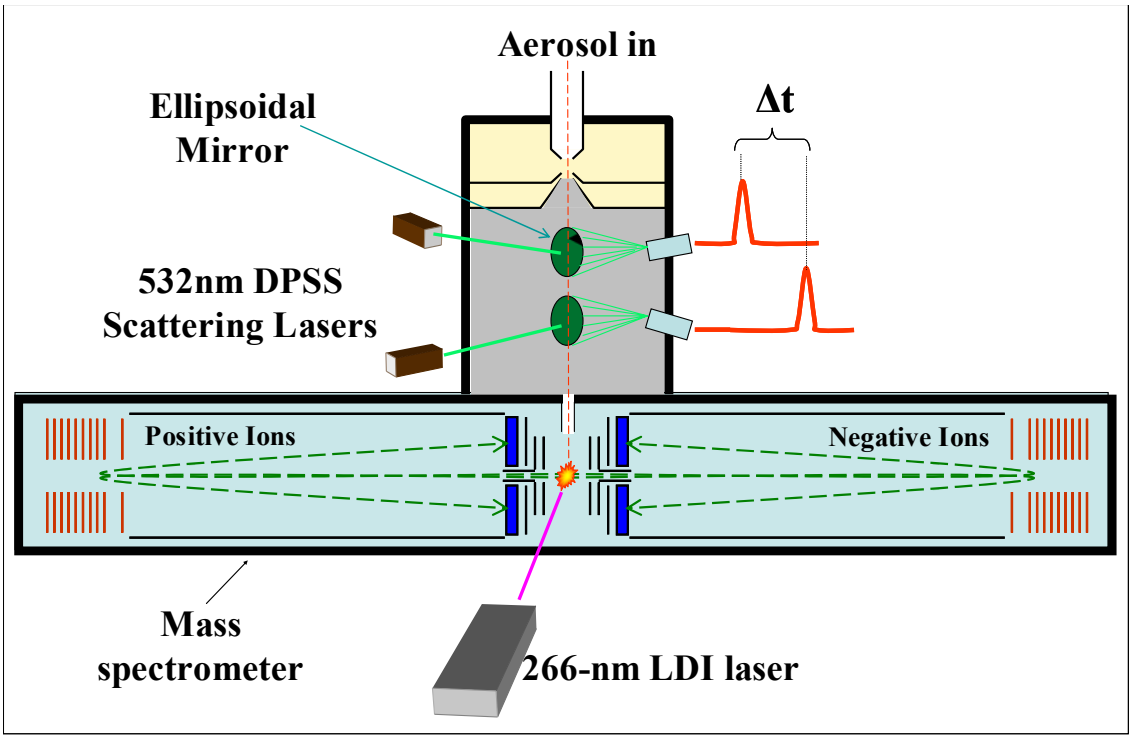

Figure 1.12. Aerosol time-of-flight mass spectrometer used to determine size resolved mixing state. The instrument can also be used to measure optical properties using light scattering.

decreases rapidly above 1μm, the AMS does not report mass distributions above that size. Lastly, it is currently unknown how the aerodynamic lens affects the other microphysical properties of the particles. Recent studies suggest that complete evaporation of aqueous salt particles occurs while the particle is inside of the aerodynamic lens [*Zelenyuk et al.*, 2006]. It is not currently known what effect this has on the ability of the AMS to quantify semivolatile species.

Real-time single particle mass spectrometry was developed in the 1990s by Prather and co-workers [*Gard et al.*, 1997; *Prather et al.*, 1994]. Since then, many others have developed similar instruments, resulting in several comprehensive reviews [*Murphy*, 2007; *Suess and Prather*, 1999]. A schematic of a single particle mass spectrometer known as an aerosol time-of-flight mass spectrometer (ATOFMS) is shown in Fig 1.12. This particular version of the ATOFMS works by pulling aerosol into vacuum through a nozzle inlet (some versions use an aerodynamic lens), where it undergoes supersonic expansion and is accelerated to a terminal velocity. The speed is measured by the time it takes to cross between two mutually orthogonal continuous wave laser beams. The aerodynamic diameter is determined by the particle velocity similar to the method used by the aerodynamic particle sizer (Sec 1.3.1.1). Using the travel time of the particle between the two laser beams, a frequency tripled Nd:YAG laser operating at 266nm desorbs and ionizes the particle in the center of the source region the mass spectrometer. The ions formed are then analyzed with the dual polarity mass spectrometer. Therefore, size and chemical composition for single aerosol particles are obtained as a function of time.

One of the major advantages of the ATOFMS is that it measures the chemical composition of single aerosol particles. This allows for the determination of what chemical species occur together (mixing state) within individual particles. Furthermore, the ATOFMS is not restricted to a set number of compounds and it is capable of analyzing both non-refractory and refractory aerosols. The major drawback of the ATOFMS is that matrix effects make the mass spectrum difficult to interpret quantitatively, and therefore the ion intensities have not been used to obtain mass concentrations. Lastly, like the AMS, the ATOFMS suffers from a non-ideal transmission efficiency. For the nozzle inlet, detection efficiencies (fraction of particles analyzed) from 10^{-3} - 10^{-6} are obtained.

1.3.2.3 Hyphenated Methods – More than Just a Measurement of size and Chemical Composition

Several of the sizing and chemical analysis methods discussed above can be combined to give more information about microphysical properties of aerosol particles such as density and refractive index. The DMA has proven useful for size-selecting aerosol particles prior to aerodynamic sizing. This allows one to determine the effective density via:

$$\rho_{eff} = \frac{\rho_0 D_a^2 C(D_a)}{D_p^2 C(D_p)} \tag{1.29}$$

where $\rho_{eff} = \rho_p/\chi_d$ is known as the effective density. The DMA has been combined with both AMS and ATOFMS instruments. In [*Spencer et al.*, 2007], it was found that different chemical classes of particles identified by the ATOFMS had different effective

densities. In [*DeCarlo et al.*, 2004; *Slowik et al.*, 2004], the AMS was used in a laboratory setting to measure the coating thickness of OC on EC particles. Effective density itself can be measured very accurately combining a DMA with other instrumentation as described by [*Geller et al.*, 2006; *McMurry et al.*, 2002].

The measurement principles of OPCs have also been extended to the AMS and ATOFMS. Murphy and co-workers showed that measuring both aerodynamic diameter and optical size allows for a determination of effective density [*Murphy et al.*, 2004]. This was followed by [*Moffet and Prather*, 2005] who showed that it is possible to obtain both refractive index and density for laboratory generated aerosol using the ATOFMS. Recently Cross and co-workers have added an OPC to the AMS, demonstrating the measurement of effective density in both the laboratory and in the field [*Cross et al.*, 2007].

1.3.3 Direct Optical Measurements

While chemically resolved size distributions may be useful for evaluating the microphysical parameters that feed radiation models, it is extremely important to measure these primary input parameters directly. For radiative transfer modeling, optical depth, single scattering albedo, and phase function are needed to calculate radiative forcing. For the calculation of radiative transfer, the full phase function is typically not needed; only an understanding of the fraction of forward to back scattering, commonly represented as g, is necessary. Nevertheless, as shown in Sec 1.2, there is information to be had in the phase functions, and therefore high resolution angular measurements may give insight into aerosol microphysical properties or how g varies as a function of morphology and

chemical composition. Since McMurry's review in 2000, significant progress has been made in the measurement of aerosol optical properties, and we provide a survey of the current knowledge here. The main advances have been made for techniques that measure absorption *in situ* (Sec 1.3.3.4) and angular information (Sec 1.3.3.1). There was a study published in 2005 called the Reno aerosol optics study (RAOS) that presented laboratory and ambient comparisons of state-of-the-art absorption measurements [*Sheridan et al.*, 2005].

1.3.3.1 Phase function – angular scattering information

Instruments that measure the dependence of scattering on angle for bulk aerosol samples are called polar nephelometers and have been used for many years [*Kerker*, 1997]. Polar nephelometers work by passing a beam of light through an aerosol sample; the light is measured using a photodetector that is mounted on a goniometer. The phase function is measured by recording scattered intensity as a function of angle. They have been used, for instance, to infer the refractive index of desert dust [*Grams et al.*, 1974] and serve as a check on atmospheric radiation studies [*Hansen and Evans*, 1980]. Basic bulk polar nephelometer instrument development is not currently an active area of research.

Most of the research on angular scattering is being done on single particles to obtain information on size, shape and refractive index. For particles greater than 1μm, Hirst and Kaye have used angular scattering to identify morphologically unique particles such as fibers [*Hirst and Kaye*, 1996; *Hirst et al.*, 1995; *Hirst et al.*, 1994; *Kaye et al.*, 2000; *Kaye et al.*, 1992]. Baumgardner and co-workers have been able to obtain size and

refractive index on large particles in clouds using angular scattering information [*Baumgardner et al.*, 1996; *Baumgardner et al.*, 2001]. Dick and McMurry were able to use an instrument developed by [*Wyatt et al.*, 1988] to collect angular information on single aerosol particles in the size range of 0.2 – 1μm and determine refractive index and morphology information [*Dick et al.*, 1994; *Dick et al.*, 1998; *Sachweh et al.*, 1995]. The most recent work has been carried out by Chang and co-workers who used an ellipsoidal reflector (similar to OPCs) to collect the light scattered by a single particle and focus it onto an intensified CCD camera. While most angular scattering experiments utilizing CCD cameras have been limited to supermicron sizes, this technique has able to obtain useful information for particles well into the accumulation mode. This has yielded very high resolution scattering patterns for forward angles and has been very useful for identifying particle morphology [*Aptowicz et al.*, 2004; *Aptowicz et al.*, 2006; *Holler et al.*, 2000; *Holler et al.*, 1998; *Holler et al.*, 1999; *Sindoni et al.*, 2006].

1.3.3.2 Scattering Coefficients by Nephelometry

The primary instrument that is used to measure the scattering coefficient is called a nephelometer. Although nephelometry has been around for quite some time, it remains an active area of research. An excellent review of the method has been written by [*Heintzenberg and Charlson*, 1996]. A schematic diagram of a typical nephelometer is shown in Fig 1.13. The output from the light source in a nephelometer is put through a diffuser to ensure that the output is lambertian (i.e. constant intensity as a function of angle: a “cosine” response). The light is directed into a sampling volume that is continuously flushed with aerosol laden sample. A photomultiplier tube is located at one

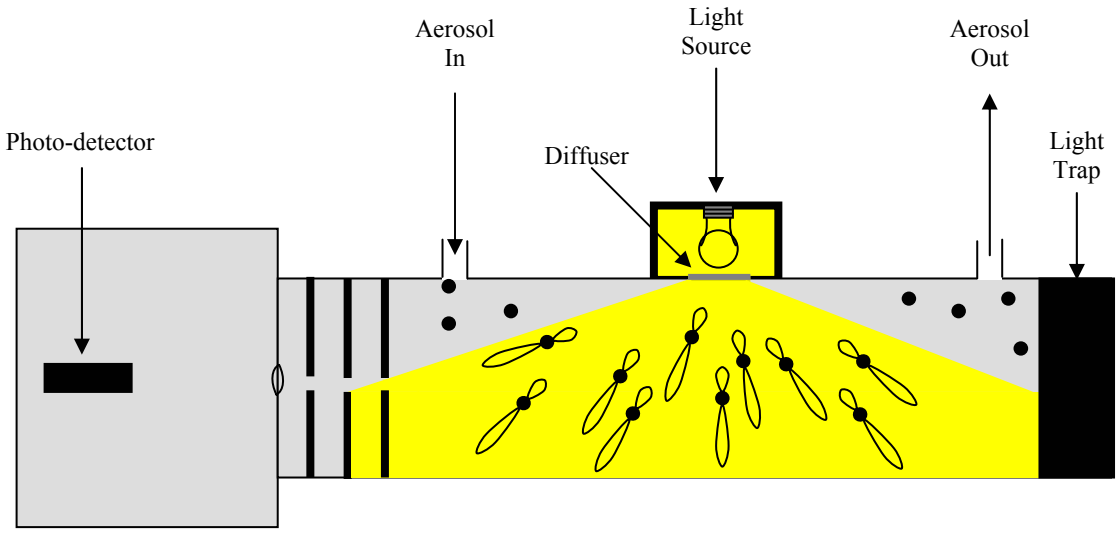

Figure 1.13. A typical integrating nephelometer used to measure the scattering coefficient. The scattering coefficent measured by the nephelometer is not exact because it does not integrate over all possible scattering angles.

end of the scattering volume, opposite a light trap. The walls of the nephelometer are typically painted black to prevent wall scatter from causing a large background signal. Some nephelometers may have detectors with notch filters in them to allow the determination of scattering as a function of wavelength, as well as estimation of theAngstrom exponent. A range of angles are collected - typically between ~10 - 170º. Because the nephelometer has a defined set of angles and a finite spectral width, care must be taken when comparing different instruments [*Anderson and Ogren*, 1998].

Because the nephelometer only collects a certain angular range, it is incapable of measuring the exact scattering coefficient, which requires integration over all angles. In fact, because large particles scatter so strongly in the forward direction, errors as large as 50% may be realized for the scattering coefficient. Anderson and co-workers used a multi-wavelength nephelometer to develop a correction scheme utilizing the Angstrom exponent [*Anderson et al.*, 1999]. Additionally, some nephelometers (such as the TSI nephelometer) have a light source that generates a great deal of heat, and as a result, the aerosol sample is heated causing evaporation of liquid water. This causes problems if sampling is to be carried out at ambient relative humidity because the scattering coefficient measured in the instrument will not be the same as that in the ambient atmosphere. For this reason, it is often desirable to control the sampling RH and measure RH and temperature inside the nephelometer. Other nephelomters exist that use different light sources and slightly different measurement configurations. Recently [*Heintzenberg et al.*, 2006] executed a comprehensive comparison of 3 common models of the nephelometer and highlighted the need for added knowledge of the response characteristics of these instruments.

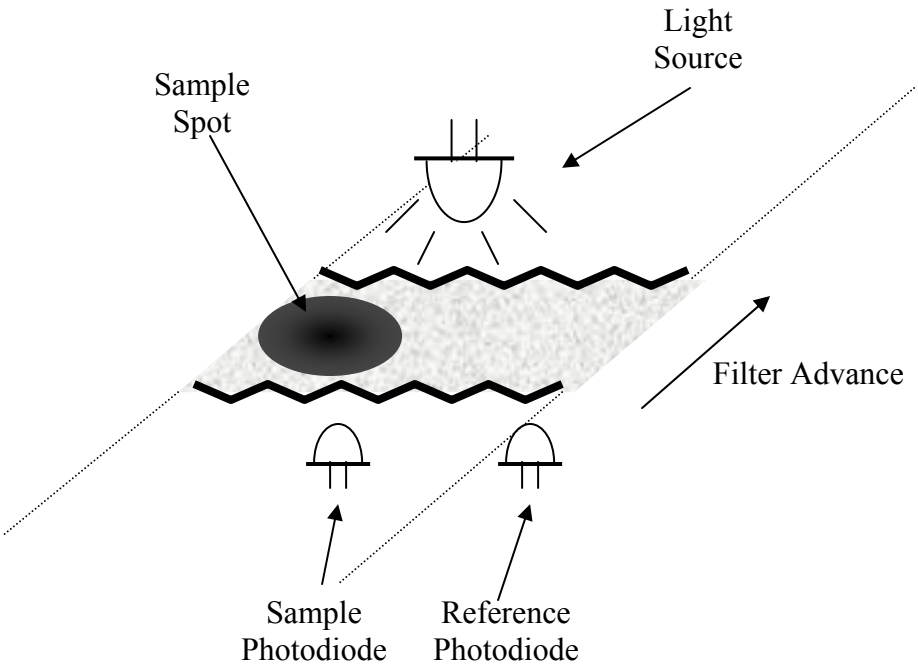

Figure 1.14. Illustration showing the measurement principle of filter based methods for measuring particle absorption.

1.3.3.3 Filter Based Absorption Techniques

The simplest way to measure aerosol absorption is by collecting it on a filter and measuring the light attenuation through the filter [*Hansen et al.*, 1984]. Some of these filter based techniques were originally developed as ways to measure black carbon mass, and others were developed to measure absorption coefficient. A schematic of this technique is shown in Fig 1.14. The sample is deposited on a spot and the sample spot is overloading the sample. The technique is complicated by the fact that particle scattering will contribute to the overall attenuation measured. Different methods have been developed to correct for scattering by using a multi-angle scattering measurement [*Petzold and Schonlinner*, 2004]. Others have applied a simple algorithm that accounts for multiple scattering [*Arnott et al.*, 2005]. Several of these techniques were compared during the Reno aerosol optics study [*Petzold et al.*, 2005; *Virkkula et al.*, 2005].

1.3.3.4 In-situ absorption techniques

Newer techniques have been developed to measure absorption by aerosol particles in-situ, rather than following collection on a filter. One problem with these techniques is that they are prone to interference by $NO_{2(g)}$. Therefore, it is important to have a measurement of NO_2 collocated with the in-situ absorption instruments so that they can be corrected for this interference.

Photoacoustic spectroscopy has recently been applied to measure particulate absorption [*Adams*, 1988; *Arnott et al.*, 1995; *Arnott et al.*, 1999; *Moosmuller et al.*, 1997]. A schematic of the photoacoustic instrument is shown in Fig 1.15. In the photoacoustic technique, a pulsed beam of light is directed through the sample. As the

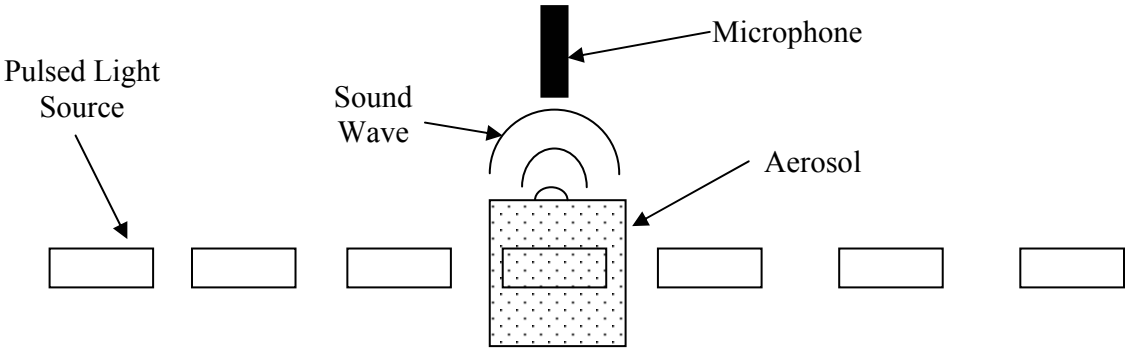

Figure 1.15. Schematic of the photoacoustic instrument used to measure aerosol absorption.

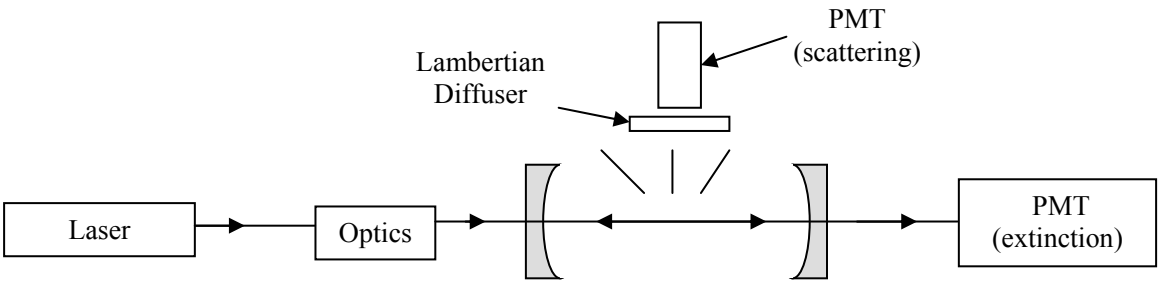

Figure 1.16. Example of a cavity ringdown instrument that measures extinction, scattering and absorption. The PMT that is orthogonal to the cavity is for measuring the scattering coefficient. The absorption coefficient is obtained by the difference of extinction and scattering.

sample absorbs the incident light, it heats the air surrounding the particle, setting up a pressure wave within the cavity. The pressure wave is then detected by a microphone, and the resulting signal is related to the absorption coefficient. Field and laboratory tests indicate that the instrument performs well [*Moosmuller et al.*, 2005]. However, this instrument is somewhat sensitive to noise and has yet to be proven aboard an aircraft platform.The cavity ring-down (CRD) technique can also be used to measure aerosol extinction [*Lack et al.*, 2006; *Pettersson et al.*, 2004; *Strawa et al.*, 2003]. A schematic of a typical CRD instrument is shown in Fig 1.16. The CRD works by transmitting a laser pulse into a cavity with two mirrors at both ends. As the pulse of light bounces back and forth in the cavity, a small amount of light leaks out at each pass. The resulting signal has an exponential decay that is related to the extinction coefficient. Some CRD instruments also simultaneously measure the scattering coefficient, which is also related to the characteristic ring-down time [*Strawa et al.*, 2003]. Knowledge of both the extinction and scattering coefficients allows for the determination of the absorption coefficient via Eq 1.11. However, this technique of measuring scattering suffers from truncation errors for large particles as was observed in nephelometry. However, the measurement of total extinction suffers from no such errors (by definition). The CRD appears to be a very robust new technology to measure scattering, absorption and extinction and has recently shown excellent results aboard an aircraft platform [*Strawa et al.*, 2006].

1.3.4 Humidity effects

As discussed in Sec 1.2.7, the interaction of water with aerosol particles plays a major role in determining their optical properties. As a result, instrumentation to measure

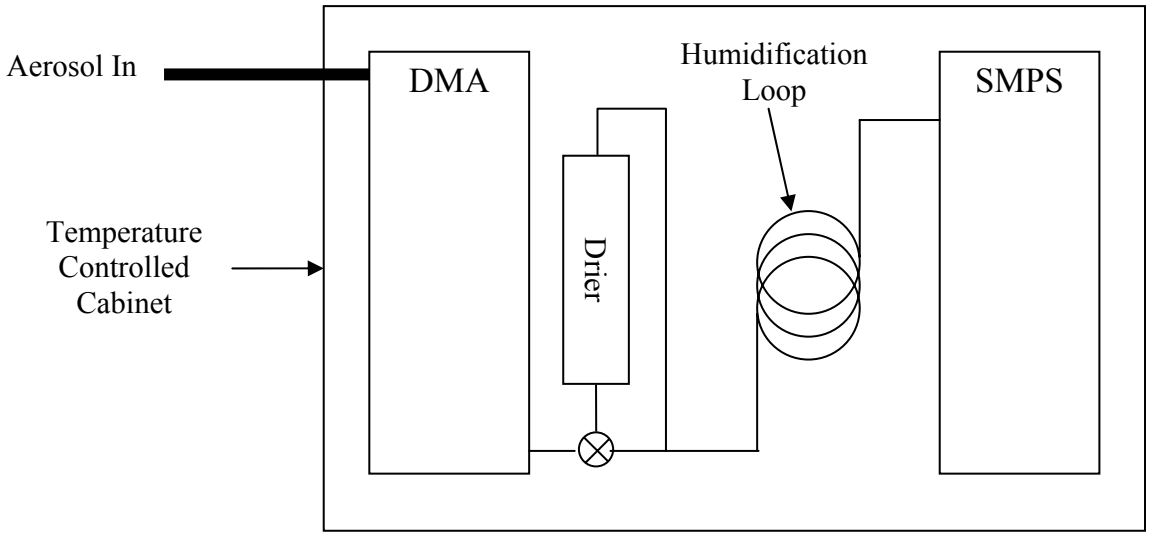

Figure 1.17. HTDMA instrument used to measure hygroscopic growth properties as a function of RH (g(RH)). To measure the g(RH), nephelometers take the place of the DMA and SMPS.

water uptake as a function of relative humidity is essential to understanding how aerosols influence climate. Figure 1.17 shows a schematic of an instrument that is capable of measuring the size change of aerosol particles at different humidities. This setup consists of one DMA to size select aerosol particles before they are transferred to an environment with controlled RH. The RH is controlled by either drying the particles or humidifying them using a nafion membrane (addition of water vapor). The size change of the aerosol is then measured with the SMPS. The configuration in Fig 1.17 is known as a humidified tandem differential mobility analyzer (HTDMA). The HTDMA instruments seem to be the instrument of choice when testing and modifying Kohler theory for water uptake of different aerosol systems including ambient aerosol [*Mcmurry and Stolzenburg*, 1989; *Rader and Mcmurry*, 1986; *Svenningsson et al.*, 1992]. Alternatively, the effect of humidity on the scattering coefficient may also be measured directly by using nephelometers in place of DMAs in the above technique [*Day et al.*, 2000; *Rood et al.*, 1987; *Rood et al.*, 1985].

1.3.5 Global Measurements & Remote Sensing

Moving on from measurements of single particles and bulk optical constants, we recognize the need to briefly cover measurements that are capable of considering aerosol optical properties on a global scale. As we will see, this is either accomplished through global networks of ground based measurements and space-borne satellites. Many of these methods involve complex retrieval processes to describe the ambient aerosols that we will not describe here, as they are outside the focus of this introduction.

1.3.5.1 Aerosol Robotic Network (AERONET)

The aerosol robotic network (AERONET) is a global measurement network that measures aerosol optical properties. The network consists of automated radiometers that measure sky radiances at a large number of different angles and wavelengths [*Dubovik et al.*, 2000]. AERONET determines the aerosol optical depth directly. Retrieval algorithms based on Mie theory give the complex refractive index and size if the aerosol loading is high enough [*Dubovik and King*, 2000]. It has also been shown that AERONET can be used to predict forcing by black carbon due to its strong absorption [*Sato et al.*, 2003]. All aerosol parameters correspond to column averages, and no vertical profiling of aerosol properties is obtained. However, light detection and ranging (LIDAR) may be used alongside AERONET to give vertical profiling information [*IPCC*, 2007].

The presence of non-spherical particles may affect the retrievals (i.e. the derivation of optical properties from algorithms). However, the presence of large numbers of non-spherical particles can be detected and effectively screened [*Dubovik et al.*, 2002; *Mishchenko et al.*, 1995; *Zhao et al.*, 2003]. Nevertheless, in order to have a complete description of aerosol properties over time, retrievals based on the T-matrix method have been developed and implemented to obtain the optical properties for non-spherical particles [*Dubovik et al.*, 2006]. The retrieval results for dust aerosol presented by Dubovik, 2006 were compared to the scattering matrices determined in the laboratory and were found to be in good agreement. One word of caution about AERONET measurements is that the retrieval accuracies have yet to be validated by an independent method [*Yu et al.*, 2006].

1.3.5.2 Satellite Measurements of Aerosol Optical and Microphysical Properties

Because satellites can capture large scale aerosol dynamics, they are the primary measurement tool used for the evaluation of global climate models [*IPCC*, 2007]. Most satellites are radiometers: instruments that measure radiation flux as a function of wavelength. Most satellites are known as passive sensors because they don't have their own light source, rather, they measure reflected/scattered solar radiation. However, newer satellites are active sensors, using light sources such as lasers to sense atmospheric phenomena. Table 1.2 gives a listing of select satellites that can be used for the retrieval of aerosol properties. It is seen from Table 1.2 that there are a variety of microphysical and optical aerosol parameters that are retrieved using complex algorithms.

The primary aerosol measurement that most satellites achieve is the measurement of aerosol optical depth (AOD or $\boldsymbol{\tau}$). Retrieval of AOD over the oceans or dark surfaces is usually facile; however over bright surfaces such as desert sand, the retrievals are more problematic due to the high background imparted by the surface. More sophisticated satellites such as MISR use multiple viewing angles to obtain retrievals of aerosol properties over bright surfaces. Some of the newer satellites such as CALIPSO use active sensing via a LIDAR instrument called CALIPSO. CALIPSO can obtain vertical distributions of clouds and aerosol plumes within the atmosphere. Other retrievals exist for determining aerosol microphysical properties such as size, refractive index and shape. Refractive index is usually obtained by fitting to a radiative transfer model employing Mie theory or T-Matrix. Because the radiometers are multiwavelength sensors, they may also retrieve size distributions using the Angstrom exponent.

Table 1.2. Satellite platforms giving aerosol related products

Instrument	Satellite	Aerosol Product	Key Refs
MODIS	Terra, Aqua	AOD, Angstrom Exp.	4,5,6
MISR	Terra	AOD, composition, size	7,8,9
CALIOP	CALIPSO	Vert. profile of extinction	10, 11
HIRLDS	Aura	AOD	10, 11
OMI	Aura	SSA	10, 11
NOAA – 6, 14	AVHRR	Angstrom exponent	12, 13
Earth Probe, Nimbus 7, Meteor 3, OMI	TOMS	AOD	14, 15
AATSR	ENVISAT	Size, AOD	16
POLDER	PARASOL	Refractive index, size, shape, AOD	1,2,3

1.[*Deuze et al.*, 2000] **2.** [*Breon et al.*, 2002] **3.** [*Herman et al.*, 1997] **4** [*Tanre et al.*, 1997] **5**.[*Chu et al.*, 2002] **6**.[*Remer et al.*, 2002] **7**[*Diner et al.*, 2002] **8** [*Kahn et al.*, 2005a; *Kahn et al.*, 2005b] **9** [*Abdou et al.*, 2005] **10** [*Stephens et al.*, 2002] 11. [*Anderson et al.*, 2005a; *Rao et al.*, 1989] **12** [*Rao et al.*, 1989] **13**[*Stowe et al.*, 1997] **14.** [*Hsu et al.*, 1999a; *Hsu et al.*, 1999b] **15.** [*Torres et al.*, 2002] **16** [*Grey et al.*, 2006]

Retrieval validation is a crucial exercise that utilizes a number of different techniques and approaches to ensure quality satellite products (retrievals that have been quality controlled). Retrievals of AOD may be validated with ground based measurements such as those available from AERONET [*Anderson et al.*, 2005b]. LIDARmeasurements close to AERONET can provide vertical profiles of AOD which can be used to validate the satellites that also obtain vertical profiling [*Campbell et al.*, 2003]. Similarly, detailed in-situ measurements aboard aircraft platforms provide detailed aerosol microphysics which can be used together with chemical and radiative modeling to validate the entire range of aerosol products from satellites [*Anderson et al.*, 2005b]. Newer satellite measurements will be used to obtain aerosol shape through the use of multiple viewing angles and polarization filters. It has been suggested to use AERONET sites to validate measurements of shape [*Mishchenko et al.*, 2004]. However, because AERONET measurements are themselves products of retrievals, it would be best to compare to direct measurements of aerosol shape.

1.4 Optical Closure Studies

Ensuring consistency between all measurement techniques should be a top priority for programs aimed towards impacting the current uncertainty levels of climate prediction. A closure study involves determining the same quantity with multiple techniques. If the different techniques agree, then closure is obtained; if the techniques do not agree, then the source of the discrepancy should be sought out. Closure studies are essential to ensure data quality for measurements used to impact policy [*Diner et al.*, 2004; *IPCC*, 2007].

In order to over determine aerosol parameters, intensive field studies are needed to bring several techniques together to simultaneously measure particles at the same time and place. Closure studies during major field campaigns should measure chemical size distributions and Mie theory to calculate scattering and absorption coefficients via Eq 1.21 and then compare them to values derived with nephelometers or sun photometers. Studies such as this usually find that the either the techniques or assumptions are not sufficient to obtain closure [*Clarke et al.*, 2002; *Quinn and Coffman*, 1998; *Wang et al.*, 2002]. It has been pointed out that studies of this sort that are successful may be of limited use due to the wide range of assumptions that go into the "forward" models to gain closure [*Reid et al.*, 2005]. Other closure studies measure aerosol coefficient directly, then compare the measured quantities. Such studies usually indicate good agreement [*Collins et al.*, 2000; *Redemann et al.*, 2003]. From this, it is apparent that our knowledge of how aerosol microphysical and chemical properties affect aerosol optics is insufficient to allow for meaningful scientific conclusions about how aerosol chemical and physical properties affect climate. Therefore more effort needs to be made to improve measurements of aerosol microphysical properties as well as the models used to calculate the bulk aerosol optical parameters.

1.5. A Brief Comment on Atmospheric Models

Models are, in general, the application of theory to describe and predict some behavior. In this introduction, one type of model was already encountered: single particle light scattering models. In atmospheric chemistry, many more models exist for describing the large scale processes on a global scale. Chemical transport models describe how the

chemical constituents of the atmosphere transform over time. Radiative transfer models describe how solar and thermal radiation interacts with the different layers and components of the atmosphere. Meteorological modeling describes complex large and small scale weather patterns and draws primarily from the field of *dynamic meteorology*. Global climate modeling combines all of these models into one utilizing simplifying assumptions and parameterizations (e.g. [*Schmidt et al.*, 2006]). Models are the primary tool with which climate predictions are made, and their output influences policy decisions [*IPCC*, 2007]. Therefore, it is imperative that we ensure accuracy within the models by checking them with the measurements outlined in the previous section.

Atmospheric models describe processes from those taking place on a single particle to processes which take place over entire oceans or continents. In order to check for sensitivity and consistency between different climate models, a coordinated research effort is needed. Such an effort is underway as part of the AeroCom project, which compares several state-of-the-art climate models [*Kinne et al.*, 2006]. Besides inter-comparing different modeling approaches, it is extremely important to test the models against measurements to ensure the models accurately cover the physical and chemical processes taking place. For example, many single particle measurement techniques have indicated that species are internally mixed through condensation and coagulation. A decade ago, the internal mixing of aerosols was rarely considered in the framework of a global model, but have recently been accounted for [*Adams and Seinfeld*, 2002; *Easter et al.*, 2004; *Stier et al.*, 2005]. When internal mixtures are accounted for using a full radiation scheme, it is found that the they have a large impact on the global aerosol radiative forcing [*Haywood et al.*, 1997; *Jacobson*, 2000; *Jacobson*, 2001]. This has been

one example of how measurements have influenced models, and each measurement described above can and has been employed to check models.

1.6. Conclusions and Direction of Thesis

For a complete understanding of how aerosols affect climate, a better knowledge of processes from those that take place on single particles to those that take place on a global scale is needed. Integrating measurements and models that cover this wide range in spatial scales is extremely problematic, and a systematic approach is needed [*Ackerman et al.*, 2004; *Seinfeld et al.*, 2004]. The data must be of sufficient quality so that the uncertainties are low enough to provide for an accurate climate forecast; only validation and closure studies of the key optical parameters will ensure this level of quality. Along these lines, there is an urgent need to validate products provided by the global AERONET network with independent measurements of detailed optical, chemical and physical properties since the AERONET is used for validation of other important measurements such as satellites. It is also important to understand that each measurement has its niche and they are all complimentary. For example, it would not be wise to compare a raw single particle chemical composition to satellite retrieval due to the large disparity in spatial scales. Rather, the single particle data may be best compared to a chemical model that captures the mixing state of the particles at a specific location that is representative of the region. Principles such as this will guide the development of better optical measurements and models.

Many new measurements are becoming available to help advance our understanding of how aerosols affect climate. Real – time methods such as ATOFMS and

AMS are continually advancing to include the measurement of additional aerosol microphysical properties beyond size and chemistry. Optical instruments such as CRD can measure scattering, extinction and absorption with unprecedented accuracy and have been deployed on aircraft to provide vertical profiling of these parameters. Remote sensing instruments on the ground and in space are becoming available to provide global products of aerosol microphysical properties that were unavailable a decade ago. All of these different measurements should be integrated to give a new and more accurate insight into the effects of aerosols on climate.

This thesis will focus on ATOFMS measurements with particular emphasis placed on optical and microphysical property measurement. It is necessary to comment on areas where the ATOFMS instrument can be improved. The ATOFMS is attractive for making optical measurements because it obtains the key single particle variables: chemical composition and size. The light scattering region of the ATOFMS can be used to make optical measurements and it will be shown in Chapter 2 that the instrument is capable of obtaining refractive index and density information in addition to chemical composition and size. The method developed in Chapter 2 will be applied to ambient aerosol in Chapters 3-4. These ATOFMS optical measurements will be useful for: 1) providing spot checks on aerosol properties for measurements such as AERONET, 2) providing point checks on chemical models, and 3) the discovery of new and important chemical processes and sources in the atmosphere to include in models. Of course the instrument could be made better in many respects. The perfect aerosol measurement would be quantitative in size, chemical composition and optical properties. The perfect aerosol measurement would be located everywhere and have infinite time resolution. The

ATOFMS still has many outstanding issues with quantitation, but advances continue to be made [*Qin et al.*, 2006]. As computers advance the time resolution also advances. In 2004, hit particle frequency was a maximum of about 3Hz; in 2006 the frequency became better than 10Hz. Lastly, efforts are currently being made to make the ATOFMS more portable enabling measurements to become integrated to airborne instrument platforms to obtain vertical profiles of aerosol properties.

This thesis will demonstrate how the ATOFMS can be used to measure refractive index, density, chemical mixing state, and size for single particle classes. This has never been accomplished before and is very important because these parameters are needed in to determine the overall optical behavior of the aerosols. These measurements have been implemented in the field to yield insights of how optical properties are apportioned over size and mixing state. Unique new aerosol types that represent specific sources continue to be discovered, and their microphysical properties can be characterized. This powerful capability can be applied to topics such as climate change, atmospheric visibility and heath effects studies.

1.7 References

Abdou, W.A., D.J. Diner, J.V. Martonchik, C.J. Bruegge, R.A. Kahn, B.J. Gaitley, K.A. Crean, L.A. Remer, and B. Holben: Comparison of coincident Multiangle Imaging Spectroradiometer and Moderate Resolution Imaging Spectroradiometer aerosol optical depths over land and ocean scenes containing Aerosol Robotic Network sites, Journal of Geophysical Research-Atmospheres, 110 (D10), -, 2005.

Ackerman, A.S., O.B. Toon, D.E. Stevens, A.J. Heymsfield, V. Ramanathan, and E.J. Welton: Reduction of tropical cloudiness by soot, Science, 288 (5468), 1042-1047, 2000.

Ackerman, T.P., A.J. Braverman, D.J. Diner, T.L. Anderson, R.A. Kahn, J.V. Martonchik, J.E. Penner, P.J. Rasch, B.A. Wielicki, and B. Yu: Integrating and interpreting

aerosol observations and models within the PARAGON framework, Bulletin of the American Meteorological Society, 85 (10), 1523-+, 2004.

Ackerman, T.P., and O.B. Toon: Absorption of Visible Radiation in Atmosphere Containing Mixtures of Absorbing and Non-Absorbing Particles, Applied Optics, 20 (20), 3661-3668, 1981.

Adams, K.M.: Real-Time Insitu Measurements of Atmospheric Optical-Absorption in the Visible Via Photoacoustic-Spectroscopy.1. Evaluation of Photoacoustic Cells, Applied Optics, 27 (19), 4052-4056, 1988.

Adams, P.J., and J.H. Seinfeld: Predicting global aerosol size distributions in general circulation models, Journal of Geophysical Research-Atmospheres, 107 (D19), -, 2002.

Anderson, T.L., R.J. Charlson, N. Bellouin, O. Boucher, M. Chin, C.S. A., J. Haywood, Y.J. Kaufman, S. Kinne, J.A. Ogren, L.A. Remer, T. Takemura, D. Tanr´e, O. Torres, C.R. Trepte, B.A. Wielicki, D.M. Winker, and H. Yu: An "ATrain" strategy for quantifying direct aerosol forcing of climate, Bull. Am. Met. Soc., 86 (12), 1795-1809, 2005a.

Anderson, T.L., D.S. Covert, J.D. Wheeler, J.M. Harris, K.D. Perry, B.E. Trost, D.J. Jaffe, and J.A. Ogren: Aerosol backscatter fraction and single scattering albedo: Measured values and uncertainties at a coastal station in the Pacific Northwest, Journal of Geophysical Research-Atmospheres, 104 (D21), 26793-26807, 1999.

Anderson, T.L., and J.A. Ogren: Determining aerosol radiative properties using the TSI 3563 integrating nephelometer, Aerosol Science and Technology, 29 (1), 57-69, 1998.

Anderson, T.L., Y.H. Wu, D.A. Chu, B. Schmid, J. Redemann, and O. Dubovik: Testing the MODIS satellite retrieval of aerosol fine-mode fraction, Journal of Geophysical Research-Atmospheres, 110 (D18), -, 2005b.

Andreae, M.O., C.D. Jones, and P.M. Cox: Strong present-day aerosol cooling implies a hot future, Nature, 435 (7046), 1187-1190, 2005.

Angstrom, A.: On the atmospheric transmission of sun radiation and on dust in the air, Geografiska Ann., 11, 156-166, 1929.

Aptowicz, K.B., Y.L. Pan, R.K. Chang, R.G. Pinnick, S.C. Hill, R.L. Tober, A. Goyal, T. Leys, and B.V. Bronk: Two-dimensional angular optical scattering patterns of microdroplets in the mid infrared with strong and weak absorption, Optics Letters, 29 (17), 1965-1967, 2004.

Aptowicz, K.B., R.G. Pinnick, S.C. Hill, Y.L. Pan, and R.K. Chang: Optical scattering patterns from single urban aerosol particles at Adelphi, Maryland, USA: A classification relating to particle morphologies, Journal of Geophysical Research-Atmospheres, 111 (D12), -, 2006.

Arnott, W.P., K. Hamasha, H. Moosmuller, P.J. Sheridan, and J.A. Ogren: Towards aerosol light-absorption measurements with a 7-wavelength Aethalometer: Evaluation with a photoacoustic instrument and 3-wavelength nephelometer, Aerosol Science and Technology, 39 (1), 17-29, 2005.

Arnott, W.P., H. Moosmuller, R.E. Abbott, and M.D. Ossofsky: Thermoacoustic Enhancement of Photoacoustic-Spectroscopy - Theory and Measurements of the Signal-to-Noise Ratio, Review of Scientific Instruments, 66 (10), 4827-4833, 1995.

Arnott, W.P., H. Moosmuller, C.F. Rogers, T.F. Jin, and R. Bruch: Photoacoustic spectrometer for measuring light absorption by aerosol: instrument description, Atmospheric Environment, 33 (17), 2845-2852, 1999.

Bartley, D.L., A.B. Martinez, P.A. Baron, D.R. Secker, and E. Hirst: Droplet distortion in accelerating flow, Journal of Aerosol Science, 31 (12), 1447-1460, 2000.

Baumgardner, D., J.E. Dye, B. Gandrud, K. Barr, K. Kelly, and K.R. Chan: Refractive, indices of aerosols in the upper troposphere and lower stratosphere, Geophysical Research Letters, 23 (7), 749-752, 1996.

Baumgardner, D., H. Jonsson, W. Dawson, D. O'Connor, and R. Newton: The cloud, aerosol and precipitation spectrometer: a new instrument for cloud investigations, Atmospheric Research, 59, 251-264, 2001.

Biswas, P., C.L. Jones, and R.C. Flagan: Distortion of Size Distributions by Condensation and Evaporation in Aerosol Instruments, Aerosol Science and Technology, 7 (2), 231-246, 1987.

Bohren, C.F., and D.R. Huffman: Absorption and Scattering of Light by Small Particles, John Wiley and Sons, INC., New York, 1981.

Bond, T.C., and R.W. Bergstrom: Light absorption by carbonaceous particles: An investigative review, Aerosol Science and Technology, 40 (1), 27-67, 2006.

Bond, T.C., G. Habib, and R.W. Bergstrom: Limitations in the enhancement of visible light absorption due to mixing state, Journal of Geophysical Research-Atmospheres, 111 (D20), -, 2006.

Breon, F.M., D. Tanre, and S. Generoso: Aerosol effect on cloud droplet size monitored from satellite, Science, 295 (5556), 834-838, 2002.

Cahill, T.A., and P. Wayakabashi: Compositional analysis of size segregated aerosol samples, ACS Adv. Chem. Ser., 232, 211-228, 1993.

Campbell, J.R., E.J. Welton, J.D. Spinhirne, Q. Ji, S.C. Tsay, S.J. Piketh, M. Barenbrug, and B.N. Holben: Micropulse lidar observations of tropospheric aerosols over northeastern South Africa during the ARREX and SAFARI 2000 dry season experiments, Journal of Geophysical Research-Atmospheres, 108 (D13), -, 2003.

Canagaratna, M.R., J.T. Jayne, J.L. Jimenez, J.D. Allan, M.R. Alfarra, Q. Zhang, T.B. Onasch, F. Drewnick, H. Coe, A. Middlebrook, A. Delia, L.R. Williams, A.M. Trimborn, M.J. Northway, P.F. DeCarlo, C.E. Kolb, P. Davidovits, and D.R. Worsnop: Chemical and microphysical characterization of ambient aerosols with the aerodyne aerosol mass spectrometer, Mass Spectrometry Reviews, 26 (2), 185-222, 2007.

Charlson, R.J., S.E. Schwartz, J.M. Hales, R.D. Cess, J.A. Coakley, J.E. Hansen, and D.J. Hofmann: Climate Forcing by Anthropogenic Aerosols, Science, 255 (5043), 423-430, 1992.

Chu, D.A., Y.J. Kaufman, C. Ichoku, L.A. Remer, D. Tanre, and B.N. Holben: Validation of MODIS aerosol optical depth retrieval over land, Geophysical Research Letters, 29 (12), -, 2002.

Clarke, A.D., S. Howell, P.K. Quinn, T.S. Bates, J.A. Ogren, E. Andrews, A. Jefferson, A. Massling, O. Mayol-Bracero, H. Maring, D. Savoie, and G. Cass: INDOEX aerosol: A comparison and summary of chemical, microphysical, and optical properties observed from land, ship, and aircraft, Journal of Geophysical Research-Atmospheres, 107 (D19), -, 2002.

Collins, D.R., H.H. Jonsson, J.H. Seinfeld, R.C. Flagan, S. Gasso, D.A. Hegg, P.B. Russell, B. Schmid, J.M. Livingston, E. Ostrom, K.J. Noone, L.M. Russell, and J.P. Putaud: In situ aerosol-size distributions and clear-column radiative closure during ACE-2, Tellus Series B-Chemical and Physical Meteorology, 52 (2), 498-525, 2000.

Cross, E.S., J.G. Slowik, P. Davidovits, J.D. Allan, D.R. Worsnop, J.T. Jayne, D.K. Lewis, M. Canagaratna, and T.B. Onasch: Laboratory and Ambient Particle Density Determinations using Light Scattering in Conjunction with Aerosol Mass Spectrometry, Aerosol Science and Technology, 41, 343-359, 2007.

Dahneke, B.: Aerosol Beam Spectrometry, Nature-Physical Science, 244 (134), 54-55, 1973.

Davidson, C.I., R.F. Phalen, and P.A. Solomon: Airborne particulate matter and human health: A review, Aerosol Science and Technology, 39 (8), 737-749, 2005.

Day, D.E., W.C. Malm, and S.M. Kreidenweis: Aerosol light scattering measurements as a function of relative humidity, Journal of the Air & Waste Management Association, 50 (5), 710-716, 2000.

DeCarlo, P.F., J.R. Kimmel, A. Trimborn, M.J. Northway, J.T. Jayne, A.C. Aiken, M. Gonin, K. Fuhrer, T. Horvath, K.S. Docherty, D.R. Worsnop, and J.L. Jimenez: Field-deployable, high-resolution, time-of-flight aerosol mass spectrometer, Analytical Chemistry, 78 (24), 8281-8289, 2006.

DeCarlo, P.F., J.G. Slowik, D.R. Worsnop, P. Davidovits, and J.L. Jimenez: Particle morphology and density characterization by combined mobility and aerodynamic diameter measurements. Part 1: Theory, Aerosol Science and Technology, 38 (12), 1185-1205, 2004.

Deuze, J.L., P. Goloub, M. Herman, A. Marchand, G. Perry, S. Susana, and D. Tanre: Estimate of the aerosol properties over the ocean with POLDER, Journal of Geophysical Research-Atmospheres, 105 (D12), 15329-15346, 2000.

Dick, W.D., P.H. Mcmurry, and J.R. Bottiger: Size-Dependent and Composition-Dependent Response of the Dawn-a Multiangle Single-Particle Optical-Detector, Aerosol Science and Technology, 20 (4), 345-362, 1994.

Dick, W.D., P.J. Ziemann, P.F. Huang, and P.H. McMurry: Optical shape fraction measurements of submicrometre laboratory and atmospheric aerosols, Measurement Science & Technology, 9 (2), 183-196, 1998.

Diner, D.J., T.P. Ackerman, T.L. Anderson, J. Bosenberg, A.J. Braverman, R.J. Charlson, W.D. Collins, R. Davies, B.N. Holben, C.A. Hostetler, R.A. Kahn, J.V. Martonchik, R.T. Menzies, M.A. Miller, J.A. Ogren, J.E. Penner, P.J. Rasch, S.E. Schwartz, J.H. Seinfeld, G.L. Stephens, O. Torres, L.D. Travis, B.A. Wielicki, and B. Yu: PARAGON - An integrated approach for characterizing aerosol climate impacts and environmental interactions, Bulletin of the American Meteorological Society, 85 (10), 1491-+, 2004.

Diner, D.J., M.M. Verstraete, and J.V. Martonchik: Foreword to special section on MISR, Ieee Transactions on Geoscience and Remote Sensing, 40 (7), 1447-1448, 2002.

Dockery, D.W., C.A. Pope, X.P. Xu, J.D. Spengler, J.H. Ware, M.E. Fay, B.G. Ferris, and F.E. Speizer: An Association between Air-Pollution and Mortality in 6 United-States Cities, New England Journal of Medicine, 329 (24), 1753-1759, 1993.

Draine, B.T., and P.J. Flatau: Discrete-Dipole Approximation for Scattering Calculations, Journal of the Optical Society of America a-Optics Image Science and Vision, 11 (4), 1491-1499, 1994.

Drewnick, F., S.S. Hings, P. DeCarlo, J.T. Jayne, M. Gonin, K. Fuhrer, S. Weimer, J.L. Jimenez, K.L. Demerjian, S. Borrmann, and D.R. Worsnop: A new time-of-flight aerosol mass spectrometer (TOF-AMS) - Instrument description and first field deployment, Aerosol Science and Technology, 39 (7), 637-658, 2005.

Dubovik, O., B.N. Holben, T. Lapyonok, A. Sinyuk, M.I. Mishchenko, P. Yang, and I. Slutsker: Non-spherical aerosol retrieval method employing light scattering by spheroids, Geophysical Research Letters, 29 (10), -, 2002.

Dubovik, O., and M.D. King: A flexible inversion algorithm for retrieval of aerosol optical properties from Sun and sky radiance measurements, Journal of Geophysical Research-Atmospheres, 105 (D16), 20673-20696, 2000.

Dubovik, O., A. Sinyuk, T. Lapyonok, B.N. Holben, M. Mishchenko, P. Yang, T.F. Eck, H. Volten, O. Munoz, B. Veihelmann, W.J. van der Zande, J.F. Leon, M. Sorokin, and I. Slutsker: Application of spheroid models to account for aerosol particle nonsphericity in remote sensing of desert dust, Journal of Geophysical Research-Atmospheres, 111 (D11), -, 2006.

Dubovik, O., A. Smirnov, B.N. Holben, M.D. King, Y.J. Kaufman, T.F. Eck, and I. Slutsker: Accuracy assessments of aerosol optical properties retrieved from Aerosol Robotic Network (AERONET) Sun and sky radiance measurements, Journal of Geophysical Research-Atmospheres, 105 (D8), 9791-9806, 2000.

Dusek, U., G.P. Frank, L. Hildebrandt, J. Curtius, J. Schneider, S. Walter, D. Chand, F. Drewnick, S. Hings, D. Jung, S. Borrmann, and M.O. Andreae: Size matters more than chemistry for cloud-nucleating ability of aerosol particles, Science, 312 (5778), 1375-1378, 2006.

Easter, R.C., S.J. Ghan, Y. Zhang, R.D. Saylor, E.G. Chapman, N.S. Laulainen, H. Abdul-Razzak, L.R. Leung, X.D. Bian, and R.A. Zaveri: MIRAGE: Model description and evaluation of aerosols and trace gases, Journal of Geophysical Research-Atmospheres, 109 (D20), -, 2004.

Egan, W.G., and T.W. Hilgeman: Optical Properties of Inhomogenous Materials, Academic Press, New York, 1979.

EPA, U.S.: Regional Haze Regulations, Federal Register, 64, 35714 - 35774, 1999.

Finlayson-Pitts, B.J., and J.N. Pitts: Chemistry of the Upper and Lower Atmosphere: Theory, Experiments, and Applications, Academic Press, San Diego, 2000.

Friedlander, S.K., and C.S. Wang: Self-Preserving Particle Size Distribution for Coagulation by Brownian Motion, Journal of Colloid and Interface Science, 22 (2), 126-&, 1966.

Fuller, K.A., W.C. Malm, and S.M. Kreidenweis: Effects of mixing on extinction by carbonaceous particles, Journal of Geophysical Research-Atmospheres, 104 (D13), 15941-15954, 1999.

Gard, E., J.E. Mayer, B.D. Morrical, T. Dienes, D.P. Fergenson, and K.A. Prather: Real-time analysis of individual atmospheric aerosol particles: Design and performance of a portable ATOFMS, Analytical Chemistry, 69 (20), 4083-4091, 1997.

Geller, M., S. Biswas, and C. Sioutas: Determination of Particle Effective Densty in Urban Environments with a Differential Mobility Analyzer and Aerosol Particle Mass Analyzer, Aerosol Sci. Technol., 40 (9), 2006.

Grams, G.W., I.H. Blifford, D.A. Gillette, and P.B. Russell: Complex Index of Refraction of Airborn Soil Particles, Journal of Applied Meteorology, 13 (4), 459-471, 1974.

Grey, W.M.F., P.R.J. North, S.O. Los, and R.M. Mitchell: Aerosol optical depth and land surface reflectance from Multiangle AATSR measurements: Global validation and intersensor comparisons, Ieee Transactions on Geoscience and Remote Sensing, 44 (8), 2184-2197, 2006.

Hansen, A.D.A., H. Rosen, and T. Novakov: The Aethalometer - an Instrument for the Real-Time Measurement of Optical-Absorption by Aerosol-Particles, Science of the Total Environment, 36 (Jun), 191-196, 1984.

Hansen, J.E., M. Sato, A. Lacis, R. Ruedy, I. Tegen, and E. Matthews: Climate forcings in the Industrial era, Proceedings of the National Academy of Sciences of the United States of America, 95 (22), 12753-12758, 1998.

Hansen, M.Z., and W.H. Evans: Polar Nephelometer for Atmospheric Particulate Studies, Applied Optics, 19 (19), 3389-3395, 1980.

Haywood, J.M., D.L. Roberts, A. Slingo, J.M. Edwards, and K.P. Shine: General circulation model calculations of the direct radiative forcing by anthropogenic sulfate and fossil-fuel soot aerosol, Journal of Climate, 10 (7), 1562-1577, 1997.

Heintzenberg, J., and R.J. Charlson: Design and applications of the integrating nephelometer: A review, Journal of Atmospheric and Oceanic Technology, 13 (5), 987-1000, 1996.

Heintzenberg, J., A. Wiedensohler, T.M. Tuch, D.S. Covert, P. Sheridan, J.A. Ogren, J. Gras, R. Nessler, C. Kleefeld, N. Kalivitis, V. Aaltonen, R.T. Wilhelm, and M. Havlicek: Intercomparisons and aerosol calibrations of 12 commercial integrating nephelometers of three manufacturers, Journal of Atmospheric and Oceanic Technology, 23 (7), 902-914, 2006.

Herman, M., J.L. Deuze, C. Devaux, P. Goloub, F.M. Breon, and D. Tanre: Remote sensing of aerosols over land surfaces including polarization measurements and application to POLDER measurements, Journal of Geophysical Research-Atmospheres, 102 (D14), 17039-17049, 1997.

Hinds, W.C.: Aerosol Technology, John Wiley and Sons, INC., New York, 1999.

Hirst, E., and P.H. Kaye: Experimental and theoretical light scattering profiles from spherical and nonspherical particles, Journal of Geophysical Research-Atmospheres, 101 (D14), 19231-19235, 1996.

Hirst, E., P.H. Kaye, K.M. Buckley, and S.J. Saunders: A Method for Investigating the Orientational Behavior of Fibrous Particles in Gaseous Flow, Particle & Particle Systems Characterization, 12 (1), 3-9, 1995.

Hirst, E., P.H. Kaye, and J.R. Guppy: Light-Scattering from Nonspherical Airborne Particles Experimental and Theoretical Comparisons, Applied Optics, 33 (30), 7180-7186, 1994.

Holler, S., J.C. Auger, B. Stout, Y. Pan, J.R. Bottiger, R.K. Chang, and G. Videen: Observations and calculations of light scattering from clusters of spheres, Applied Optics, 39 (36), 6873-6887, 2000.

Holler, S., Y.L. Pan, R.K. Chang, J.R. Bottiger, S.C. Hill, and D.B. Hillis: Two-dimensional angular optical scattering for the characterization of airborne microparticles, Optics Letters, 23 (18), 1489-1491, 1998.

Holler, S., M. Surbek, R.K. Chang, and Y.L. Pan: Two-dimensional angular optical scattering patterns as droplets evolve into clusters, Optics Letters, 24 (17), 1185-1187, 1999.

Hsu, N.C., J.R. Herman, J.F. Gleason, O. Torres, and C.J. Seftor: Satellite detection of smoke aerosols over a snow/ice surface by TOMS, Geophysical Research Letters, 26 (8), 1165-1168, 1999a.

Hsu, N.C., J.R. Herman, O. Torres, B.N. Holben, D. Tanre, T.F. Eck, A. Smirnov, B. Chatenet, and F. Lavenu: Comparisons of the TOMS aerosol index with Sun-photometer aerosol optical thickness: Results and applications, Journal of Geophysical Research-Atmospheres, 104 (D6), 6269-6279, 1999b.

IPCC, Climate Change 2007: The Physical Science Basis, Cambridge University Press, 2007.

Jacobson, M.Z.: A physically-based treatment of elemental carbon optics: Implications for global direct forcing of aerosols, Geophysical Research Letters, 27 (2), 217-220, 2000.

Jacobson, M.Z.: Strong radiative heating due to the mixing state of black carbon in atmospheric aerosols, Nature, 409 (6821), 695-697, 2001.

Kahn, R., W.H. Li, J.V. Martonchik, C.J. Bruegge, D.J. Diner, B.J. Gaitley, W. Abdou, O. Dubovik, B. Holben, A. Smirnov, Z.H. Jin, and D. Clark: MISR calibration and implications for low-light-level aerosol retrieval over dark water, Journal of the Atmospheric Sciences, 62 (4), 1032-1052, 2005a.

Kahn, R.A., B.J. Gaitley, J.V. Martonchik, D.J. Diner, K.A. Crean, and B. Holben: Multiangle Imaging Spectroradiometer (MISR) global aerosol optical depth validation based on 2 years of coincident Aerosol Robotic Network (AERONET) observations, Journal of Geophysical Research-Atmospheres, 110 (D10), -, 2005b.

Kaufman, Y.J., D. Tanre, and O. Boucher: A satellite view of aerosols in the climate system, Nature, 419 (6903), 215-223, 2002.

Kaye, P.H., J.E. Barton, E. Hirst, and J.M. Clark: Simultaneous light scattering and intrinsic fluorescence measurement for the classification of airborne particles, Applied Optics, 39 (21), 3738-3745, 2000.

Kaye, P.H., E. Hirst, J.M. Clark, and F. Micheli: Airborne Particle-Shape and Size Classification from Spatial Light-Scattering Profiles, Journal of Aerosol Science, 23 (6), 597-611, 1992.

Kerker, M.: Light scattering instrumentation for aerosol studies: An historical overview, Aerosol Science and Technology, 27 (4), 522-540, 1997.

Khlystov, A., C. Stanier, and S.N. Pandis: An algorithm for combining electrical mobility and aerodynamic size distributions data when measuring ambient aerosol, Aerosol Science and Technology, 38, 229-238, 2004.

Kinne, S., M. Schulz, C. Textor, S. Guibert, Y. Balkanski, S.E. Bauer, T. Berntsen, T.F. Berglen, O. Boucher, M. Chin, W. Collins, F. Dentener, T. Diehl, R. Easter, J. Feichter, D. Fillmore, S. Ghan, P. Ginoux, S. Gong, A. Grini, J.E. Hendricks, M. Herzog, L. Horowitz, L. Isaksen, T. Iversen, A. Kirkavag, S. Kloster, D. Koch, J.E. Kristjansson, M. Krol, A. Lauer, J.F. Lamarque, G. Lesins, X. Liu, U. Lohmann, V. Montanaro, G. Myhre, J.E. Penner, G. Pitari, S. Reddy, O. Seland, P. Stier, T. Takemura, and X. Tie: An AeroCom initial assessment - optical

properties in aerosol component modules of global models, Atmospheric Chemistry and Physics, 6, 1815-1834, 2006.

Knutson, E.O., and K.T. Whitby: Aerosol Classification by Electric Mobility: Apparatus, Theory, and Application, Journal of Aerosol Science, 7 (3), 219-229, 1975.

Lack, D.A., E.R. Lovejoy, T. Baynard, A. Pettersson, and A.R. Ravishankara: Aerosol absorption measurement using photoacoustic spectroscopy: Sensitivity, calibration, and uncertainty developments, Aerosol Science and Technology, 40 (9), 697-708, 2006.

Lai, F.S., G.M. Hidy, Friedlan.Sk, and J. Pich: Self-Preserving Particle-Size Distribution for Brownian Coagulation in Free-Molecule Regime, Journal of Colloid and Interface Science, 39 (2), 395-&, 1972.

Lesins, G., P. Chylek, and U. Lohmann: A study of internal and external mixing scenarios and its effect on aerosol optical properties and direct radiative forcing, Journal of Geophysical Research-Atmospheres, 107 (D10), -, 2002.

Lide, D.R.: CRC Handbook of Chemistry and Physics, CRC Press, Boca Raton, FL, 2006.

Lippmann, M., M. Frampton, J. Schwartz, D. Dockery, R. Schlesinger, P. Koutrakis, J. Froines, A. Nel, J. Finkelstein, J. Godleski, J. Kaufman, J. Koenig, T. Larson, D. Luchtel, L.J.S. Liu, G. Oberdorster, A. Peters, J. Sarnat, C. Sioutas, H. Suh, J. Sullivan, M. Utell, E. Wichmann, and J. Zelikoff: The US Environmental Protection Agency particulate matter health effects research centers program: A midcourse report of status, progress, and plans, Environmental Health Perspectives, 111 (8), 1074-1092, 2003.

Liu, B.Y.H., K.T. Whitby, and D.Y.H. Pui: Portable Electrical Analyzer for Size Distribution Measurement of Submicron Aerosols, Journal of the Air Pollution Control Association, 24 (11), 1067-1072, 1974.

Liu, P., P.J. Ziemann, D.B. Kittelson, and P.H. Mcmurry: Generating Particle Beams of Controlled Dimensions and Divergence.1. Theory of Particle Motion in Aerodynamic Lenses and Nozzle Expansions, Aerosol Science and Technology, 22 (3), 293-313, 1995a.

Liu, P., P.J. Ziemann, D.B. Kittelson, and P.H. Mcmurry: Generating Particle Beams of Controlled Dimensions and Divergence.2. Experimental Evaluation of Particle Motion in Aerodynamic Lenses and Nozzle Expansions, Aerosol Science and Technology, 22 (3), 314-324, 1995b.

Mallina, R.V., A.S. Wexler, and M.V. Johnston: Particle Growth in High-Speed Particle Beam Inlets, J. Aerosol Sci., 28 (2), 223-238, 1997.

Malm, W.C., and S.M. Kreidenweis: The effects of models of aerosol hygroscopicity on the apportionment of extinction, Atmospheric Environment, 31 (13), 1965-1976, 1997.

Malm, W.C., and J.F. Sisler: Spatial patterns of major aerosol species and selected heavy metals in the United States, Fuel Processing Technology, 65, 473-501, 2000.

Marple, V., K. Rubow, G. Ananth, and H.J. Fissan: Micro-Orifice Uniform Deposit Impactor, Journal of Aerosol Science, 17 (3), 489-494, 1986.

Marple, V.A., B.Y.H. Liu, and G.A. Kuhlmey: A Uniform Deposit Impactor, Journal of Aerosol Science, 12 (4), 333-337, 1981.

Marple, V.A., and K. Willeke: Impactor Design, Atmospheric Environment, 10 (10), 891-896, 1976.

May, K.R.: The Cascade impactor: an instrument for sampling coarse aerosols, J. Sci. Inst., 22, 187-195, 1945.

McMurry, P.H.: A review of atmospheric aerosol measurements, Atmospheric Environment, 34 (12-14), 1959-1999, 2000.

Mcmurry, P.H., and M.R. Stolzenburg: On the Sensitivity of Particle-Size to Relative-Humidity for Los-Angeles Aerosols, Atmospheric Environment, 23 (2), 497-507, 1989.

McMurry, P.H., X. Wang, K. Park, and K. Ehara: The relationship between mass and mobility for atmospheric particles: A new technique for measuring particle density, Aerosol Science and Technology, 36 (2), 227-238, 2002.

Mie, G.: Beitrage zur Optik truber Mediien speziell kolloidaler Metallosungen, Ann. Phys., 25, 377 - 445, 1908.

Mikhailov, E.F., S.S. Vlasenko, I.A. Podgorny, V. Ramanathan, and C.E. Corrigan: Optical properties of soot-water drop agglomerates: An experimental study, Journal of Geophysical Research-Atmospheres, 111 (D7), -, 2006.

Mishchenko, M.I., B. Cairns, J.E. Hansen, L.D. Travis, R. Burg, Y.J. Kaufman, J.V. Martins, and E.P. Shettle: Monitoring of aerosol forcing of climate from space: analysis of measurement requirements, Journal of Quantitative Spectroscopy & Radiative Transfer, 88 (1-3), 149-161, 2004.

Mishchenko, M.I., J.W. Hovenier, and L.D. Travis: Light Scattering by Nonspherical Particles: Theory, Measurements and Applications, Academic Press, San Diego, 2000.

Mishchenko, M.I., A.A. Lacis, B.E. Carlson, and L.D. Travis: Nonsphericity of Dust-Like Tropospheric Aerosols - Implications for Aerosol Remote-Sensing and Climate Modeling, Geophysical Research Letters, 22 (9), 1077-1080, 1995.

Mishchenko, M.I., L.D. Travis, and D.W. Mackowski: T-matrix computations of light scattering by nonspherical particles: A review, Journal of Quantitative Spectroscopy & Radiative Transfer, 55 (5), 535-575, 1996.

Moffet, R.C., and K.A. Prather: Extending ATOFMS measurements to include refractive index and density, Analytical Chemistry, 77 (20), 6535-6541, 2005.

Moosmuller, H., W.P. Arnott, and C.F. Rogers: Methods for real-time, in situ measurement of aerosol light absorption, Journal of the Air & Waste Management Association, 47 (2), 157-166, 1997.

Moosmuller, H., R. Varma, and W.P. Arnott: Cavity ring-down and cavity-enhanced detection techniques for the measurement of aerosol extinction, Aerosol Science and Technology, 39 (1), 30-39, 2005.

Murphy, D.M.: The design of single particle laser mass spectrometers, Mass Spectrometry Reviews, 26 (2), 150-165, 2007.

Murphy, D.M., D.J. Cziczo, P.K. Hudson, M.E. Schein, and D.S. Thomson: Particle density inferred from simultaneous optical and aerodynamic diameters sorted by composition, Journal of Aerosol Science, 35 (1), 135-139, 2004.

Nenes, A., W.C. Conant, and J.H. Seinfeld: Black carbon radiative heating effects on cloud microphysics and implications for the aerosol indirect effect - 2. Cloud microphysics, Journal of Geophysical Research-Atmospheres, 107 (D21), -, 2002.

Oskouie, A.K., H.C. Wang, R. Mavliev, and K.E. Noll: Calculated calibration curves for particle size determination based on time-of-flight (TOF), Aerosol Science and Technology, 29 (5), 433-441, 1998.

Peters, T.M., and D. Leith: Concentration measurement and counting efficiency of the aerodynamic particle sizer 3321, Journal of Aerosol Science, 34 (5), 627-634, 2003.

Pettersson, A., E.R. Lovejoy, C.A. Brock, S.S. Brown, and A.R. Ravishankara: Measurement of aerosol optical extinction at 532nm with pulsed cavity ring down spectroscopy, Journal of Aerosol Science, 35 (8), 995-1011, 2004.

Petzold, A., H. Schloesser, P.J. Sheridan, W.P. Arnott, J.A. Ogren, and A. Virkkula: Evaluation of multiangle absorption photometry for measuring aerosol light absorption, Aerosol Science and Technology, 39 (1), 40-51, 2005.

Petzold, A., and M. Schonlinner: Multi-angle absorption photometry - a new method for the measurement of aerosol light absorption and atmospheric black carbon, Journal of Aerosol Science, 35 (4), 421-441, 2004.

Prather, K.A., T. Nordmeyer, and K. Salt: Real-Time Characterization of Individual Aerosol-Particles Using Time-of-Flight Mass-Spectrometry, Analytical Chemistry, 66 (9), 1403-1407, 1994.

Prenni, A.J., P.J. De Mott, and S.M. Kreidenweis: Water uptake of internally mixed particles containing ammonium sulfate and dicarboxylic acids, Atmospheric Environment, 37 (30), 4243-4251, 2003.

Qin, X.Y., P.V. Bhave, and K.A. Prather: Comparison of two methods for obtaining quantitative mass concentrations from aerosol time-of-flight mass spectrometry measurements, Analytical Chemistry, 78 (17), 6169-6178, 2006.

Quinn, P.K., and D.J. Coffman: Local closure during the First Aerosol Characterization Experiment (ACE 1): Aerosol mass concentration and scattering and backscattering coefficients, Journal of Geophysical Research-Atmospheres, 103 (D13), 16575-16596, 1998.

Raabe, O.G., D.A. Braaten, R.L. Axelbaum, S.V. Teague, and T.A. Cahill: Calibration Studies of the Drum Impactor, Journal of Aerosol Science, 19 (2), 183-195, 1988.

Rader, D.J., and P.H. Mcmurry: Application of the Tandem Differential Mobility Analyzer to Studies of Droplet Growth or Evaporation, Journal of Aerosol Science, 17 (5), 771-787, 1986.

Rao, C.R.N., L.L. Stowe, and E.P. Mcclain: Remote-Sensing of Aerosols over the Oceans Using Avhrr Data Theory, Practice and Applications, International Journal of Remote Sensing, 10 (4-5), 743-749, 1989.

Redemann, J., S.J. Masonis, B. Schmid, T.L. Anderson, P.B. Russell, J.M. Livingston, O. Dubovik, and A.D. Clarke: Clear-column closure studies of aerosols and water vapor aboard the NCAR C-130 during ACE-Asia, 2001, Journal of Geophysical Research-Atmospheres, 108 (D23), -, 2003.

Reid, J.S., T.F. Eck, S.A. Christopher, R. Koppmann, O. Dubovik, D.P. Eleuterio, B.N. Holben, E.A. Reid, and J. Zhang: A review of biomass burning emissions part III: intensive optical properties of biomass burning particles, Atmospheric Chemistry and Physics, 5, 827-849, 2005.

Remer, L.A., Y.J. Kaufman, Z. Levin, and S. Ghan: Model assessment of the ability of MODIS to measure top-of-atmosphere direct radiative forcing from smoke aerosols, Journal of the Atmospheric Sciences, 59 (3), 657-667, 2002.

Richards, T.W., and W.C. Schumb: Refractive Index and Solubilities of the Nitrates of Lead Isotopes, Proc. Nat. Acad. Sci., 4, 386-387, 1918.

Rood, M.J., D.S. Covert, and T.V. Larson: Temperature and Humidity Controlled Nephelometry - Improvements and Calibration, Aerosol Science and Technology, 7 (1), 57-65, 1987.

Rood, M.J., T.V. Larson, D.S. Covert, and N.C. Ahlquist: Measurement of Laboratory and Ambient Aerosols with Temperature and Humidity Controlled Nephelometry, Atmospheric Environment, 19 (7), 1181-1190, 1985.

Rood, M.J., M.A. Shaw, T.V. Larson, and D.S. Covert: Ubiquitous Nature of Ambient Metastable Aerosol, Nature, 337 (6207), 537-539, 1989.

Sachweh, B.A., W.D. Dick, and P.H. Mcmurry: Distinguishing between Spherical and Nonspherical Particles by Measuring the Variability in Azimuthal Light-Scattering, Aerosol Science and Technology, 23 (3), 373-391, 1995.

Sato, M., J. Hansen, D. Koch, A. Lacis, R. Ruedy, O. Dubovik, B. Holben, M. Chin, and T. Novakov: Global atmospheric black carbon inferred from AERONET, Proceedings of the National Academy of Sciences of the United States of America, 100 (11), 6319-6324, 2003.

Schmidt, G.A., R. Ruedy, J.E. Hansen, I. Aleinov, N. Bell, M. Bauer, S. Bauer, B. Cairns, V. Canuto, Y. Cheng, A. Del Genio, G. Faluvegi, A.D. Friend, T.M. Hall, Y.Y. Hu, M. Kelley, N.Y. Kiang, D. Koch, A.A. Lacis, J. Lerner, K.K. Lo, R.L. Miller, L. Nazarenko, V. Oinas, J. Perlwitz, J. Perlwitz, D. Rind, A. Romanou, G.L. Russell, M. Sato, D.T. Shindell, P.H. Stone, S. Sun, N. Tausnev, D. Thresher, and M.S. Yao: Present-day atmospheric simulations using GISS ModelE: Comparison to in situ, satellite, and reanalysis data, Journal of Climate, 19 (2), 153-192, 2006.

Schnaiter, M., C. Linke, O. Mohler, K.H. Naumann, H. Saathoff, R. Wagner, U. Schurath, and B. Wehner: Absorption amplification of black carbon internally mixed with secondary organic aerosol, Journal of Geophysical Research-Atmospheres, 110 (D19), -, 2005.

Secker, D.R., P.H. Kaye, R.S. Greenaway, E. Hirst, D.L. Bartley, and G. Videen: Light scattering from deformed droplets and droplets with inclusions. I. Experimental results, Applied Optics, 39 (27), 5023-5030, 2000.

Secker, D.R., P.H. Kaye, and E. Hirst: Real-time observation of the change in light scattering from droplets with increasing deformity, Optics Express, 8 (6), 290-295, 2001.

Seinfeld, J.H., R.A. Kahn, T.L. Anderson, R.J. Charlson, R. Davies, D.J. Diner, J.A. Ogren, S.E. Schwartz, and B.A. Wielicki: Scientific objectives, measurement needs, and challenges motivating the PARAGON aerosol initiative, Bulletin of the American Meteorological Society, 85 (10), 1503-+, 2004.

Sheridan, P.J., W.P. Arnott, J.A. Ogren, E. Andrews, D.B. Atkinson, D.S. Covert, H. Moosmuller, A. Petzold, B. Schmid, A.W. Strawa, R. Varma, and A. Virkkula: The Reno Aerosol Optics Study: An evaluation of aerosol absorption measurement methods, Aerosol Science and Technology, 39 (1), 1-16, 2005.

Sienfeld, J.H., and S.N. Pandis: Atmospheric Chemistry and Physics, John Wiley and Sons INC., New York, 1998.

Sindoni, O.I., R. Saija, M.A. Iati, F. Borghese, P. Denti, G.E. Fernandes, Y.L. Pan, and R.K. Chang: Optical scattering by biological aerosols: experimental and computational results on spore simulants, Optics Express, 14 (15), 6942-6950, 2006.

Slowik, J.G., K. Stainken, P. Davidovits, L.R. Williams, J.T. Jayne, C.E. Kolb, D.R. Worsnop, Y. Rudich, P.F. DeCarlo, and J.L. Jimenez: Particle morphology and density characterization by combined mobility and aerodynamic diameter measurements. Part 2: Application to combustion-generated soot aerosols as a function of fuel equivalence ratio, Aerosol Science and Technology, 38 (12), 1206-1222, 2004.

Spencer, M.T., L.G. Shields, and K.A. Prather: Simultaneous measurement of the effective density and chemical composition of ambient aerosol particles, Environmental Science & Technology, 41 (4), 1303-1309, 2007.

Stein, S.W., B.J. Gabrio, D. Oberreit, P. Hairston, P.B. Myrdal, and T.J. Beck: An evaluation of mass-weighted size distribution measurements with the Model 3320 aerodynamic particle sizer, Aerosol Science and Technology, 36 (7), 845-854, 2002.

Stein, S.W., P.B. Myrdal, B.J. Gabrio, D. Obereit, and T.J. Beck: Evaluation of a new Aerodynamic Particle Sizer (R) spectrometer for size distribution measurements of solution metered dose inhalers, Journal of Aerosol Medicine-Deposition Clearance and Effects in the Lung, 16 (2), 107-119, 2003.

Stephens, G.L., D.G. Vane, R.J. Boain, G.G. Mace, K. Sassen, Z.E. Wang, A.J. Illingworth, E.J. O'Connor, W.B. Rossow, S.L. Durden, S.D. Miller, R.T. Austin,

A. Benedetti, C. Mitrescu, C.S. Team, and: The cloudsat mission and the a-train - A new dimension of space-based observations of clouds and precipitation, Bulletin of the American Meteorological Society, 83 (12), 1771-1790, 2002.

Stier, P., J. Feichter, S. Kinne, S. Kloster, E. Vignati, J. Wilson, L. Ganzeveld, I. Tegen, M. Werner, Y. Balkanski, M. Schulz, O. Boucher, A. Minikin, and A. Petzold: The aerosol-climate model ECHAM5-HAM, Atmospheric Chemistry and Physics, 5, 1125-1156, 2005.

Stowe, L.L., A.M. Ignatov, and R.R. Singh: Development, validation, and potential enhancements to the second-generation operational aerosol product at the national environmental satellite, data, and information service of the national oceanic and atmospheric administration, Journal of Geophysical Research-Atmospheres, 102 (D14), 16923-16934, 1997.

Strawa, A.W., R. Castaneda, T. Owano, D.S. Baer, and B.A. Paldus: The measurement of aerosol optical properties using continuous wave cavity ring-down techniques, Journal of Atmospheric and Oceanic Technology, 20 (4), 454-465, 2003.

Strawa, A.W., R. Elleman, A.G. Hallar, D. Covert, K. Ricci, R. Provencal, T.W. Owano, H.H. Jonsson, B. Schmid, A.P. Luu, K. Bokarius, and E. Andrews: Comparison of in situ aerosol extinction and scattering coefficient measurements made during the Aerosol Intensive Operating Period, Journal of Geophysical Research-Atmospheres, 111 (D5), -, 2006.

Suess, D.T., and K.A. Prather: Mass spectrometry of aerosols, Chemical Reviews, 99 (10), 3007-+, 1999.

Sullivan, R.C., and K.A. Prather: Recent advances in our understanding of atmospheric chemistry and climate made possible by on-line aerosol analysis instrumentation, Analytical Chemistry, 77 (12), 3861-3885, 2005.

Svenningsson, I.B., H.C. Hansson, A. Wiedensohler, J.A. Ogren, K.J. Noone, and A. Hallberg: Hygroscopic Growth of Aerosol-Particles in the Po Valley, Tellus Series B-Chemical and Physical Meteorology, 44 (5), 556-569, 1992.

Tanre, D., Y.J. Kaufman, M. Herman, and S. Mattoo: Remote sensing of aerosol properties over oceans using the MODIS/EOS spectral radiances, Journal of Geophysical Research-Atmospheres, 102 (D14), 16971-16988, 1997.

Thornburg, J., S.J. Cooper, and D. Leith: Counting efficiency of the API Aerosizer, Journal of Aerosol Science, 30 (4), 479-488, 1999.

Torres, O., P.K. Bhartia, J.R. Herman, A. Sinyuk, P. Ginoux, and B. Holben: A long-term record of aerosol optical depth from TOMS observations and comparison to

AERONET measurements, Journal of the Atmospheric Sciences, 59 (3), 398-413, 2002.

Twomey, S.: Pollution and Planetary Albedo, Atmospheric Environment, 8 (12), 1251-1256, 1974.

van de Hulst, H.C.: Light Scattering by Small Particles, Dover, 1981, 1957.

Virkkula, A., N.C. Ahlquist, D.S. Covert, W.P. Arnott, P.J. Sheridan, P.K. Quinn, and D.J. Coffman: Modification, calibration and a field test of an instrument for measuring light absorption by particles, Aerosol Science and Technology, 39 (1), 68-83, 2005.

Volckens, J., and T.M. Peters: Counting and Particle Transmission Efficency of the Aerodynamic Particle Sizer, Journal of Aerosol Science, 36 (12), 1400-1408, 2005.

Wang, J., R.C. Flagan, J.H. Seinfeld, H.H. Jonsson, D.R. Collins, P.B. Russell, B. Schmid, J. Redemann, J.M. Livingston, S. Gao, D.A. Hegg, E.J. Welton, and D. Bates: Clear-column radiative closure during ACE-Asia: Comparison of multiwavelength extinction derived from particle size and composition with results from Sun photometry, Journal of Geophysical Research-Atmospheres, 107 (D23), -, 2002.

Wang, S.C., and R.C. Flagan: Scanning Electrical Mobility Spectrometer, Journal of Aerosol Science, 20 (8), 1485-1488, 1989.

Watson, J.G.: Visibility: Science and regulation, Journal of the Air & Waste Management Association, 52 (6), 628-713, 2002.

Wyatt, P.J., K.L. Schehrer, S.D. Phillips, C. Jackson, Y.J. Chang, R.G. Parker, D.T. Phillips, and J.R. Bottiger: Aerosol-Particle Analyzer, Applied Optics, 27 (2), 217-221, 1988.

Yu, H., Y.J. Kaufman, M. Chin, G. Feingold, L.A. Remer, T.L. Anderson, Y. Balkanski, N. Bellouin, O. Boucher, S. Christopher, P. DeCola, R. Kahn, D. Koch, N. Loeb, M.S. Reddy, M. Schulz, T. Takemura, and M. Zhou: A review of measurement-based assessments of the aerosol direct radiative effect and forcing, Atmospheric Chemistry and Physics, 6, 613-666, 2006.

Zelenyuk, A., D. Imre, and L.A. Cuadra-Rodriguez: Evaporation of water from particles in the aerodynamic lens inlet: An experimental study, Analytical Chemistry, 78 (19), 6942-6947, 2006.

Zhao, T.X.P., I. Laszlo, O. Dubovik, B.N. Holben, J. Sapper, D. Tanre, and C. Pietras: A study of the effect of non-spherical dust particles on the AVHRR aerosol optical thickness retrievals, Geophysical Research Letters, 30 (6), -, 2003.

2. Extending ATOFMS Measurements to Include Refractive Index and Density

2.1 Synopsis

An absolute calibration of the light scattering region in an aerosol time-of-flight mass spectrometer (ATOFMS) has been performed enabling a direct comparison of the average experimentally measured light scattering intensity to theory. A fitting procedure allows for the determination of both refractive index and density for spherical homogenous particles. The scattering information has been correlated with the other single particle information measured by the ATOFMS. Size, chemical composition, and scattering intensity can all be linked to establish a better understanding of the relationships between the chemical and physical properties of aerosol particles. Currently, inputs into climate models are derived from data acquired from bulk aerosol composition measurements, and therefore, assumptions must be made regarding the chemical associations within individual particles (mixing state) to enable modelers to calculate the relevant aerosol optical properties. These new measurements aim for the goal of directly testing the model assumptions by utilizing single particle chemical information to derive the optical properties of the resulting particle classes.

2.2 Introduction

During the last several decades, a number of techniques for characterizing single aerosol particles have been developed to include measurements of chemical composition, size, optical properties, shape and density[*Kaye*, 1998; *Kerker*, 1997; *McMurry*, 2000; *Sipin et al.*, 2003]. Each of these techniques focuses on measuring one or two properties of the aerosol at once. Researchers are now making an effort to couple techniques to obtain as many pieces of information as possible on a single particle simultaneously rather than having to do separate measurements and subsequently correlate the data acquired using independent analytical techniques. In particular, such efforts are underway by groups performing single particle mass spectrometry. In these single particle mass spectrometric techniques, optical detection is often required prior to mass spectral analysis. Therefore, a technique which determines the size and chemical composition of the particles is well suited for measuring the optical properties as well.

The optical region of a commercial ATOFMS has recently been used to determine aerosol optical properties[*Dutcher et al.*, 2004]. In these measurements, aerosol particles were size selected by electrical mobility diameter prior to entering the instrument where their light scattering intensity was measured. Using the mobility diameter and comparing the theoretical and measured light scattering intensity, a refractive index could be calculated. However, measurements did not associate aerodynamic diameter or chemical composition with scattering intensity for individual aerosol particles. Another version of a single particle mass spectrometer, PALMS, has been used to simultaneously measure the light scattering intensity, aerodynamic diameter (D_a) and chemical composition to infer a density for real atmospheric particles [*Murphy et al.*, 2004]. However, since no

calibration relationship was established between the light scattering signal and the flux of scattered light, they could not perform a systematic determination of refractive index. To accomplish this task, one needs to calibrate the optical system based on the geometry of the light collection optics and incident radiation while using standard particles and applying an appropriate light scattering theory.

In the present paper, we introduce a procedure enabling an absolute calibration of the light scattering region of the ATOFMS. With an absolute calibration, the pulse height or area produced during a scattering event can be transformed into a partial scattering cross section, computed here using Mie theory, enabling the calculation of absolute experimental values for refractive index and density. Because the chemical composition of each particle is measured, particles can be sorted based on chemical composition before performing any scattering calculation. Therefore, it is possible to perform measurements of effective density, refractive index, and aerodynamic diameter on aerosols separated on the basis of chemical composition.

2.3 Experimental Details

The ATOFMS used in this study has been described previously [*Gard et al.*, 1997] and the specifics of the additional light scattering data acquisition hardware and software have been described by Dienes [*Dienes and Prather*, 2003]. It is important to point out that in the ATOFMS, light is scattered at two points separated by a known distance in a vacuum chamber so that the particle velocity (and thus size) can be measured and used to trigger the desorption/ionization laser used for mass spectral analysis. An additional two channel, 12 bit, 50 MS/s digitizer (CompuScope 1250, Gage

Applied Technologies, Lachine, QC, Canada) is used to capture the scattering signal produced by the two photomultiplier tubes (PMT). The digitizer is triggered using the Nd:YAG trigger pulse from the timing circuit of the ATOFMS. Each scattering signal is recorded with the velocity, time, and mass spectral information. Even if the particle does not produce a mass spectrum, the scattering signal and velocity information are still written to a file.

The YAADA (http://www.yaada.org/) single particle analysis software written in MATLAB (The MathWorks, Inc., Natick, MA) was used to analyze the single particle data in this study. Portions of YAADA were re-written to incorporate the single particle scattering information into the database. Four new columns were added to the database representing the pulse height and pulse area for PMTs A and B. Having these new columns in the YAADA database allows one to search on a variable (e.g. chemical composition) and link the subset of particles with all of the other variables – including the scattering information from the two PMTs.

ART-2a, an algorithm that groups chemically similar mass spectra, was used to isolate different particle types in this study [*Song et al.*, 1999]. ART-2a was run with a vigilance factor of 0.85, a learning rate of 0.05 and 20 iterations. Thirty-five of the resulting clusters, comprising 97% of the chemically analyzed particles, were grouped by hand into two classes based on a visual inspection of single particle spectra from laboratory generated particles.

The test particles used in this study were polystyrene latex spheres (PSL) (Interfacial Dynamics Corp., Portland, OR) and dioctyl sebacate (DOS) (Aldrich, Milwaukee, WI). The DOS and PSL aerosols were generated by adding ~2 drops of DOS or PSL to ~200

mL methanol or water. The aerosols were generated from the solutions using a Collison atomizer utilizing N_2 as the carrier gas.

2.4 Results

2.4.1 Background on Theory

Response Calculations for the ATOFMS Scattering Optics

Calculating the theoretical response of the single particle light scattering signal collected by the ellipsoidal mirrors of the ATOFMS follows the same procedure used for calculating the theoretical response of optical particle counters (OPCs). Assuming linearly polarized incident radiation, the response of the ATOFMS is given by

$$R_{ATOFMS} = \frac{1}{k^2} \cdot \iint \left(|S_1|^2 Sin^2\phi + |S_2|^2 Cos^2\phi \right) Sin\theta \, d\theta \, d\phi \,, \qquad \text{(Eq. 2.1)}$$

where k is the wavenumber, **f** is the azimuth angle from the plane of polarization, **q** is the polar angle and S_1 and S_2 are known as the scattering amplitude matrix elements. The scattering amplitude matrix elements are calculated from Mie theory and are functions of the refractive index, particle size, wavelength of light (**l**), and **q**.[10] For spheres, there is no dependence of S_1 and S_2 on **f**. The refractive index is given by $m = n + ik$ with n and k being real constants and $i = \sqrt{-1}$. R_{ATOFMS} is essentially a partial scattering cross section because only a fraction of the total scattered light is collected by the ellipsoidal reflector.

The integral of Eq 1. must be evaluated over the angular range for which the light is collected by the ATOFMS light collection mirror. This integration process is done in two parts: one part for axisymmetric scattering and one for off-axis scattering. The details

of these methods follow those of Hodkinson and Greenfield [*Hodkinso.Jr and Greenfie.Jr*, 1965] and McMurry [*McMurry*, 2000]. The axisymmetric scattering geometry is shown in Figure 2.1. In Figure 2.1 the shaded areas represent the surfaces of the light collection mirror. The laser beam of the ATOFMS traverses the segment OG, therefore, there are holes in the mirrors to let the laser through. These holes determine the range of **q** in Eq. 1 to be between 7.2º and 172.8º while **f** is taken from 0 to 360º. The axisymmetric response (R_{AS}) can now be defined as

$$R_{AS} = \frac{1}{k^2} \cdot \int_{0°}^{360°} \int_{7.2°}^{172.8°} \left(|S_1|^2 \, Sin^2\phi + |S_2|^2 \, Cos^2\phi \right) Sin\theta \, d\theta \, d\phi \,. \qquad \text{(Eq. 2.2)}$$

Next, the off axis portion of light that is not collected by the ellipsoidal mirror needs to be calculated and subtracted from R_{AS}. Consider the off-axis geometry shown in Figure 2.2. In this figure, the laser is traveling along the segment ON. The intersection of the cone of scattered light with the collection sphere at a given **q** is represented by the circle MCLE. This cone of scattered light from the particle at point O is intercepted by the mirror aperture KCBE of semi angle **b** – this is the portion of light that is not collected by the ATOFMS ellipsoidal mirrors. For this case, there is an interdependence of **f** and **q**; that is, for a different value of **q** there will be a different integration range for **f**. For this reason, it is useful to write an expression for the upper and lower bounds of **f**:

$$\begin{aligned} \phi_{lo} &= \chi - \angle DAC(\theta) \\ \phi_{hi} &= \chi + \angle DAC(\theta) \end{aligned} \,, \qquad \text{(Eq. 2.3)}$$

where **c** is the azimuth of the mirror's large aperture from the plane of polarization . For the ATOFMS, **c** = 90º. Figure 2.2b illustrates these azimuthal limits more clearly.

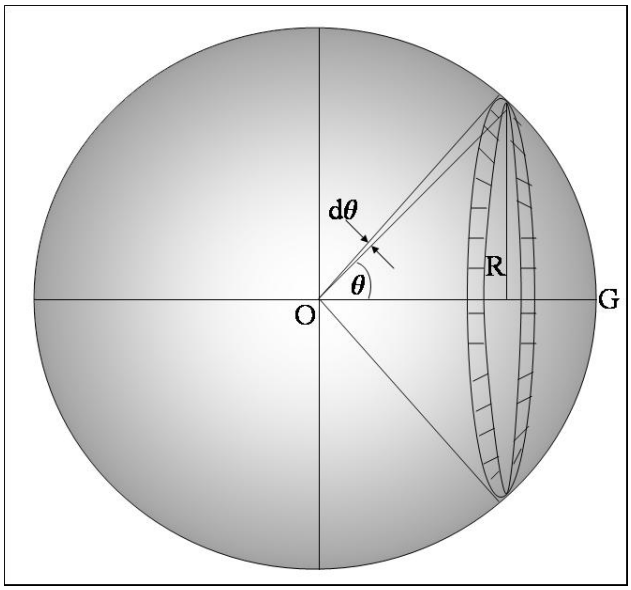

Figure 2.1. Diagram showing the axisymmetric scattering geometry. Segment OG represents the laser beam axis and the centerline perpendicular to that segment represents the aerosol beam axis.

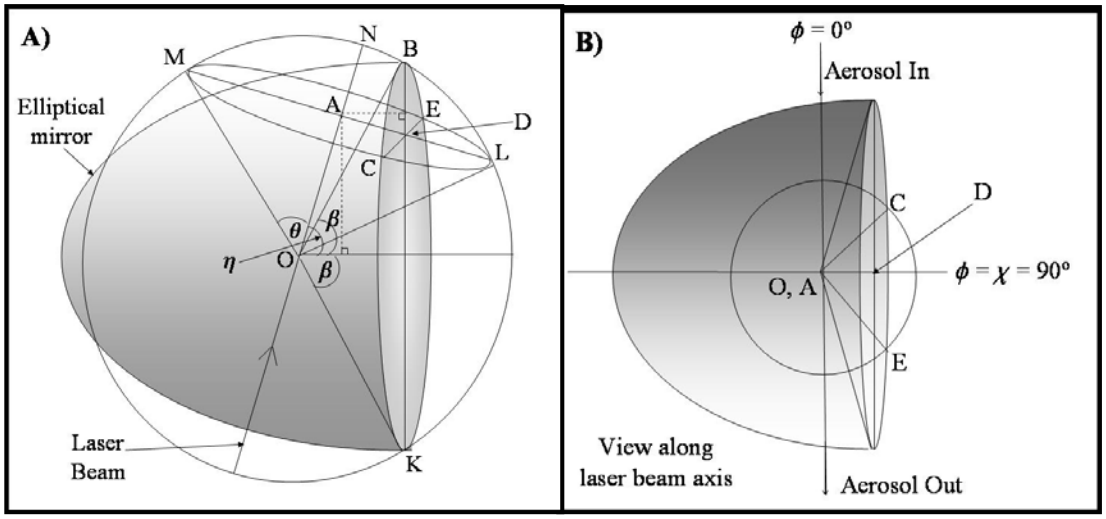

Figure 2.2. A) Diagram showing the off axis scattering geometry. B) Off axis scattering with the laser beam normal to the page at point O.

Hodkinson and Greenfield define ∠DAC as:

$$\angle DAC = Cos^{-1}\left(\frac{Cos\beta - Cos\theta\, Cos\eta}{Sin\,\theta\, Sin\,\eta}\right), \qquad \text{(Eq. 2.4)}$$

where **h** = 90º and **b** = 72º for the ATOFMS geometry. To further simplify the integration laid out in Eq. 1, we define

$$\alpha_1 = \int_{\phi_{lo}}^{\phi_{hi}} Sin^2\phi\, d\phi = \left(\frac{\phi}{2} - \frac{Sin2\phi}{2}\right)\Bigg|_{\phi_{lo}}^{\phi_{hi}} = \frac{\phi_{hi} - \phi_{lo}}{2} - \frac{Sin2\phi_{hi}}{4} + \frac{Sin2\phi_{lo}}{4}, \qquad \text{(Eq. 2.5)}$$

and

$$\alpha_2 = \int_{\phi_{lo}}^{\phi_{hi}} Cos^2\phi\, d\phi = \left(\frac{\phi}{2} + \frac{Sin2\phi}{2}\right)\Bigg|_{\phi_{lo}}^{\phi_{hi}} = \frac{\phi_{hi} - \phi_{lo}}{2} + \frac{Sin2\phi_{hi}}{4} - \frac{Sin2\phi_{lo}}{4}, \qquad \text{(Eq. 2.6)}$$

and then write an expression for the off-axis portion of light not collected:

$$R_{OA} = \frac{1}{k^2}\cdot\int_{\eta-\beta}^{\eta+\beta}\left(|S_1|^2\,\alpha_1 + |S_2|^2\,\alpha_2\right)Sin\theta\, d\theta\,. \qquad \text{(Eq. 2.7)}$$

Note that the integral over **q** is taken from **h** - **b** to **h** + **b** because these polar angles define the bounds of the mirror's aperture KCBE. Finally, we calculate the overall response of the ATOFMS scattering optics by calculating the cross section (excluding holes for the laser) and subtracting the off-axis cone of light that is not collected:

$$R_{ATOFMS} = R_{AS} - R_{OA}\,. \qquad \text{(Eq. 2.8)}$$

The integrals R_{AS} and R_{OA} are evaluated numerically with a Romberg quadrature routine. There are also holes to allow the aerosol to flow through the mirror, but these holes are small and are at an angle where their presence does not make a large (i.e. >1%) impact on R_{ATOFMS}.

2.4.2 Results and Discussion

Calibration using Standard Spheres

In order to compare the ATOFMS light scattering measurements to theory, we need to arrive at a functional relationship between the measured light scattering response and the theoretical response. Since the PMT is operating within the linear range and the A/D converter is quantitative, the pulse area (R_{meas}) is linear with theoretical response. From a linear fit of pulse area vs. theoretical intensity, we obtain a function that will allow the transformation of R_{meas} to $R_{ATOFMS,\ meas}$ enabling a direct comparison to theory:

$$R_{ATOFMS,meas} = R_{meas} \cdot G + R_0 . \qquad \text{(Eq. 2.9)}$$

Here G and R_0 is the slope and intercept of the linear fit. In order to produce the linear relationship experimentally, a series of PSLs of different diameters (each size producing a different intensity) were sampled with the ATOFMS enabling R_{meas} to be collected for each size. The speeds of several monodisperse PSL samples (ranging from 0.3-2.7μm) were selected to fall within ±1m/s which corresponds to a ±7.5nm range in aerodynamic diameter (D_a). The number of particles in these 15 nm bins ranged from 353-902, and R_{meas} is equal to the average of the scattering signals in that bin. Then, using the refractive index stated by the PSL manufacturer (1.59) and the particle size, R_{ATOFMS} was calculated with Mie theory using Eq. 9. The resulting calibration curve shows a strong linear correlation ($R^2 = 0.993$) as shown in Figure 2.3. Separate curves are constructed for PMTs A and B. Calibration procedures such as these are used to transform all pulse areas

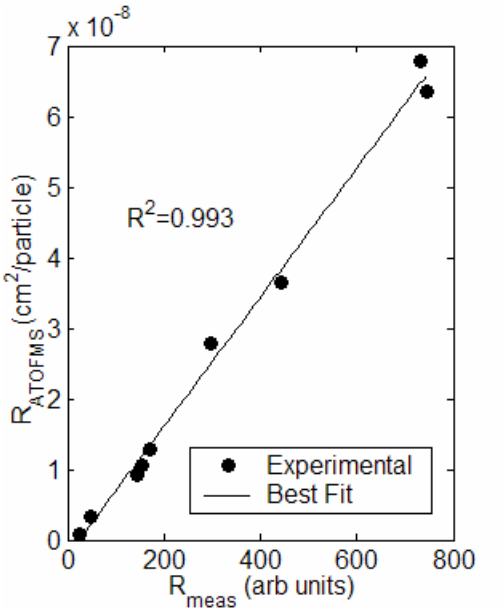

Figure 2.3. The theoretical response (R_{ATOFMS}) compared with the measured response (R_{meas}) of the ATOFMS instrument to scattered light from PSL particles of varying sizes. This curve is used to transform the experimental response to a partial scattering cross section, enabling a quantitative comparison with theory.

collected for other experimental samples into a partial scattering cross section ($R_{ATOFMS, meas}$) that can be fit to theory.

Experimental Data Processing

For developing the data processing routine, data from DOS particles were collected and analyzed. DOS was selected because of its polydispersity, ease of particle generation, spherical shape, and chemical homogeneity. The data were collected and imported into the YAADA database, allowing the scattering information from both PMTs to be linked with D_a, date and time of sampling, and dual polarity mass spectra. After the database was set up and the calibration curve was generated, the raw scattering data could then be transformed into partial scattering cross sections using Eq. 9. This process usually involved searching either on time or chemical composition to separate a certain particle type and plotting the scattering intensity as a function of D_a. Figure 2.4 shows a plot of R_{ATOFMS} as a function D_a for ~20,000 DOS particles. The figure distinctly shows the ripple structure due to the resonant electromagnetic modes of the sphere around the 1 μm region at the upper limit of scattering intensity. The distribution of scattered intensity for a given size is broad due to the lack of sheath air used to confine particles to a tight sensing region. Because a converging nozzle was used as the inlet in this study, the particles diverged rapidly and thus many of the particles encountered the fringes of the Gaussian laser beam, giving a lower value for the average scattered intensity than theoretically predicted. Therefore, a range of intensities from nearly zero to some upper

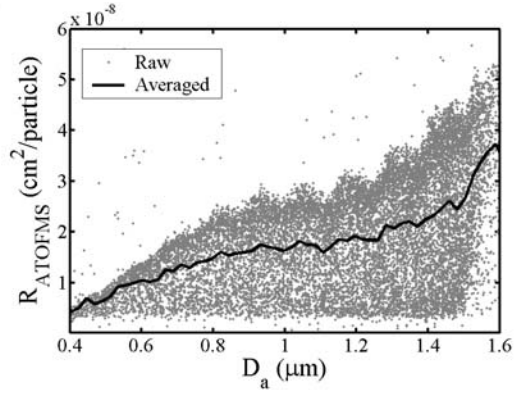

Figure 2.4. Raw and averaged partial scattering cross section as a function of aerodynamic diameter for dioctyl sebacate (DOS) particles.

limit was obtained for particles of the same size and chemical composition. This upper limit corresponds to an event where the particle traveled through the middle of the Gaussian laser beam. Particles that produced scattering signals above the upper limit were most likely "contamination" particles or agglomerates, and not single DOS particles. For the purposes of this study, the average of the scattered light intensity was used in the calibration and data processing steps because of its robustness compared with edge detection algorithms that serve to trace the upper edge of the scattering curve. The edge detection algorithms normally produced similar results to those obtained using the average scattering signal when a large number of particles of a given size were analyzed. However, when the number of particles in a particular region of the scattering curve was low, the edge detection algorithm produced large errors.

The single particle scattering data were collected as a function of D_a, then binned according to size and averaged before a comparison to theory can be done. The dark line in Figure 2.3 shows an average of the single particle scattering data binned in 10 nm size bins. For datasets with fewer particles, it was necessary to increase the bin width for averaging. Any bin with fewer than 10 particles was discarded. We see that the average line is able to recreate some of the ripple structure seen in the raw data. With the average scattering intensity as a function of D_a, we could then compare our scattering measurements to theory.

Experimental Data Fitting

The processed data obtained via the procedure described above are compared with Mie theory using a nonlinear fitting technique. This fitting procedure was used to fit

$R_{ATOFMS,meas}$ to the theoretical value ($R_{ATOFMS,test}$) involves an implementation of the simplex algorithm[13] to minimize the error function given by:

$$SqErr = \sum_{j=1}^{N}\left[\frac{\left(R_{ATOFMS,\,meas} - R_{ATOFMS,\,test}\left(n, D_p\right)\right)^2}{\sigma_{meas}^{\;2}}\right] \qquad \text{(Eq. 2.10)}$$

Here σ_{meas} is the standard error of the light scattering signals for the N bins used. $R_{ATOFMS,test}$ was produced by varying *n*, D_p, or both to find the value(s) that minimized SqErr. For initial trials of the fitting algorithm, D_a was used in place of D_p. To ensure convergence to a global minimum, several initial values for *n* were provided to the fitting algorithm. Figure 2.5a shows the results of the fitting routine to scattering data from DOS particles with D_p fixed and *n* was varied so as to obtain the best fit. The best fit value of n in this case was *n* = 1.50.

To improve on this fitting procedure, we use Eq. 10 along with the relation

$$D_a = D_p\sqrt{\frac{C(D_p)\,\rho_p}{\chi_d\;C(D_a)\,\rho_0}} \qquad \text{(Eq. 2.11)}$$

to change ρ_p, the particle density, into a fitting parameter. Here ρ_0 is a standard density (1.054 g/cm^3 in the case of standard PSL particles), *C(D)* is the Cunningham slip correction factor and χ_d is the dynamic shape factor. χ_d = 1 for the case of spherical particles. Because Mie theory calculates the scattering intensity given D_p, and not D_a we should obtain a more valid fit to theory if we are able to predict a correct D_p; to do this we let both D_p and n vary in the calculation of R_{test} during the minimization of SqErr. The results of this two parameter fit are shown in Figure 2.5b. The fit has improved and, in contrast to Figure 2.5a, the fine structure of the scattering curve fits better as well. For example, small peaks in Figure 2.5a are anticorrelated due to the fact they were

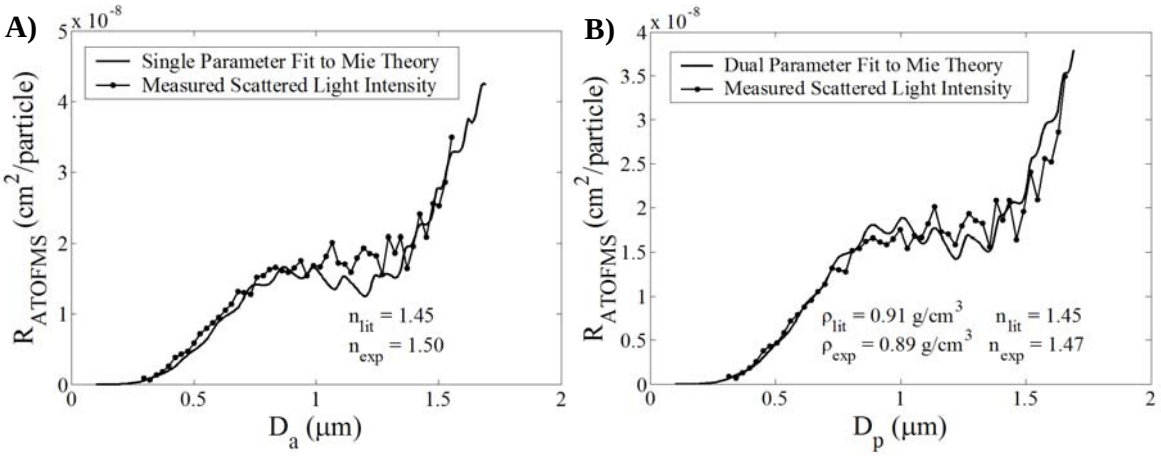

Figure 2.5. Theoretical and measured partial scattering cross section (R_{ATOFMS}) as a function of size. A) A single parameter fit to Mie theory, where only refractive index is determined. B) A dual parameter fit to Mie theory in which the refractive index and particle density are determined.

approximately shifted by $\sqrt{\rho}$, whereas in Figure 2.5b they are correlated and the shift was taken into account by finding the correct value for **r**. From the fit we determined $\mathbf{r}_{p,meas}$ = 0.9g/cm^3, compared with the manufacturer's value of $\mathbf{r}_{p,lit}$ = 0.914g/cm^3. The value of *n* was experimentally determined to be 1.47 compared to the literature value of 1.4510. In this case, the two parameter fit is more accurate than the single parameter fit for the real part of refractive index.

Incorporation of Chemical Information

To test whether the chemical information can be linked to the aerodynamic size and scattering intensity, an ART-2a analysis was run to separate samples of DOS and PSL on the basis of their chemical composition. The clusters from the ART-2a analysis were arranged visually into two groups based only on chemical signatures. Figure 2.6 shows the average mass spectra for the two classes together with their scattering intensities plotted against D_a. The average mass spectra for PSL single particle class are distinctly different from the DOS single particle class. Most notably, there was significantly more sodium (m/z = 23) as an impurity in the DOS sample. This alone allows the distinction of the particles. The plots of scattering intensity vs. D_a (insets to Figures 2.6a and 2.6b) confirm the scattering intensity was correctly linked to the size and chemical composition as the PSLs have discrete sizes and DOS particles have a continuous size distribution. Furthermore, the scattering plot for the DOS cluster shows scattering signals for a continuum of sizes with the scattering signal showing the sharp

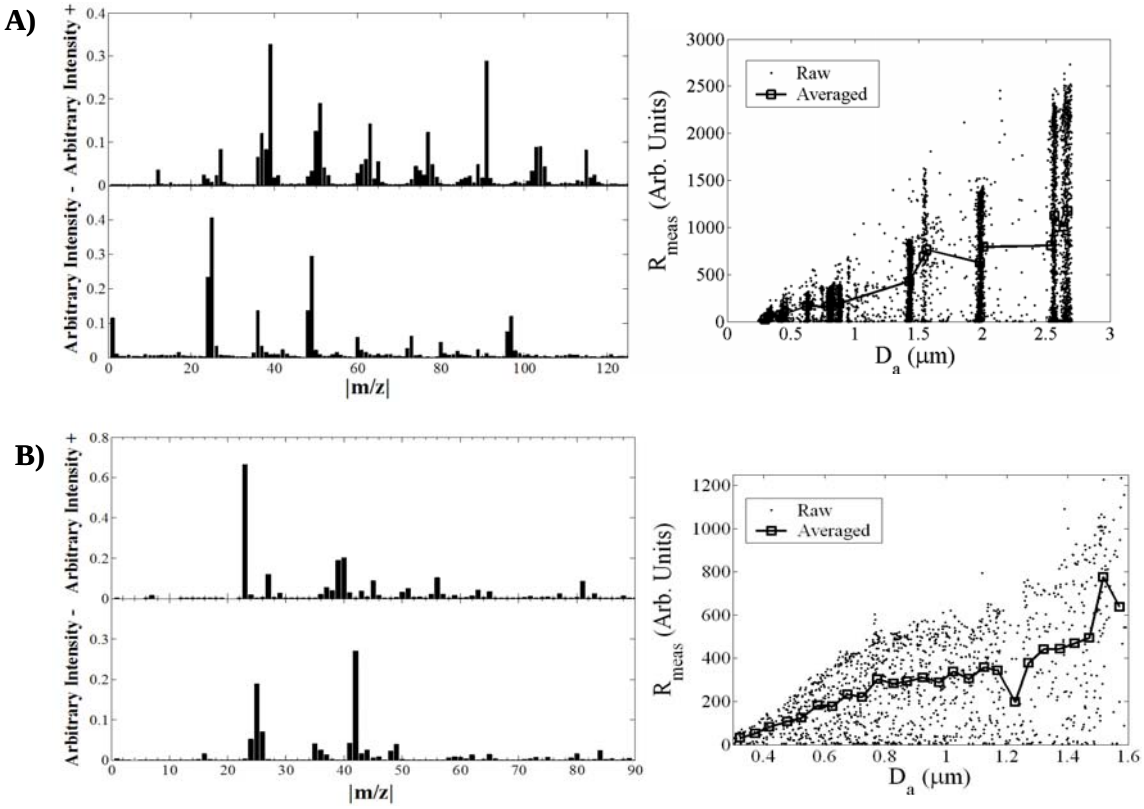

Figure 2.6. Average mass spectra (left) and scattering curves (right) for the PSL (A) and DOS (B) classes.

cutoff at the largest intensities – a characteristic of scattering by morphologically and chemically identical particles. The same pattern is seen in Figure 2.4, but for a different

To further test the reliability of our fitting routine, the same samples of DOS and PSL were separated on the basis of date/time stamp (the time when the sample was analyzed with the ATOFMS) and compared with the corresponding subset of particles separated based on single particle chemical composition. Table 2.1 shows the results of this comparison for the single and dual parameter fits described above. For each segregation method, we only fit one parameter and held the density at a constant, known value for the particular sample or both the refractive index and density were allowed to vary for the dual parameter fits. Uncertainties represent the standard deviation of the fitting results for two separate experiments using data from both PMTs, resulting in 4 independent measurements.

For the time searches, the refractive index obtained for PSLs was higher than for DOS, as expected. The time searches returned 3055 and 22482 particles for the DOS analysis time and 23615 and 10574 particles for the PSL analysis time range. The two values represent the number of particles for each sample during the two experiments. From these results, it is evident that the *n* determined for PSL is close to the literature value (1.59) and *n* determined for DOS is slightly higher than the literature value (1.45). The densities obtained for the two parameter fits of the particles separated by time are also in agreement with the values quoted by the manufacturers.

For the chemical searches, the results obtained for refractive index and density for PSL and DOS less accuracy for refractive index, but all retrieved values for refractive

Table 2.1. Measured values for density (ρ) and refractive index (*n*) for laboratory generated test particles.

Sample[a]	Separation Method[b]	Number of Parameters Fit	ρ (g/cm^3)	*n*
DOS	Time	1	1.0(1)	1.51(7)
DOS	Time	2	Fixed at 0.91	1.46(3)
DOS	Chem	1	0.7(2)	1.42(7)
DOS	Chem	2	Fixed at 0.91	1.47(4)
PSL	Time	1	1.1(2)	1.64(6)
PSL	Time	2	Fixed at 1.05	1.59(2)
PSL	Chem	1	1.0(2)	1.62(9)
PSL	Chem	2	Fixed at 1.05	1.61(9)

[a]PSL has n = 1.59 and ρ = 1.05 g/cm^3 and DOS has n = 1.45 and ρ = 0.914 g/cm^3.
[b]Particles are separated by either chemical composition or time.

index and density are within the limits of experimental uncertainty. The chemical searches returned 585 and 1482 particles for the PSL analysis time and 7383 and 2368 particles for the DOS analysis time. Presumably, because the smaller sample size in the chemically segregated light scattering data, the fits produced larger uncertainties. In the future, the fits should be constrained to limit the possible values for density and refractive index obtained by the fitting procedure to physically sensible values. Take for example aqueous NaCl aerosol identified by the mass spectrometer. In this case the determined values for n and ρ could be kept in between those of pure water (n=1.3 and ρ=1g/cm^3) and those of the crystallized solute (n=1.54 and ρ=2.17 g/cm^3). Procedures such as this will help minimize the spread of possible values, thereby reducing the overall uncertainty for the measurement by keeping the algorithm from giving unrealistic answers resulting from divergence.

2.5 Conclusions

To date, the ATOFMS has been used to perform real-time measurements of the size and chemical composition of single aerosol particles. As described in this paper, the ATOFMS can now measure the light scattering intensity from individual particles, the average of which can give the optical properties of single particle classes. This direct link between particle mixing state and optical properties is a vital yet missing component in global climate models. The new scattering measurements will allow one to establish correlations between the optical (refractive index) and physical (density) properties of aerosols as functions of time, chemical composition, and size. For spherical, homogenous particles, the current method will work well, but it has yet to be thoroughly tested using

non-spherical particles. Preliminary results show that the current method is useful for distinguishing between optical information for non-spherical (dry) versus spherical (wet) salt particles. The goal of these and future studies is to help test the assumptions in current global climate models regarding how particle mixing state impacts aerosol optical properties. Moreover, it is hoped that density and morphology information will facilitate the transformation of particle number concentrations to mass concentrations for different particle types - something that has not been possible for single particle data collected in previous measurement campaigns.

The overall quality of the fitting procedure to the scattering data obtained with the converging nozzle used in the early versions of the ATOFMS will improve with the use of an aerodynamic lens which provides much less divergence of the particle beam. Preliminary results show that sharper pulse height distributions are obtained with an aerodynamic compared to a nozzle. These results are supported by the observations of Dutcher and McMurry [*Dutcher et al.*, 2004]. Therefore, for the aerodynamic lens, a smaller number of particles will be needed to produce values of density and refractive index. In this current study with a converging nozzle, we showed that sample sizes as small as 585 particles can provide an estimation of refractive index and density.

Future light scattering measurements with the ATOFMS should focus on determining the angular variation of scattered intensity by single particles and tying it in with the current suite of information provided by the ATOFMS. The angular variation in light intensity is quantified by the so called “phase function”. The phase function describes how scattering intensity varies as a function of angle. This is an important parameter in global climate models, as it relates to how much solar radiation is reflected

back to space. To have the phase function linked with the information described in this paper will represent a significant advance in our ability to characterize the properties of individual particle types as a function of size.

2.6 Acknowledgements

Chapter 2, in full, is a reprint of the material as it appears in:

Moffet, R. C.; Prather, Kimberly A. (2005) Extending ATOFMS Measurements to Include Refractive Index and Density *Analytical Chemistry* 77, 6535-6541. The dissertation author was the primary author of this paper.

The authors gratefully acknowledge the assistance of Dabrina Dutcher-Stolzenberg and Mark Stolzenberg from the McMurry group for the original FORTRAN code that provided a basis of the program used here to carry out the Mie integrations as well as for providing detailed explanations when needed. Robert Schwarzenbacher and Lukasz Jaroszewski provided useful discussions for testing some of the initial computations. Finally, we would like to thank the NSF for funding this work under ATM-0321362

2.7 References

Diens, T., and K.A. Prather, University of California, Riverside, Riverside, 2003.

Dutcher, D.D., P.H. Mc Murry, and D.S. Gross, in *AAAR Annual Conference*, pp. 199, AAAR, 2004.

Gard, E., J.E. Mayer, B.D. Morrical, T. Dienes, D.P. Fergenson, and K.A. Prather: Real-time analysis of individual atmospheric aerosol particles: Design and performance of a portable ATOFMS, Analytical Chemistry, 69 (20), 4083-4091, 1997.

Hodkinso.Jr, and Greenfie.Jr: Response Calculations for Light-Scattering Aerosol Counters and Photometers, Applied Optics, 4 (11), 1463-&, 1965.

Kaye, P.H.: Spatial light-scattering analysis as a means of characterizing and classifying non-spherical particles, Measurement Science & Technology, 9 (2), 141-149, 1998.

Kerker, M.: Light scattering instrumentation for aerosol studies: An historical overview, Aerosol Science and Technology, 27 (4), 522-540, 1997.

McMurry, P.H.: A review of atmospheric aerosol measurements, Atmospheric Environment, 34 (12-14), 1959-1999, 2000.

Murphy, D.M., D.J. Cziczo, P.K. Hudson, M.E. Schein, and D.S. Thomson: Particle density inferred from simultaneous optical and aerodynamic diameters sorted by composition, Journal of Aerosol Science, 35 (1), 135-139, 2004.

Sipin, M.F., S.A. Guazzotti, and K.A. Prather: Recent advances and some remaining challenges in analytical chemistry of the atmosphere, Analytical Chemistry, 75 (12), 2929-2940, 2003.

Song, X.H., P.K. Hopke, D.P. Fergenson, and K.A. Prather: Classification of single particles analyzed by ATOFMS using an artificial neural network, ART-2A, Analytical Chemistry, 71 (4), 860-865, 1999.

3

Measurement of Ambient Aerosols in Northern Mexico City by Single Particle Mass Spectrometry

3.1 Synopsis

Continuous ambient measurements with aerosol time-of-flight mass spectrometry (ATOFMS) were carried out in an industrial/residential section in the northern part of Mexico City as part of the Mexico City Metropolitan Area – 2006 campaign (MCMA-2006) between March 7 – 27, 2006. Biomass and organic carbon (OC) particle types were found to dominate the accumulation mode both day and night. The concentrations of both organic carbon and biomass particles were roughly equal early in the morning, but biomass became the largest contributor to the accumulation mode mass from the late morning until early evening. The diurnal pattern can be attributed to aging and/or a change in meteorology. Fresh elemental carbon (EC) particles were observed in the early morning, while the majority of the detected EC particles were mixed with nitrate, sulfate, organic carbon, potassium and peaked later in the day. Submicron particles from industrial sources in the northeast were composed of an internal mixture of Pb, Zn, EC and Cl and peaked early in the morning. A unique nitrogen-containing organic (NOC) particle type was observed, and is hypothesized to be from industrial emissions based on the temporal profile and back trajectory analysis. This study provides unique insights into the real-time changes in single particle mixing state as a function of size and time for aerosols in Mexico City. These new findings indicate that biomass burning and industrial

operations make significant contributions to particles in Mexico City and these sources have received relatively little attention in previous studies.

3.2 Introduction

The Mexico City Metropolitan Area (MCMA) is a megacity that allows for a unique opportunity to study air pollution. High levels of criteria pollutants are a product of the city's high population density, meteorology, and unique geographical location. Both gas and particle phase contaminants are generated that degrade human health and affect climate and visibility. A voluminous body of literature has resulted from studies of pollutants in the MCMA, with research focusing on a wide range of topics that include health effects, gas and particle phase measurements, modeling, economics and policy [*Molina*, 2002; *Raga et al.*, 2001]. The basic approach has been to use Mexico City as a case study of air pollution mitigation while major advances continue to improve the regional air quality.

To help decrease particulate matter (PM) pollution in Mexico City, one needs a better understanding of the spatial and temporal variability of the sources, size distribution, and chemical composition of the ambient aerosol. Knowledge of these parameters enables well-guided strategies for decreasing the PM fraction that is suspected to be the most harmful to human health. Prior to the development of the Automatic Ambient Air Quality Monitoring Network (RAMA) measurements that began in the mid 1980s, there were very few detailed measurements of particulate matter chemical composition in Mexico City. From the late 1980's to present, Aldape, Miranda, Flores

and co-workers measured PM chemical composition in Mexico City by using filters to collect PM followed by analysis with Proton Induced X-Ray Emission (PIXE) [*Aldape et al.*, 1996a; *Aldape et al.*, 1996b; *Cahill et al.*, 1996; *Flores et al.*, 1999; *Miranda et al.*, 2004; *Miranda et al.*, 1998; *Miranda et al.*, 1992]. Flores (1999) showed that there were increased concentrations of lead, copper and zinc in the northern (industrial) part of the city. These results were further corroborated by later results from the sampling period [*Mugica et al.*, 2002].

In the late 1990s, as part of the Aerosol and Visibility Evaluation Research (IMADA-AVER) campaign, Chow and co-workers measured the chemical composition of $PM_{2.5}$ and PM_{10} at a variety of sites using filter based techniques while also publishing complementary results characterizing the chemical composition of fugitive dust sources [*Chow et al.*, 2002a; *Chow et al.*, 2002b; *Vega et al.*, 2002]. Moya and co-workers examined the gas-particle equilibrium of ammonium and nitrate during the same campaign for purposes of evaluating thermodynamic models [*Moya et al.*, 2001]. They followed up those studies with size resolved measurements focusing on ammonium and sulfate from winter of 2000 to fall of 2001, but also included measurements of other cations [*Moya et al.*, 2003]. From January to February of 2003, Moya and co-workers provided a size-resolved characterization of inorganic species. They found an unexpectedly large concentration of K particles, which they attributed to dust from the dry lake bed of Texcoco in the northeastern part of the city [*Moya et al.*, 2004].

The most recent and detailed studies of aerosols in Mexico City were carried out during the MCMA-2003 campaign [*Baumgardner et al.*, 2004; *Dunn et al.*, 2004; *Jiang*

et al., 2005; *Jimenez et al.*, 2004; *Marr et al.*, 2006]. Electron microscopy was used to infer the mixing state and transformation of soot particles [*Johnson et al.*, 2005]. Chemically resolved $PM_{2.5}$ mass distributions were obtained using a variety of techniques including Aerosol Mass Spectrometry (AMS), and other filter based techniques [*Salcedo et al.*, 2006]. Salcedo et al. (2006) was also able to track mass concentrations of select, non-refractory aerosol components with a higher time resolution than previously reported by Chow et al. (2002a), while showing a general agreement between the two studies. Newer source apportionment measurements during the MCMA-2003 campaign were able to classify major sources of particles including industrial emissions using factor analysis [*Johnson*, 2006]. Industrial emissions in Johnston et al. (2006) were found to be well correlated with Na and Zn as well as other metals.

Many earlier studies of aerosol size and composition in Mexico City from 1990 to the present day were carried out as a part of major campaigns funded through an international effort [*Molina*, 2002]. Prior to 2006, there were three major research initiatives that measured aerosol physico-chemical properties: The Mexico City Air Quality Research Initiative (MARI), IMADA-AVER and MCMA-2003. The current effort: MILAGRO (Megacity Initiative: Local and Global Research Observations) is the largest to date representing the collaboration of over 400 scientists, from more than 120 institutions. A component of MILAGRO, MCMA-2006, with cooperation from NSF, DOE and a variety of Mexican and European agencies, represents an effort to characterize boundary layer emissions within the MCMA. The single particle mass spectrometry measurements discussed herein represented a new approach for studying air quality in Mexico City and were conducted as part of MCMA – 2006. The goal of this

current paper is to provide unique insights into the real-time changes in single particle mixing state as a function of size and time for aerosols in Mexico City.

3.3 Experimental

3.3.1 Sampling Site – T0

The ATOFMS instrument was located at the Instituto Mexicano del Petroleo (IMP) in the northern part of Mexico City (19º29’23.60 N, 99º08’55.60W). This was one of the three supersites selected for the MILAGRO measurement campaign to characterize the transport of emissions from the urban areas in the MCMA to the surrounding regions. Figure 3.1 shows the geographical location of the IMP site, referred as T0 (urban site). Measurements were located in a secondary structure on top of a five-story building. Sampling lines were placed >10’ above the building’s roof to minimize the effects of sampling from the building ventilation exhaust ports. To the north was an 800 m high mountain, Cerro del Chiquihuite, that served to block most of the winds coming from the north. An industrialized area existed to the west, while urban areas resided to the east and south. A dry lake bed of Lake Texcoco was located to the east. A busy roadway was located on the east side of the site with traffic jams during most of the day and street vendors cooking primarily during the morning and afternoon.

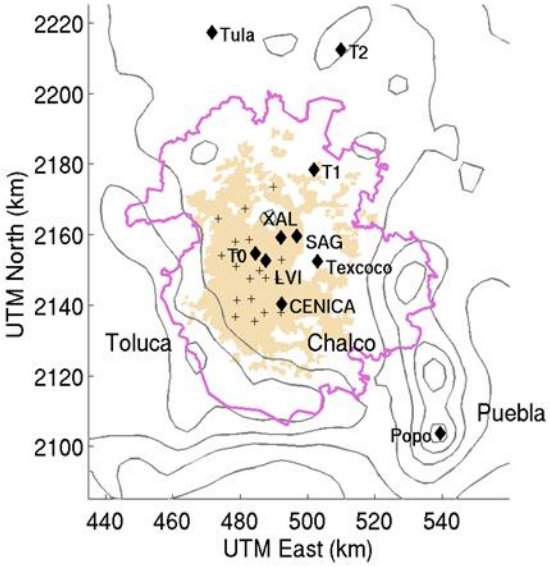

Figure 3.1. A map of the Mexico City Metropolitan Area (MCMA). The sampling site these measurements were carried out at was called T0, and was located at the Instituto Mexicano Del Petroleo (IMP). RAMA sites are shown as the + symbol. The political border of the MCMA as of 2003 is in pink and urban area as of 1995 are in beige. Terrain contours are every 500 m.

3.3.2 ATOFMS Measurements and Clustering Analysis

The ATOFMS is an instrument designed to measure real-time size and chemical composition of aerosols. The specific model of the instrument used in Mexico City is described in [*Gard et al.*, 1997]. The aerosols are drawn through a nozzle- inlet where the gas undergoes a supersonic expansion, and the particles are accelerated to a specific terminal velocity depending on their aerodynamic size. The particle velocity is determined by measuring the time-of-flight between two 50 mW diode pumped, solid state, frequency doubled Nd:YAG lasers operating at 532 nm. The single-particle scattering intensities from the two light scattering channels were acquired and saved along with the other single particle data as described in Moffet (2005) [*Moffet and Prather*, 2005]. The particle size is then calculated from the speed using a calibration curve generated with known sizes of standard polystyrene spheres. The speed of the particle is also used to time the arrival of the particle in the ion source region of the dual-polarity time-of-flight mass spectrometer. Once the particle is in the source region, a frequency quadrupled Nd:YAG laser operating at 266 nm with a typical pulse energy of 1.2 mJ desorbs and ionizes each particle. The ATOFMS measures both the positive and negative mass spectra of each particle simultaneously.

The ATOFMS has wide dynamic range capabilities. This is accomplished by taking the two signals from the two mass spectra being measured (positive and negative ion) and splitting them into an attenuated (30 dB) and non-attenuated channel, making four signals in total. The ATOFMS was operated from 06-Mar-2006 to 29-Mar-2006. Due to damage incurred during shipment, from 06-Mar-2006 19:00:01 to 13-Mar-2006

16:00:01, the instrument was operated without the negative wide dynamic range channel. After Mar-2006 16:00:01, both the negative and positive mass spectra were acquired using wide dynamic range.

A total of 1.6 million particles were sized and chemically analyzed with the mass spectrometer. The typical percentage of particles producing both size and chemical information was 50%; of these particles, 88% produced both positive and negative spectra. This percentage showed little variation over the study, indicating chemical matrix effects did not play a major role [*Wenzel et al.*, 2003]. Data from the ATOFMS were imported into a Matlab database program known as YAADA (www.yaada.org). Once in the Matlab database, the particles were split into four groups: sub and super-micron having wide dynamic range and non-wide dynamic range. The 48,000 particles from the four subsets of particles were separately classified using ART-2a, a clustering algorithm [*Song et al.*, 1999], run with a vigilance factor of 0.80 and a learning rate of 0.05. The clusters resulting from each analysis were matched to the rest of the particles in the complete dataset. In order to classify 1.4 million out of 1.6 million particles, 60 sub-micron and 200 super-micron clusters were considered (for each of the four groups) and accounted for 88% of the chemically analyzed particles. The 200,000 particles not classified made up a large number of sparsely populated clusters. The unclassified particles did not have any major temporal spikes indicating that the original number of particles given to ART-2a was sufficient. The particle *clusters* resulting from the ART-2a analysis were grouped by hand into 15 general particle *types*.

Hourly scaling functions were derived by scaling the ATOFMS data with size distribution data acquired with an aerodynamic particle sizer (APS, TSI, Inc.) using the method developed previously by our group [*Qin et al.*, 2006]. These scaled data were then used to derive mass concentrations of the specific particle classes by assuming the densities suggested by Qin et al.

3.4 Results and Discussion

For the 3.5 weeks that the ATOFMS operated at the T0 site, unique anthropogenic particle types and mixing states were observed in northern Mexico City. These unique particle types primarily contained different metals and organic nitrogen species. The majority of particles in the accumulation mode were either identified as biomass (from meat cooking or biomass burning), or organic carbon (OC). In the coarse (super-micron) mode, inorganic dust types were found to dominate. For all particle types, hourly time series (Sec. 3.4.4) and chemically resolved size distributions were obtained (Sec. 3.4.2). Average diurnal trends indicate that industrial emissions primarily occur in the early morning and that biomass and OC make the largest contributions to aerosol mass during the early morning to late afternoon hours. To identify possible source regions, a concentration field analysis was performed by combining ATOFMS time series with stochastic Lagrangian back trajectories (Sec. 3.4.5).

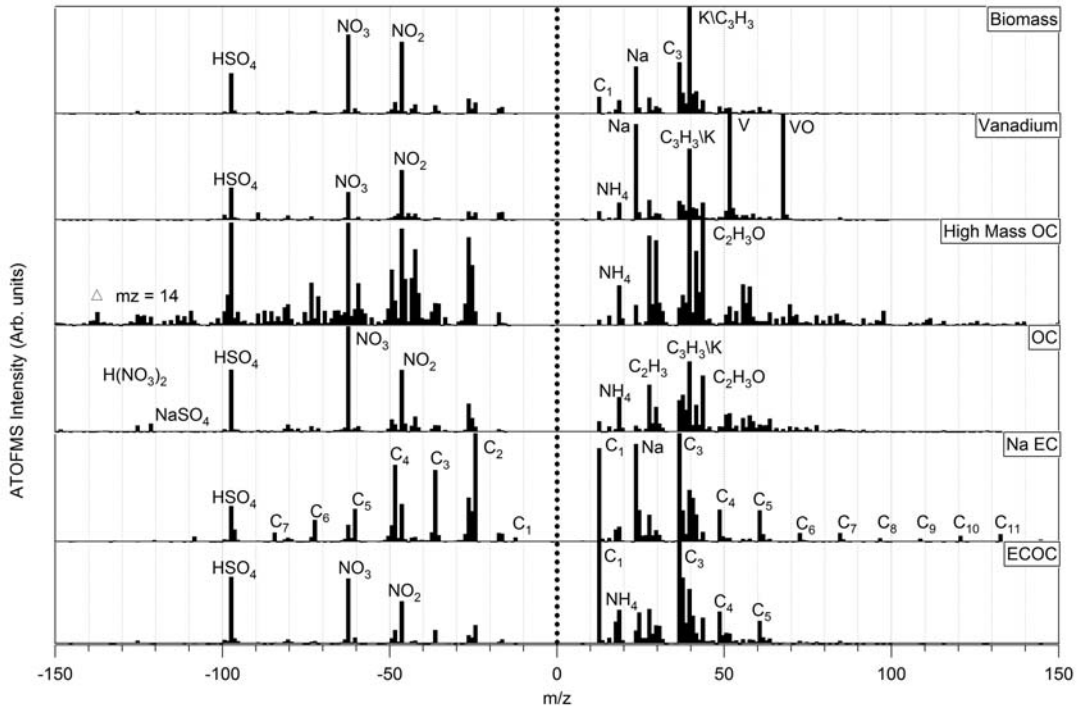

Figure 3.2a. Average spectra of single particle types as determined with the ART-2a clustering algorithm. The particle types shown here occurred mainly in the submicron portion of the size distribution.

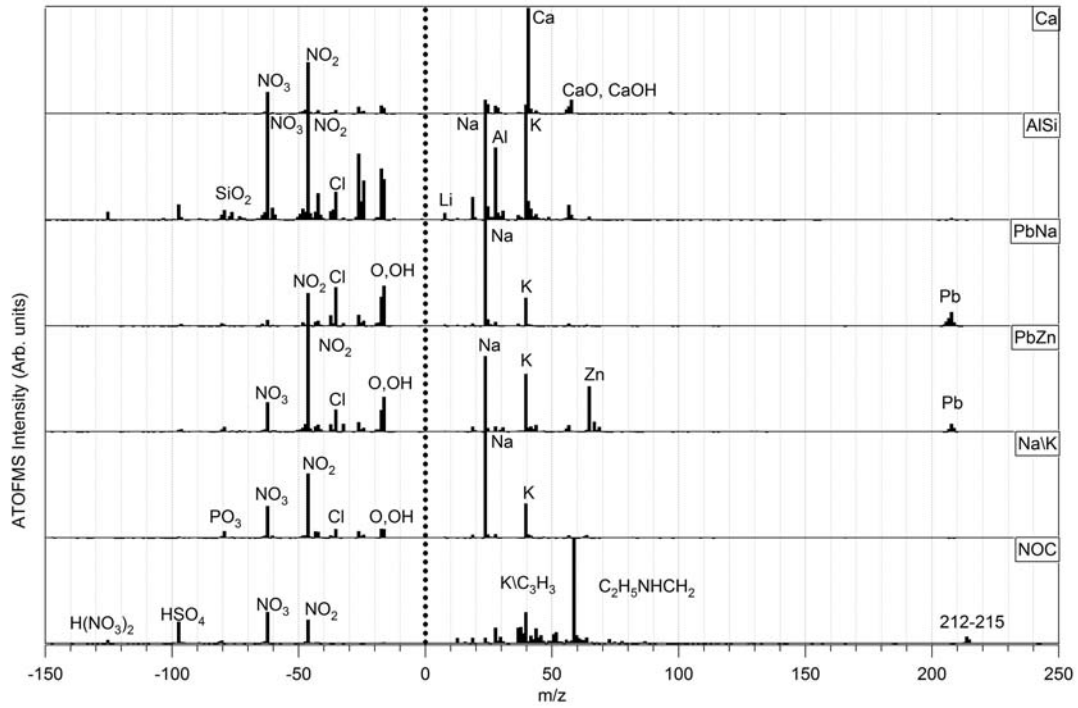

Figure 3.2b. Average spectra of single particle types as determined with the ART-2a clustering algorithm. The m/z range is extend to 250 Da compared to Figure 3.2a to show important peaks such as Pb for the industrial types and the unknown markers at 212-215 for the NOC type. Common coarse mode particle types shown here include: Ca, AlSi and Na/K. NOC was primarily of submicron sizes.

3.4.1 Mass Spectral Analysis of the Major Particle Types

Overall, out of the 1.6 million particles analyzed, 88% of the particles were placed into 15 general types by hand grouping the 60 submicron and 200 supermicron clusters from the ART-2a analysis. The average mass spectra for the single particle types are displayed in Figs. 3.2a and 3.2b. A feature that is common to all of the particle types is that $^{46}NO_2^-$ and $^{62}NO_3^-$ are detected in the negative ion spectra, indicating a significant amount of secondary processing. Other secondary markers occur in the positive ion spectra, namely $^{18}NH_4^+$ and $^{43}C_2H_3O^+$. Fine mode particles, especially carbonaceous types, contain sulfate ($^{97}HSO_4^-$) in their negative spectra. Conversely, coarse mode particle types (AlSi, NaK, Ca Dust) often contain other different markers in their negative ion mass spectra such as $^{35}Cl^-$ and $^{79}PO_3^-$.

3.4.1.1 Carbonaceous Particle Types

OC: Organic carbon (OC) particles were one of the most abundant particle types observed during this study. These particles are similar to those detected in other ATOFMS field studies [*Liu et al.*, 2003; *Noble and Prather*, 1996; *Pastor et al.*, 2003] and vehicular source characterization studies [*Sodeman et al.*, 2005; *Toner et al.*, 2006]. OC particles are typified by a large number of hydrocarbon envelope peaks that start with the base carbon peak $^{12n}C_n^+$. In Fig. 3.2a, the major hydrocarbon-containing peaks are identified as $^{27}C_2H_3^+$ and $^{43}C_2H_3O^+$. Many spectra also contain a large peak at m/z 39 (K+), indicating agglomeration between OC and biomass types.

Biomass: Previous ATOFMS studies have provided a solid basis for the identification of biomass particles [*Guazzotti et al.*, 2003; *Silva et al.*, 1999]. Particles classified as biomass always have $^{39}K^+$ as one of the largest peaks in the positive ion mass spectrum. Additionally, the biomass mass spectrum contains carbon marker ions. Na^+ is more prominent in the biomass particles than it is in the other carbonaceous particle types (with the exception of the NaEC type). Particles having these chemical signatures can be emitted as a result of biomass burning or cooking operations [*Silva*, 2000].

NaEC: The NaEC type is characterized by elemental carbon cluster ions at spacing of 12 m/z units in both the positive and negative ion spectra. This type has a dominant $^{23}Na^+$ peak. This combination of EC and Na ions is consistent with observations in other single particle mass spectrometry measurements of heavy duty vehicle (HDV) emissions [*Toner et al.*, 2006] and field studies [*Guazzotti et al.*, 2001; *Liu et al.*, 2003; *Noble and Prather*, 1996; *Pastor et al.*, 2003].

ECOC: The Elemental Carbon/Organic Carbon (ECOC) type is characterized by a positive ion mass spectrum that is dominated by clusters of carbon atoms. In addition to the major elemental carbon markers, minor signals occur from organic carbon envelopes along with many of the typical OC markers.

High Mass OC: The high mass organic carbon class was made to be a separate particle type due to the presence of hydrocarbon envelopes in the positive ions extending above 100Da. Typically these hydrocarbon envelopes have a $\Delta m/z = 14$, which is due to successive losses of a $^{14}CH_2$ group. Although not shown in the figure, the hydrocarbon

envelopes can extend out to m/z = 200 and above. High mass negative ions have been shown in lab secondary organic aerosol (SOA) studies [*Gross et al.*, 2006] and have been attributed to oligomeric species. Positive ion laser desorption ionization mass spectra at 266 nm with such high mass signatures are typically attributed to polycyclic aromatic hydrocarbons (PAH) [*Gross et al.*, 2000].

Vanadium: Vanadium particles have been identified with other analytical methods as well as single particle mass spectrometry in studies of light duty vehicle (LDV) emissions [*Sodeman et al.*, 2005], from industrial urban areas [*Noble and Prather*, 1996; *Tolocka et al.*, 2004], and from coal and oil fired power plant emissions [*Suarez and Ondov*, 2002]. Particles containing vanadium produce a very unique mass spectrum with peaks at $^{51}V^{+}$ and $^{67}VO^{+}$. Oxalate was seen in the negative mass spectrum at m/z = -89, having the chemical formula $^{89}C_2O_3OH^{-}$. Secondary sulfate and primary vanadium are a result of emissions from fossil fuel combustion. Oxalate may be from either biomass burning, or VOC oxidation followed by subsequent cloud processing [*Chebbi and Carlier*, 1996; *Morawska and Zhang*, 2002]. The fraction of the oxalic acid mass formed by cloud processing is currently a topic of research [*Ervens et al.*, 2004; *Kanakidou et al.*, 2005].

Nitrogen-containing organic (NOC): One of the new particle types detected in this study includes the NOC particle type. The "NOC" label is used due to the large peak at m/z = 58 which we hypothesize is due to $^{58}C_2H_5NHCH_2^{+}$ which has been identified by ATOFMS and in other laboratory studies [*Angelino et al.*, 2001; *Pitts et al.*, 1978]. There

is also a grouping of peaks at m/z = 212-215 of unknown identity. Although the peaks are small, they occur on almost every NOC particle detected.

3.4.1.2 Coarse Mode Particle Types

NaK: Some particles are characterized by having the majority of the positive spectrum dominated by $^{23}Na^+$ or $^{39}K^+$. The negative spectrum shows nitrate $^{46}NO_2^-$ and $^{62}NO_3^-$ as the major peaks, but there is also significant signal from $^{79}PO_3^-$ and $^{35,37}Cl^-$. Coarse mode Na and K have been found to be in soil dust, biogenic material, and sea salt [*Beddows et al.*, 2004].

AlSi: $^{27}Al^+$ was frequently found to be mixed with $^{23}Na^+$, $^{39}K^+$ and $^{35}Cl^-$. If Al was associated with silicon markers $^{60}SiO_2^-$ and $^{76}SiO_3^-$, the particle was placed in the Al/Si class. The presence of these peaks suggests that the particle was an aluminosilicate species common to mineral dust. ^7Li was another common peak seen in the positive spectrum of the Al/Si type. The peak at m/z = 56 could occur from $^{56}Fe^+$ or $^{56}KOH^+$; and possibly even contributions from $^{56}CaO^+$ when there is a corresponding peak at m/z = 40, indicating $^{40}Ca^+$.

Ca: At m/z = 40 $^{40}Ca^+$ stands out as the largest peak in the positive ion spectrum accompanied by smaller peaks at m/z = 56 and 57 due to $^{56}CaO^+$ and $^{57}CaOH^+$. Previous studies have described the ability of $CaCO_3$ dust to react with nitric acid to form $Ca(NO_3)_2$ [*Krueger et al.*, 2004; *Laskin et al.*, 2005]. It is likely that the calcium dust shown herein has undergone this reaction as indicated by the negative ion mass spectrum

which shows intense markers for nitrite and nitrate at $^{46}NO_2^-$ and $^{62}NO_3^-$. Minor peaks are seen in the positive spectrum at 24 and 27, likely due to Mg and Al, respectively.

3.4.1.3 Metal-Rich Particles

PbZn: Zn is one of the largest contributors to the positive ion spectrum occurring at m/z = +64, +66, +67 and +68. Often internally mixed with Zn, Pb shows up at m/z = +206, +207, and +208. Other major peaks in the positive spectrum were $^{23}Na^+$ and $^{39}K^+$. It has been observed in other studies that Pb, Zn and Na were associated with the industrial areas in northern Mexico City [*Chow et al.*, 2002a; *Flores et al.*, 1999; *Johnson et al.*, 2006; *Miranda et al.*, 1994]. In addition to $^{46}NO_2^-$ and $^{62}NO_3^-$, $^{35}Cl^-$ was one of the most abundant markers in the negative ion spectrum. In general, zinc and lead chlorides have relatively low boiling points (732ºC and 950ºC respectively), and their precursors may be present in high temperature combustion sources such as waste incinerators [*Hu et al.*, 2003; *Olmez et al.*, 1988; *Ondov and Wexler*, 1998]. Upon cooling, these compounds will condense into the solid phase, forming submicron Cl-containing particles.

PbNa: It was common for Pb to occur without Zn, so the Pb/Na particles were separated to highlight this difference in mixing state. The Pb/Na type has Pb as the major transition metal marker. As for the PbZn type, Na was typically the largest peak in the positive ion mass spectrum, followed by potassium. Another similarity between Pb/Na and Pb/Zn is the appearance of the $^{35}Cl^-$ peak in the negative mass spectrum.

Other metal types: The other minor particle types that account for less than 1.3% of the total particles analyzed during the study were given the following labels: Cu, Fe,

and miscellaneous metals (MiscMetals). The Cu particle type typically was mixed with EC, Pb, Cl, Na and K. MiscMetals contained a combination of different particle types containing various elements including Mg, Mn, Ti, and Ag.

3.4.2 Chemically Resolved Particle Size Distributions

Figure 3.3 presents the average mass distribution of the major particle types detected with the ATOFMS during the MCMA-2006. This size distribution was determined by scaling the ATOFMS data to the APS using a separate density for each particle class to transform the volume distribution into a mass distribution. In this study, we used the density value of 1.9 g/cm^3 for carbonaceous particles, 2.7 g/cm^3 for dust particles, 1.9 g/cm^3 for Na-rich salt particles, 2.0 g/cm^3 for biomass emission particles and EC rich particles, and 1.9 g/cm^3 for the rest of the particle types. This follows the method developed by Qin et al. [*Qin et al.*, 2006]. By integrating the size distribution shown in Fig. 3.3, we determine the average $PM_{2.5}$ mass to be 43.5μg/m^3. This mass concentration is close to the value of 44.34μg/m^{3}obtained by Chow et al [*Chow et al.*, 2002a; *Chow et al.*, 2002b] at the Xalostoc site (XAL in Fig. 3.1; close to T0), as well as that obtained at the RAMA site (38.1μg/m^3) during the same time period as the current measurements. The RAMA site was located 1 km away from the T0 site.

With the exception of the high mass OC type, which peaked around 1 μm,

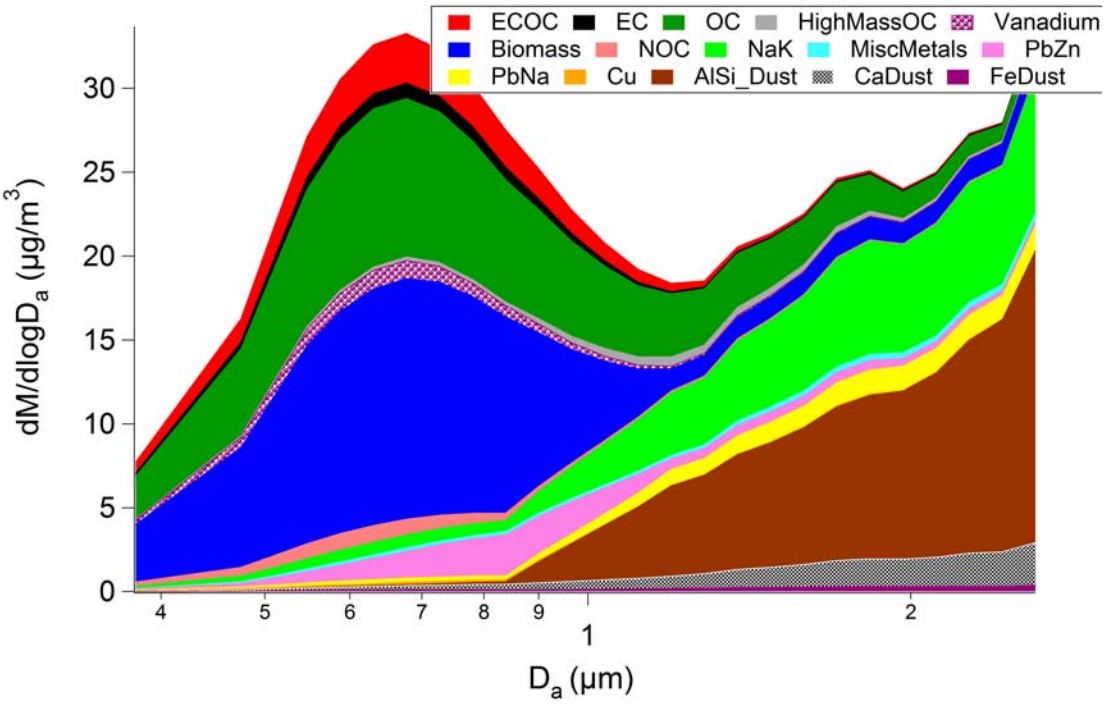

Figure 3.3. Average scaled $PM_{2.5}$ mass distribution, showing the contribution of the single particle types for the MCMA – 2006 campaign. The individual distributions are stacked upon one another.

carbonaceous particle types are typically located in the accumulation mode between 0.1 and 1 μm, whereas the super-micron coarse mode particles were inorganic dust and salt particles as seen in previous ATOFMS studies [*Noble and Prather*, 1996]. The high mass OC type may occur at larger sizes due to the higher degree of chemical aging or fog/cloud processing these particles have undergone. Given that this particle type typically peaked at night when the relative humidity was high, this is likely the case [*Qin and Prather*, 2006].

The lead and zinc types have interesting size characteristics: the PbNa particle type is primarily supermicron, whereas the PbZn particle type occurs at smaller sizes with a mode at about 850 nm. If these particles were formed by condensation, this size characteristic may be due to different concentrations and physical properties of the vapor. Vanadium particles occur primarily in the submicron portion of the size distribution. Based on their size, the submicron metals are most likely a result of combustion processes.

3.4.3 Analysis of Mixing State Using the Peak Search Method

In addition to the cluster analysis presented above, a separate analysis involving a peak search method was employed to highlight trends in the aerosol mixing state of the various particle types. A series of markers were selected to represent the different primary and secondary species. The m/z values used for primary and secondary species are shown in Tables 3.1 and 3.2. All ion intensities were set to be above or equal to an absolute peak area (≥100 units) that is just above

Table 3.1. Peak searching criteria for secondary species.

Secondary Marker	**m/z**
NH_4	+18
NO_2	-46
NO_3	-62
SO_3	-80
HSO_4	-97
C_2O_3OH	-89
C_2H_3O	+43

Table 3.2. Peak searching criteria for primary species.

Primary Species	**Marker**	**m/z**	**Logical**
C	C	12	
Cl	Cl	-35	
PO_3	PO_3	-79	
Na	Na	23	
K	K	39	
NaKCl	Na	23	
	K	39	And
	Cl	-35	And
NaCl only	Na	23	
	Cl	-35	And
	K	39	AndNot
Zn not Pb	Zn	64	
	Zn	66	And
	Pb	206-209	AndNot
CaEC	C_3	36	
	C_4	48	And
	C_5	60	And
	Ca	40	And
Ca	Ca	40	

the noise level (<50). To see which of the selected markers were associated with the various particle types, the particles with the species defined in Tables 3.1 and 3.2 were intersected with the major particle types derived from the ART-2a clustering analysis (Sec. 3.3.2). Figures 3.3 and 3.4 show the results of these intersections, where the color scale represents the fraction of particles of each major type (y-axis) associated with a particular marker (x-axis).

3.4.3.1 Mixing State of Secondary Species

The presence of secondary species on the various particle types (Fig. 3.4) provides an indication of the type of chemical processing the particles have undergone in the atmosphere. The key question is: are there differences in the associations of the major secondary species (e.g., sulfate, nitrate, and ammonium) with each of the major particle types? For instance, the EC and NOC types contain the fewest particles with ammonium, nitrate and sulfate, indicating that they may be freshly emitted. As these particles age through condensation and coagulation, they can accumulate other markers to become other particle types such as OC, ECOC and even biomass. Ammonium is seen to be constrained mainly to the submicron ECOC and OC types, whereas coarse mode particle types that contain NH_4^+ are mainly limited to the AlSi and Cu types. For the AlSi type, the NH_4^+ does not necessarily come from the atmosphere because it is common to find NH_4^+ in soils [*Schlesinger and Hartley*, 1992], and therefore may not be indicative of aging in this particle type.

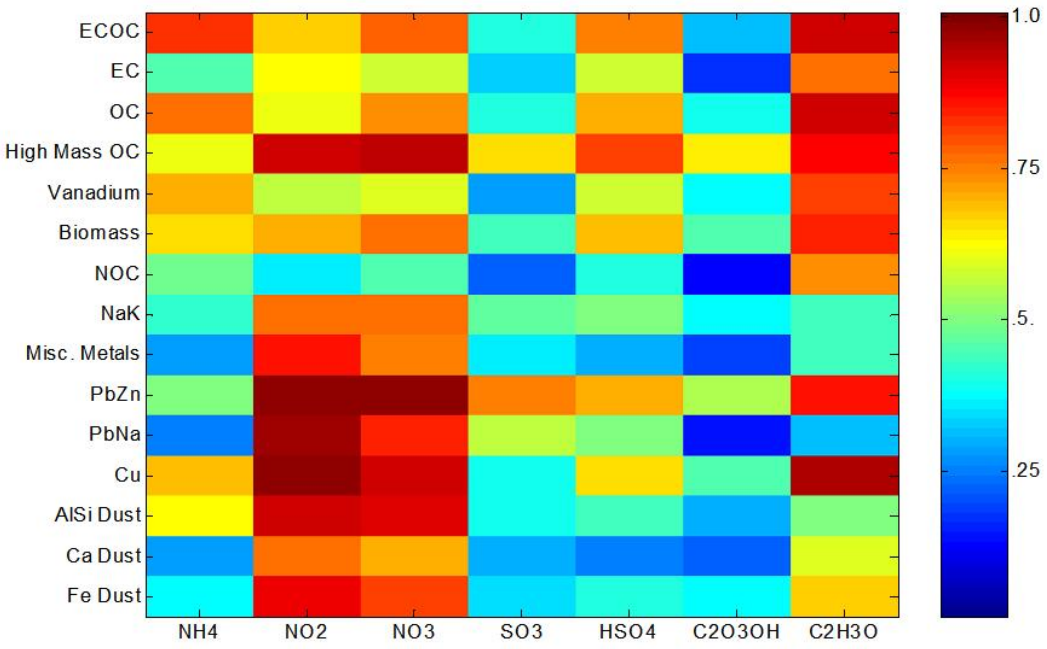

Figure 3.4. Mixing state of secondary species on the various single particle types. The secondary species were identified by the peak searching criteria described in Table 3.1. The peak searches were applied to the entire dataset and then intersected with the particle classes. The color scale represents the fraction of particles within a single particle type (y-axis) that contain the secondary species (x-axis).

Inorganic nitrogen species, such as NO_2 and NO_3, mostly occur on primary inorganic particles such as dust. However, more than 50% of the fine carbonaceous particles are associated with NO_2 and NO_3, and show nitrate is often associated with fine mode particles. Differences in abundance are most likely due to preferential partitioning of the NO_2/NO_3 to the coarse mode particle types (size distribution presented in Sec. 3.4.2). This is because of the competition between nitrate and sulfate for surface area. Since sulfate is non-volatile, it remains on the smaller particles (limited by gas diffusion), whereas the more volatile ammonium nitrate can evaporate from the smaller particles (Kelvin effect) and condense on coarse mode particles [*Bassett and Seinfeld*, 1984].

The Pb/Na, Cu, and Pb/Zn particle types are more strongly associated with NO_2/NO_3 compared to any other particle class. The Pb/Zn type is primarily a fine mode particle type, and it is unusual for particles in this size range to be so strongly associated with nitrate. Given that these industrial metal types are likely to be freshly emitted, this is an indicator that these particle classes are emitted with an air mass that contains large amounts of NO_x that reacted to form particulate nitrate. It is likely the NOx displaced the Cl that was originally in the particles.

The organic carbon markers used to highlight mixing with other particle types were chosen to be $^{43}C_2H_3O^+$ and $C_2O_3OH^-$ (oxalate). It is apparent that $^{43}C_2H_3O$ is mainly associated with the fine mode particles but occurs in over 40% of the supermicron particles (with the exception of the PbNa type). This organic carbon likely comes from secondary reactions and gas-to-particle conversion. The oxalate marker is an indicator of the presence of oxalic acid. Oxalic acid may be emitted as a part of vehicle exhaust and

biomass burning [*Chebbi and Carlier*, 1996; *Falkovich et al.*, 2005; *Kawamura and Kaplan*, 1987] but most commonly through secondary processes including photochemistry followed by condensation, fog processing or aerosol surface reactions [*Blando and Turpin*, 2000; *Faust*, 1994; *Kawamura and Ikushima*, 1993; *Yao et al.*, 2002]. Oxalate is associated with biomass and vanadium types, as shown in Fig. 3.4, where 37 and 45% of the particles in these classes contain the oxalate marker, respectively.

3.4.3.2 Mixing State of Primary Species

A marker for EC, $^{36}C_3$, was chosen to highlight the distribution of carbon – especially in the non-carbonaceous particle types. This marker can come from secondary species as well, but is more commonly detected in primary particles. In Fig. 3.5, it is seen that the PbZn and Cu types are mixed with EC. This result, combined with the predominately fine mode size distribution (Fig. 3.3), provides further evidence that the PbZn and Cu particles are products of high temperature combustion. While $^{36}C_3$ can be used to identify particle classes that are internally mixed with EC, ^{40}Ca can be used to identify unique sources of EC. Source studies indicate that particles containing both Ca and EC are primarily associated with heavy duty vehicle emissions [*Toner et al.*, 2006]. The mixing of elemental carbon with Ca is observed by searching for the typical EC markers together with Ca (CaEC). From

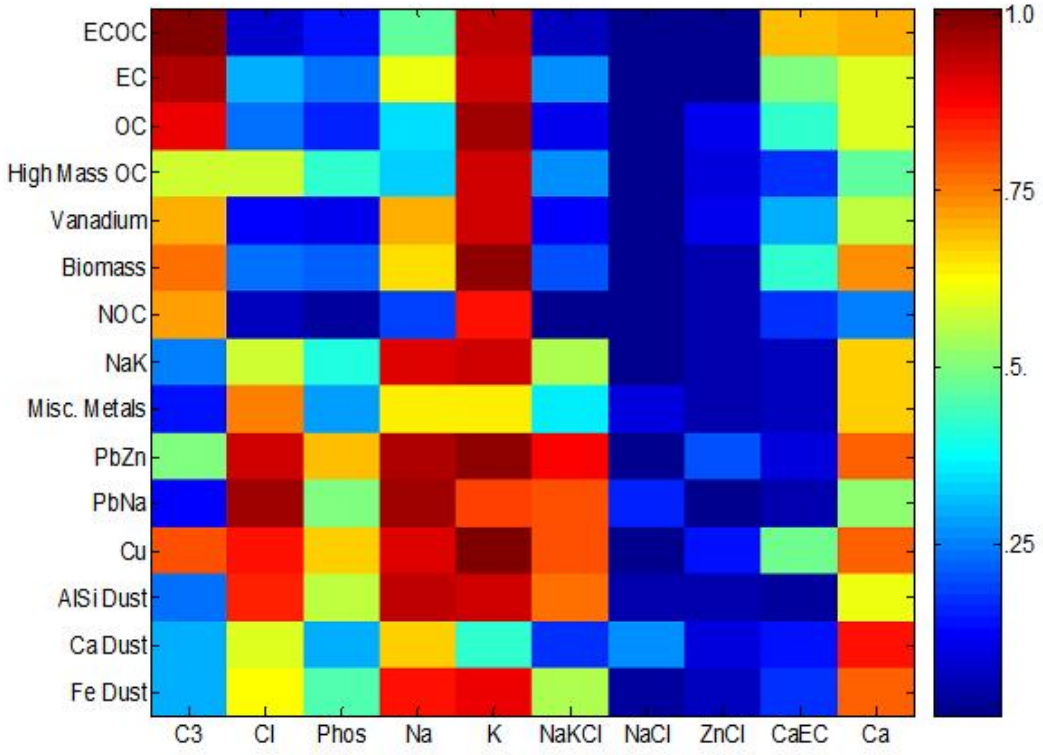

Figure 3.5. Mixing state of primary species on the various single particle types. The primary species were identified by the peak searching criteria described in Table 3.2. The peak searches were applied to the entire dataset and then intersected with the particle classes. The color scale represents the fraction of particles within a single particle type (y-axis) that contain the primary species (x-axis).

Fig. 3.5, it is apparent that about 50% of the EC is associated with Ca, suggesting diesel vehicles produce a substantial fraction of EC/soot in this region.

Chlorine (m/z -35 and -37) is mainly associated with the inorganic particle types. This is supported by Fig. 3.5 which shows a strong degree of internal mixing between metals, K, Na and Cl. Cl is also strongly associated with the AlSi type and moderately associated with the NaK and Ca dust particle types. For Ca dust, there is much less Na and K associated with Cl compared to the other inorganic particle classes. A secondary source of Cl is HCl, which can be formed by heterogeneous displacement when primary particles composed of NaCl, KCl, $PbCl_2$, or $ZnCl_2$ react with acidic (i.e.. HNO_3 or H_2SO_4) gases. The resulting HCl can then partition to other particles. This suggests that for the metals and AlSi dust, the Cl is primary and for the Ca dust, the Cl is secondary. It has been shown in previous studies that the mixing between Cl and Ca is due mainly to secondary processing by HCl gas [*Sullivan et al.*, 2007].

In Fig. 3.5, K particles are present in both the coarse and fine mode particles, whereas Na particles appear to be constrained mainly to the coarse mode. Caution is necessary when interpreting this result because of the interference of ^{39}K with organic markers (e.g., $^{39}C_3H_3^+$). This may explain why a large fraction of the organic carbon particles appear to contain K. On the other hand, it is likely that organic particles also contain K, given the high relative intensity of the K ion peak. Biomass particles are a prime example of a submicron particle type that definitely contains K and organic carbon as an internal mixture. Comparison of the OC Art-2a clusters from Mexico City and

Riverside, CA reveals that the peak at m/z=39 makes a larger contribution to Mexico City particles, indicating biomass represents a more significant source in Mexico City.

3.4.4 Temporal Characteristics of Single Particle Types

The temporal characteristics of the single particle types can provide a great deal of insight into the origin of the particles. In this section, the temporal profiles for sub- and super-micron particle types are described in detail. Three major events are labeled on the temporal profiles shown in Fig. 3.6. The first event (E1) was a large dust event where the PM_{10} concentration exceeded 1 mg/m^3. The second event (E2) was a holiday weekend and the third event (E3) was a heavy rain event. Figure 3.7 shows an average diurnal cycle of scaled mass concentrations representing the average of 19 days for the study.

3.4.4.1 Temporal of the Entire Study

Examining the study as a whole, major features in the overall submicron temporal trends (Fig. 3.6a) show sharp spikes of metal and nitrogen organic carbon (NOC) particles. Frequently the metal and NOC classes peaked in the morning, usually with relatively short spikes compared with the trends of the other particle classes (organics, biomass etc). This feature suggests that the source of these particles is local. The total $PM_{2.5}$ mass concentrations during these early morning spikes were typically around $50\mu g/m^3$ at the La Villa RAMA site. The weekend event (E2)

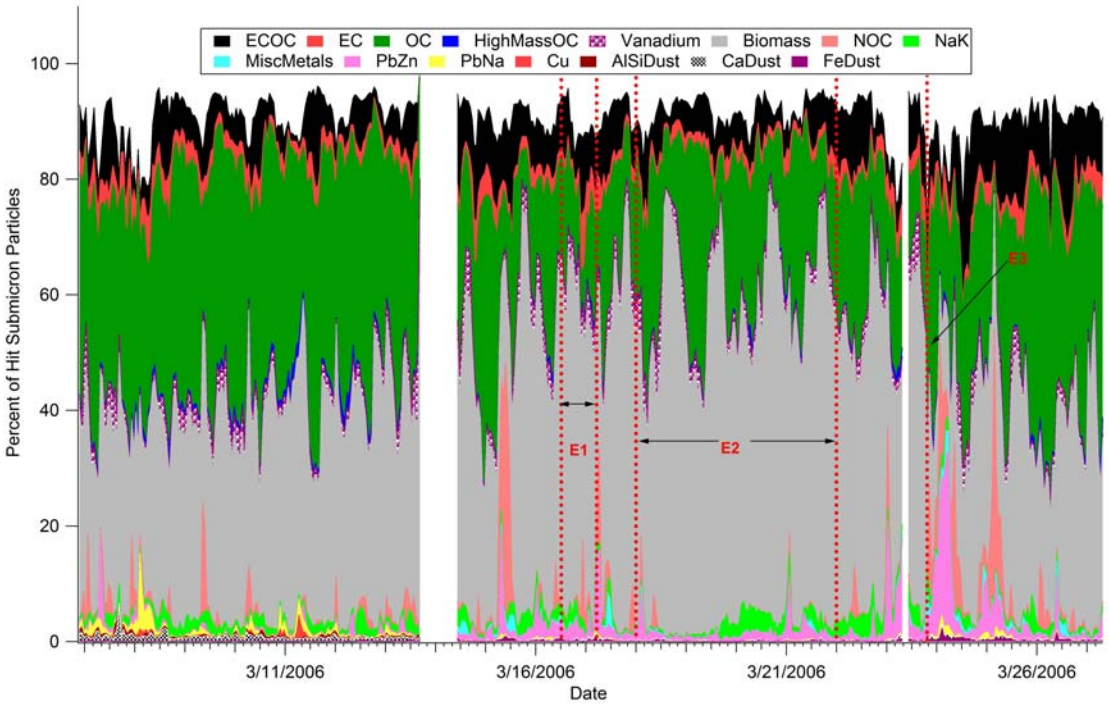

Figure 3.6a. Temporal of the submicron particle types during MCMA-2006.

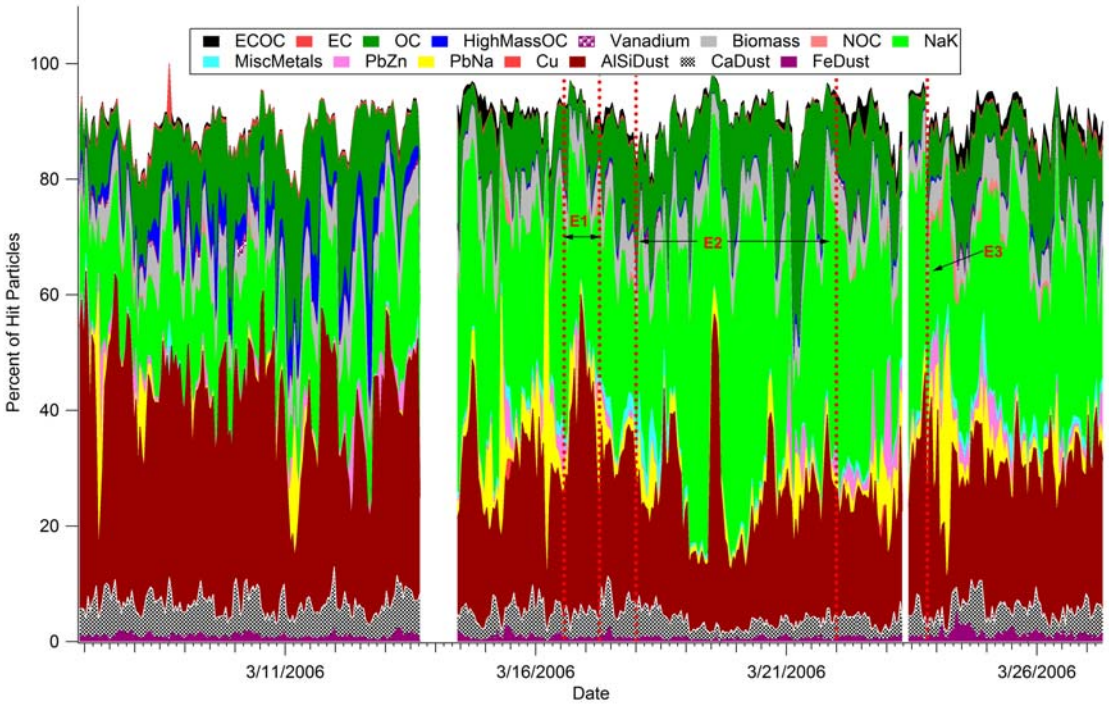

Figure 3.6b. Temporal of the supermicron particle types during MCMA-2006.

showed lower contributions from the metal and NOC types, indicating these particles may be associated with industry. After the rain event (E3), the fractional contribution from the biomass decreased while OC, NOC, and metal particles increased. This trend continued for the rest of the measurement period, during which evening rain events occurred on a regular basis. Overall, the submicron classes exhibited a fairly strong diurnal behavior which will be examined further in Section 3.4.4.2.

Figure 3.6b shows the temporal profiles of the major supermicron particle types. There was one particularly large dust event caused by strong winds on 3/16/06 beginning at 16:00 CST (E1) during which the measured PM_{10} exceeded 1mg/m^3 at the San Agustin and Xalostoc RAMA sites (near the dry lake bed Texcoco, SAG and XAL in Fig. 3.1) and almost 700 μg/m^3 at the La Villa RAMA site closest to T0. The wind blew from these sites towards the west in the direction of T0. Our results show that the Na/K and Al/Si particle types dominated the chemical composition for this time period, thus indicating that the dry lake bed and fugitive sources nearby are major contributors to these particle types. This is consistent with the observations of Chow et al (2002a,b), who found concentrations of Al, Si, K, and Na to be highest around the SAG and XAL sites compared to other sites around the city.

3.4.4.2 Average Diurnal Trends

Figure 3.7 shows the average diurnal trends for the most abundant submicron particle classes. Metal and NOC particles reached their highest concentrations in the early morning hours between midnight and 10 AM. The most dominant particle types in the early morning (from 3 – 8 AM) were the OC and biomass particle classes. As

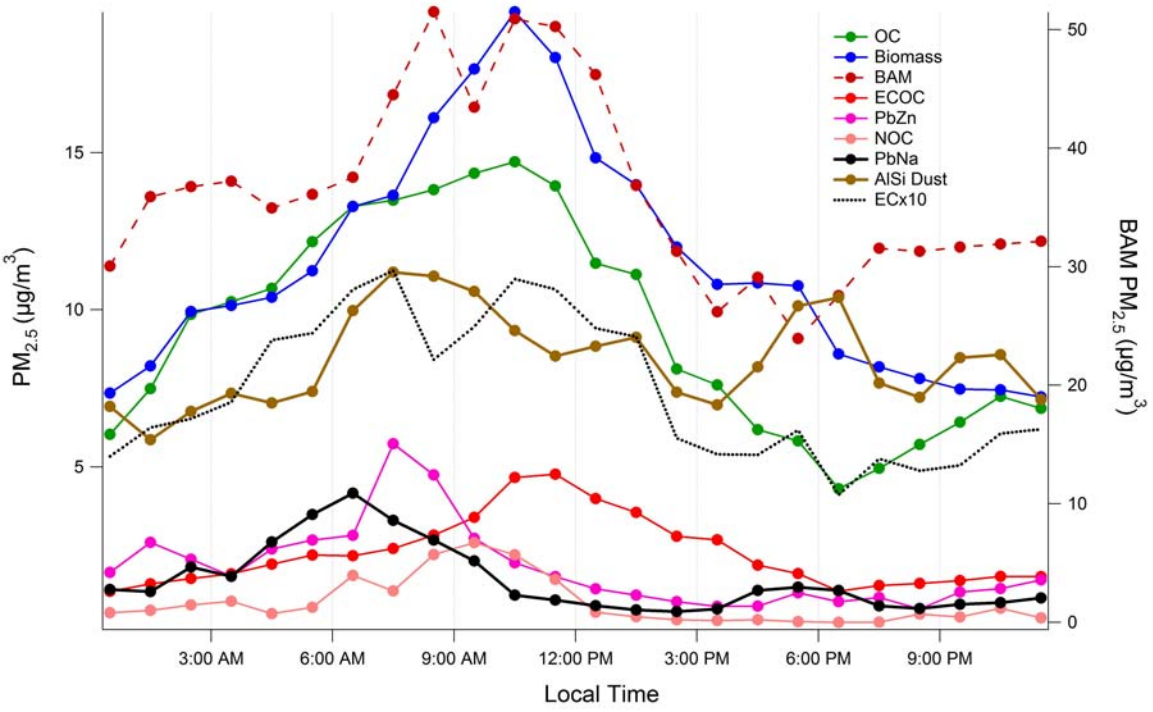

Figure 3.7. Average diurnal cycle of selected types. The ATOFMS scaled mass concentration is shown on the left axis and the mass concentration derived from the Beta Attenuation Monitor (BAM) is shown on the right axis for comparison.

the day continued, the relative proportion of ECOC and biomass increased. Biomass was the most abundant particle class from 8 AM to 5:30 PM. Frequently, in the late afternoon, numerous fires were observed on the periphery of the city. In the late evening into the morning, the concentration of the OC particle types increased compared to the other classes. This may be due to increased gas-to-particle phase partitioning of OC as the temperature decreased, or due to less dilution caused by a lower boundary layer. If the latter were true, this would indicate that more of the OC particles were retained within the basin at night [*Qin and Prather*, 2006].

Although it appears that biomass particles are the major source of particulate mass in the afternoons, one must use caution when interpreting this result. In the afternoon, there is more secondary organic carbon coating all of the particle classes – including the biomass class. Furthermore, coagulation can also cause a great deal of external mixing on a timescale of about 12 hours [*Jacobson*, 2002]. Because the ATOFMS has a high sensitivity to K, it is likely that if an OC particle coagulated with a biomass particle, the resulting particle would be classified as a biomass particle. Therefore, the ATOFMS would see more OC and less biomass particles in the late afternoon. On the other hand, the flow conditions in the afternoon were much different than in the morning and the relative increase in biomass particles may be indicative of influences from different sources. This aspect will be discussed further in the following section using a back trajectory analysis.

Elemental carbon showed a bimodal diurnal temporal profile with the largest temporal peak at 7:30 am and the second mode occurring at 11:30 am at the same

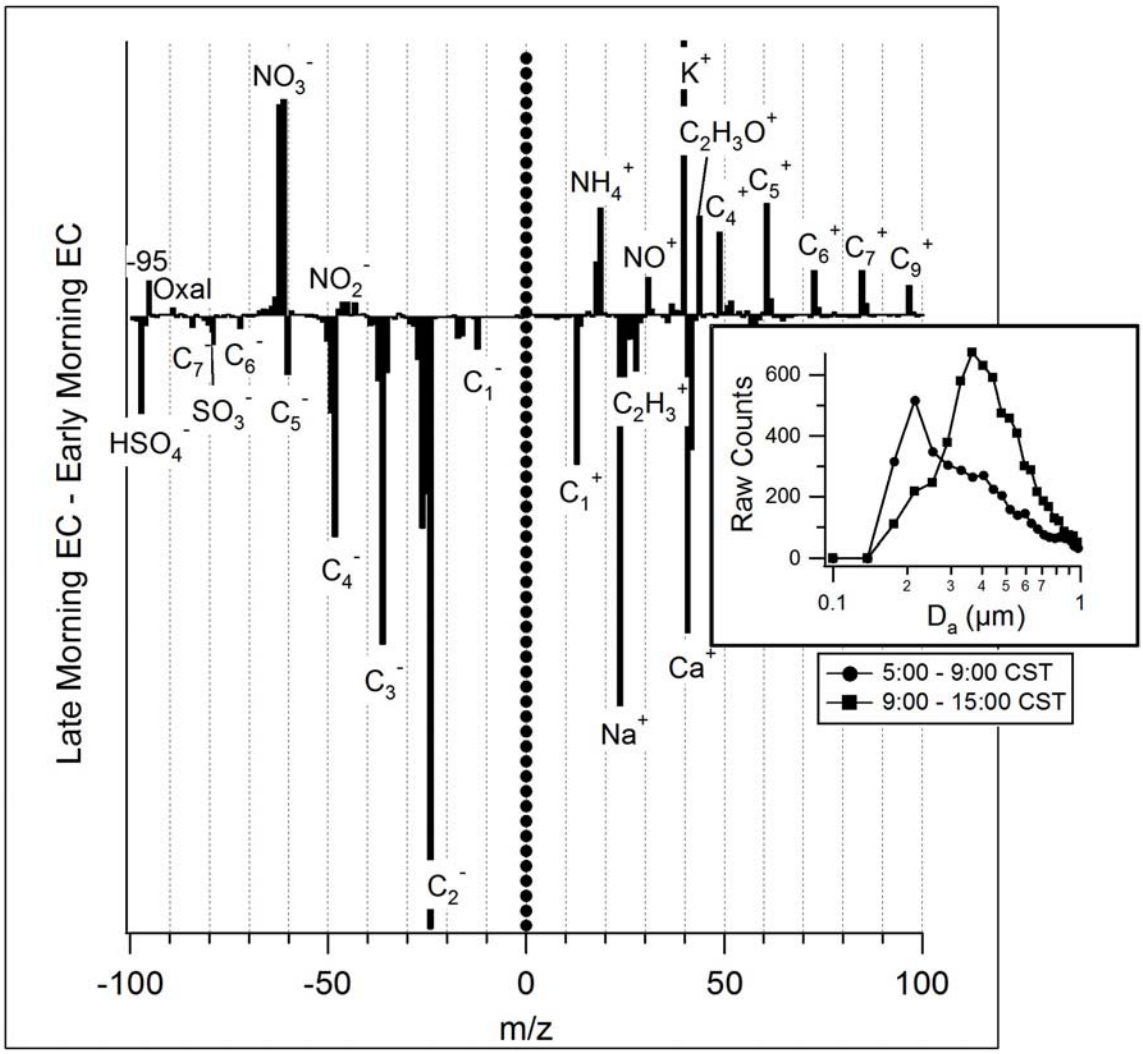

Figure 3.8. A subtraction spectrum for EC particles peaking later in the morning (9a – 3p) minus particles peaking early in the morning (5-9a). This shows that early morning EC particles have less contribution from markers of secondary photochemistry and more markers from freshly emitted EC (sulfate, Na^+, and Ca^+). Furthermore, the increase in K^+ later in the day suggests a contribution from a different primary source of EC.

time as the total mass concentration peaked. According to Fig. 3.8, the EC particles sampled during the early peak had smaller aerodynamic diameters (number distribution mode = 0.20 μm) than those sampled at the later peak (number distribution mode = 0.38 μm). In Fig. 3.8, it is also shown that the EC particles later in the day had more ion intensity from NO_3^-, NH_4^+, $C_3H_3O^+$, and K^+. With the exception of K^+, these markers are indicative of secondary photochemical processing. Early morning EC particles had more intensity from $^{12n}C_n^-$ clusters and sulfates in the negative ions as well as more intensity from Na^+ and Ca^+ in the positive ion mass spectrum. Most of these markers indicate primary species emitted with the elemental carbon particles. Based on these facts, it can be concluded that the early morning peak of EC is comprised of more freshly emitted particles than the EC particles which peak later in the day. In addition, the fact that the EC particles sampled later in the day have more K^+ signal indicates that a different source of EC particles begins to have a larger influence as the day progresses.

3.4.5 Back Trajectory Analysis

A Concentration Field Analysis [*Seibert*, 1994] was carried out using back-trajectories from the FLEXPART model [*Stohl et al.*, 2005]. To accomplish this, 100 stochastic particles are released from T0 every 2 hours and tracked for 3 days. All the positions of the particles every hour are summed into a gridded field indicating the source region of the air mass at each release time. These gridded fields, called Residence Time Analyses, are then multiplied by the ATOFMS normalized particle counts at the release

site and summed over the entire campaign. Potential source regions are highlighted by normalizing with the sum of the unscaled residence time analysis. The method was used to analyze data from the MCMA-2003 field campaign [*de Foy*, 2006a]. Analysis of CO data showed that the method was able to correctly identify urban emissions and analysis of SO_2 data identified possible impacts of the Tula industrial complex. This analysis was performed for each of the fifteen particle types seen during MCMA-2006; the results of this analysis are shown in Figs. 3.8-3.10. For particle types with only a few sharp peaks, a back trajectory corresponding to peak concentrations is shown.

The wind fields for the trajectories were simulated using the MM5 model with modifications for the land surface [*de Foy and Molina*, 2006c]. Additional modifications were made to the simulation procedure [*de Foy et al.*, 2006b]. These include finer and larger domains with 92x116, 91x145 and 97x97 cells at 27, 9 and 3 km resolution respectively and 41 sigma levels in the vertical, as well as corrections to the sea surface latent heat fluxes.

3.4.5.1 Spatial Distribution of Industrial Emissions

The T0 site is located in the heart of the industrial sector of the MCMA. As a result, a large fraction of the particles detected at the T0 site are expected to be from local industrial emissions. Typically, local point sources emit pollutants over short timescales. Such pollutant spikes were discussed in Sec. 3.4.4.1 for the metal and NOC particle types; therefore it is likely that these particle types are from local

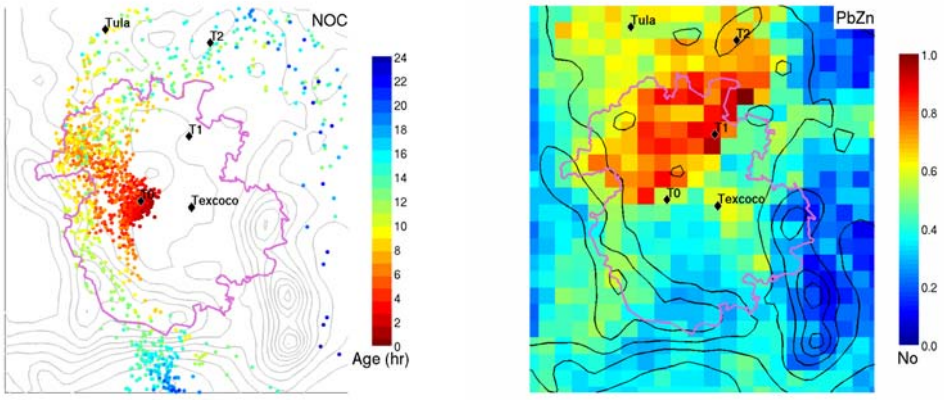

Figure 3.9. Spatial distributions of industrial emissions in Mexico City. A) Particle back-trajectories for a release on 15 March, 8:00-9:00 CST, for a representative nitrogen containing organic carbon (NOC) peak. Particle positions are plotted every hour and color indicates age. B) Concentration field analysis for PbZn particles. High non-dimensional number (red) indicates possible source regions, low numbers (blue) indicate areas with low or zero emissions.

industry. For the NOC type, this is verified by looking at the FLEXPART back trajectory shown in Fig. 3.9 for the largest NOC spike occurring at 9:00am on Mar- 15, 2006. This figure indicates that flow was stagnant during the periods of peak NOC emissions, and thus the source was most likely local. Similar flow conditions

were observed during other periods of the study when the NOC particle type was most abundant.

From Fig. 3.7, one can see that the diurnal profile of the PbNa and PbZn classes occurred from midnight to about 10:00 (CST). The concentration field analysis in Fig. 3.9 indicates possible source regions north of T0 for PbZn, as well as for PbNa (not shown). Concentrations of Pb and Zn in northern Mexico City have been historically high compared to other regions of Mexico City [*Chow et al.*, 2002b]. There is evidence for transport of Na and Zn particles from the northern to southern parts of the city, as Johnson et al. (2006) have shown. At the same site, Salcedo et al. (2006) noticed sharp spikes of particulate Cl in the early morning hours. In this study, we observe early morning spikes of chloride as well, and show that it is internally mixed with Pb, Zn, Na and K. Johnson et al. attributed the Na and Zn to an industrial source in their factor analysis, and Salcedo et al. suggested that most of the Cl was present as NH_4Cl. The results obtained herein show that all Na, Cl, and Zn are likely industrial and internally mixed within the same particles (Fig. 3.5). The speciation of Cl does not necessarily have to be exclusively NH_4Cl because NaCl, KCl, $ZnCl_2$ or $PbCl_2$ are also possible. For all of these species, displacement of Cl by NO_3 explains the strong association of the metal particle classes with NO_2/NO_3.

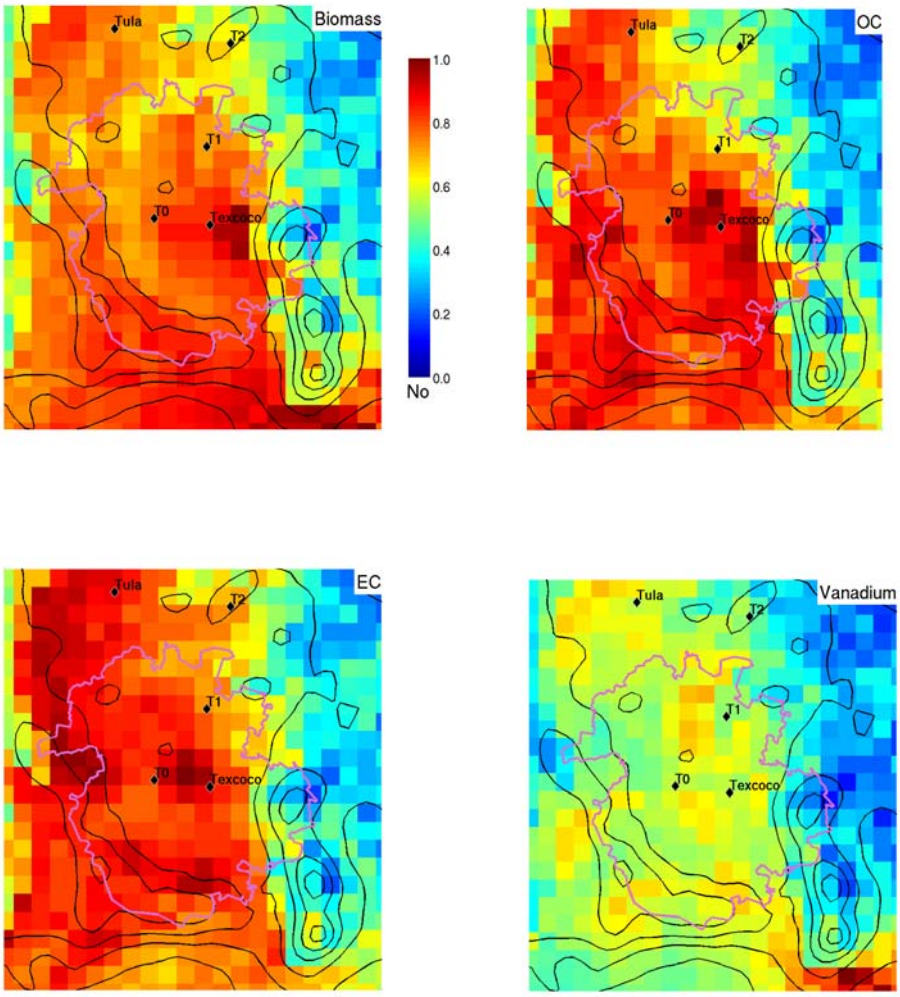

Figure 3.10. Concentration field analysis for select carbonaceous particle types. High non-dimensional number (red) indicates possible source regions, low numbers (blue) indicate areas with low emissions.

3.4.5.2 Spatial Trends of Carbonaceous Particle Types

Carbonaceous particle types in Mexico City are expected to be produced by a variety of urban and regional sources, both primary and secondary. The concentration field analysis shown in Fig. 3.10 for the OC particle type shows that these particles originated from all across the basin. The EC particle type shows more intensity close to T0 and in the northwest. Because the EC particle type represents a freshly emitted particle type and also because concentrations are highest when winds are weak and variable, the Concentration Field Analysis does not indicate a preferred source region. EC particles coming from the north may be due to combustion operations or other industrial operations in the north. Biomass particles show a strong correlation with flow through the gap in the mountains to the southeast of the city - a region where large fires occurred. This type of flow usually occurs in the afternoon when the biomass particles peaked and is associated with vertical advection and basin venting [*de Foy et al.*, 2005; *de Foy et al.*, 2006c]. There is also slightly more source strength for the biomass particles near the hillsides of the basin. This may be due to the fact that there were frequently numerous small fires on these hills that were used to clear fields for the upcoming crop season. Lastly, vanadium particles are also correlated with the gap flow from the south with a smaller signature from the north-northwest. Johnson et al. (2006) had found a single vanadium peak time period during the MCMA-2003 that was strongly correlated with SO_2 and back-trajectories from the

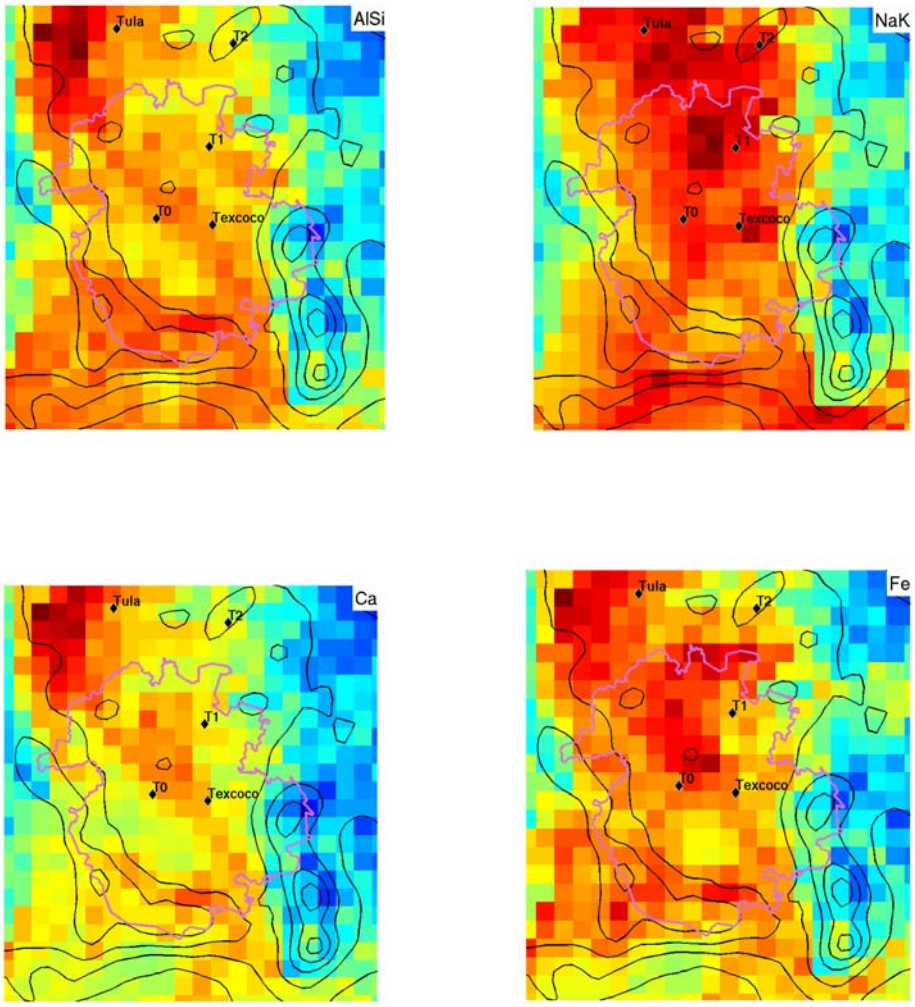

Figure 3.11. Concentration field analysis for select coarse mode particle types. High non-dimensional number (red) indicates possible source regions, low numbers (blue) indicate areas with low or zero emissions.

Tula complex. During MCMA-2006, there were half a dozen peaks in the vanadium types in addition to substantial diurnal and day-to-day variations. Some of the peaks are associated with SO_2 and trajectories from the north, while others are associated with weak and variable winds followed by the strong gap flow sweeping through the basin. At this time, it is unknown whether there are any large sources of vanadium particles in the MCMA. Some of the major sources that burn fuel-oil are located in the north, where Fig. 3.10 shows a mild influence from the vanadium particle type.

3.4.5.3 Spatial Trends in Coarse Mode Particle Types

The concentration field analysis from the coarse (super-micron) mode particle types is shown in Fig. 3.11. AlSi, Ca and Fe dust all had similar spatial footprints where the highest concentration events correlated well with the flow from the northwest near the Tula region. For the Ca type, this would be consistent with the fact that the cement plants in that region emit dust with high concentrations of Ca [*Vega et al.*, 2001]. The Fe particle type had slightly more influence from the northwest than did the AlSi or Ca types. The NaK particle type was significantly different from any other coarse mode particle type, showing more contributions from the east to northeast. The dry lake bed Texcoco is located in the east, and has been historically correlated with increased quantities of Na and K compared to the rest of Mexico City. Also, the NaK particle type was far more distributed spatially than the other coarse mode particle types. It is also possible that the NaK type contains contributions from vegetative detritus and biomass

burning, thus providing a possible explanation for its broad spatial distribution and stronger southerly signature.

3.5 Conclusions

ATOFMS observations during MCMA-2006 provide chemical mixing state measurements with high temporal and size resolution. A new nitrogen-containing organic (NOC) particle type was detected, and lead particles internally mixed with Zn and Cl were also frequently observed. Both of these particle types peaked in the morning hours and were likely the result of industrial emissions. Given the spatial and temporal characteristics of particles with the PbZnCl mixing state, these particles are directly associated with the source of early morning particulate Cl. Furthermore, these same metal particles are likely associated with the source of high Pb and Zn concentrations in the north as seen in previous investigations. These particles and their chemistry will be the subject of a forthcoming paper.

The most abundant particle types seen in the MCMA include biomass and other carbonaceous types for the submicron size range, and dust and inorganic types for the coarse (super-micron) mode. The mixing of these different particle types with secondary species was analyzed in further detail using a peak searching method. Organic carbon was found to be on almost 50% of the coarse mode dust types, while 45% of the biomass and 37% of the vanadium particles were associated with the oxalate ion. It was determined that 58% of the EC particles and 73% of the ECOC particles contained sulfate. This indicates that these freshly emitted particles contain a significant amount of

other inorganic components as a result of the source and of secondary chemical processing.

A temporal analysis of the different particle types gives insight into the possible sources and transformations of the particles. Distinct diurnal variations for the OC and biomass particle types were observed with the Biomass and OC present as the most abundant particle classes in the early morning, then after 10:00 CST, biomass particles took over as the most concentrated carbonaceous particle class. This suggests that either transport and/or aging processes served to transform the chemical composition of the carbonaceous particles. After 18:00 CST, OC particles start to increase in concentration while biomass particles decrease. This diurnal variation has a potential to serve as a "clock" of the aging and transport characteristics of the aerosol in the heart of the MCMA, thus providing a timescale by which measurements can be compared with models. These temporal profiles provided by the ATOFMS were used, together with meteorological modeling to provide source regions for the major particle types. Knowledge gained from this analysis will ultimately be combined with emissions inventories for the MCMA to give the most likely sources for each of the major particle types.

3.6 Acknowledgements

Chapter 3, in full, is a reprint of the material as it appears in:

Moffet, R.C., B. de Foy, L.T. Molina, M.J. Molina, and K.A. Prather: Measurement of Ambient Aerosols in Northern Mexico City by Single Particle Mass Spectrometry,

Atmospheric Chemistry and Physics Discussions, 6413-6457, 2007. The dissertation author was the primary author of this paper.

This field campaign is the collaborative effort of a large number of participants with the support of multi-national agencies. The authors would like to thank Gustavo Sosa, Philip Sheehy, Rainer Volkamer, Jose Luis Jimenez, and Ken Docherty for their help and guidance during the MCMA-2006 field study. Rene Sanchez overcame the location problems of our digitizers. Robert Osborne and Don Collins helped organize and consolidate the shipment of equipment into Mexico as well as providing APS data. Tania Perez and Ricardo Cepeda provided much needed and timely logistical support. Rafael Ramos graciously provided gas phase and PM data from the RAMA monitoring network. We thank NSF for funding under ATM-0511803 and ATM-0528227.

3.7 References

Aldape, F., J. Flores, R.V. Diaz, and D. Crumpton: Upgrading of the PIXE system at ININ (Mexico) and report on elemental composition of atmospheric aerosols from 1990 in the ZMCM, Nucl. Instrum. Methods Phys. Res., Sect. B, 109, 459-464, 1996a.

Aldape, F., J. Flores, R. Garcia, and J.W. Nelson: PIXE analysis of atmospheric aerosols from a simultaneous three site sampling during the autumn of 1993 in Mexico City, Nucl. Instrum. Methods Phys. Res., Sect. B, 109, 502-505, 1996b.

Angelino, S., D.T. Suess, and K.A. Prather: Formation of aerosol particles from reactions of secondary and tertiary alkylamines: Characterization by aerosol time-of-flight mass spectrometry, Environ. Sci. Technol. , 35 (15), 3130-3138, 2001.

Bassett, M.E., and J.H. Seinfeld: Atmospheric equilibrium-model of sulfate and nitrate aerosols 2: Particle-size analysis, Atmospheric Environment, 18 (6), 1163-1170, 1984.

Baumgardner, D., G.B. Raga, and A. Muhlia: Evidence for the formation of CCN by photochemical processes in Mexico City, Atmos. Env., 38 (3), 357-367, 2004.

Beddows, D.C.S., R.J. Donovan, R.M. Harrison, M.R. Heal, R.P. Kinnersley, M.D. King, D.H. Nicholson, and K.C. Thompson: Correlations in the chemical composition of rural background atmospheric aerosol in the UK determined in real time using time-of-flight mass spectrometry, Journal of Environmental Monitoring, 6 (2), 124-133, 2004.

Blando, J.D., and B.J. Turpin: Secondary organic aerosol formation in cloud and fog droplets: a literature evaluation of plausibility, Atmos. Env., 34 (10), 1623-1632, 2000.

Cahill, T.A., R. Morales, and J. Miranda: Comparative aerosol studies of Pacific Rim cities - Santiago, Chile (1987); Mexico City, Mexico (1987-1990); and Los Angeles, USA (1973 and 1987), Atmos. Env., 30 (5), 747-749, 1996.

Chebbi, A., and P. Carlier: Carboxylic acids in the troposphere, occurrence, sources, and sinks: A review, Atmos. Env., 30 (24), 4233-4249, 1996.

Chow, J.C., J.G. Watson, S.A. Edgerton, and E. Vega: Chemical composition of PM2.5 and PM10 in Mexico City during winter 1997, Sci. Total Environ., 287 (3), 177-201, 2002a.

Chow, J.C., J.G. Watson, S.A. Edgerton, E. Vega, and E. Ortiz: Spatial differences in outdoor PM10 mass and aerosol composition in Mexico City, Journal of the Air & Waste Management Association, 52 (4), 423-434, 2002b.

de Foy, B., E. Caetano, V. Magana, A. Zitacuaro, B. Cardenas, A. Retama, R. Ramos, L.T. Molina, and M.J. Molina: Mexico City basin wind circulation during the MCMA-2003 field campaign, Atmos. Chem. Phys., 5, 2267-2288, 2005.

de Foy, B., A. Clappier, L.T. Molina, and M.J. Molina: Distinct wind convergence patterns in the Mexico City basin due to the interaction of the gap winds with the synoptic flow, Atmos. Chem. Phys., 6, 1249-1265, 2006a.

de Foy, B., Lei, W., Zavala, M., Volkamer, R., Samuelsson, J., Mellqvist, J., Galle, B., Martinez, A. P., grutter, M., Molina, L. T.: Modelling Constraints on the emission inventory and on vertical diffusion for CO and SO2 in the Mexico City Metropolitan Area using Solar FITR and zenith sky UV spectroscopy, Atmos. Chem. Phys. Discussions (6), 6125-6181, 2006b.

de Foy, B., and L.T. Molina, MODIS Land Surface Parameters for Improved MM5 Simulations in the Mexico City basin during the MILAGRO Field Campaign, in *7th Annual WRF User's Workshop*, Boulder, Colorado, 2006.

de Foy, B., J.R. Varela, L.T. Molina, and M.J. Molina: Rapid ventilation of the Mexico City basin and regional fate of the urban plume, Atmos. Chem. Phys., 6, 2321-2335, 2006c.

Dunn, M.J., J.L. Jimenez, D. Baumgardner, T. Castro, P.H. McMurry, and J.N. Smith: Measurements of Mexico City nanoparticle size distributions: Observations of new particle formation and growth, Geophys. Res. Lett., 31 (10), -, 2004.

Ervens, B., G. Feingold, G.J. Frost, and S.M. Kreidenweis: A modeling study of aqueous production of dicarboxylic acids: 1. Chemical pathways and speciated organic mass production, Journal of Geophysical Research-Atmospheres, 109 (D15), -, 2004.

Falkovich, A.H., E.R. Graber, G. Schkolnik, Y. Rudich, W. Maenhaut, and P. Artaxo: Low molecular weight organic acids in aerosol particles from Rondonia, Brazil, during the biomass-burning, transition and wet periods, Atmos. Chem. Phys., 5, 781-797, 2005.

Faust, B.C.: Photochemistry of Clouds, Fogs, and Aerosols, Environ. Sci. Technol. , 28 (5), A217-a222, 1994.

Flores, J., F. Aldape, R.V. Diaz, B. Hernandez-Mendez, and R. Garcia: PIXE analysis of airborne particulate matter from Xalostoc, Mexico: winter to summer comparison, Nucl. Instrum. Methods Phys. Res., Sect. B, 150 (1-4), 445-449, 1999.

Gard, E., J.E. Mayer, B.D. Morrical, T. Dienes, D.P. Fergenson, and K.A. Prather: Real-time analysis of individual atmospheric aerosol particles: Design and performance of a portable ATOFMS, Anal. Chem. , 69 (20), 4083-4091, 1997.

Gross, D.S., M.E. Galli, M. Kalberer, A.S.H. Prevot, J. Dommen, M.R. Alfarra, J. Duplissy, K. Gaeggeler, A. Gascho, A. Metzger, and U. Baltensperger: Real-time measurement of oligomeric species in secondary organic aerosol with the aerosol time-of-flight mass spectrometer, Anal. Chem. , 78 (7), 2130-2137, 2006.

Gross, D.S., M.E. Galli, P.J. Silva, S.H. Wood, D.Y. Liu, and K.A. Prather: Single particle characterization of automobile and diesel truck emissions in the Caldecott Tunnel, Aerosol Sci. Technol., 32 (2), 152-163, 2000.

Guazzotti, S.A., K.R. Coffee, and K.A. Prather: Continuous measurements of size-resolved particle chemistry during INDOEX-Intensive Field Phase 99, Journal of Geophysical Research-Atmospheres, 106 (D22), 28607-28627, 2001.

Guazzotti, S.A., D.T. Suess, K.R. Coffee, P.K. Quinn, T.S. Bates, A. Wisthaler, A. Hansel, W.P. Ball, R.R. Dickerson, C. Neususs, P.J. Crutzen, and K.A. Prather: Characterization of carbonaceous aerosols outflow from India and Arabia: Biomass/biofuel burning and fossil fuel combustion, Journal of Geophysical Research-Atmospheres, 108 (D15), -, 2003.

Hu, C.W., M.R. Chao, K.Y. Wu, G.P. Chang-Chien, W.J. Lee, L.W. Chang, and W.S. Lee: Characterization of multiple airborne particulate metals in the surroundings of a municipal waste incinerator in Taiwan, Atmos. Env., 37 (20), 2845-2852, 2003.

Jacobson, M.Z.: Analysis of aerosol interactions with numerical techniques for solving coagulation, nucleation, condensation, dissolution, and reversible chemistry among multiple size distributions, Journal of Geophysical Research-Atmospheres, 107 (D19), -, 2002.

Jiang, M., L.C. Marr, E.J. Dunlea, S.C. Herndon, J.T. Jayne, C.E. Kolb, W.B. Knighton, T.M. Rogers, M. Zavala, L.T. Molina, and M.J. Molina: Vehicle fleet emissions of black carbon, polycyclic aromatic hydrocarbons, and other pollutants measured by a mobile laboratory in Mexico City, Atmos. Chem. Phys., 5, 3377-3387, 2005.

Jimenez, J.C., G.B. Raga, D. Baumgardner, T. Castro, I. Rosas, A. Baez, and O. Morton: On the composition of airborne particles influenced by emissions of the volcano Popocatepetl in Mexico, Natural Hazards, 31 (1), 21-37, 2004.

Johnson, K.S., B. de Foy, B. Zuberi, L.T. Molina, M.J. Molina, Y. Xie, A. Laskin, and V. Shutthanandan: Aerosol composition and source apportionment in the Mexico City Metropolitan Area with PIXE/PESA/STIM and multivariate analysis, Atmos. Chem. Phys. Discussions, 6, 3997-4022, 2006.

Johnson, K.S., B. Zuberi, L.T. Molina, M.J. Molina, M.J. Iedema, J.P. Cowin, D.J. Gaspar, C. Wang, and A. Laskin: Processing of soot in an urban environment: case study from the Mexico City Metropolitan Area, Atmos. Chem. Phys., 5, 3033-3043, 2005.

Johnson, K.S., de Foy, B., B., Zuberi, B., Molina, L. T., Molina, M. J., Xie, Y., Laskin, A., Shutthanandan, V.: Aerosol Composition and Source Apportionment in the Mexico City Metropolitan Area with PIXE/PESA/STIM and Multivariate Analysis, Atmos. Chem. Phys. Discussions, 6, 3997-4022, 2006.

Kanakidou, M., J.H. Seinfeld, S.N. Pandis, I. Barnes, F.J. Dentener, M.C. Facchini, R. Van Dingenen, B. Ervens, A. Nenes, C.J. Nielsen, E. Swietlicki, J.P. Putaud, Y. Balkanski, S. Fuzzi, J. Horth, G.K. Moortgat, R. Winterhalter, C.E.L. Myhre, K. Tsigaridis, E. Vignati, E.G. Stephanou, and J. Wilson: Organic aerosol and global climate modelling: a review, Atmos. Chem. Phys., 5, 1053-1123, 2005.

Kawamura, K., and K. Ikushima: Seasonal changes in the distribution of dicarboxylic acids in the urban atmosphere, Environ. Sci. Technol. , 27 (10), 2227-2235, 1993.

Kawamura, K., and I.R. Kaplan: Motor exhaust emissions as a primary source for dicarboxylic-acids in Los-Angeles ambient air, Environ. Sci. Technol. , 21 (1), 105-110, 1987.

Krueger, B.J., V.H. Grassian, J.P. Cowin, and A. Laskin: Heterogeneous chemistry of individual mineral dust particles from different dust source regions: the importance of particle mineralogy, Atmos. Env., 38 (36), 6253-6261, 2004.

Laskin, A., T.W. Wietsma, B.J. Krueger, and V.H. Grassian: Heterogeneous chemistry of individual mineral dust particles with nitric acid: A combined CCSEM/EDX, ESEM, and ICP-MS study, Journal of Geophysical Research-Atmospheres, 110 (D10), -, 2005.

Liu, D.Y., R.J. Wenzel, and K.A. Prather: Aerosol time-of-flight mass spectrometry during the Atlanta Supersite Experiment: 1. Measurements, Journal of Geophysical Research-Atmospheres, 108 (D7), -, 2003.

Marr, L.C., K. Dzepina, J.L. Jimenez, F. Reisen, H.L. Bethel, J. Arey, J.S. Gaffney, N.A. Marley, L.T. Molina, and M.J. Molina: Sources and transformations of particle-bound polycyclic aromatic hydrocarbons in Mexico City, Atmos. Chem. Phys., 6, 1733-1745, 2006.

Miranda, J., V.A. Barrera, A.A. Espinosa, O.S. Galindo, A. Nunez-Orosco, R.C. Montesinos, A. Leal-Castro, and J. Meinguer: PIXE analysis of atmospheric aerosols from three sites in Mexico City, Nucl. Instrum. Methods Phys. Res., Sect. B, 219-20, 157-160, 2004.

Miranda, J., T.A. Cahill, J.R. Morales, F. Aldape, J. Flores, and R.V. Diaz: Determination of elemental concentrations in atmospheric aerosols in Mexico-City usingproton-induced X-Ray emission, proton elastic-scattering, and laser-absorption, Atmos. Env., 28 (14), 2299-2306, 1994.

Miranda, J., A. Lopez-Suarez, R. Paredes-Gutierrez, S. Gonzalez, O.G. de Lucio, E. Andrade, J.R. Morales, and M.J. Avila-Sobarzo: A study of atmospheric aerosols from five sites in Mexico city using PIXE, Nucl. Instrum. Methods Phys. Res., Sect. B, 137, 970-974, 1998.

Miranda, J., J.R. Morales, T.A. Cahill, F. Aldape, and J. Flores: A Study of Elemental Contents in Atmospheric Aerosols in Mexico-City, Atmosfera, 5 (2), 95-108, 1992.

Moffet, R.C., and K.A. Prather: Extending ATOFMS measurements to include refractive index and density, Anal. Chem. , 77 (20), 6535-6541, 2005.

Molina, L.T., Molina, M. J.: Air Quality in the Mexico Megacity: An Integrated Assessment, Kluwer Academic Publishers, Boston, 2002.

Morawska, L., and J.F. Zhang: Combustion sources of particles. 1. Health relevance and source signatures, Chemosphere, 49 (9), 1045-1058, 2002.

Moya, M., A.S. Ansari, and S.N. Pandis: Partitioning of nitrate and ammonium between the gas and particulate phases during the 1997 IMADA-AVER study in Mexico City, Atmos. Env., 35 (10), 1791-1804, 2001.

Moya, M., T. Castro, M. Zepeda, and A. Baez: Characterization of size-differentiated inorganic composition of aerosols in Mexico City, Atmos. Env., 37 (25), 3581-3591, 2003.

Moya, M., M. Grutter, and A. Baez: Diurnal variability of size-differentiated inorganic aerosols and their gas-phase precursors during January and February of 2003 near downtown Mexico City, Atmos. Env., 38 (33), 5651-5661, 2004.

Mugica, V., M. Maubert, M. Torres, J. Munoz, and E. Rico: Temporal and spatial variations of metal content in TSP and PM10 in Mexico City during 1996-1998, Journal of Aerosol Science, 33 (1), 91-102, 2002.

Noble, C.A., and K.A. Prather: Real-time measurement of correlated size and composition profiles of individual atmospheric aerosol particles, Environ. Sci. Technol. , 30 (9), 2667-2680, 1996.

Olmez, I., A.E. Sheffield, G.E. Gordon, J.E. Houck, L.C. Pritchett, J.A. Cooper, T.G. Dzubay, and R.L. Bennett: Compositions of particles from selected sources in philadelphia for receptor modeling applications, JAPCA-the International Journal of Air Pollution Control and Hazardous Waste Management, 38 (11), 1392-1402, 1988.

Ondov, J.M., and A.S. Wexler: Where do particulate toxins reside? An improved paradigm for the structure and dynamics of the urban mid-Atlantic aerosol, Environ. Sci. Technol. , 32 (17), 2547-2555, 1998.

Pastor, S.H., J.O. Allen, L.S. Hughes, P. Bhave, G.R. Cass, and K.A. Prather: Ambient single particle analysis in Riverside, California by aerosol time-of-flight mass spectrometry during the SCOS97-NARSTO, Atmos. Env., 37, S239-S258, 2003.

Pitts, J.N., D. Grosjean, K. Vancauwenberghe, J.P. Schmid, and D.R. Fitz: Photo-oxidation of aliphatic-amines under simulated atmospheric conditions - formation of nitrosamines, nitramines, amides, and photo-chemical oxidant, Environ. Sci. Technol. , 12 (8), 946-953, 1978.

Qin, X.Y., P.V. Bhave, and K.A. Prather: Comparison of two methods for obtaining quantitative mass concentrations from aerosol time-of-flight mass spectrometry measurements, Anal. Chem. , 78 (17), 6169-6178, 2006.

Qin, X.Y., and K.A. Prather: Impact of biomass emissions on particle chemistry during the California Regional Particulate Air Quality Study,Int. J. Mass Spectrom., 258 (1-3), 142-150, 2006.

Raga, G.B., D. Baumgardner, T. Castro, A. Martinez-Arroyo, and R. Navarro-Gonzalez: Mexico City air quality: a qualitative review of gas and aerosol measurements (1960-2000), Atmos. Env., 35 (23), 4041-4058, 2001.

Salcedo, D., T.B. Onasch, K. Dzepina, M.R. Canagaratna, Q. Zhang, J.A. Huffman, P.F. DeCarlo, J.T. Jayne, P. Mortimer, D.R. Worsnop, C.E. Kolb, K.S. Johnson, B. Zuberi, L.C. Marr, R. Volkamer, L.T. Molina, M.J. Molina, B. Cardenas, R.M. Bernabe, C. Marquez, J.S. Gaffney, N.A. Marley, A. Laskin, V. Shutthanandan, Y. Xie, W. Brune, R. Lesher, T. Shirley, and J.L. Jimenez: Characterization of ambient aerosols in Mexico City during the MCMA-2003 campaign with Aerosol Mass Spectrometry: results from the CENICA Supersite, Atmos. Chem. Phys., 6, 925-946, 2006.

Schlesinger, W.H., and A.E. Hartley: A Global Budget for Atmospheric NH3, Biogeochemistry, 15 (3), 191-211, 1992.

Seibert, P., Kromp-Kolb, H., Baltensperger, U., Jost, D.T., and Schwikowski, M.: Trajectory analysis of high-alpine air pollution data, in, Plenum Press, New York, 1994.

Silva, P.J., D.Y. Liu, C.A. Noble, and K.A. Prather: Size and chemical characterization of individual particles resulting from biomass burning of local Southern California species, Environ. Sci. Technol. , 33 (18), 3068-3076, 1999.

Silva, P.J.P., K.A., Source profiling and apportionment of airborne particles: A new approach using aerosol time-of-filght mass sepctrometry, University of California, Riverside, Riverside, 2000.

Sodeman, D.A., S.M. Toner, and K.A. Prather: Determination of single particle mass spectral signatures from light-duty vehicle emissions, Environ. Sci. Technol. , 39 (12), 4569-4580, 2005.

Song, X.H., P.K. Hopke, D.P. Fergenson, and K.A. Prather: Classification of single particles analyzed by ATOFMS using an artificial neural network, ART-2A, Anal. Chem. , 71 (4), 860-865, 1999.

Stohl, A., C. Forster, A. Frank, P. Seibert, and G. Wotawa: Technical note: The Lagrangian particle dispersion model FLEXPART version 6.2, Atmos. Chem. Phys., 5, 2461-2474, 2005.

Suarez, A.E., and J.M. Ondov: Ambient aerosol concentrations of elements resolved by size and by source: Contributions of some cytokine-active metals from coal- and oil-fired power plants, Energy & Fuels, 16 (3), 562-568, 2002.

Sullivan, R.C., S.A. Guazzotti, D.A. Sodeman, and K.A. Prather: Direct observations of the atmospheric processing of Asian mineral Dust, Atmos. Chem. Phys., 7, 1213-1236, 2007.

Tolocka, M.P., D.A. Lake, M.V. Johnston, and A.S. Wexler: Number concentrations of fine and ultrafine particles containing metals, Atmos. Env., 38 (20), 3263-3273, 2004.

Toner, S.M., D.A. Sodeman, and K.A. Prather: Single particle characterization of ultrafine and accumulation mode particles from heavy duty diesel vehicles using aerosol time-of-flight mass spectrometry, Environ. Sci. Technol. , 40 (12), 3912-3921, 2006.

Vega, E., V. Mugica, E. Reyes, G. Sanchez, J.C. Chow, and J.G. Watson: Chemical composition of fugitive dust emitters in Mexico City, Atmos. Env., 35 (23), 4033-4039, 2001.

Vega, E., E. Reyes, G. Sanchez, E. Ortiz, M. Ruiz, J. Chow, J. Watson, and S. Edgerton: Basic statistics of PM2.5 and PM10 in the atmosphere of Mexico city, Sci. Total Environ., 287 (3), 167-176, 2002.

Wenzel, R.J., D.Y. Liu, E.S. Edgerton, and K.A. Prather: Aerosol time-of-flight mass spectrometry during the Atlanta Supersite Experiment: 2. Scaling procedures, Journal of Geophysical Research-Atmospheres, 108 (D7), -, 2003.

Yao, X.H., M. Fang, and C.K. Chan: Size distributions and formation of dicarboxylic acids in atmospheric particles, Atmos. Env., 36 (13), 2099-2107, 2002.

4

Determining Chemically Segregated Optical and Microphysical Properties of Ambient Aerosols Using Single Particle Mass Spectrometry with Aerodynamic Sizing and Light Scattering

4.1. Synopsis

This work presents the first direct measurements of optical and microphysical properties of ambient aerosols as a function of size and mixing state. These coupled single particle measurements of aerosol chemical composition, light scattering, and aerodynamic size are used to derive chemically segregated refractive index and effective density for ambient and laboratory generated aerosol. In order to show that the microphysical properties of the aerosols measured by the ATOFMS are representative of how the aerosol exists at atmospheric relative humidity, laboratory experiments were carried out. It was found that the effective density and refractive index of the aqueous salt particles agreed well with theoretical thermodynamic predictions at 45 and 70% relative humidity. The ambient data were gathered in Riverside and Mexico City. It was found that the different single particle classes in Riverside all had similar refractive index and density, suggesting a large degree of internal mixing. Aerosol in Mexico City was observed to exhibit a wide range of densities (1.1 - 3.4 g/cm^3) for the major particle types, suggesting a largely externally mixed aerosol population. The wide range of

aerosol effective densities in Mexico City is attributed mainly to particle nonsphericity and chemical composition. Nonspherical mineral dust particles were observed in both studies. Mexico had an additional class of nonspherical particles containing Zn and Pb that had a high effective density (2.4 – 3.4g/cm^3). The major difference between Riverside and Mexico City is believed to be due to particle aging: Mexico City has many fresh industrial and secondary aerosol sources that vary strongly as a function of time, whereas the particles sampled in Riverside have aged for several days which results in secondary species determining the similar microphysical properties.

4.2. Introduction

Aerosols affect climate directly by scattering and absorbing solar radiation and indirectly by changing cloud properties. The most recent report by the IPCC stated that aerosols remain one of the dominant sources of uncertainty when judging radiative forcing [*IPCC*, 2007]. In order to reduce these uncertainties, accurate in situ measurements of aerosol optical, physical and chemical properties are necessary. Specifically, optical constants coupled with size distribution measurements for ambient aerosol are needed to assess the direct aerosol effect [*Charlson et al.*, 1992; *IPCC*, 2007; *Tegen et al.*, 1996]. Optical constants are inherently linked to the chemical composition through refractive index, and therefore, simultaneous determination of chemical composition is essential. Chemical composition also affects how the particles interact with water vapor, and therefore impact cloud formation, resulting in the indirect affect on climate [*Ackerman et al.*, 2000; *Ramanathan et al.*, 2001]. Clearly, a complete physical

and chemical view of aerosol particles must be constructed before we can fully understand how aerosols truly affect climate.

In order to model how ambient aerosols interact with radiation and force climate, values for refractive index as a function of size and chemistry are needed. Particles that scatter light most efficiently are in the size range from 0.1 – 10 μm. For polluted atmospheres, particles in this size range make up the majority of the total aerosol mass. Scattering and absorption by particles of this size can neither be described by Rayleigh scattering nor by geometric optics. Mie scattering, which is the exact solution to Maxwell's equations for scattering and absorption by a sphere, is needed to predict small particle scattering and absorption [*Bohren and Huffman*, 1981]. Other methods are available to compute scattering and absorption of small nonspherical or heterogeneously mixed particles [*Draine and Flatau*, 1994; *Mishchenko et al.*, 2000; *Mishchenko et al.*, 1996]. Each method has its own set of assumptions and limitations but they all require size and chemical composition (refractive index) as inputs. Detailed information about the size and refractive index for *ambient* aerosols that these state-of-the art models require is sparse. Therefore it is important to obtain accurate real-world measurements.

Aerosols are a complex system to measure and accurate values for key optical parameters that are resolved by size, time and chemical compostion remain elusive. This is because aerosols are often composed of many different species that are internally mixed and therefore do not represent the idealized case of one pure component [*Gard et al.*, 1998; *Li et al.*, 2003; *Liu et al.*, 1997; *Murphy et al.*, 1998]. Internal mixing of particles strongly affects optical properties, in addition to affecting hygroscopicity which influences size, and again, optical properties [*Jacobson*, 2001; *Kreidenweis et al.*,

2003]. While *in situ* chemically resolved measurements of size, chemical composition and optical properties are rare, instrumentation is advancing to the point where it is becoming feasible to measure all of these properties in one field campaign, or even with one instrument. Perhaps the most significant advance in aerosol measurements has been made using mass spectrometry [*Canagaratna et al.*, 2007; *Murphy*, 2007]. Mass spectrometers are capable of measuring the size and chemical composition of aerosols on time resolutions of less than 1hr. Furthermore, new efforts are being made to couple light scattering measurements to these aerosol mass spectrometers to give information on density [*Cross et al.*, 2007; *Murphy et al.*, 2004] and refractive index [*Moffet and Prather*, 2005]. For single particle mass spectrometers, which are typically regarded as non-quantitative for particulate mass, the addition of density information pushes the technique towards being able to measure mass concentrations of aerosol segregated on the basis of chemical composition. This is remarkable because these instruments also directly measure mixing state and size on a single particle basis. Coupling light scattering techniques to single particle mass spectrometers promises to add a more complete set of information to help identify sources in addition to giving more information on climate relevant microphysical properties such as refractive index and density.

In this paper, we present results from a new measurement technique to obtain refractive index and density for size resolved ambient aerosols that have been classified according to mixing state. The measurements were carried out in both Riverside and Mexico City. Spherical and non-spherical particles are identified in both cities. For some of the spherical particles, we were able to find a best fit refractive index and effective density using Mie theory. For non-spherical particles a best estimate is provided for the

effective density. These new results lead to new insights of how interconnected aerosol microphysical and optical properties compare and contrast in two well-studied megacities.

4.3 Experimental

4.3.1 Field Studies

Results presented here were obtained in two different field campaigns. The two sampling locations were chosen because of their unique, extensively studied aerosols. While the two cities have many characteristics in common (large number of vehicles), they also differ in many ways (industrial and regional sources). In order to study the aerosol characteristics in each campaign, an aerosol time-of-flight mass spectrometer (ATOFMS) with a converging nozzle inlet was used which is similar to the instrument described in Gard, 1997 [*Gard et al.*, 1997]. Measurements in Riverside, California were carried out as part of the Study of Organic Aerosols in Riverside II (SOARII) campaign. Sampling took place from October 27 to November 21, 2005 at UC Riverside (33º58'18.16N, 117º19'21.44W). The sampling relative humidity for the campaign averaged 50% had a standard deviation of 26%, minimum of 12% and a maximum of 99%. The average O_3 and $PM_{2.5}$ levels for this study were approximately 23 ppb and 29 $\mu g/m^3$.

Measurements in Mexico City took place from March 7 to 31, 2006 as part of the Megacity Initiative: Local and Global Research Operations (MILAGRO) campaign. The measurement site was located in the northern part of Mexico City (19º29'23.22N, 99º08'55.76W). Sampling details for the study may be found elsewhere [*Moffet et al.*,

2007]. The relative humidity during the campaign averaged 40% and had a standard deviation of 21%, minimum of 3.6% and maximum of 89%. The average O_3 and $PM_{2.5}$ levels for this study were approximately 37 ppb and 40 $\mu g/m^3$.

4.3.2 Laboratory Studies with Controlled Relative Humidity

In order to test if the ATOFMS is able to measure the microphysical and optical properties of metastable particles, a laboratory validation was done using metastable sea salt particles. Sea salt aerosol was generated by atomizing a solution of 0.04g/mL synthetic sea salt (Sigma Aldrich) dissolved in MilliQ water using a Collison type atomizer. The particles were then directed into a flow tube where the relative humidity could be controlled and varied. Relative humidity was controlled by mixing dry nitrogen with varying amounts of nitrogen saturated with water vapor. Water vapor was generated by passing a separate stream of dry nitrogen through a bubbler placed in a hot water bath. At the exit of the flow tube, the aerosol was directed into an ATOFMS for single particle size, chemistry, and optical measurements. A sample of Maldives dust was run using the same laboratory setup. To test the instrument response for nonspherical particles, laboratory studies of dust were carried out using the ATOFMS. The dust was placed in a jar and disturbed with a magnetic stirrer while a flow of N_2 gas carried the dust particles to the RH controlled flow tube. The dust experiment was run at an RH of 50%.

4.3.3 Data Processing , Scattered Pulse Distributions, and Particle and Laser Beam Alignment

The nozzle type inlet used in these studies has a transmission curve that varies strongly with aerodynamic diameter, showing peak transmission at about 1.7μm [*Moffet et al.*, 2004; *Qin et al.*, 2006]. Because the particle beam is larger than the laser beam, there will always be a population of particles that clip the edge of the light scattering laser beam. The clipping of the Gaussian laser beam causes the particles to scatter less light than they would if they traveled through the center of the beam. This effect is magnified for particles that are smaller or larger than the most efficiently transmitted size, for missed particles, and for particles that are nonspherical. Other groups using an aerosol mass spectrometer (AMS) noted that using a wider laser beam alleviates the problem of beam clipping by divergent particles [*Cross et al.*, 2007]. While this is feasible for the AMS which has a lager particle collection target, doing so for the ATOFMS may decrease the particle hit percentage.

Earlier methodology [*Moffet and Prather*, 2005] of processing the ATOFMS partial scattering cross section (R) as a function of size relied on taking a rolling average of the raw data. This method was used to calibrate the photodetector by taking the average of discrete sizes of monodispersed polystyrene sphere particles and relating them to the theoretical intensity predicted by Mie theory. However, if the ambient particles have a pulse distribution that has more population at lower intensities due to beam divergence, the average will be lower than for spherical particles having the same geometric diameter and refractive index. There is a need to circumvent this problem.

To get around the difficulties resulting from particle beam divergence, a new method of processing the raw scattering data was developed. The method involves finding the upper limit of the scattering data through the use of an edge finding algorithm

similar to those used in image processing. The algorithm works by binning the scattering data by size, then taking the difference in R for the particles in a given size bin. A monotonic regression is performed on these differences and an empirical threshold is set based on the parameters given by the monotonic regression. This method is better than just simply taking the maximum scattering value at a given size because it is not affected by outliers.

This upper limit method for processing the raw scattering data is used in both calibration and ambient data analysis. Results from the calibration of PSL particles are shown in Fig. 4.1. The solid lines in Fig 4.1 indicate the points where the edge finding algorithm indicated an edge. Raw data was transformed by a linear calibration of the form $R = R_{raw}*G$, where R is the theoretical scattering cross section predicted by Mie theory, R_{raw} is the output from the raw data processed with the edge finding algorithm, and G is the slope. In Fig 4.1, data from both channels of the ATOFMS sizing region are shown. There is a systematic discrepancy for channel A and B. Above and below the size of peak transmission (~1.7μm), PMT A scatters less light than PMT B. It is further seen in Fig 4.1 that PMT B agrees well with the scattering curve predicted theoretically. We believe that the PMT A shows a systematic deviation due to the way the laser is aligned relative to the particle beam. For this reason, ambient data from PMT A were not used in any quantitative interpretation of refractive index or density. Before, during, and after each field study these light scattering calibrations to PSL particles were performed to check for this systematic error. Although it is not currently known how to correct for this error, there may be several solutions. If the problem is due to imperfections causing focusing problems with the particle beam, a new nozzle may have to be machined.

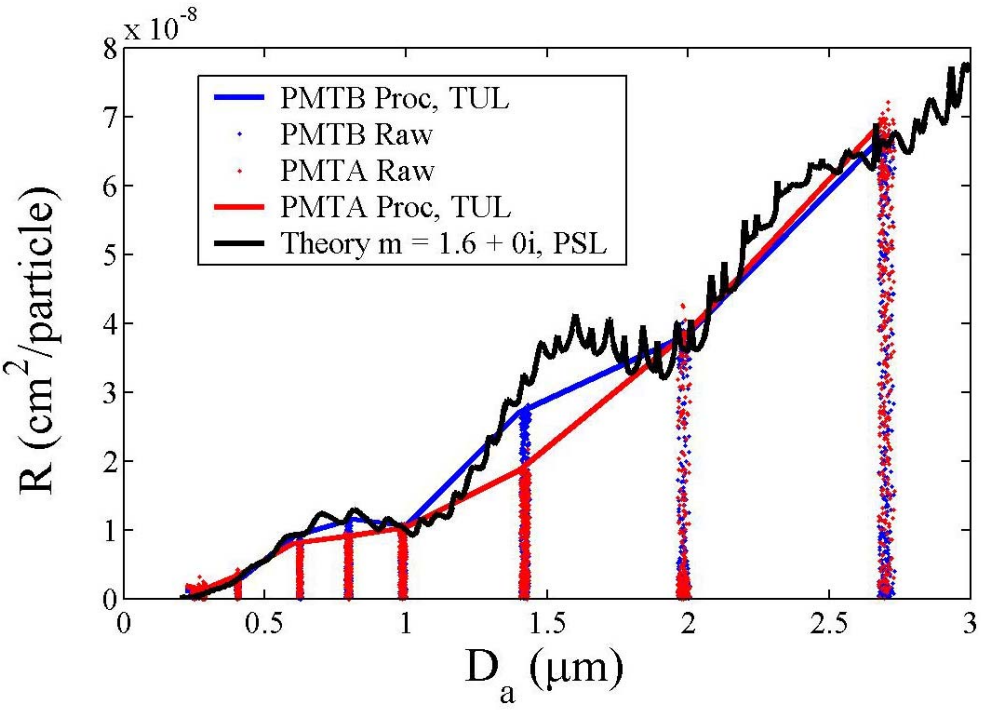

Figure 4.1. PSL calibration data for two channels (A & B) of the ATOFMS. Channel A shows a systematically low scattered intensity at certain sizes due to a non-ideal laser-particle beam alignment. This can cause errors in retrieving refractive index and density.

4.3.4 Refractive Index and Density Retrieval for Ambient Aerosol Particles

Finding the refractive index and density for particles below ~600 nm is a multi-valued problem [*Flatau*, 2006] that was not described in Moffet (2005). This aspect of the problem is illustrated in Fig 4.2 by plotting R vs n*D where n is the real part of the refractive index and D is the particle diameter. It is seen that all of the scattering curves below 600 nm fall on one curve. Therefore, an infinite number of different combinations of n and D will produce equivalent solutions.

We use the best fit value for effective density (ρ_{eff}) to obtain D, by the relation

$$\mathbf{D} = \mathbf{D_a}\sqrt{\frac{\mathbf{C(D_a)}}{\rho_{\mathbf{eff}}\mathbf{C(D)}}} \qquad \text{(Eq. 4.1)}$$

where D_a is the aerodynamic diameter measured by the ATOFMS. Therefore, an infinite number of combinations of n and ρ_{eff} will produce equivalent fits to Mie theory below 600nm. In light of this observation, we do not attempt to obtain both n and ρ_{eff} for particle types that do not have a significant population above 600 nm. However, we can assume a range of n to retrieve a range of possible values for ρ_{eff}. This is done using a method similar to Cross (2007). The assumed values for n typically range from 1.33 (pure water) to about 1.55 (organics), but this range depends on the chemical composition.

For particles that have a significant population both above and below 600nm, our previously published method of retrieving the refractive index and density [*Moffet and Prather*, 2005] is implemented, except using the processing methods described in the previous section. It can be seen in Fig 4.2 that above this 600 nm cut, the scattering curves begin to "tip over" at characteristic values of refractive index enabling both n and ρ_{eff} to be determined from experimental data. Fig 4.2. shows that ambient data from

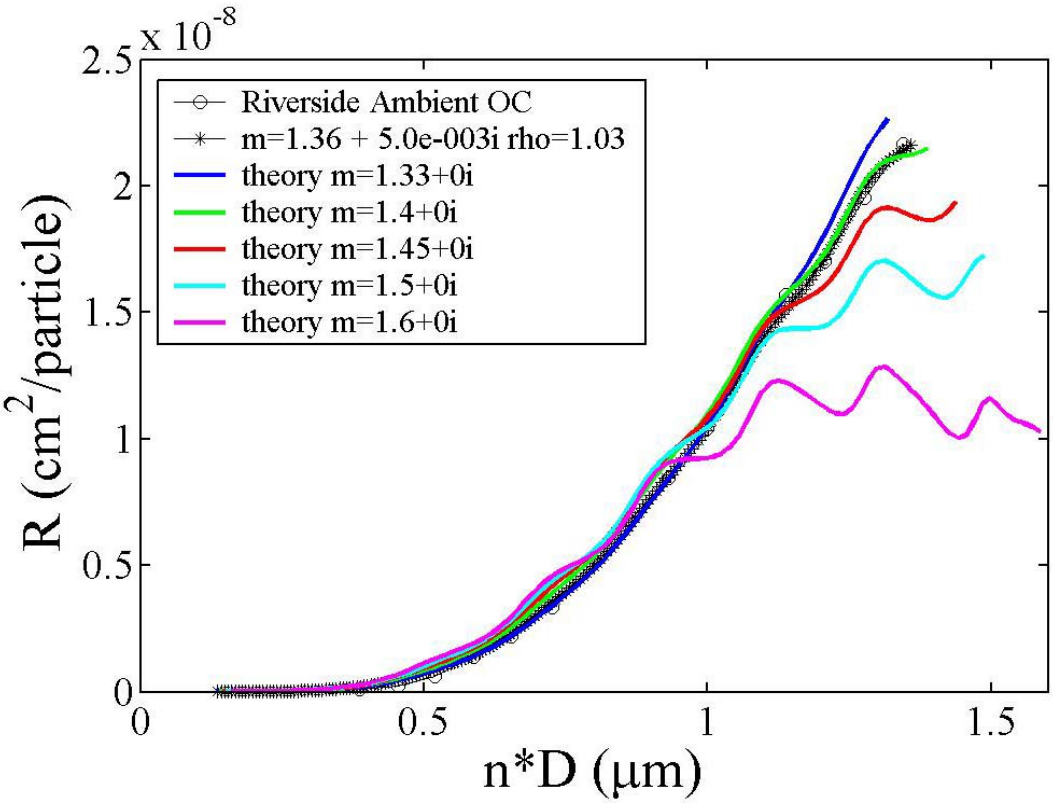

Figure 4.2. Diagram demonstrating that many different combinations of refractive index (n) and size (or density) can give the same value for scattered intensity at small sizes.

organic carbon (OC) particles in Riverside most closely follow the theoretical curve for n = 1.4.

Error estimates of the refractive index and density for spherical particle types having significant population above 600 nm were determined through a sensitivity analysis. The major source of error for refractive index and density is the PMT calibration described in the previous section. The upper and lower 95% confidence bounds on the linear calibration curve were used to transform the raw data. For each bound, the refractive index and density and density were retrieved. The range in the values is reported in parentheses throughout this manuscript.

4.4. Results

In this section, the results are presented for the optical and microphysical properties of both laboratory and ambient aerosols segregated on the basis of chemical composition. To validate the results for ambient aerosols, laboratory measurements (Sec 4.4.1) for metastable sea salt aerosols and dust particles are presented to show how the instrument responds to these different particle types. Then, chemically segregated light scattering measurements are presented from both Riverside and Mexico City in Sec 4.4.2. These results present the relations between chemical composition, density, morphology and optical properties measured *in situ* for two major urban areas in North America.

4.4.1 Instrument Response to Laboratory Test Aerosol

Sampling laboratory test aerosol is essential for understanding instrumental response to different particle types expected in the ambient atmosphere. In Moffet, 2005,

we used liquid organic particles to develop our calibration and data inversion method. In that work, it was shown that homogenous spherical particles gave an instrument response that could be modeled with Mie theory. However, the ATOFMS scattering response has not been tested previously for aqueous and nonspherical particles. In this section, results for both particle types are shown in Figs 4.3 and 4.4 and then compared with the particle types observed in the ambient atmosphere in Sec 4.4.2. These laboratory characterizations will lead to a well-guided interpretation of the ambient data set through a better understanding of instrumental response.

To test whether the standard ATOFMS inlet dries salt particles, synthetic sea salt particles were prepared by atomization of a dilute solution, and sampled with the ATOFMS. The scattering curves at relative humidities of 70% ,45%, and 25% are shown in Fig 4.3 along with best fits to the refractive index and density. Based on previous work on the efflorescence and deliquescence of sea salt, the particles should remain roughly spherical even after the crystallization of NaCl at 45%. For comparison, theoretical plots for NaCl at the specified RH using the aerosol inorganics model (AIM) [*Clegg et al.*, 1998; *Wexler and Clegg*, 2002] and Mie theory. We see that at both relative humidities, the AIM predicted refractive index and density agree closely with the measured values by the ATOFMS, proving that the ATOFMS does not evaporate this particular salt solution in the light scattering region. The sea salt particles at 25% show a much larger values for refractive index and density, suggesting that the NaCl has crystallized within the droplets. Recent results by Zelenyuk et al indicate that NaCl evaporation dynamics are complicated when measured using an aerodynamic lens [*Zelenyuk et al.*, 2006]. For

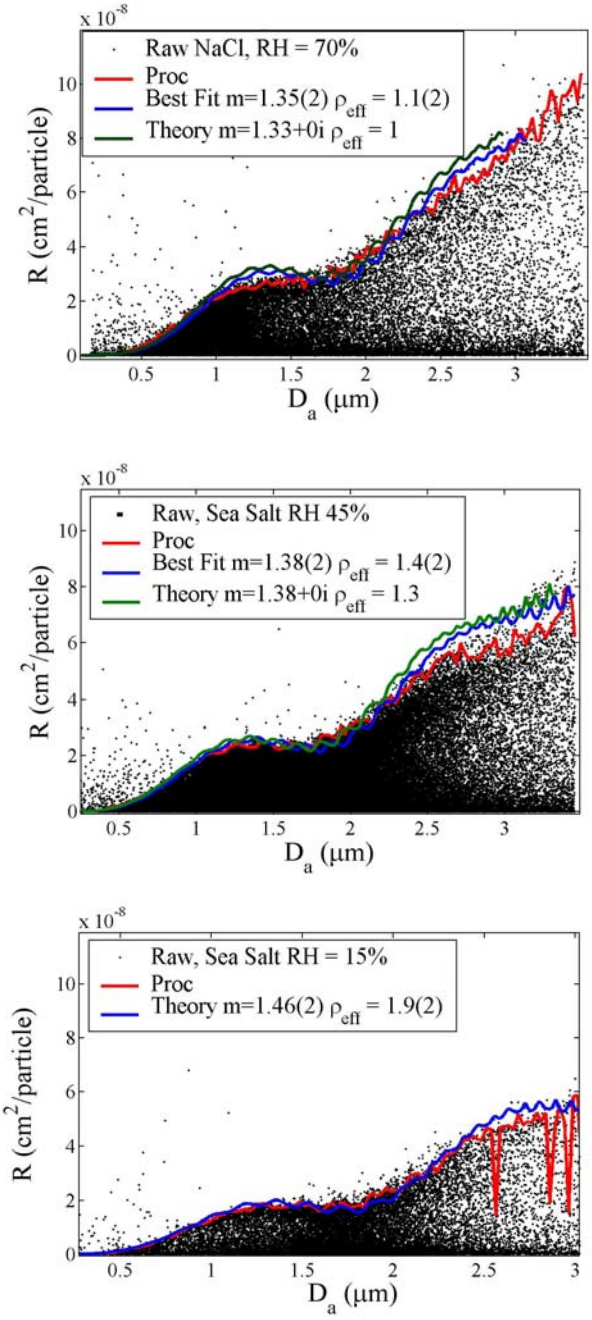

Figure 4.3. Laboratory generated NaCl particles a) at 70% b) near crystallization of NaCl at ~45% c) after crystallization of NaCl at 15%. The retrieved values for refractive index and density are in agreement with what is predicted in the ambient atmosphere.

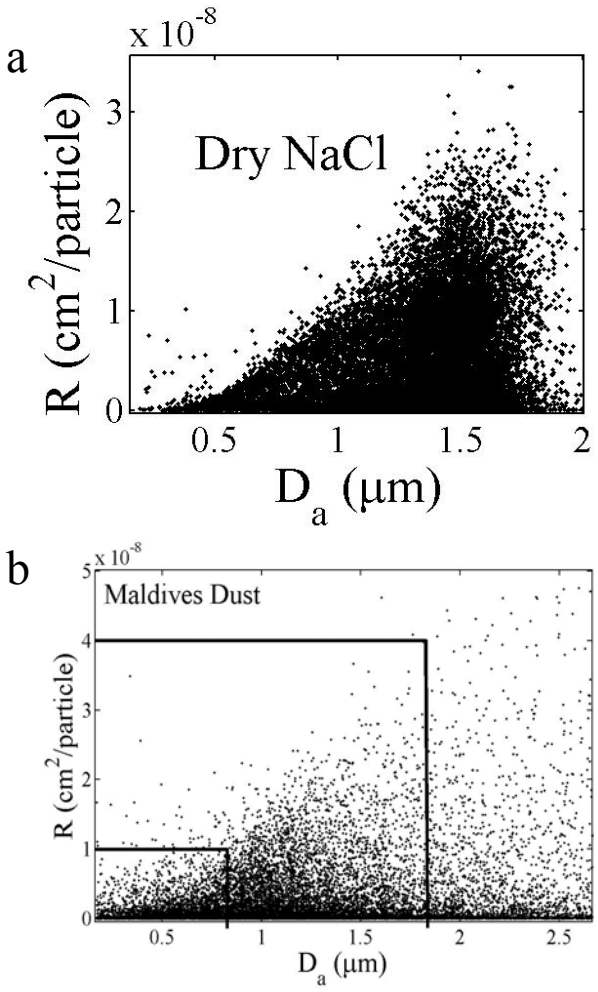

Figure 4.4. Scattering curves for a) dry NaCl and b) Laboratory re-suspended dust.

orifice type inlets such as the one used in this study, it has been thought that condensation may occur [*Mallina et al.*, 1997; *Murphy*, 2007]. Our results demonstrate that evaporation or particle growth due to condensation of water in the inlet appears to be negligible, or within the errors of our measurement.

In order to test the instrument response for nonspherical particles, dust and dry NaCl particles were sampled with the ATOFMS. The scattering curve for dry NaCl particles is shown in Fig 4.4a, and it is apparent that it does not scatter light like the more spherical metastable sea salt particles. The upper limit to the scattering curve does not fit well to what is predicted by Mie theory. Similar results are found for calcium-rich dust from the Maldives islands shown in Fig 4.4b. For the Maldives dust sample, there is an enhanced population of particles that scatter light at low intensities, suggesting that a larger proportion of the particles are clipping the laser beam in the light scattering region of the ATOFMS than for the NaCl sample. Based on the difference between the spherical sea salt particles and the nonspherical NaCl and dust particles, it is seen that the presence of non-spherical particles can be identified. Furthermore, because the nozzle inlet does not remove a significant amount of water from particles, the optical properties, density and refractive index reported by the ATOFMS should be representative of the water content of the particles in the ambient atmosphere.

4.4.2 Microphysical and Optical Properties for Ambient Aerosol

Prior to analysis of the ambient light scattering measurements, the single particle data from both Riverside and Mexico City were separated on the basis of chemical composition using the ART-2a algorithm [*Song et al.*, 1999]. The light scattering as a

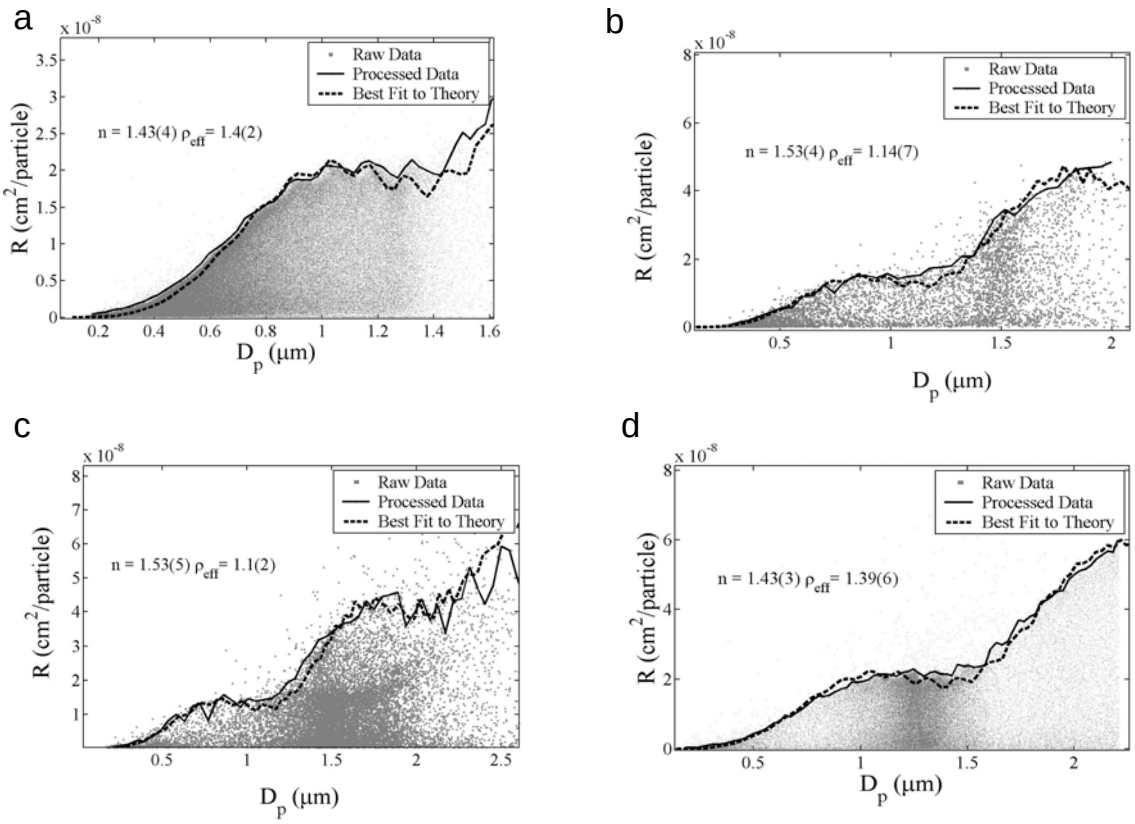

Figure 4.5. Scattering curves for spherical particle types a) ECOC in Riverside b) HMOC Mexico City c) Ca Rich, Mexico City d) Na rich, Riverside

function of size for each cluster helps to identify spherical particle types (Sec 4.4.2.1), particles that have mixed microphysical parameters (Sec 4.4.2.2), and nonspherical particles (Sec 4.4.2.3).

4.4.2.1 Spherical Ambient Particle Types

By comparing ambient scattering curves to those predicted by Mie theory (e.g. Fig 4.1), spherical particles can be identified. Chemically segregated scattering curves that indicate spherical morphology are shown in Fig 4.5. An organic carbon particle type identified in Riverside (Fig 4.5a) shows a scattering curve with well defined resonances above 600 nm. The fit obtained with the edge finding algorithm is overlaid upon the raw data along with the best fit to Mie theory. The processed data curve highlights the Mie resonances and it is seen that the positions of these resonances are fit well by Mie theory. Note that below about 700 nm, a significant fraction of particles produce higher scattered intensity than predicted by Mie theory, indicating that these particles may either have a lower effective density or refractive index. The difference in effective density is either due to a difference in shape or material density. This means that the assumption of a refractive index and density that does not depend on size is not entirely accurate. However the assumption works well for describing the overall relationship for how light scattering varies with size.

Values derived through least squares fitting of the processed data to Mie theory are shown in Table 4.1. We find that for Riverside, mixed elemental carbon/organic carbon particles (ECOC), the refractive index and effective density are 1.44 and 1.40, respectively. These are well within the values measured by [*Geller et al.*, 2006]. It was

Table 4.1. Retrieved refractive index (n) and effective density (ρ_{eff}) for spherical particles observed in Riverside, CA and Mexico City, Mexico.

Study	Particle Type	n	ρ_{eff} (g/cm^3)	Size Range (μm)	Notes
Riverside	ECOC	1.43(4)	1.4(2)	0.1 – 1.6	Mie resonances observed
Riverside	OC	1.44(3)	1.38(6)	0.1 – 1.5	
Mexico City	Amine	1.40 – 1.55	1.3 – 1.7	0.1 – 0.7	Poor stats >0.7μm, likely industrial
Mexico City	OC	1.4 – 1.55	1.44-1.70	0.3 – 0.73	Nighttime, poor stats >0.8μm, no negative ions
Riverside	Na Rich	1.43(3)	1.4(1)	0.1 – 2.5	Mie resonances observed
Mexico City	Na Rich	1.45(3)	2.0(1)	0.1 – 1.85	Large Nitrate Signal – noon
Riverside	Ca Rich	1.50(6)	0.8(2)	0.1 – 1.5	
Mexico City	Ca Rich	1.53(5)	1.1(2)	0.1 – 2.5	50 nm size resolution
Mexico City	HMOC	1.53(4)	1.14(7)	0.1 – 2	High mass organic (HMOC), Nighttime

found that for Riverside, the majority of the particles had spherical morphologies with the exception of dust, which is discussed below (Sec 4.4.2.3). Furthermore, the particle types in Riverside all exhibited very similar values for refractive index and ρ_{eff}, suggesting that from a bulk perspective they are internally mixed. This is the same conclusion obtained for heavily aged Riverside aerosol in the summer time [*Spencer et al.*, 2007]. For example the Na rich particle class, which we believe to be aged sea salt, has similar values for n and ρ_{eff} to the other particle types shown in Fig 4.5d and Table 4.1. This is consistent with the observation that the particles sampled in Riverside during the fall are heavily aged and have had a significant amount of time to become internal mixtures through condensation, heterogeneous chemistry and coagulation processes [*Hughes et al.*, 2000; *Hughes et al.*, 2002; *Sardar et al.*, 2005]. On the other hand, it is possible that the salt and organic particles have a different chemical mixing state but have the same refractive index and density.

Calcium rich particles from both Mexico City and Riverside exhibited a scattering pattern indicative of spherical particles because of the strong fit with Mie theory predictions. Figure 4.5c shows the scattering curve for Ca rich particles sampled in Mexico City. The scattering curves for Ca rich particles in Mexico City and Riverside exhibited effective densities of ~1g/cm^3, and refractive indices of ~1.5 (Table 4.1). Recent research has pointed to the possibility for Ca containing dust particles to react with nitric acid in the atmosphere. This would create $Ca(NO_3)_2$ - a compound which is known to be hygroscopic [*Gibson et al.*, 2006]. The hygroscopic growth curves published in Gibson et al indicate that the $Ca(NO_3)_2$ particles have a substantial amount of water on them at humidities ranging from 20-90%. Thus, it is possible that some of the Ca

particles we observe here are $Ca(NO_3)_2 \cdot xH_2O$, as indicated by the strong internal mixing of these particles with nitrate markers [*Moffet et al.*, 2007].

Other spherical particles observed in Mexico City were usually associated with organic carbon markers (Table 4.1: Amine, OC, high mass OC). All of the effective densities retrieved for the OC particles fall on the lower end of the range between 1.1 and 1.7g/cm^3. For the OC, and amine particle types, a range of refractive indices were assumed to retrieve the effective density as described in Sec 4.3.4 due to poor statistics above 600 nm. The high mass OC (HMOC) particle class had sufficient particle counts above 600 nm to enable a retrieval of refractive index and density. It was found that the density of the HMOC particles was 1.1g/cm^3, which could be due to the fact that they were positively correlated with RH, while reaching highest concentrations at night. These HMOC particle types were also found in California central valley – a region with strong biomass burning influence - and peaked during periods with high RH. The interaction of these particles with water is supported by their absence of negative ion spectra; this was observed for the OC class as well. In general the effective densities for the spherical organic particle types are in agreement with the effective densities obtained for Riverside. However, Mexico City typically had low RH conditions that caused a prevalence of nonspherical particles as described in the following two sections.

4.4.2.2 Mixed Ambient Particle Types: Spherical to Nonspherical, Dense to Less Dense, Fresh to Aged

In Mexico City, some of the aerosol particles exhibited a more complex scattering dependence versus size which is attributed to the presence of both compact and irregularly shaped particles within the Art-2a clusters. It was observed that for the most populous aerosol classes (NaK-nitrate, biomass and OC) there were two regimes in the scattering curves. The scattering curves for the NaK-nitrate and biomass classes are presented in Fig 6 and the retrieved (n and ρ_{eff}) for the two limits of these curves are shown in Table 2. The OC scattering curve was omitted, but it closely resembled that of the biomass.

The scattering curve for the NaK-nitrate class shown is shown in Fig 6a. The particles exhibited two strikingly different characteristics in the supermicron region: one region of higher scattering intensities (black dots), and another at lower scattered intensities (red dots). The red dots represent an NaK particle class that is heavily aged with nitrate as indicated by the marker at m/z=-125. These particles had a very reproducible temporal profile, peaking every day around 12p, indicating the accumulation of nitrate produced by photochemistry. This region of lower scattering intensity is compared to a theoretical Mie curve calculated using a refractive index of 1.45 and an effective density of $2 g/cm^3$. This refractive index and effective density combination is consistent for values obtained for dry salts of nitrate, sodium and potassium. The region above this low intensity portion of the NaK scattering curve gives best fit parameters to of n = 1.51 and ρ_{eff} = 0.95. It is uncommon to find substances other than organics that have this combination of refractive index and density, therefore it is likely that this different pattern in scattering is caused by

nonspherical particles since no organic markers were observed for the NaK class. While it is not totally correct to use Mie theory for nonspherical particles, Mie theory provides a estimate of scattering intensity by the particle. Furthermore, we have found using nonspherical particle scattering models that the scattering by an orientation averaged cube is approximately the same as a sphere.

The biomass particle type was the most abundant particle class (by number) observed in Mexico City. It is identified as biomass by the presence of a significant potassium ion peak. The scattering curve for the biomass particle type is shown in Fig 6b. The majority of the biomass particles occurred in the submicron size range. In this region of Fig 6b there appears to be two separate trends. This behavior was reproduced by plotting two Mie curves between n = 1.48 – 1.54 and effective densities between 1.10 and 1.93g/cm^3. The values for the effective density encompass the values expected for many substances: water, organics and dry inorganic salts. There are several causes for this behavior: 1) the biomass particles may be changing in effective density due to water uptake 2) some of the particles may contain more organics, thus giving a lower density or 3) some of the particles may be non-spherical, giving a lower effective density. Another type of particle that exhibited a scattering curve with two regimes was the OC particle types for Mexico City that gave temporal maxima during rush hour (early morning). During rush hour in Mexico City, a great deal of nonspherical particles have been observed using scanning electron microscopy [*Johnson et al.*, 2006b]. Also, the other major Mexico City OC type that peaked later in the day was observed to be spherical

a

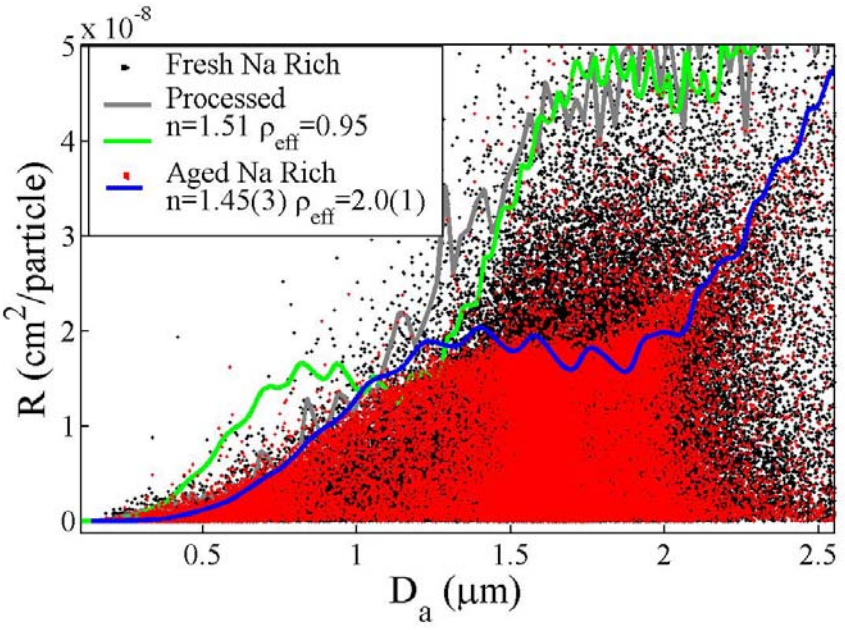

b

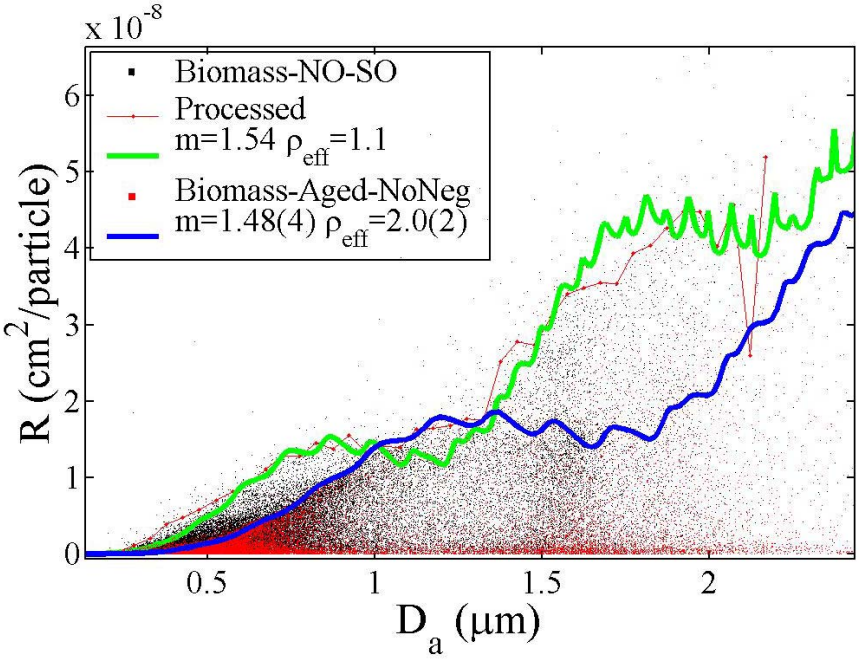

Figure 4.6. Particle types displaying either mixed density and/or mixed morphology a) Na/K rich in Mexico City shows two distinct regions of scattering behavior as indicated by the red and black dots. b) Biomass, Mexico City. The green theoretical curve in both a and b was added for reference only. Absolute errors for spherical particle refractive index and density are shown in brackets. The error is in the last digit reported.

Table 4.2. Retrieved refractive index (n) and effective density (ρ_{eff}) for particles exhibiting scattering curves containing two patterns

Study	Particle Type	n	ρ_{eff} (g/cm^3)	Size Range (μm)	Notes
Mexico City	Na/K Rich	1.46 – 1.51	2.2 – 0.95	0.1 – 2.5	Dust/NaCl
Mexico City	Biomass	1.51 – 1.54	2.0 – 1.0	0.1 – 2	Afternoon Peak
Mexico City	OC	1.55 – 1.48	1.1 – 1.9	0.1 – 1.5	Rush hour peak

(Sec 3.2.1). This is consistent with the above observation that photochemical ageing of the particles causes a more compact morphological structure. Therefore, particle nonsphericity is the most likely explanation the presence of the lower density (Table 2) OC particles observed during rush hour.

Contrasting the mixing state and density between Mexico City and Riverside gives further insight into how chemical composition and effective density are linked. As mentioned in the previous section, the majority of the inorganic salt and organic particles in Riverside were observed to have scattering curves that predominantly resembled scattering by homogenous spherical particles. In contrast, different particle effective densities were observed for particles of similar chemical composition in Mexico City. This suggests that the particles in Mexico City may have either had different amounts of the different secondary and primary species or had a different morphology. In Mexico City, the majority of the aerosol was freshly emitted whereas in Riverside, the majority of the aerosols were transported from other regions of the Los Angeles basin and significantly aged. In Riverside, the particles that had the same ATOFMS mixing state also had similar values for effective density. It is interesting that particles in Riverside can give different mass spectra, yet have very similar microphysical properties. A similar result was also observed by Spencer et al. 2006 and attributed to the majority of the particle mass being dominated by secondary organic/inorganic species with a smaller core that retains the specific chemical signature from the primary source. This would yield particles with very similar density but different mass spectrum. This highlights the ability of the ATOFMS to obtain information with regards to the primary source even when particle mass is dominated by secondary processing.

4.4.2.3 Nonspherical Ambient Particle Types

Nonspherical particles typically give scattering curves that have no well defined upper limit. Scattering curves for nonspherical particles identified in Riverside and Mexico City are shown in Fig 4.7, and best fit values for density are presented in Table 4.3. As expected, mineral dust particles were observed to be nonspherical in both Mexico City and Riverside (Figs 4.7a, b). In Mexico City, there appeared to be an industrial source of nonspherical particles. A major chemical characteristic of these particles was the presence of Zn and Pb. Because there was no structure in the raw data to validate our fits to refractive index and density, we constrained our analysis to only retrieve effective density given a range of assumed refractive indices.

For both Riverside and Mexico City, dust clusters from the ART-2a analysis were identified by the presence of a large $^{27}Al^{+}$ peak together with the silicate markers $^{60}SiO_2^{-}$ and $^{76}SiO_3^{-}$. The range of refractive indices used was taken from typical ranges found for aluminosilicate minerals in the book by Egan and Hilgeman [*Egan and Hilgeman*, 1979]. The complex part of the index of refraction for typical aluminosilicate minerals is usually less than 1e-3, therefore, we assume that absorption is negligible for our retrieval of effective densities. In Table 4.3, submicron particles have effective densities of 1.64 – 1.87 and 1.26 – 1.40g/cm^3 for Riverside and Mexico City, respectively. For the super micron sizes, the effective density decreases to 0.8 – 1.4 and 0.83 – 1.17g/cm^3 for Riverside and Mexico City, respectively. The trend of decreasing effective density with

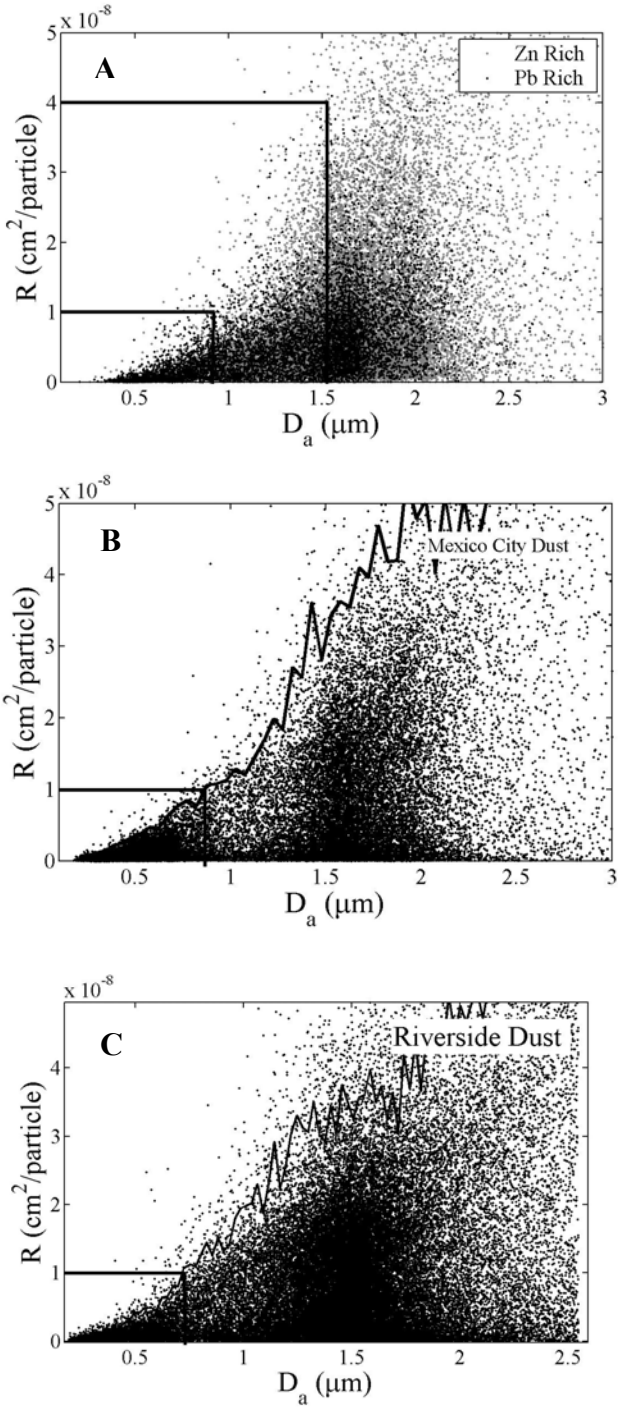

Figure 4.7. Scattering curves for nonspherical particles a) Metal rich particles in Mexico city b) AlSi dust in Mexico city c) AlSi Dust in Riverside

Table 4.3. Retrieved effective density (ρ_{eff}) from assumed refractive indices (n) for nonspherical particle types using Mie theory.

Study	Particle Type	Assumed n	ρ_{eff} (g/cm^3)	Size Range (μm)	Notes
Riverside	AlSiDust	1.4 – 1.7	1.64 – 1.87	0.1 – 0.6	
Riverside	AlSiDust	1.4 – 1.7	0.8 – 1.4	1 – 3	
Mexico City	AlSiDust	1.4 – 1.7	1.26 – 1.40	0.1 – 0.6	
Mexico City	AlSiDust	1.4 – 1.7	0.83 – 1.17	1 – 3	
Mexico City	Pb Rich	1.4 – 2.0	2.4 – 3.4	0.1 – 1	Industry
Mexico City	Zn Rich	1.4 – 2.0	2.4 – 3.4	0.1 – 0.6	Industry

increasing particle size suggests that the dynamic shape factor increases with particle size, meaning that the larger particles are more nonspherical. It is also interesting to note that the dust particles in Mexico City have lower effective densities than the dust particles in Riverside. This may suggest that the dust in Mexico City either has a lower material density or that they are more nonspherical than the dust in Riverside due to ageing.

Particles rich in Zn and Pb were frequently observed from 12 – 10 am in Mexico City and are believed to be a result of industrial emissions [*Johnson et al.*, 2006a; *Moffet et al.*, 2007]. To retrieve effective density for these metal rich particles we assumed a refractive index between 1.4 and 2.0 which roughly correspond to an aqueous particle and pure ZnO. The upper limit of ZnO was chosen because ZnO was identified to be a component of these particles using scanning transmission X-Ray microscopy coupled to near edge X-Ray fine structure spectroscopy (see Chapter 6). Based on this wide range of refractive indices, we estimate the effective density of these particles to be greater than 2.4g/cm^3. This high effective density is expected because the material densities for compounds of Pb and Zn frequently exceed 4g/cm^3. No attempt was made to report effective densities for particles above 1μm due to large uncertainties caused by our large range of assumed refractive indices. However, it appears that the Pb particles (black points in Fig 4.7a) have less scattered intensity than do Zn particles having the same aerodynamic diameter. Therefore, according to Eq. 4.1, these particles will have a high effective density, large aerodynamic diameter, and small geometric diameter. This suggests that the supermicron Pb particles may be more dense than the Zn particles as expected from bulk material densities.

4.5 Conclusions

In this paper, we have successfully demonstrated the ability to measure relationships between chemical composition, size, density, morphology and refractive index for ambient aerosols. For Mexico City, the aerosol exhibited a wide range of refractive indices and density in contrast to Riverside where many of the aerosol classes were found to have very similar values for refractive index and effective density. The aerosols in Riverside all had similar microphysical properties which suggests that they were internal mixtures of secondary components such as water, nitrate, and sulfate. Most of the major particle types observed in Riverside were spherical, which enabled us to determine their refractive index and density using Mie theory. In Mexico City, it was observed that the major particle types (NaK rich, biomass, and OC) were external mixtures of particles having different effective densities, either due to different shape factors or material densities. Nonspherical particles common to both cities showed chemical signatures indicative of dust particles. Nonspherical particles sampled in Mexico City that were rich in Zn and Pb were found to have high effective densities ($>2 g/cm^3$) compared to aluminosilicate dust particles ($1\text{-}2 g/cm^3$).

Spherical particles observed in the ambient atmosphere were found to have characteristic values for refractive index and density. The refractive index and density for these particles was determined with errors of approximately 2 and 10% respectively. Calcium rich particles were observed to give scattering curves similar to those given by spherical particles; the effective density for these spherical particles was found to be 0.9-$1.1 g/cm^3$ for Riverside and Mexico City. The refractive index for these particles (>1.5) was found to be higher than typical particle classes observed in both cities. Other

spherical organic particle types were found to peak at night, and produced fewer negative ion mass spectra. We have attributed this to the presence of water and other secondary species.

The behavior of aqueous sea salt particles in the inlet region of the ATOFMS was measured. It was found that the values for refractive index and density for the aqueous particles agreed well with the properties predicted by a thermodynamic model and Mie theory. This suggests that the nozzle-type inlet used in this study may be useful for investigating the chemical dependant water uptake of real ambient aerosols – an experiment that, to this date, has never been done. Furthermore, these results for aqueous salt particles validate the measurements of refractive index and density made in the field. Overall, these coupled optical and microphysical properties represent a step forward in single particle mass spectrometry measurements.

The method used here is not without its limitations, and we briefly comment on the most important challenges here. First, the use of Mie theory implies that the particles are homogenous spherical particles. However, even the spherical particle types observed in this study may be inhomongeously mixed. Using core-shell modeling, it is noted that the scattering behavior of the entire particle is strongly dependant on the surface composition. Therefore, reporting one value for refractive index of a particle may be an oversimplification, but may reproduce the observed scattering pattern. Second, we assume the refractive index and density to be constant with size in our retrieval algorithm. Based on the fits obtained in this work, it is often seen that there is a systematic difference between the measured and best fit model. Often the effective density decreases with size for small particles or decreases with increasing size for

particles such as dust. The same argument may also hold for refractive index, but may be harder to identify due to the complex dependence on scattered light with refractive index. Third, the time resolution of the current method is low. We estimate that at least 20,000 chemically analyzed particles are needed to successfully estimate refractive index or density or both. To break the particle set up in time decreases our ability to say anything about the microphysical properties of the particles. However, instrumentation is continuing to evolve. Instruments that have higher time resolution, and that can collect scattered light at multiple angles should help push these measurements towards the single particle level. The multiple angle approach would measure more independent variables at once, enabling a refractive index inversion for single particles. Lastly, perhaps the key to reducing the time resolution is to reduce the spread in scattered intensity due to the particles clipping the edge of the Gaussian scattering laser beam. To alleviate this, a wide scattering laser beam with a constant intensity profile would allow each single particle to be counted and used for the analysis approach outlined here. As it stands now, particles that clip the laser beam and give off a low intensity are not used in the analysis.

4.6 Acknowledgements

Chapter 4, in full, is a manuscript to be submitted:

Ryan C. Moffet, Sharon Qin, Thomas Rebotier, Hiroshi Furutani and Kimberly A. Prather: Determining Chemically Segregated Optical and Microphysical Properties of Ambient Aerosols Using Single Particle Mass Spectrometry with Aerodynamic Sizing and Light Scattering, *In Preparation*. The dissertation author was the primary author of this paper.

We would like to thank all members of Dr. Prather's research group at UCSD for their help during the field studies. Rainer Volkamer, Jose Jimenez, Gustavo Sosa, and Luisa Molina helped in many ways during the Mexico City field campaign. We are grateful for funding from NSF (ATM-0511803 and ATM-0528227) and the Molina Center for Energy and the Environment (MCE^2).

4.7 References

Ackerman, A.S., O.B. Toon, D.E. Stevens, A.J. Heymsfield, V. Ramanathan, and E.J. Welton: Reduction of tropical cloudiness by soot, Science, 288 (5468), 1042-1047, 2000.

Bohren, C.F., and D.R. Huffman: Absorption and Scattering of Light by Small Particles, John Wiley and Sons, INC., New York, 1981.

Canagaratna, M.R., J.T. Jayne, J.L. Jimenez, J.D. Allan, M.R. Alfarra, Q. Zhang, T.B. Onasch, F. Drewnick, H. Coe, A. Middlebrook, A. Delia, L.R. Williams, A.M. Trimborn, M.J. Northway, P.F. DeCarlo, C.E. Kolb, P. Davidovits, and D.R. Worsnop: Chemical and microphysical characterization of ambient aerosols with the aerodyne aerosol mass spectrometer, Mass Spectrometry Reviews, 26 (2), 185-222, 2007.

Charlson, R.J., S.E. Schwartz, J.M. Hales, R.D. Cess, J.A. Coakley, J.E. Hansen, and D.J. Hofmann: Climate Forcing by Anthropogenic Aerosols, Science, 255 (5043), 423-430, 1992.

Clegg, S.L., P. Brimblecombe, and A.S. Wexler: Thermodynamic model of the system H+-NH4+-Na+-SO42--NB3--Cl--H2O at 298.15 K, Journal of Physical Chemistry A, 102 (12), 2155-2171, 1998.

Cross, E.S., J.G. Slowik, P. Davidovits, J.D. Allan, D.R. Worsnop, J.T. Jayne, D.K. Lewis, M. Canagaratna, and T.B. Onasch: Laboratory and Ambient Particle Density Determinations using Light Scattering in Conjunction with Aerosol Mass Spectrometry, Aerosol Science and Technology, 41, 343-359, 2007.

Draine, B.T., and P.J. Flatau: Discrete-Dipole Approximation for Scattering Calculations, Journal of the Optical Society of America a-Optics Image Science and Vision, 11 (4), 1491-1499, 1994.

Egan, W.G., and T.W. Hilgeman: Optical Properties of Inhomogenous Materials, Academic Press, New York, 1979.

Flatau, P.J., 2006. Personal Communication

Gard, E., J.E. Mayer, B.D. Morrical, T. Dienes, D.P. Fergenson, and K.A. Prather: Real-time analysis of individual atmospheric aerosol particles: Design and performance of a portable ATOFMS, Analytical Chemistry, 69 (20), 4083-4091, 1997.

Gard, E.E., M.J. Kleeman, D.S. Gross, L.S. Hughes, J.O. Allen, B.D. Morrical, D.P. Fergenson, T. Dienes, M.E. Galli, R.J. Johnson, G.R. Cass, and K.A. Prather: Direct observation of heterogeneous chemistry in the atmosphere, Science, 279 (5354), 1184-1187, 1998.

Geller, M., S. Biswas, and C. Sioutas: Determination of Particle Effective Densty in Urban Environments with a Differential Mobility Analyzer and Aerosol Particle Mass Analyzer, 2006.

Gibson, E.R., P.K. Hudson, and V.H. Grassian: Physicochemical properties of nitrate aerosols: Implications for the atmosphere, Journal of Physical Chemistry A, 110 (42), 11785-11799, 2006.

Hughes, L.S., J.O. Allen, P. Bhave, M.J. Kleeman, G.R. Cass, D.Y. Liu, D.F. Fergenson, B.D. Morrical, and K.A. Prather: Evolution of atmospheric particles along trajectories crossing the Los Angeles basin, Environmental Science & Technology, 34 (15), 3058-3068, 2000.

Hughes, L.S., J.O. Allen, L.G. Salmon, P.R. Mayo, R.J. Johnson, and G.R. Cass: Evolution of nitrogen species air pollutants along trajectories crossing the Los Angeles area, Environmental Science & Technology, 36 (18), 3928-3935, 2002.

IPCC, Climate Change 2007: The Physical Science Basis, Cambridge University Press, 2007.

Jacobson, M.Z.: Strong radiative heating due to the mixing state of black carbon in atmospheric aerosols, Nature, 409 (6821), 695-697, 2001.

Johnson, K.S., B. de Foy, B. Zuberi, L.T. Molina, M.J. Molina, Y. Xie, A. Laskin, and V. Shutthanandan: Aerosol composition and source apportionment in the Mexico City Metropolitan Area with PIXE/PESA/STIM and multivariate analysis, Atmospheric Chemistry and Physics, 6, 4591-4600, 2006a.

Johnson, K.S., R. Gonzalez, L.T. Molina, R.J. Hopkins, A.V. Tivanski, M.K. Gilles, Y. Desyaterik, V. Shutthanandan, J. Wang, Y. Liu, and A. Laskin, Microscopy and Microprobe Studies of Individual Atmospheric Particles Collected During MILAGRO 2006, in *First MILAGRO Science Meeting*, 2006b.

Kreidenweis, S.M., C.J. Walcek, G. Feingold, W.M. Gong, M.Z. Jacobson, C.H. Kim, X.H. Liu, J.E. Penner, A. Nenes, and J.H. Seinfeld: Modification of aerosol mass and size distribution due to aqueous-phase SO2 oxidation in clouds: Comparisons of several models, Journal of Geophysical Research-Atmospheres, 108 (D7), -, 2003.

Li, J., M. Posfai, P.V. Hobbs, and P.R. Buseck: Individual aerosol particles from biomass burning in southern Africa: 2, Compositions and aging of inorganic particles, Journal of Geophysical Research-Atmospheres, 108 (D13), -, 2003.

Liu, D.Y., D. Rutherford, M. Kinsey, and K.A. Prather: Real-time monitoring of pyrotechnically derived aerosol particles in the troposphere, Analytical Chemistry, 69 (10), 1808-1814, 1997.

Mallina, R.V., A.S. Wexler, and M.V. Johnston: Particle Growth in High-Speed Particle Beam Inlets, J. Aerosol Sci., 28 (2), 223-238, 1997.

Mishchenko, M.I., J.W. Hovenier, and L.D. Travis: Light Scattering by Nonspherical Particles: Theory, Measurements and Applications, Academic Press, San Diego, 2000.

Mishchenko, M.I., L.D. Travis, and D.W. Mackowski: T-matrix computations of light scattering by nonspherical particles: A review, Journal of Quantitative Spectroscopy & Radiative Transfer, 55 (5), 535-575, 1996.

Moffet, R.C., B. de Foy, L.T. Molina, M.J. Molina, and K.A. Prather: Measurement of Ambient Aerosols in Northern Mexico City by Single Particle Mass Spectrometry, Atmos. Chem. Phys. Discuss., Accepted, 2007.

Moffet, R.C., and K.A. Prather: Extending ATOFMS measurements to include refractive index and density, Analytical Chemistry, 77 (20), 6535-6541, 2005.

Moffet, R.C., L.G. Shields, J. Bernsten, R.B. Devlin, and K.A. Prather: Characterization of an ambient coarse particle concentrator used for human exposure studies: Aerosol size distributions, chemical composition, and concentration enrichment, Aerosol Science and Technology, 38 (11), 1123-1137, 2004.

Murphy, D.M.: The design of single particle laser mass spectrometers, Mass Spectrometry Reviews, 26 (2), 150-165, 2007.

Murphy, D.M., J.R. Anderson, P.K. Quinn, L.M. McInnes, F.J. Brechtel, S.M. Kreidenweis, A.M. Middlebrook, M. Posfai, D.S. Thomson, and P.R. Buseck: Influence of sea-salt on aerosol radiative properties in the Southern Ocean marine boundary layer, Nature, 392 (6671), 62-65, 1998.

Murphy, D.M., D.J. Cziczo, P.K. Hudson, M.E. Schein, and D.S. Thomson: Particle density inferred from simultaneous optical and aerodynamic diameters sorted by composition, Journal of Aerosol Science, 35 (1), 135-139, 2004.

Qin, X.Y., P.V. Bhave, and K.A. Prather: Comparison of two methods for obtaining quantitative mass concentrations from aerosol time-of-flight mass spectrometry measurements, Analytical Chemistry, 78 (17), 6169-6178, 2006.

Ramanathan, V., P.J. Crutzen, J.T. Kiehl, and D. Rosenfeld: Atmosphere - Aerosols, climate, and the hydrological cycle, Science, 294 (5549), 2119-2124, 2001.

Sardar, S.B., P.M. Fine, and C. Sioutas: Seasonal and spatial variability of the size-resolved chemical composition of particulate matter (PM10) in the Los Angeles Basin, Journal of Geophysical Research-Atmospheres, 110 (D7), -, 2005.

Song, X.H., P.K. Hopke, D.P. Fergenson, and K.A. Prather: Classification of single particles analyzed by ATOFMS using an artificial neural network, ART-2A, Analytical Chemistry, 71 (4), 860-865, 1999.

Spencer, M.T., L.G. Shields, and K.A. Prather: Simultaneous measurement of the effective density and chemical composition of ambient aerosol particles, Environmental Science & Technology, 41 (4), 1303-1309, 2007.

Tegen, I., A.A. Lacis, and I. Fung: The influence on climate forcing of mineral aerosols from disturbed soils, Nature, 380 (6573), 419-422, 1996.

Wexler, A.S., and S.L. Clegg: Atmospheric aerosol models for systems including the ions H+, NH4+, Na+, SO42-, NO3-,Cl-, Br-, and H2O, Journal of Geophysical Research-Atmospheres, 107 (D14), -, 2002.

Zelenyuk, A., D. Imre, and L.A. Cuadra-Rodriguez: Evaporation of water from particles in the aerodynamic lens inlet: An experimental study, Analytical Chemistry, 78 (19), 6942-6947, 2006.

5

Coupled Optical and Chemical Measurements of Single Elemental Carbon Particles in the Ambient Atmosphere

5.1 Synopsis

Elemental carbon (EC) or soot particles represent one of the largest sources of uncertainty with respect to climate forcing by aerosols. Current measurements have been unable to accurately represent EC optical and microphysical properties in the ambient atmosphere. Such measurements are crucial for accurate model descriptions of EC particles. Recently, optical measurements have been coupled to simultaneous measurements of the size and chemical composition in single particle mass spectrometers. This new method has allows for the determination of the optical and microphysical properties for particles sorted by chemical composition. Using this new measurement technique, in data from two urban locations, we have identified a subclass of EC particles that scatter light in a manner suggesting they are spherical or coated spherical particles. Over 90% of the spherical-type soot particles are mixed with soluble ions (nitrate, sulfate, ammonium, K, and Na). For these spherical EC particles, we can determine a coating refractive index as well as an estimated shell thickness. We estimate that these particles have core sizes below 300 nm, while the overall particle size can be well over 1 μm. Water and secondary species including nitrate, sulfate, and ammonium make up the size difference. In urban locations, it is estimated that most of the EC particles are non spherical, but with the majority of these particles being internally mixed

with non absorbing species. These results show that the well-known coated spheres single particle scattering model can be used for aged particles. However, for non spherical particles, which are predominant in urban areas, the coated spheres model should be validated against a single particle scattering model, such as the discrete dipole approximation, that accounts for the true physical morphology and mixing state as indicated here. This represents an important first step in that the mixing state and associated properties as a function of size are being directly measured. The next step will involve using these *in situ* measurements to constrain model parameters (e.g. single scattering albedo) used to calculate forcing by these complex EC particles.

5.2 Introduction

Soot or Elemental Carbon (EC) particles are *the* major class of strongly absorbing aerosols at visible wavelengths, near the peak of the solar spectrum at about 500 nm. This means that these microscopic (0.03 – 2 μm) particles can warm the earth directly by absorbing the sun's incoming energy at these atmospherically relevant wavelengths. Indirectly, soot may change cloud properties by heating the atmosphere or by serving as a nucleus for forming cloud drops, thereby changing natural cloud properties, which, in turn, affects how sunlight interacts with the Earth's atmosphere [*Ramanathan et al.*, 2005; *Ramanathan et al.*, 2001; *Twohy et al.*, 1989; *Twomey*, 1974]. Not surprisingly, soot's importance to climate change has been heavily studied [*Ackerman and Toon*, 1981; *Bond and Bergstrom*, 2006; *Haywood et al.*, 1997; *Haywood and Shine*, 1995; *Jacobson*, 2001; *Menon et al.*, 2002]. Some studies have even indicated that depending on the optical properties of soot, it may have a global warming potential second only to CO_2

[*Jacobson*, 2000; *Sato et al.*, 2003]. However, large uncertainties still exist due to difficulties in obtaining accurate measurements of how these particles interact with solar radiation. This directly limits our ability to model the effect that soot has on the climate and make policy decisions as a result of these models [*Bond and Sun*, 2005].

It turns out that the optical properties of soot are very sensitive to how the EC particle is mixed with other constituents such as condensed organic carbon, sulfate, nitrate and water. In fact, having the strongly absorbing soot particle surrounded by a non-absorbing shell of non absorbing material is known to enhance its absorption [*Ackerman and Toon*, 1981; *Fuller et al.*, 1999; *Mikhailov et al.*, 2006; *Schnaiter et al.*, 2005]. Many authors have suggested that the use of a single particle optical model of an absorbing spherical core surrounded by a mantle of absorbing material represents an appropriate model for aged aerosol [*Bond et al.*, 2006; *Bond and Sun*, 2005; *Jacobson*, 2000]. In these cases, the use of the core-shell model was well rationalized in the case of aged aerosols. However, for fresh aerosol, Mie type codes may be unreliable for accurately predicting the optical properties of highly fractal and nonspherical EC [*Bond and Bergstrom*, 2006; *Fuller et al.*, 1999; *Sorensen*, 2001]. To date, there does not appear to be any global modeling studies that calculate soot optical properties with these ageing constraints on optical calculations included.

Capturing how the changing chemical properties of soot as it undergoes aging alter the optical properties for a given mixing state is not possible to measure with current techniques. The most detailed ambient measurements of soot chemical composition and morphology have been obtained with electron microscopy techniques [*Johnson et al.*, 2005; *Katrinak et al.*, 1992; *Katrinak et al.*, 1993; *Posfai et al.*, 1999; *Posfai et al.*, 2003;

van Poppel et al., 2005]. It was some of these measurements which inspired others to model soot as an internal mixture using core-shell morphologies. The drawback to microscopy techniques is that they are done offline and in a vacuum. Thus, particles seen under the microscope may not be representative of those in the ambient atmosphere especially with respect to water content and semivolatile organic carbon species. Microscopy can also be very time consuming and therefore it is difficult to get a large statistical sample with these techniques. Furthermore, electron microscopy can provide unique insights into soot mixing state but it cannot be used to probe the optical properties as a function of size as done in this paper. Herein, we use a single particle mass spectrometry to measure how the optical properties change as a function of chemical mixing state and size of individual EC aerosol particles [*Gross et al.*, 2000; *Lee et al.*, 2002; *Toner et al.*, 2006]. Recently, optical measurement capabilities have been integrated into single particle mass spectrometers by simply measuring the intensity of scattered light as it passes through each sizing laser [*Moffet and Prather*, 2005; *Murphy et al.*, 2004]. A semi-quantitative picture of the relative amounts of different chemical constituents within the single particles can be obtained from these measurements.

In this current work, we utilize this new technique to present in situ measurements of EC chemical composition, morphology, optical properties, and size for two different geographical locations: Riverside, CA, and Mexico City, Mexico. The measurements presented here are able to determine the fraction of EC particles that exhibit the core-shell morphology. We comment on the chemical mixing state of these core-shell particles, as well as the mixing state of non-spherical EC particles which are prevalent in urban locations.

5.3 Experimental

In each of the three field campaigns used for this study, an aerosol time-of-flight mass spectrometer (ATOFMS) with a converging nozzle inlet was used. This instrument is similar to the one described in Gard, 1997 [*Gard et al.*, 1997]. Measurements in Riverside, California were carried out as part of the Study of Organic Aerosols in Riverside II (SOARII) campaign. Sampling took place from October 27 to November 21, 2005. The measurements were located in the laboratory of Dr. Paul Ziemann at UC Riverside (33º58'18.16N, 117º19'21.44W). Measurements in Mexico City took place from March 7 to 31, 2006 as part of the Megacity Initiative: Local and Global Research Operations (MILAGRO) campaign. The measurement site was located in the northern part of Mexico City (19º29'23.22N, 99º08'55.76W). Sampling details for each study may be found elsewhere [*Moffet et al.*, 2007; *Qin et al.*, 2007]. For each study, particle cluster analysis was carried out using the ART-2a algorithm [*Song et al.*, 1999]. ART-2a was run with a vigilance factor of and regrouped with a vigilance factor of 0.85. EC clusters were isolated (Sec 5.4.1) and light scattering analysis was performed on these chemically segregated clusters.

The scattering data analysis procedure is similar to that outlined in Moffet, 2005, but has been refined; the pertinent differences are detailed here. A linear calibration curve was obtained by taking the upper limit of raw scattering response from the PMT (R_{raw}) for several sizes of standard polystyrene sphere particles. R_{raw} was then fit to the partial scattering cross section (R) predicted by Mie theory. It is crucial that the calibration be

done using the upper limit of scattering when analyzing ambient data. This is because non-spherical particles tend to clip the laser beam due to large particle beam divergence, giving a lower scattered intensity while only a few particles travel through the center. If the simple average of the data was taken, a lower intensity would erroneously be interpreted as an optical property of the ambient aerosol when fitting to a theoretical model. The method of taking the upper limit involves an implementation of an algorithm similar to edge detection algorithms used in image processing. It starts by breaking the scattering data up into aerodynamic size bins of 20 nm. Then, for the 100 most intense scatters, the intensities are sorted, and a monotonic regression is done using the difference of sorted intensities. An empirical threshold for finding the upper limit is set using the parameters from the monotonic regression. The method has proved to be quite robust when there are outliers above the upper limit of scattering.

5.4 Results and Discussion

The main purpose of this paper is to show the optical a morphological difference of EC particles due to aging. In Sec 5.4.1, it is shown that the mass spectrum of EC particles may be used to classify aged and fresh aerosol. Examining the scattering behavior (Secs 5.4.2 & 5.4.3) confirms that the fresh EC classes have distinctly different optical and morphological properties. By using a coated spheres model to fit the scattering properties of the more aged EC particles, we show that the single scattering albedo of the most spherical particles are strongly dependant on core size (Secs 5.4.4-5.4.5). Lastly, it is shown that spherical and nonspherical EC particles are able to be

separated using a statistical technique (Sec 5.4.6). The smallest, most numerous EC particles (Sec 5.4.7) are found to be nonspherical but still internally mixed, suggesting that a model that accounts for the inhomogeneous mixing and nonsphericity of the particles should be used to calculate optical properties.

5.4.1 EC Mass Spectra and Mixing State

In Riverside and Mexico City there were two distinctly different types of EC particle classes: fresh and aged. Figure 5.1 shows representative aged and fresh EC particle types that were observed in Mexico City. We discriminate between aged and fresh particle types on the basis of the intensity of the carbon cluster peaks ($^{12n}C_n$). When the base carbon cluster peaks are larger than all other peaks in the spectrum, the particle type is called "fresh". After the first part of the name, we indicate other important peaks in order of peak intensity. For example, in Fig 5.1a the cluster Fresh_SO_NO is named so because the carbon cluster peaks are larger than any other in the spectrum, followed by sulfate and nitrate. The labels of fresh and aged are justified by examining the average diurnal temporal profiles shown in Fig 5.1b. The fresh EC particles peak early in the morning when traffic first starts (fresh emission) and the photochemical production of secondary organics and nitrate is not active. The aged EC particle class peaks around noon when photochemistry provides an abundance of secondary species to cause ageing of the particles. Other classes of aged EC are likely to be from biomass burning due to a large ^{39}K signal.

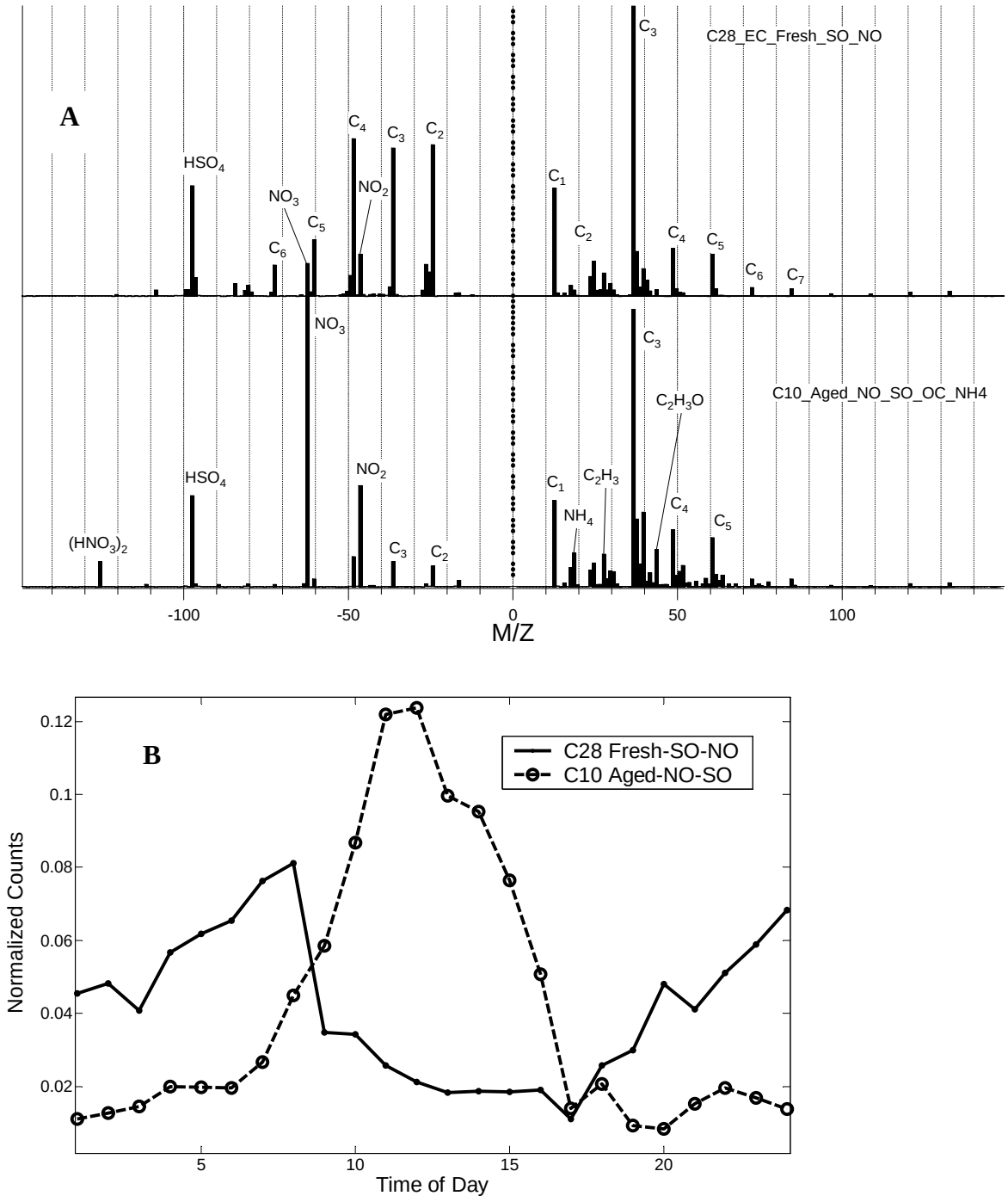

Figure 5.1. A) Examples of fresh and aged EC particles from Mexico City. Internally mixed species are indicated in order of intensity within the name shown on the upper right hand corner of each panel B) Average diurnal temporal profiles of the classes shown in A. The fresh EC type peaks early in the morning and the aged type peaks in the afternoon due to photochemistry.

Aging and matrix effects likely play coupled a role in determining the labels used for the particle types. For instance, whenever a large K signal is seen in the positive spectrum, the positive EC markers are suppressed (add Imre ref for PSLs + matrix). Likewise, whenever large signals for nitrate or sulfate are seen in the negative ion spectrum, the negative EC clusters are suppressed. Since ART-2a performs clustering using the ion intensities, this will determine how we define our clusters. Moreover, it is seen that a significant fraction of the EC particles fail to produce a negative ion spectrum (shown in Table 5.1 as "NoNeg"). We hypothesize that this is due to a large amount of aging, and that the particles likely contain a large amount of water and secondary species (nitrate and sulfate), thereby suppressing the negative ion spectra [*Neubauer et al.*, 1997]. As will be shown in the following section, the EC particles that do not produce negative ions scatter light like spherical particles providing further evidence that they have water and secondary species condensed species on them.

Frequently, secondary species such as $^{46}NO_2^-$, $^{62}NO_3^-$, $^{97}HSO_4^-$, OC, and $^{18}NH_4^+$ are found internally mixed with EC. To give an idea of how many particles are internally mixed with these species, we separated fresh and aged EC ART-2a clusters and then calculated the fraction of these particles that were associated with these secondary markers. Table 5.1 shows the results of this comparison using the data from all three geographical locations. Over 90% of the aged EC particles were associated with nitrate and about 80% of them were associated with OC and sulfate. The majority of the fresh EC particles were also associated with other inorganic species: over 80% having nitrate and the majority of particles having sulfate and OC. It is interesting to note that the fresh EC from Mexico City is coupled with sulfate which suggests the sulfate comes from the

Table 5.1. Summary of fresh and aged particles that are internally mixed with the secondary species indicated in the columns. The fractions are derived from all of the field studies considered in this work.

Study	Class	N	%	NH4	NO_	SO_	C2O4H	C2H3O	Na	K/C3H3
Mexico City	C10 Aged_NO_SO_OC_NH4	25319	38	0.93	1.00	0.84	0.18	0.99	0.38	0.99
	C13 Aged_K_OC_NH4_NoNeg	16504	25	0.29				0.52	0.14	0.97
	C19 Aged_OC_NoNeg	12365	18	0.28				0.54	0.10	0.71
	C26 Aged_K_NO_SO_Na	6976	10	0.42	0.92	0.72	0.38	0.78	0.84	1.00
	C28 Fresh_SO_NO_K_Na	6105	9	0.52	0.92	0.90	0.25	0.93	0.72	0.98
Riverside	C1 Aged_OC_NH4_NO	59573	75	1.0	0.97	0.90	0.1	1.0	0.36	1.0
	C10 Fresh_NO_SO_OC_Na	23056	10	0.34	0.80	0.39	0.02	0.78	0.31	0.70
	C15 Aged_NoNeg	11727	5	0.10				0.34	0.07	0.31
	C16 Aged_NO_OC_K_SO_Na_NH4	11324	5	0.63	0.99	0.44	0.03	0.93	0.34	0.88
	C19 Aged_NO_Na_OC_SO_NH4	9155	4	0.89	1.00	0.84	0.21	0.99	0.59	0.98

sulfur in the fuel. Table 5.1 also shows that Riverside has more "Fresh EC". However, based on aethalometer measurements averaged over each study, Mexico City had higher EC mass concentrations (5.6 $\mu g/m^3$) than Riverside (1.6 $\mu g/m^3$). This might be because the fresh EC in Mexico City was more fractile than in Riverside, and was missed by the ATOFMS due to its strong divergence in the particle beam.

5.4.2 Microphysical Properties of EC in Mexico City

The light scattering measurements in Mexico City show clear differences in how light is scattered as a function of size for the different EC particle types. Figure 5.2 shows the scattering curves for each of the major Mexico City EC particle clusters. The EC particles that are freshly emitted exhibit a scattering pattern that is strikingly different from the scattering behavior of the other EC clusters. The aged EC particles exhibit a well defined upper limit to the amount of scattered light, whereas the fresh EC gives a great deal of scattered light at low aerodynamic diameters in addition to a more diffuse pattern overall. The shape of the curve for aged EC is predicted theoretically for homogenous spheres using Mie theory as shown by the black curve in Fig 5.2. We found that the particle types that fail to produce negative ions (the "NoNeg" type) have a spherical morphology. This strengthens our hypothesis in Sec 5.4.1 that negative ion suppression is caused by the presence of condensed species. Moreover, particles that are rich in K also appear to be spherical and therefore have a mixing state that is linked to this morphology. This is consistent with other studies which found that particles from

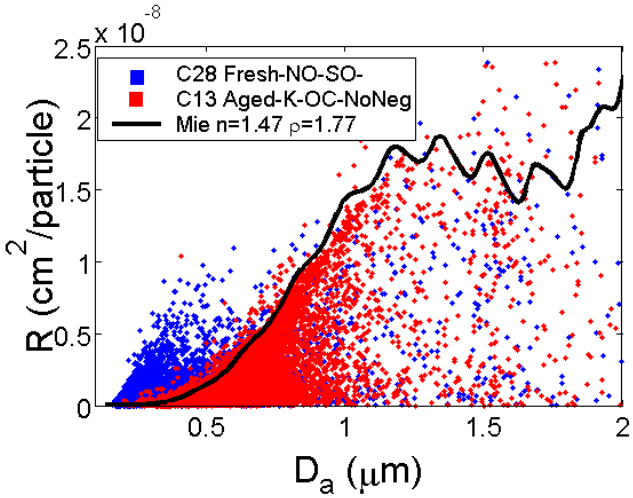

Figure 5.2. EC particle clusters from Mexico City showing the influence of ageing on the light scattering curves. The fresh type of particles have a low effective density as indicated by a large amount of scattered light at small aerodynamic diameters. The more aged particles follow a pattern similar to that obtained for homogenous spheres. The most heavily aged EC particles do not give negative ion mass spectra

biomass burning rich in K, resulting in a particle that is internally mixed with water soluble species and have a compact overall morphology [*Li et al.*, 2003; *Posfai et al.*, 1999; *Posfai et al.*, 2003].

Fresh EC particles scatter more light at smaller aerodynamic sizes because they are highly nonspherical; to understand this behavior, it is useful to examine the relationship between optical (D_o) and aerodynamic diameters (D_a):

$$D_a \propto D_o\sqrt{\frac{\rho}{\chi_d}} = D_o\sqrt{\rho_{eff}} \tag{5.1}$$

The quantity ρ/χ_d is known as the effective density (ρ_{eff}), where ρ is the material density of the particle and χ_d is the shape factor. The shape factor will be greater than one for a nonspherical particle. Now, one can see that if a particle is aerodynamically small compared to its geometric diameter, it is because either its material density is smaller or it has $\chi_d>1$, meaning it is more nonspherical. Both of these effects result in a low effective density. Using the methodology of [Cross et al., 2007], except utilizing a refractive index of m=1.85+0.71i as suggested by Bond (2006) and the upper limit to scattering, we estimate that the effective density of this fresh EC type is $0.7 \leq 0.5$ g/cm^3. This falls in the center of the measured range for diesel soot (~0.4-1 g/cm^3) [*Olfert et al.*, 2007]. Given that fresh EC particles are nonspherical, they will have a lower effective density than an EC particle with a compact, more spherical morphology. For the two more aged EC types (C13 and C28 in Fig 5.2), the scattering curve is best fit to Mie theory using a refractive index of m=1.47 and ρ_{eff}=1.8 g/cm^3 as shown in Fig 5.2. This represents the limiting case of a small EC core and results in this being an upper limit to the effective density. This will be discussed further in Sec 5.4.5. If we assume that the fresh EC particles have the

same material density as the aged EC particles, we can estimate that the fresh EC particles have a shape factor of ~2.5. This falls within the range predicted and measured for fractal soot particles (~2.2-5.8) [*Colbeck*, 1990; *McMurry et al.*, 2002; *Spencer et al.*, 2007].

At this point, it is important to discuss whether or not the retrieved density of 1.8 g/cm^3 as an upper limit for the aged particles is consistent with previous studies. Bond, 2006 recommends using 1.7-1.9 g/cm^3 for pure soot. As described in Sec 5.4.1, EC is mixed with a variety of inorganic cations and anions. Considering the range of possibilities given the mass spectra in Sec 5.4.1, the densities of these inorganic compounds range from 1.46 for $Na_2SO_4 \cdot 10H_2O$ to 2.66 g/cm^3 for K_2SO_4. Atmospheric chemists usually assume that the most likely form of nitrate and sulfate are their ammonium salts with densities of 1.73 and 1.77g/cm^3 respectively. These being the possibilities for ionic compositions, there is not enough water to drastically change the density of the particles with the smallest cores since the density of water is 1 g/cm^3. The fact that there is not a large amount of water associated with the particles is consistent with the frequently low relative humidity experienced in Mexico City. Furthermore, many of the aged soot particles in Mexico City (e.g. C10, Fig 5.1) peaked when RH was near its lowest value.

5.4.3 Microphysical Properties of EC Particles in Riverside, California

The dependence of scattering on D_a for Riverside was significantly different than was observed for Mexico City. Figure 5.3 shows scattering as a function of D_a for fresh

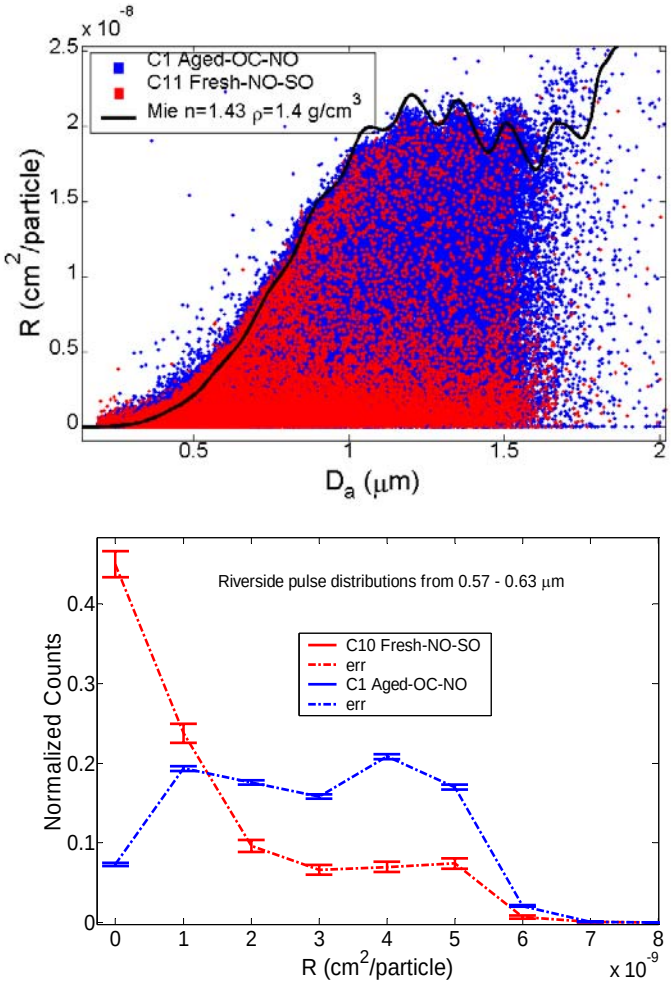

Figure 5.3. Light scattering obtained from Riverside, CA showing the difference between fresh and aged EC particles. Most of the fresh EC particles appear to be clipping the laser beam as demonstrated by the fact that more particles exhibit a low scattered intensities. Similar to Mexico City, the most strongly scattering fresh EC particles have more intensity at small sizes than do the aged particles, also indicating nonsphericity. The blue curve is shifted farther to the left compared to the aged Mexico City particles due to a lower effective density.

and aged EC types measured for Riverside. For the aged type, the scattering curve indicates that the particles are spherical as indicated by the characteristic ripple structure that is predicted by Mie theory. For the fresh EC type, there a high number of scatter signals below the well defined upper limit. This is better illustrated by examining the pulse distribution for a fixed size range, shown in the right hand panel in Fig 5.3, where it is seen that the fresh EC particles have many more scatters at low intensity. This can be attributed to the fact that the nonspherical particles will have a greater divergence in the particle beam than the spherical particles due to lift forces perpendicular to the particle bean axis [*Huffman et al.*, 2005]. The result is that they end up clipping the scattering laser beam, producing less scattered light from the less intense edges of the Gaussian laser beam. It is unlikely that this is a laser alignment issue because the pulse distributions of the ECOC class match well with PSL particles, indicating that the ECOC particles are mostly spherical. This is examined later in Sec 5.4.7, where a description of non-spherical particles is given for each geographical location using a statistical comparison to spherical PSL particles.

We found that the density for the large ECOC particles, and the spherical fresh EC particles fit best to theory using ρ_{eff}=1.4 g/cm^3. Again, since this is the limiting case of small core size, this represents an upper limit to effective density. In order to obtain these fits, particle sizes up to 2 μm were considered, and it was noted that at small sizes, there were frequently data points that exceeded the theoretical fits. This implies that there is a size dependence to ρ_{eff}: small sizes have more particles with lower effective densities, while larger sizes have a higher effective densities. Others have found that the effective density of EC emitted from diesel engines decreases with mobility diameters from 50 –

220 nm in size [*Park et al.*, 2004]. This behavior is not observed here, and is most likely because the particles analyzed here were from 0.150 – 2 μm in aerodynamic diameter: an entirely different size range. The size dependence observed here is most likely due to the more compact structure of the particles as size increases. The size dependence and absolute value of effective densities is in agreement with studies done by our group in Riverside using a differential mobility analyzer coupled to an ultrafine ATOFMS [*Spencer et al.*, 2007]. In that study, effective densities as low as 0.27g/cm^3 were found for EC particles in the 120 nm bin, and as high as ~1 g/cm^3 for 450 nm OC particles during the same time period. It should be noted that these measurements were done during a Santa Ana event, which brings extremely low RH to southern California. Spencer et al found that the density of the aerosol ranged from 1.0-1.5 g/cm^3 during summer time in Riverside. The measurements shown here include both the Santa Ana event, as well as the period with higher RH conditions preceding the event.

From the above analysis, it should be emphasized that the effective density of the spherical EC particles in Riverside is much lower than it is for Mexico City (1.4 and 1.8 g/cm^3, respectively). The lower density for the spherical EC particles in Riverside helps to explain why there was such a visible discrepancy between fresh and aged EC in Mexico City, but not in Riverside. Because the spherical EC particles in Riverside have a lower effective density than the spherical EC particles in Mexico City, the scattering data are shifted to smaller D_a, causing more overlap with the fresh EC. Nevertheless, it is apparent that the fresh EC in Mexico City was more abundant at smaller sizes, resulting in more scattered light at these smaller sizes. This is probably due to atmospheric aging and water uptake. Mexico City was strongly influenced by continually changing emission

sources and strong winds that did not allow for a large buildup of pollution over a period of more than one day; rather, air was transported out of the basin each day [*Fast et al.*, 2007]. In contrast, the Riverside was conducted in the Fall and experienced large "buildup" episodes where the aerosol stagnated for several days allowing for the condensation and coagulation of many different particle types. Spencer et al. noticed that the effective density of the particles in Riverside was dependent on atmospheric water content, and therefore it is likely that water accounts for the lower effective density in Riverside. Another possibility is that there is a greater abundance of low density secondary organic species associated with the soot particles in Riverside.

5.4.4 Single Particle Optical Properties: Estimation of Core-Shell ratio

In order to gain information on the optical properties of the spherical soot particles, we use a new data processing method together with the coated spheres codes available in Borhen and Huffman [*Bohren and Huffman*, 1981]. The data processing method, described in Sec 5.3, serves to trace the upper limit of the raw scattering data using an edge detection algorithm. In so doing, we are selecting only the particles that scatter at the upper limit of the curve, which in this case, corresponds to the spherical EC particle types. Another benefit of doing this is that it takes away the complications of particles clipping the beam.

Once the data have been processed, they were fit to refractive index and density values assuming a core size of zero. Then, curves of varying core sizes were calculated and overlaid on the raw data to get an idea of the range of possible core sizes. In doing this,

the shell refractive index (m_s) is taken to be the refractive index assuming spherical, homogenous, non-absorbing particles. The resulting plots are shown in Fig 5.4. One behavior that is immediately evident is that as one increases the core size, the steep region of the scattering curve shifts to larger aerodynamic diameters. This shift has the same effect as increasing the effective density. For this reason, the effective densities retrieved for the non-absorbing (zero core diameter) case represent an upper limit to density and a lower limit to core size. In Fig 5.4, it is seen that core sizes from 0-0.3μm fit the raw data well. However, when densities lower than the upper limit densities are used in Fig 5.5, the fit is not as good suggesting that these densities are likely close to the actual values for the compact EC particles. From this analysis, the most spherical EC particles lie in the regime of a small (0-300 nm) EC core surrounded by a large (300-3000 nm) coating. These results clearly show that the scattering pattern can be modeled using the traditional coated spheres calculation and that the assumption of homogenous mixing of EC with a non absorbing species is not followed. Bond (2006a) has demonstrated that this region of large shell surrounded by a small core will lead to the largest amplification of absorption. As Bond (2006a) pointed out, models that capture the ageing dynamics of aerosols (such as the model used in Jacobson (2001)) have begun to capture this behavior in scattering and absorption by coated EC particles. The Mexico City EC particles often did not produce as well a defined upper limit to scattering as the Riverside EC particles due to the predominance of freshly emitted particles in Mexico City. This is easily seen in the raw data shown in Fig 5.4. Although there is a well defined curve that is fit nicely by the coated spheres model, there appears to be another regime possessing an upper limit to scattering at submicron sizes. Using graphical methods, we estimate that these particles

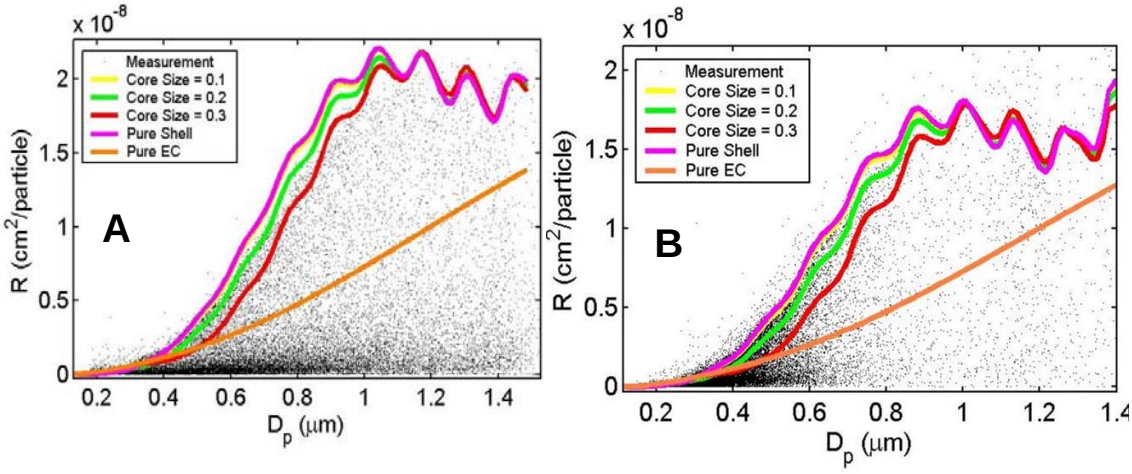

Figure 5.4. Measurements of light scattering by elemental carbon compared with a coated spheres theoretical model. A) Riverside California ms=1.43+0i, ρ=1.4 g/cm3. B) Mexico City, Mexico ms=1.49, ρ=1.8. For all samples mc=1.8+0.71i.

have a lower effective density of ~1.5 g/cm^3. When the scattering curves were isolated as a function of RH, no distinct separation of scattering properties between high and low RH episodes was seen. Thus it is likely that the different densities correspond to different chemical compositions other than water. This phenomenon was seen more clearly in other particle types (biomass and OC) in Mexico City and will be covered in a forthcoming paper.

5.4.5 Single Scattering Albedo (SSA) of Coated EC Particles

The single scattering albedo (SSA) is a key parameter used in models that describes the fraction of the incident light that is scattered. How the SSA varies as a function of size for EC depends strongly on how the aerosol is mixed. Models that assume external mixing of EC and sulfate will demonstrate a much different size dependence of SSA. Drawing on the analysis in the previous section, if one assumes a core shell morphology for the EC particles, SSA is predicted to vary strongly with size as shown in Fig 5.5. Notice that the point at which the shell takes on a coating, the SSA increases rapidly. Therefore, the SSA is very sensitive to the coating thickness and the core size. Figure 5.5 also shows that the size dependence of SSA is weakly dependent on the refractive index of the shell. For the Mexico City EC aerosol, the refractive index was 1.49 and in Riverside it was 1.43. The difference between the two results in a very small difference in SSA. This result is corroborated by Bond (2006a) who states that for particles with a thick coating, the scattering depends weakly on shell thickness, but the absorption depends strongly on core size.

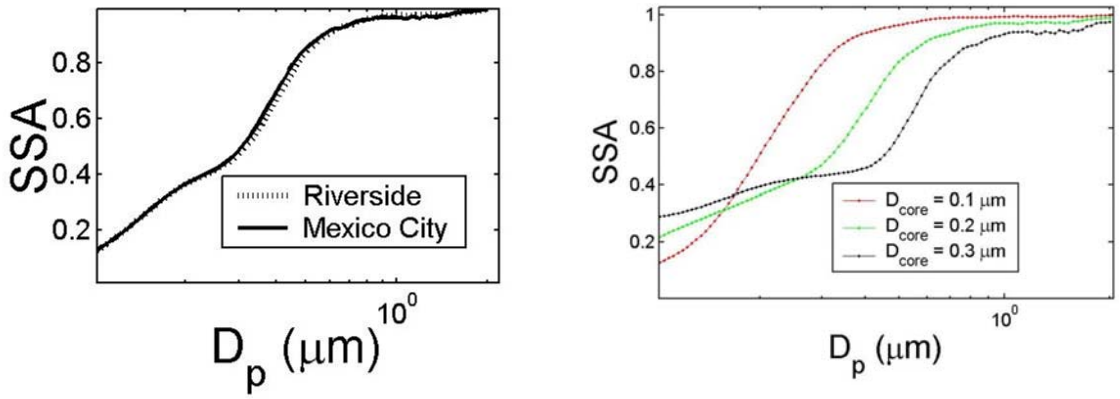

Figure 5.5. Single Scattering Albedo (SSA) for spherical EC particles derived using a core-shell model. SSA is weakly dependant on shell refractive index as demonstrated in the left hand panel, but is strongly dependent on core size.

For nonspherical EC particles, it is difficult to determine optical properties, and therefore SSA. From Figs 5.2-5.4, it is apparent that there are a significant portion of particles that scatter light at low intensities. This may be either due to particle nonsphericity or because the optical properties are different from the EC particles that scatter light at the upper limit. For the current measurements, we cannot tell whether or not a particle scatters less light because it is absorbing more, or because it is clipping the beam. For this reason, we are only able to retrieve optical properties for the particles that have well defined scattering curves at the upper limit of scattered light. However, from the mass spectrometer measurements, it is apparent that EC is almost always mixed with sulfate, nitrate, or both (Table 5.1). Therefore, it is likely that most of the smallest non-spherical EC particles measured here with aerodynamic sizes of 180-600 nm have at least a thin coating of secondary species on them.

5.4.6 Nonspherical Particle Classification

As noted in previous sections, it is evident that a substantial portion of the EC particles in the urban areas are nonspherical. It has been shown here and noted in previous studies that nonspherical particles will exhibit a greater beam divergence and therefore give a wider distribution of scattered light [*Huffman et al.*, 2005; *Murphy*, 2007; *Salcedo et al.*, 2007]. Many previous studies have suggested that the beam width can be used as a shape measurement. Here, we utilize the scattered pulse distribution, instead of beam width, to identify the nonspherical particles.

In Fig 5.6, we show the pulse distributions obtained with spherical PSL particles and ambient EC particles from Riverside that had the same range of D_a. It was noticed

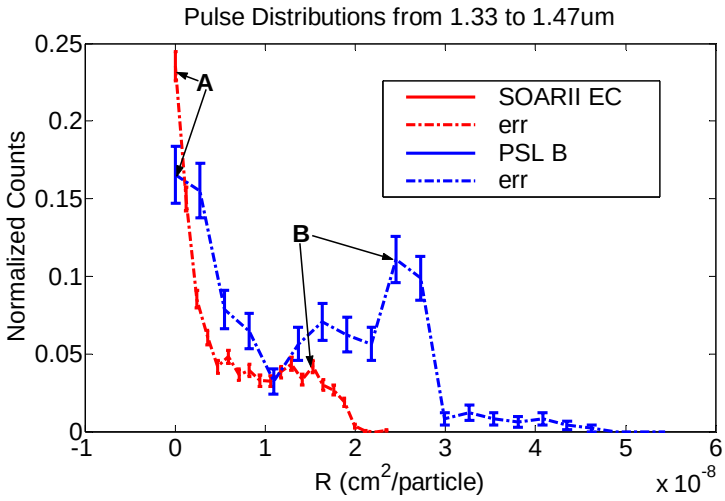

Figure 5.6. Pulse distributions for spherical PSL particles and ambient EC particles from Riverside, CA. More of the EC particles give lower intensities, suggesting they are clipping the laser beam. Peak B represents the upper limit to scattered intensity. The ratio of peak A and B can be used to derive sphericity information as described in Sec 5.4.6.

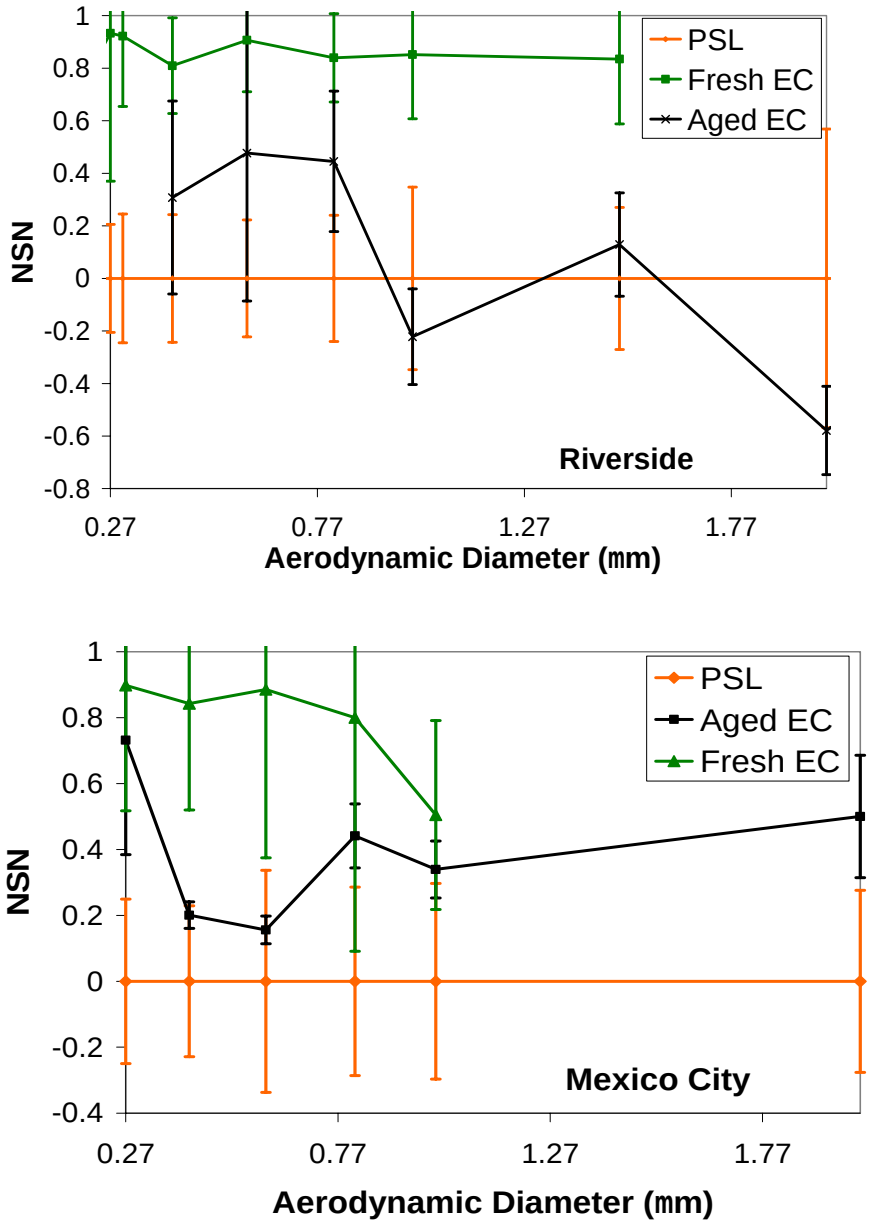

Figure 5.7. Nonsphericity Number (NSN) derived for the different EC particle types in a) Mexico City b) Riverside, CA. A NSN of 0 indicates that the particles behave areodynamically similar to polystyrene spheres. The fresh EC particles are mainly non-spherical.

that the peak A (labeled in Fig 5.6) would become larger compared to peak B for nonspherical particles. For non-spherical particles, peak A is larger because more of the particles clip the beam due to their high degree of divergence compared to spheres. This phenomenon can be used to judge the degree of non-sphericity of a particle class. To this end, we define a "nonsphericity number", NSN, as:

$$\mathbf{NSN} = 1 - \frac{(\mathbf{N_{PA}} / \mathbf{N_{PB}})}{(\mathbf{N_A} / \mathbf{N_B})} \tag{5.2}$$

Where N_{PA} and N_A represent the normalized counts of PSL and sample for peak A and so on for peak B. NSN will approach 0 if the sample pulse distribution matches the sphere's and 1 if it is drastically different.

To test ambient EC particles for sphericity, we calculate the NSN for PSL spheres and ambient EC particles and compare them in Fig 5.7. We see that the aged EC particles are not significantly different than spheres (NSN<0.3). This is inline with the hypothesis that they are aged and have a great deal of condensed species and water on them. Fresh EC particles from both Riverside and Mexico City are significantly different from spheres, as they have the highest NSN in both cases. For both Riverside, the Aged_NoNeg (the most abundant) type appeared to be spherical whereas the all of the other EC types were nonspherical. For Mexico City, most of the EC types shown in Fig 5.7 were nonspherical (NSN>0.3), except in a few cases where the data (including errorbars) overlap the spherical data.

5.4.7 Scaled EC Size Distributions

In the ambient atmosphere, it is important to keep in mind that the optical properties of single particle types are weighted by the size distribution. Therefore,

knowledge of the size distribution is essential for fully interpreting the optical properties of EC particles. To derive size distributions for the single particle types described herein, we have scaled the ATOFMS counts to the measured size SMPS and APS distributions. The resulting size distributions for the representative Mexico City fresh and aged types are shown in Fig 5.8. Not surprisingly, the fresh EC types have the highest concentrations at the smallest sizes sizes. Because of the ATOFMS detection limit (~200nm), the full distribution of fresh EC cannot be obtained, but the ATOFMS captures the upper tail-end of the distribution. Although the ATOFMS does not detect particles below ~200 nm, it does capture particles in the middle of the accumulation mode – a region where the optical cross sections are much larger. Comparing the Mexico City size distribution to the BC size distribution given in Baumgardner et al [*Baumgardner et al.*, 2007], we see that the sizes for the fresh EC particles are roughly equivalent. It is important to keep in mind that the distributions are shown in terms of D_a, and that the sizes will be larger for the Milagro fresh EC because they have lower effective densities. For Riverside, previous studies have indicated that there is more EC mass above 180 nm (D_a) [*Sardar et al.*, 2005], indicating that we have captured the greater part of the EC size distribution in this study. In accord with the results shown here, it should be stressed that the sizes of the EC particle cores is smaller than is indicated in Fig 5.8, because the total size represents the sum of the EC particle plus any secondary material. In terms of the overall optical properties of the EC particles, sizes above 100 nm will scatter and absorb more light, and therefore, have more of an impact on optical properties. Below this size limit, scattering and absorption coefficients are seen to decrease dramatically.

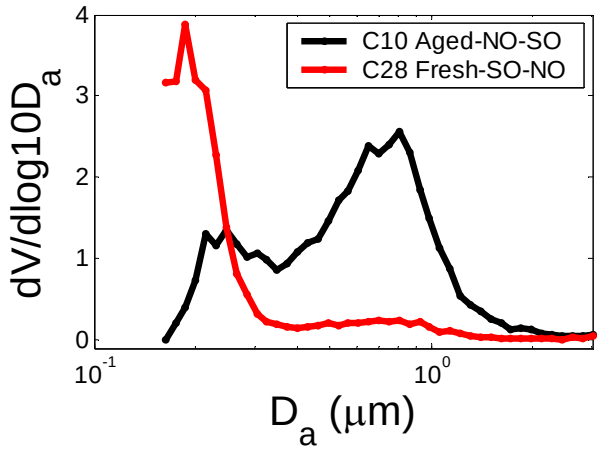

Figure 5.8. Scaled size distributions obtained with the ATOFMS. For Mexico City. The fresh EC particles are much smaller than the aged particles.

5.5 Conclusions

For the two distinct urban environments of Riverside, CA and Mexico City, we have analyzed EC particles to gain information on their chemical mixing state, optical properties, size and morphology. For both locations, a fraction of the EC particles scatter light like coated spherical particles. For aged EC particles, using a statistical analysis, it is shown that all of the EC particles were morphologically similar to spheres. This scattering pattern can be fit using the widely used coated spheres model using core sizes between 0-0.3 μm. This indicates that for sizes larger than 500 nm, the coating thickness is usually much larger than the core. These particles were found to be more strongly associated with secondary species indicating that aged EC particles scatter light like spheres in accordance with the coated spheres model of light scattering.

In both Mexico City and Riverside, CA, it was found that there is a significant fraction of the particles that are nonspherical. These nonspherical particles are still found to be internally mixed with secondary species. Given that these particles are nonspherical and likely coated with non-absorbing secondary species, the coated spheres approximation should be validated against a coated, non-spherical model. For both Mexico City and Riverside, the fresh, nonspherical EC particles usually peaked early in the morning with the start of rush hour. As the day progressed, more of the spherical-type EC classes peaked. This suggests that the optical and microphysical characteristics of the EC/soot particles will change significantly within the period of one day and this needs to be taken into account in models.

5.6 Acknowledgements

Chapter 5, in full, is a manuscript to be submitted:

Ryan C. Moffet, Sharon Qin, Thomas Rebotier, and Kimberly A. Prather: Coupled Optical and Chemical Measurements of Single Elemental Carbon Particles in the Ambient Atmosphere , *In Preparation,*. The dissertation author was the primary author of this paper.

We thank all of the people involved the three field studies described here. We regret that there is not enough space to thank each person individually. We appreciate funding from: NSF (ATM-0511803 and ATM-0528227) and the Molina Center for Energy and the Environment (MCE^2).

5.7 References

Ackerman, T.P., and O.B. Toon: Absorption of Visible Radiation in Atmosphere Containing Mixtures of Absorbing and Non-Absorbing Particles, Applied Optics, 20 (20), 3661-3668, 1981.

Baumgardner, D., G.L. Kok, and G.B. Raga: On the Diurnal Variability of Particle Properties Related to Black Carbon in Mexico City, Atmos. Chem. Phys. Diss., 7, 1623-1653, 2007.

Bohren, C.F., and D.R. Huffman: Absorption and Scattering of Light by Small Particles, John Wiley and Sons, INC., New York, 1981.

Bond, T.C., and R.W. Bergstrom: Light absorption by carbonaceous particles: An investigative review, Aerosol Science and Technology, 40 (1), 27-67, 2006.

Bond, T.C., G. Habib, and R.W. Bergstrom: Limitations in the enhancement of visible light absorption due to mixing state, Journal of Geophysical Research-Atmospheres, 111 (D20), -, 2006.

Bond, T.C., and H.L. Sun: Can reducing black carbon emissions counteract global warming? Environmental Science & Technology, 39 (16), 5921-5926, 2005.

Colbeck, I.: Dynamic Shape Factors of Fractal Clusters of Carbonaceous Smoke, Journal of Aerosol Science, 21, S43-S46, 1990.

Cross, E.S., J.G. Slowik, P. Davidovits, J.D. Allan, D.R. Worsnop, J.T. Jayne, D.K. Lewis, M. Canagaratna, and T.B. Onasch: Laboratory and Ambient Particle Density Determinations using Light Scattering in Conjunction with Aerosol Mass Spectrometry, Aerosol Science and Technology, 41, 343-359, 2007.

Fast, J.D., B. De Foy, F. Acevodo Rosas, E. Caetano, G. Carmichael, L. Emmons, D. McKenna, M. Mena, W. Skamarock, X. Tie, R.L. Coulter, J.C. Barnard, C. Wiedinmyer, and S. Madronich: A Meterological Overview of the MILAGRO Field Campaigns, Atmos. Chem. Phys., 7 (2233-2257), 2007.

Fuller, K.A., W.C. Malm, and S.M. Kreidenweis: Effects of mixing on extinction by carbonaceous particles, Journal of Geophysical Research-Atmospheres, 104 (D13), 15941-15954, 1999.

Gard, E., J.E. Mayer, B.D. Morrical, T. Dienes, D.P. Fergenson, and K.A. Prather: Real-time analysis of individual atmospheric aerosol particles: Design and performance of a portable ATOFMS, Analytical Chemistry, 69 (20), 4083-4091, 1997.

Gross, D.S., M.E. Galli, P.J. Silva, S.H. Wood, D.Y. Liu, and K.A. Prather: Single particle characterization of automobile and diesel truck emissions in the Caldecott Tunnel, Aerosol Science and Technology, 32 (2), 152-163, 2000.

Haywood, J.M., D.L. Roberts, A. Slingo, J.M. Edwards, and K.P. Shine: General circulation model calculations of the direct radiative forcing by anthropogenic sulfate and fossil-fuel soot aerosol, Journal of Climate, 10 (7), 1562-1577, 1997.

Haywood, J.M., and K.P. Shine: The Effect of Anthropogenic Sulfate and Soot Aerosol on the Clear-Sky Planetary Radiation Budget, Geophysical Research Letters, 22 (5), 603-606, 1995.

Huffman, J.A., J.T. Jayne, F. Drewnick, A.C. Aiken, T. Onasch, D.R. Worsnop, and J.L. Jimenez: Design, modeling, optimization, and experimental tests of a particle beam width probe for the aerodyne aerosol mass spectrometer, Aerosol Science and Technology, 39 (12), 1143-1163, 2005.

Jacobson, M.Z.: A physically-based treatment of elemental carbon optics: Implications for global direct forcing of aerosols, Geophysical Research Letters, 27 (2), 217-220, 2000.

Jacobson, M.Z.: Strong radiative heating due to the mixing state of black carbon in atmospheric aerosols, Nature, 409 (6821), 695-697, 2001.

Johnson, K.S., B. Zuberi, L.T. Molina, M.J. Molina, M.J. Iedema, J.P. Cowin, D.J. Gaspar, C. Wang, and A. Laskin: Processing of soot in an urban environment:

case study from the Mexico City Metropolitan Area, Atmospheric Chemistry and Physics, 5, 3033-3043, 2005.

Katrinak, K.A., P. Rez, and P.R. Buseck: Structural Variations in Individual Carbonaceous Particles from an Urban Aerosol, Environmental Science & Technology, 26 (10), 1967-1976, 1992.

Katrinak, K.A., P. Rez, P.R. Perkes, and P.R. Buseck: Fractal Geometry of Carbonaceous Aggregates from an Urban Aerosol, Environmental Science & Technology, 27 (3), 539-547, 1993.

Lee, S.H., D.M. Murphy, D.S. Thomson, and A.M. Middlebrook: Chemical components of single particles measured with Particle Analysis by Laser Mass Spectrometry (PALMS) during the Atlanta SuperSite Project: Focus on organic/sulfate, lead, soot, and mineral particles, Journal of Geophysical Research-Atmospheres, 107 (D1-D2), -, 2002.

Li, J., M. Posfai, P.V. Hobbs, and P.R. Buseck: Individual aerosol particles from biomass burning in southern Africa: 2, Compositions and aging of inorganic particles, Journal of Geophysical Research-Atmospheres, 108 (D13), -, 2003.

McMurry, P.H., X. Wang, K. Park, and K. Ehara: The relationship between mass and mobility for atmospheric particles: A new technique for measuring particle density, Aerosol Science and Technology, 36 (2), 227-238, 2002.

Menon, S., J. Hansen, L. Nazarenko, and Y.F. Luo: Climate effects of black carbon aerosols in China and India, Science, 297 (5590), 2250-2253, 2002.

Mikhailov, E.F., S.S. Vlasenko, I.A. Podgorny, V. Ramanathan, and C.E. Corrigan: Optical properties of soot-water drop agglomerates: An experimental study, Journal of Geophysical Research-Atmospheres, 111 (D7), -, 2006.

Moffet, R.C., B. de Foy, L.T. Molina, M.J. Molina, and K.A. Prather: Measurement of Ambient Aerosols in Northern Mexico City by Single Particle Mass Spectrometry, Atmos. Chem. Phys. Diss., 6413-6457, 2007.

Moffet, R.C., and K.A. Prather: Extending ATOFMS measurements to include refractive index and density, Analytical Chemistry, 77 (20), 6535-6541, 2005.

Murphy, D.M.: The design of single particle laser mass spectrometers, Mass Spectrometry Reviews, 26 (2), 150-165, 2007.

Murphy, D.M., D.J. Cziczo, P.K. Hudson, M.E. Schein, and D.S. Thomson: Particle density inferred from simultaneous optical and aerodynamic diameters sorted by composition, Journal of Aerosol Science, 35 (1), 135-139, 2004.

Neubauer, K.R., M.V. Johnston, and A.S. Wexler: On-line analysis of aqueous aerosols by laser desorption ionization, International Journal of Mass Spectrometry and Ion Processes, 163 (1-2), 29-37, 1997.

Olfert, J.S., J.P.R. Symonds, and N. Collings: The effective density and fractal dimension of particles emitted from a light-duty diesel vehicle with a diesel oxidation catalyst, Journal of Aerosol Science, 38 (1), 69-82, 2007.

Park, K., D.B. Kittelson, and P.H. McMurry: Structural properties of diesel exhaust particles measured by transmission electron microscopy (TEM): Relationships to particle mass and mobility, Aerosol Science and Technology, 38 (9), 881-889, 2004.

Posfai, M., J.R. Anderson, P.R. Buseck, and H. Sievering: Soot and sulfate aerosol particles in the remote marine troposphere, Journal of Geophysical Research-Atmospheres, 104 (D17), 21685-21693, 1999.

Posfai, M., R. Simonics, J. Li, P.V. Hobbs, and P.R. Buseck: Individual aerosol particles from biomass burning in southern Africa: 1. Compositions and size distributions of carbonaceous particles, Journal of Geophysical Research-Atmospheres, 108 (D13), -, 2003.

Qin, X., L.G. Shields, S.M. Toner, and K.A. Prather: Single Particle Characterization in Riverside, CA during the SOAR 2005 Campaign - Part 1: Seasonal Comparisons, In preparation, 2007.

Ramanathan, V., C. Chung, D. Kim, T. Bettge, L. Buja, J.T. Kiehl, W.M. Washington, Q. Fu, D.R. Sikka, and M. Wild: Atmospheric brown clouds: Impacts on South Asian climate and hydrological cycle, Proceedings of the National Academy of Sciences of the United States of America, 102 (15), 5326-5333, 2005.

Ramanathan, V., P.J. Crutzen, J.T. Kiehl, and D. Rosenfeld: Atmosphere - Aerosols, climate, and the hydrological cycle, Science, 294 (5549), 2119-2124, 2001.

Salcedo, D., T.B. Onasch, M.R. Canagaratna, K. Dzepina, J.A. Huffman, J.T. Jayne, D.R. Worsnop, C.E. Kolb, S. Weimer, F. Drewnick, J.D. Allan, A.E. Delia, and J.L. Jimenez: Technical Note: Use of a beam width probe in an Aerosol Mass Spectrometer to monitor particle collection efficiency in the field, Atmospheric Chemistry and Physics, 7, 549-556, 2007.

Sardar, S.B., P.M. Fine, P.R. Mayo, and C. Sioutas: Size-fractionated measurements of ambient ultrafine particle chemical composition in Los Angeles using the NanoMOUDI, Environmental Science & Technology, 39 (4), 932-944, 2005.

Sato, M., J. Hansen, D. Koch, A. Lacis, R. Ruedy, O. Dubovik, B. Holben, M. Chin, and T. Novakov: Global atmospheric black carbon inferred from AERONET, Proceedings of the National Academy of Sciences of the United States of America, 100 (11), 6319-6324, 2003.

Schnaiter, M., C. Linke, O. Mohler, K.H. Naumann, H. Saathoff, R. Wagner, U. Schurath, and B. Wehner: Absorption amplification of black carbon internally mixed with secondary organic aerosol, Journal of Geophysical Research-Atmospheres, 110 (D19), -, 2005.

Song, X.H., P.K. Hopke, D.P. Fergenson, and K.A. Prather: Classification of single particles analyzed by ATOFMS using an artificial neural network, ART-2A, Analytical Chemistry, 71 (4), 860-865, 1999.

Sorensen, C.M.: Light scattering by fractal aggregates: A review, Aerosol Science and Technology, 35 (2), 648-687, 2001.

Spencer, M.T., L.G. Shields, and K.A. Prather: Simultaneous measurement of the effective density and chemical composition of ambient aerosol particles, Environmental Science & Technology, 41 (4), 1303-1309, 2007.

Toner, S.M., D.A. Sodeman, and K.A. Prather: Single particle characterization of ultrafine and accumulation mode particles from heavy duty diesel vehicles using aerosol time-of-flight mass spectrometry, Environmental Science & Technology, 40 (12), 3912-3921, 2006.

Twohy, C.H., A.D. Clarke, S.G. Warren, L.F. Radke, and R.J. Charlson: Light-Absorbing Material Extracted from Cloud Droplets and Its Effect on Cloud Albedo, Journal of Geophysical Research-Atmospheres, 94 (D6), 8623-8631, 1989.

Twomey, S.: Pollution and Planetary Albedo, Atmospheric Environment, 8 (12), 1251-1256, 1974.

van Poppel, L.H., H. Friedrich, J. Spinsby, S.H. Chung, J.H. Seinfeld, and P.R. Buseck: Electron tomography of nanoparticle clusters: Implications for atmospheric lifetimes and radiative forcing of soot, Geophysical Research Letters, 32 (24), -, 2005.

6

Characterization of Aerosols Containing Zn, Pb, and Cl from an Industrial Region of Mexico City

6.1 Synopsis

During the MILAGRO campaign which took place during March, 2006, single particle measurements in Northern Mexico City revealed the frequent appearance of particles with a characteristically high content of internally mixed Zn, Pb, Cl and P. This unique mixing state is found to match most closely to source sampling of garbage incineration rather than non-ferrous smelting. This manuscript presents results of a comprehensive study of chemical and physical properties of these particles performed using a complementary combination of aerosol measurement techniques. Individual particles were analyzed using Aerosol Time-of-Flight Mass Spectrometry (ATOFMS) and Computer Controlled Scanning Electron Microscopy/Energy Dispersive X-Ray analysis (CCSEM/EDX). Using a rule based classification method, single particle characteristics from both techniques were found to be in good agreement. Proton Induced X-Ray Emission (PIXE) analysis of bulk aerosol samples provided time-resolved mass concentrations of individual elements. The PIXE measurements indicated that the presence Zn is more strongly correlated with Cl than with any other element (including

Na) and that Zn concentrations are higher than other non-ferrous transition metals. Morphology observations from CCSEM/EDX indicate that these metal containing particles are a mixture of spherical and non-spherical particles. Many metal rich particles had a needle-like structure. Using scanning transmission x-ray microscopy coupled with near edge X-ray absorption spectroscopy (STXM/NEXAFS), we determined that these needle-like particles are composed of ZnO and/or $Zn(NO_3)_2 \cdot 6H_2O$. Given that the Zn rich particles are primarily submircron and that they are internally mixed with elemental carbon, these particles most likely originate from combustion. This unique combination of analytical techniques has allowed for a comprehensive evaluation of metal containing particles in a complex environment, highlighting unique characteristics that give powerful insights into their origin.

6.2 Introduction

It is well established that particulate air pollution increases morbidity and mortality [*Dockery, et al.*, 1993]. Although relatively little is known about the specific chemical constituents responsible for the adverse health effects, metal containing particles are implicated in a number of studies [*Dreher, et al.*, 1997; *Hodgson, et al.*, 2001; *Florea and Busselberg*, 2006]. The solubility of metal ions present in particles affects their mobility in the human body while their oxidation state often greatly affects toxicity [*Dreher, et al.*, 1997; *Hodgson, et al.*, 2001]. Other factors, such as particle size and shape, determine how deep into the respiratory tract the particle will travel. Smaller particles with a compact morphology penetrate deeper into the lungs where they are more likely to remain [*Schwartz, et al.*, 1996; *Broday and Georgopoulos*, 2001; *Londahl, et al.*,

2007]. Anthropogenic particles arising from high temperature processes (e.g. combustion and ore processing) frequently possess all of these properties responsible for negative health effects.

In urban areas, anthropogenic sources of submicron metal containing particles are plentiful. For example, the burning of fossil fuel leads to the association of Ni and V within particles [*Suarez and Ondov*, 2002]. Prior to 2000, tetraethyl lead used as a gasoline additive in many countries, resulted in the formation of submicron lead containing particles. In industrial neighborhoods, high temperature metallurgical processes such as smelting lead particulate emissions that are rich in heavy metals [*Pina, et al.*, 2002]. High temperature combustion of municipal and hazardous waste also produces submicron particles rich in Zn and Pb as well as numerous other metals that may be present in the incinerator exhaust plumes [*Linak and Wendt*, 1993]. Coincidentally, Zn and Pb are often found to be internally mixed in individual particles found in different regions of the globe [*Murphy, et al.*, 2007]. Finally, although predominantly supermicron in size, dust stirred up through anthropogenic activities (such as construction) may also contain metals [*Vega, et al.*, 2001]. Each of these sources emits particles with unique elemental and molecular compositions that can lead to their identification using appropriate analytical techniques.

In this study, particulate matter is characterized using both real time particle measurements and laboratory based analyses of collected aerosol samples. Aerosol Time-of-Flight Mass Spectrometry (ATOFMS) is an online (real time) method for analyzing the size and chemical composition of a statistical number of particles. ATOFMS provides the necessary data for determining broad particles classes and mixing states [*Prather, et*

al., 1996]. Light scattering measurements coupled to the ATOFMS are used to estimate particle morphology, refractive index, and density [*Moffet and Prather*, 2005]. A Davis Rotating drum Universal size-cut Monitoring (DRUM) impactor [*Cahill and Wayakabashi*, 1993] and Time Resolved Aerosol Collector (TRAC) [*Laskin, et al.*, 2006] are used for collecting samples for laboratory analysis. Laboratory analysis provides mass loading data and characterization of non-volatile single particles. The principle techniques for laboratory analyses are (a) Proton-Induced X-ray Emission (PIXE) Spectroscopy, (b) Computer Controlled Scanning Electron Microscopy with Energy Dispersed analysis of X-rays (CCSEM/EDX), (c) Scanning Transmission X-ray Microscopy with Near Edge X-ray Absorption Fine Structure spectroscopy (STXM/NEXAFS). PIXE provides time resolved mass loading of different elements in bulk aerosol samples collected on the 3 stages of the DRUM impactor. Using CCSEM/EDX a statistically significant number of individual particles are analyzed to determine their size, morphology and elemental composition. STXM/NEXAFS provides more detailed information on the oxidation state and the chemical bonding of specific elements present in the particles. Combined, complementary use of these techniques employs each of them to their fullest potential and yields a rich set of qualitative and quantitative information, not otherwise possible.

To identify and quantify potentially harmful submicron metal containing particles in a highly polluted area requires an extensive suite of aerosol measurement and sampling techniques, cooperation between several research groups and coordinated field studies. In last decade, numerous extensive field studies in the Mexico City Metropolitan area (MCMA) have employed a variety of instrumentation to address particulate pollution and

air quality issues [*Molina and Molina*, 2002; *Molina, et al.*, 2007]. Researchers have found the northern part of the city to be heavily polluted, in particular with metal containing particles [*Flores, et al.*, 1999; *Mugica, et al.*, 2002; *Johnson, et al.*, 2006; *Moffet*, 2007; *Moffet, et al.*, 2007]. The research presented here was carried out during the Megacity Initiative: Local and Global Research Observations (MILAGRO) field study held in March 2006 (see *http://mce2.org/*). As part of the MILAGRO study, a sampling site, T0, was chosen in a neighborhood in Northern Mexico City that was impacted by local industrial, automotive, regional and residential emission sources [*Moffet, et al.*, 2007]. The results obtained in this study reveal detailed chemical composition, chemical speciation, size, mixing state (chemical associations) and morphology of individual particles along with quantitative estimations of their mass loadings. Peak PM_{10} of Zn and Pb were 1.4 and 1.14μg/m^3 respectively with the majority of the mass found below 2.5μm. Their peak concentration typically occurred between 12am to 9am, when the wind direction was from the north of MCMA. The spatial and temporal information suggests an industrial source for these particles.

6.3 Experimental

6.3.1 Field Site and Sample Collection

The MILAGRO study was an intensive 4-week campaign in and around Mexico city in March of 2006, with a goal of investigating the chemistry, dispersion and transport processes of pollutants emitted from the world's second largest city. The T0 site was one of the few major ground sites for the campaign, with investigators from approximately a thirty laboratories and universities making a wide range of atmospheric and

environmental measurements. The T0 sampling site was located in the northern part of Mexico City, at the "Instituto Mexicano Del Petroleo" (IMP), at 19º29'23.60 N, 99º08'55.60W, at altitude of 2200 m above sea level (~200 m above the ground). This site is surrounded by mixed industrial and residential areas as well as by city roads with heavy traffic including contributions from a major bus station. In this paper we present results from continuous ambient ATOFMS measurements along with the results of focused laboratory studies of aerosol samples collected at the T0 site.

The DRUM and TRAC devices were deployed at the T0 site to collect aerosol samples during the time of field study. The DRUM impactor collected bulk aerosol samples for PIXE analysis onto three Teflon strips in size ranges of 1.15–2.5μm (Stage A), 0.34–1.15μm (Stage B), and 0.07–0.34μm (Stage C) at a fixed air flow of 10 slpm with a rotation rate of 2mm per 12 h. The TRAC collected aerosol samples for CCSEM/EDX and STXM/NEXAFS analyses of individual particles. Aerosol samples in the size range of 0.36-2.5 μm were deposited on a rotating impaction plate with prearranged thin film TEM grid substrates. Carbon Type-B (Ted Pella, Inc., Redding, California) 50-nm thick films supported by 400-mesh copper mesh grids were used. Each substrate was exposed individually to the impactor nozzle for a preset time of 15 min.

6.3.2 Real-Time ATOFMS Measurements

The ATOFMS used in the MILAGRO study is described elsewhere [*Gard, et al.*, 1997] and operates by pulling aerosol into a vacuum through a nozzle where it undergoes acceleration to a terminal velocity. The velocity is determined by measuring the time required to pass between two 532nm CW lasers. This time is used to trigger a pulsed

laser at the instant when the particle is in the dual polarity mass spectrometer source region. The pulsed laser, operating at 266nm, imparts a 1.2 mJ pulse to desorb and ionize the particle for mass spectrometric analysis. The ATOFMS typically analyzes sizes between 200 – 3000 nm, with the peak transmission occurring at 1700 nm. Raw mass spectra, size, scattered intensity, and temporal information are imported into the MATLAB YAADA database (*http://www.yaada.org/*) where a cluster analysis was performed using the Art2a algorithm with a vigilance factor of 0.80 and learning rate of 0.05 [*Moffet, et al.*, 2007]. A time series (counts binned hourly) of the Zn and Pb containing particles in Figure 6.1 was derived from the Art2a clusters with strong Zn and Pb signals. Further analysis in YAADA was carried out using a peak search method described in Sec 6.4.1. The intensity of light scattered by the particle in the sizing region of the ATOFMS was acquired and processed as described in [*Moffet and Prather*, 2005].

6.3.3 Laboratory Based Analyses of Field-Collected Aerosol Samples.

PIXE analyses of DRUM collected aerosol samples were done within several weeks of the MILAGRO-2006 campaign at the Environmental Molecular Sciences Laboratory (EMSL) at Pacific Northwest National Laboratory (PNNL). Experimental procedures were similar to those reported previously [*Shutthanandan, et al.*, 2002] and only briefly described here. Teflon substrates were carefully removed from the impactor and mounted on a special sample holder inside a vacuum chamber which was maintained at approximately 2×10^{-7} Torr pressure. A 3.5 MeV proton beam was used for PIXE analysis. PIXE spectra were evaluated by the GUPIX program [*Maxwell, et al.*, 1989], and concentrations of elements were determined by calibration to known standards.

Elements were fit by their principal spectral lines except for Pb in which the L line (10.225 eV) was used due to S interference with M line of Pb (K [S]=2.306 eV; M [Pb]=2.342 eV).

Figure 6.1 shows time series of Zn and Pb elemental concentrations obtained from the analysis of the stage B sample. For both elements, the corresponding mass loading on stages A and C were typically 5-10 times lower. As indicated by the figure, elemental concentrations as high as 1600 and 450 ng/m^3 were recorded for Zn and Pb respectively.

CCSEM/EDX particle analysis was also performed at EMSL/PNNL within a few weeks following the campaign. A FEI XL30 digital field emission gun Environmental Scanning Electron Microscope equipped with EDX microanalysis spectrometer (EDAX, Inc.) was used for CCSEM/EDX and SEM/EDX analysis. Specific details on the CCSEM/EDX analysis over particles collected on the filmed grids are published elsewhere (Laskin et al., 2006 and references therein). The elements detected in particles for this work were C, N, O, Na, Mg, Al, Si, P, S, Cl, K, Ca, Ti, Mn, Fe, Ni, Cr, Zn, and Pb. The atomic percent data for the light elements such as C, O and N are considered semiquantitative (Laskin et al., 2006) and therefore are excluded from quantitative analysis. For all other elements, particle composition is reported either in terms of atomic ratios or as normalized atomic percent.

6.3.4 NEXAFS Spectroscopy Using STXM

Single energy images and zinc L-edge NEXAFS spectra were acquired using the STXM instrument on beamline 11.0.2 of the Advanced Light Source (Berkeley, CA) in a ~0.5 atm He-filled chamber. The apparatus and experimental method are described in

detail elsewhere [*Hopkins, et al.*, 2007; *Michelsen, et al.*, 2007; *Tivanski, et al.*, 2007]. Briefly, the x-ray beam is focused with a custom made Fresnel zone plate onto the sample, and the transmitted light is detected. The spatial resolution for these experiments was ~35 nm. Images at a single energy are obtained by raster-scanning the sample and collecting transmitted monochromatic light as a function of sample position. A collection of images at multiple, closely spaced photon energies across the Zn absorption edge is recorded and a spectra at each image pixel is extracted. Dwell times used to acquire a single image at a single photon energy are typically 1 ms per pixel. Spectra are obtained by averaging over the particle deposited on the substrate. Particles with an absorption of >1.5 OD were omitted to ensure the spectra were in the linear regime of Beer-Lambert's law. The x-ray energy calibration (accuracy of 0.1 eV) is afforded by addition of CO_2 gas (~6 torr) to the STXM chamber through comparison of the position of CO_2 Rydberg transitions at 292.74 and 294.96 eV [*Ma, et al.*, 1991].

Standard zinc oxide (ZnO), zinc sulfide (ZnS), zinc nitrate hexahydrate ($Zn(NO_3)_2 \bullet 6H_2O$), zinc chloride ($ZnCl_2$) powders and a 0.05 M solution of zinc sulfate ($ZnSO_4$) in water were purchased from Sigma-Aldrich Corp., St. Louis, MO, USA. The purity of standard reference materials was higher than 95%. Thin coatings of the standards were deposited directly onto Si_3N_4 windows by applying gentle contact between the crushed fine powder sample and the Si_3N_4 window and subsequently removing any loose sample. The $ZnSO_4$ solution sample is prepared by placing a small drop on a Si_3N_4 window and then allowing it to evaporate leaving a crystalline residue.

6.4 Results

Historically, higher concentrations of particulates containing Zn and Pb have been observed in the northern part Mexico City than in the south and it is this region we report on here. According to the time series derived from ATOFMS and PIXE data shown in Figure 6.1, temporal spikes of Zn and Pb containing particles were typical throughout the MILAGRO campaign. Table 6.1 shows the average, maximum and minimum concentrations for Zn and Pb in the PM_{10} and $PM_{2.5}$ size ranges determined with the high volume filters. The temporal spikes of Pb and Zn particles usually occurred between the night and early morning (12am – 10am local time). Air mass backtrajectories indicate that during these periods the air mass originated from the industrial area of the city, north of the sampling site. In the past, the source of the high Zn and/or Pb concentration has be was attributed to industry (Flores, 1999; Mugica, 2002; Johnson 2006). This is supported by the low concentrations of these particles measured during the holiday weekend of March 18-21 as shown in Fig 6.1.

On March 24, 5:15-5:30 CST the ATOFMS instrument at T0 measured a peak in the percentage of particles containing Zn and Pb and is indicated in Fig 6.1. This event where the peak in Zn and Pb particles occurred followed a heavy rainfall that significantly decreased the background aerosol concentration, thus providing an excellent opportunity to study the Zn and Pb-rich particles with reduced interference from other aerosol classes.

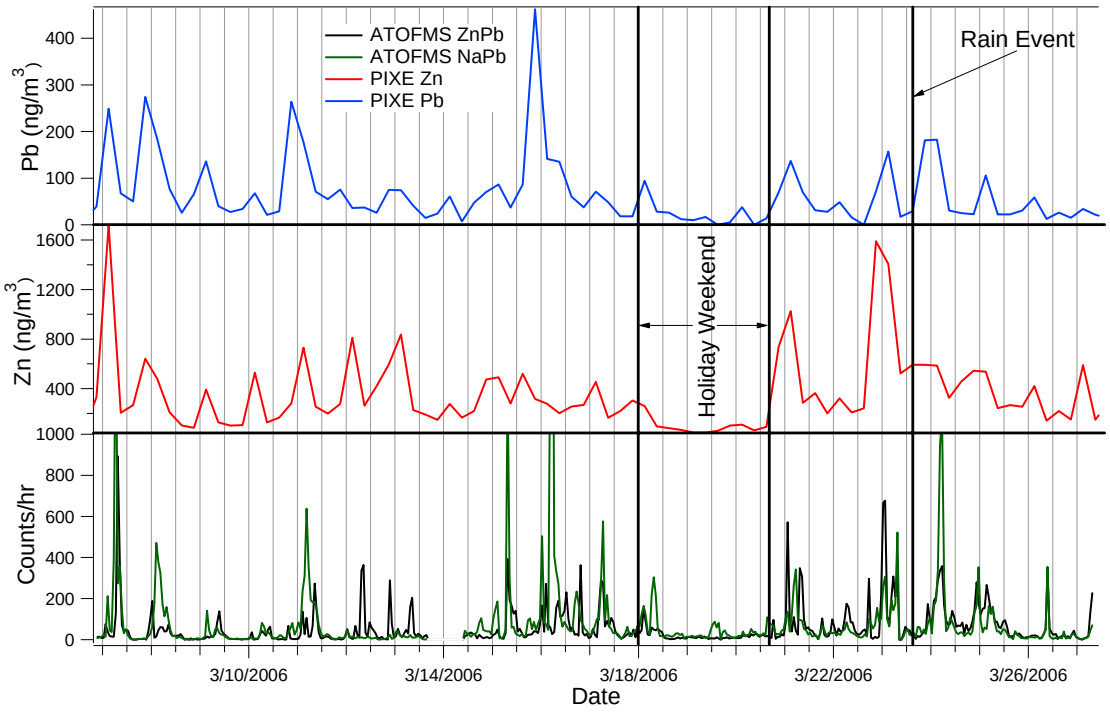

Figure 6.1. Timeseries of raw ATOFMS counts of Zn and Pb containing particles compared with the PIXE bulk mass concentrations of Zn and Pb. The major and minor tick marks occur at 12am and 12pm respectively.

Table 6.1. 24 hr average PM_{10} and $PM_{2.5}$ ($\mu g/m^3$) for Pb and Zn determined between March 6 – 30.

	Pb PM_{10}	**Pb $PM_{2.5}$**	**Zn PM_{10}**	**Zn $PM_{2.5}$**
Average	0.22	0.15	0.50	0.34
Min	0.06	0.01	0.14	0.04
Max	1.14	0.76	1.4	0.49

6.4.1 Rule Based Classification

To compare the CCSEM/EDX and ATOFMS results for Zn and Pb containing particles, a rule based classification scheme was developed and applied for the time following the heavy rain event indicated in Fig 6.1. The rule-based classification scheme shown in Figure 6.2 and detailed in Table 6.2 was motivated by the observation that most particles following the heavy rain event contained Pb, Zn, Fe and Na. Particles were first separated as containing metal (Me>0) or without metal (Me=0). The metal containing particles were further separated into two classes; those containing Pb and/or Zn (Me>0, Pb**»**Zn>0), and those without Pb or Zn (Me>0, Pb=0, Zn=0). For the CCSEM/EDX data, these classes were subdivided based on the relative abundances of Z>11 elements. For the ATOFMS data, these classes were subdivided based on peak areas using the criteria detailed in Table 6.2.

The percentages shown in black and blue in Fig 6.2 represent the percentage of particles classified for the CCSEM/EDX and the ATOFMS data sets, respectively. During this time period, 90 and 97% of the particles were found to contain metals by CCSEM/EDX and ATOFMS, respectively. The two techniques were in excellent agreement for the Na-max, Fe-max and Mg-max particle classes. In general, the CCSEM/EDX and ATOFMS results were in good agreeement, However, the higher percentages obtained from the ATOFMS data for the K max and Pb max classes may arise due to its enhanced sensitivity to these elements. This is supported by PIXE measurements, which indicated that the mass concentrations of Zn were always higher than Pb even though the two elements are positively correlated (r^2=0.35).

Table 6.2. Rules used to define ATOFMS particle classes

Particle Set	ATOFMS Rules	SEM/EDX Rules
Total	Time = [24-Mar-2006 5:15:00 24-Mar-2006 5:30:00]	Time = [24-Mar-2006 5:15:00 24-Mar-2006 5:30:00]
Zn>0	Area{64}>50 and Area{66}>50 and Area{68} > 50	N/A
Pb>0	mean(area{205 209})/mean(area{210 230}) >5	N/A
K>0	mean(area{39})/mean(area{36 38}) >2.5	N/A
Na>0	Area{23} > 50	N/A
Mg>0	Area{24}>3xArea{25} and Area{24}>3xArea{26}	N/A
Cu>0	Area{63+65}>3xArea{60+61+62}	N/A
Fe>0	Area{54}>100 and Area{56}>1000	N/A
Me>0	(Zn»Pb»K»Na»Mg»Fe) >0	(Pb»Fe »Mg»Zn»Si»Al»Mn»K) > 0
Me=0	Total - Me>0	N/A
Pb»Zn>0, Pb max	(Me>0 ... Pb>0) ... Pb>Fe,Mg,Zn	(Me>0 ... Pb>0) ... Pb>Fe,Mg,Zn,Si,Al,Mn,K
Pb»Zn>0, Zn max	(Me>0 ... Pb>0) ... Zn>Pb, Fe, Mg	(Me>0 ... Pb>0) ... Zn>Fe,Mg,Si,Al,Mn,K
Pb»Zn>0, Fe max	(Me>0 ... Pb>0) ... Fe>Pb,Mg,Zn	(Me>0 ... Pb>0) ... Fe>Mg,Zn,Si,Al,Mn,K
Pb»Zn>0, Mg max	(Me>0 ... Pb>0) ... Mg>Pb,Fe,Mg	(Me>0 ... Pb>0) ... Mg>Fe,Zn,Si,Al,Mn,K
Me>0, Pb=0	Me>0...Pb=0	Me>0 ... Pb=0
Me>0, Pb & Zn=0	Me>0 ... Pb=0 ... Zn=0	Me>0 ... Pb=0 ... Zn=0
Me>0, Pb & Zn=0, Na max	(Me>0, Pb & Zn=0) ... Na>K,Fe,Mg,Al	(Me>0, Pb & Zn=0) ... Na>K,Fe,Mg,Si,Al,Mn
Me>0, Pb & Zn=0, K max	(Me>0, Pb & Zn=0) ... K> Na,Fe,Mg,Al	(Me>0,Pb & Zn=0) ... K>Na,Fe,Mg,Si,Al,Mn
Me>0, Pb & Zn=0, Fe max	(Me>0, Pb & Zn=0) ... Fe> K,Na,Mg,Al	(Me>0, Pb & Zn=0) ... Fe>K,Na,Mg,Si,Al,Mn
Me>0, Pb & Zn=0, Mg max	(Me>0, Pb & Zn=0)...Mg> K,Na,Fe,Al	(Me>0, Pb & Zn=0) ... Mg> K,Na,Fe,Si,Al,Mn
Me>0, Pb & Zn=0, Al max	(Me>0, Pb & Zn=0) ... Al> K,Na,Mg,Fe	(Me>0, Pb & Zn=0) ... Al> K,Na,Fe,Mg,Si,Mn

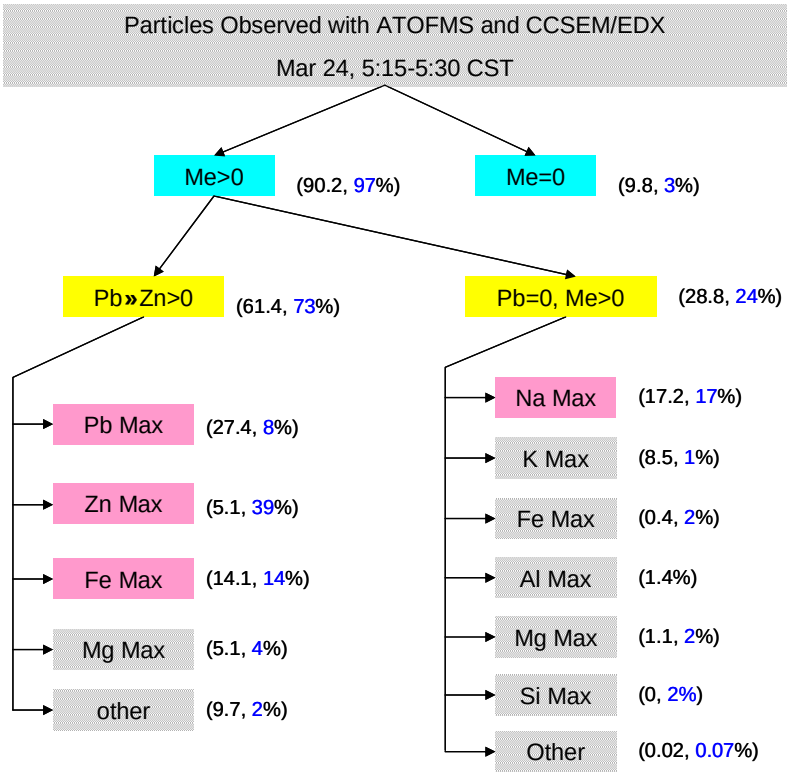

Figure 6.2. Rule based classification from ATOFMS and CCSEM/EDX data. The percent of particles in a class out of the total number of analyzed particles is indicated in black (ATOFMS) and blue (CCSEM/EDX. The precense of Pb or Zn is indicated by Pb**»**Zn>0.

6.4.2 Mixing State and Elemental Cross Correlations

In the following analysis, we compare single particle mixing states obtained from ATOFMS and CCSEM/EDX data (Figures 6.3, 6.4 and 6.6) and PIXE elemental cross correlations (Figure 6.5). As these measurements are fundamentally different from one another, instrumental characteristics need to be considered when comparing the results. In the ATOFMS technique, atomic and molecular ionization efficiencies may differ, as well as matrix effects for particles of different composition. The relative abundance is calculated from EDX spectra as the atomic percent of Z>11 elements in the particles [*Laskin, et al.*, 2006]. In addition, PIXE data provides an inter-comparison of the time series of bulk concentrations for Z>11 elements. Combining this complementary information provides detailed insight into particle composition.

6.4.2.1 Mixing State of the Me>0, Pb«Zn>0 Class

In order to understand the source and formation routes of the metal rich particles, it is useful to determine the chemical associations in the individual particles. Both the CCSEM/EDX and the ATOFMS are methods that can be used to determine the chemical mixing state of single particles. Figure 6.3 shows stacked bar charts for ~ 4400 (CCSEM/EDX) and ~800 (ATOFMS) individual metal containing (Me>0) particles detected shortly after the rain event. Stacked bars are plotted for individual particles and the colored area indicates the percent of each metal normalized to sum of the total constituents. Potassium was omitted from Fig 6.3b because it often dominated the ATOFMS signal and hindered our ability to graphically compare mixing states of particles detected with ATOFMS and CCSEM/EDX. Figure 6.3 clearly shows that Zn, Pb

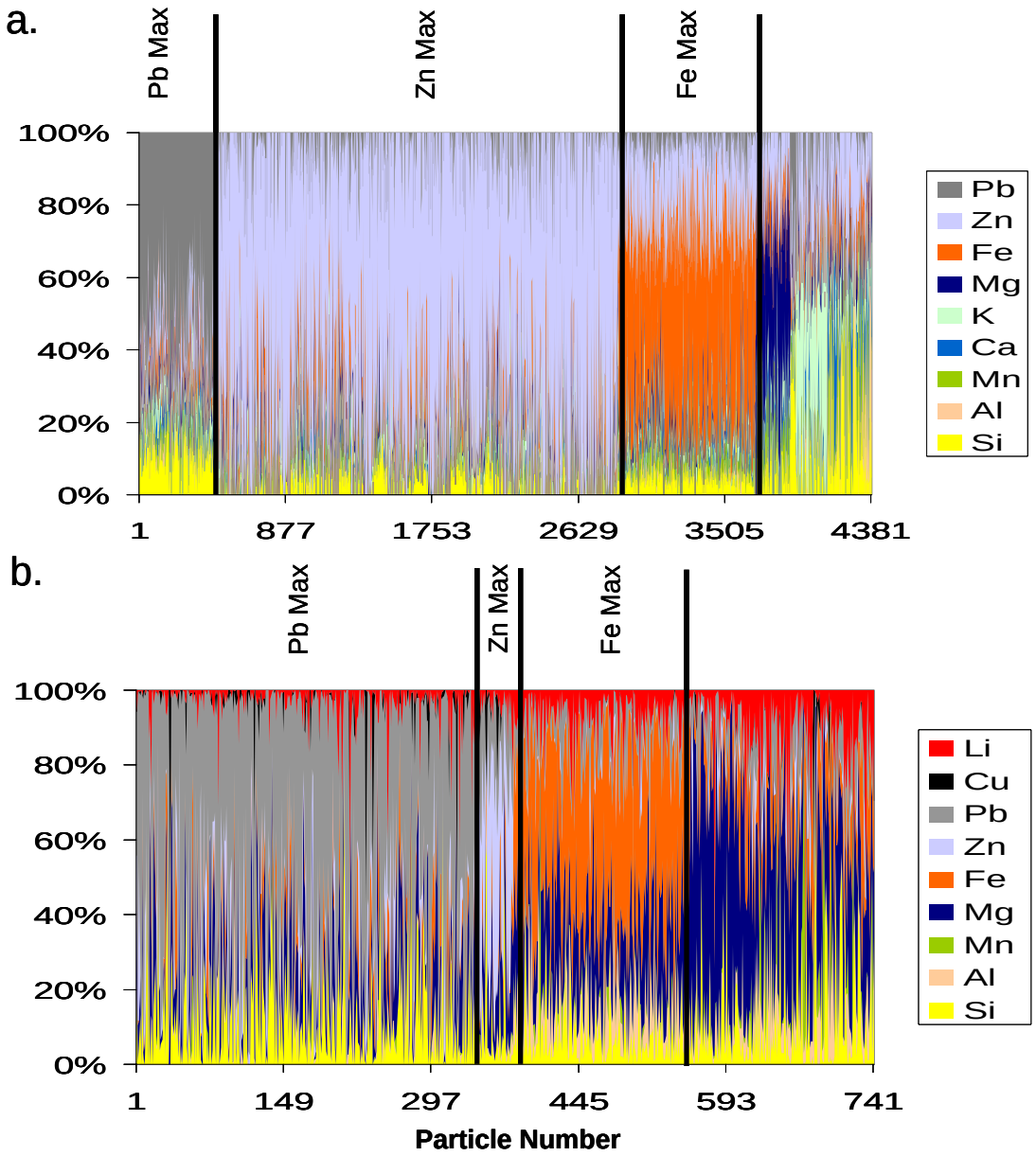

Figure 6.3. Chemical associations (mixing state) for single particles containing Zn and Pb sampled on Mar, 24 5:15-5:30 UTC derived from the CCSEM/EDX (Top) and the ATOFMS (Bottom)

and Fe are the most abundant metals in the Pb**»**Zn>0 class indicating that these metals are typically internally mixed. The relative proportions of the Pb max and Zn max particles are differ between the two techniques due to the enhanced sensitivity the ATOFMS has for Zn and Pb as noted earlier. Additional metals in the Pb**»**Zn>0 class include Mg, Al, Ca, Mn, K and Si. Here, Si, Al, and Mg show only minor presence although they are more abundant in the Fe max and "other" classes.

Another way to look at mixing state is by comparing the percentage of particles in a certain class that are mixed with a specific chemical species. In Fig 6.4 the mixing states of the major classes within the Pb**»**Zn > 0 group can be seen for both the ATOFMS (4a) and CCSEM/EDX (4b) data sets. Particle classes are indicated on the y axis and the color scale represents the fraction of the particles in these classes that contain the chemical markers on the x-axis. By Fig 6.4, both CCSEM/EDX and ATOFMS confirm that Zn and Pb containing particles are strongly mixed with Na, K, and Cl. Within the Zn Max class, both CCSEM/EDX and ATOFMS data show a strong association with sulfate. The ATOFMS data indicates that the secondary nitrogen markers $^{46}NO_2^-$ and $^{62}NO_3^-$ are strongly coupled with all particles containing Zn and Pb. Phosphorous markers ($^{79}PO_3^-$, $^{95}PO_4$), represented in Figure 6.4a as PO, are found to be mainly associated with the Pb**»**Zn > 0 set and weakly associated with Me>0, Pb & Zn = 0 particles. The CCSEM/EDX measurements reveal that P is mostly present in the Pb**»**Zn>0 class as well, but in fewer of the particles. This result suggests that P is a trace element in Pb**»**Zn>0 particles.

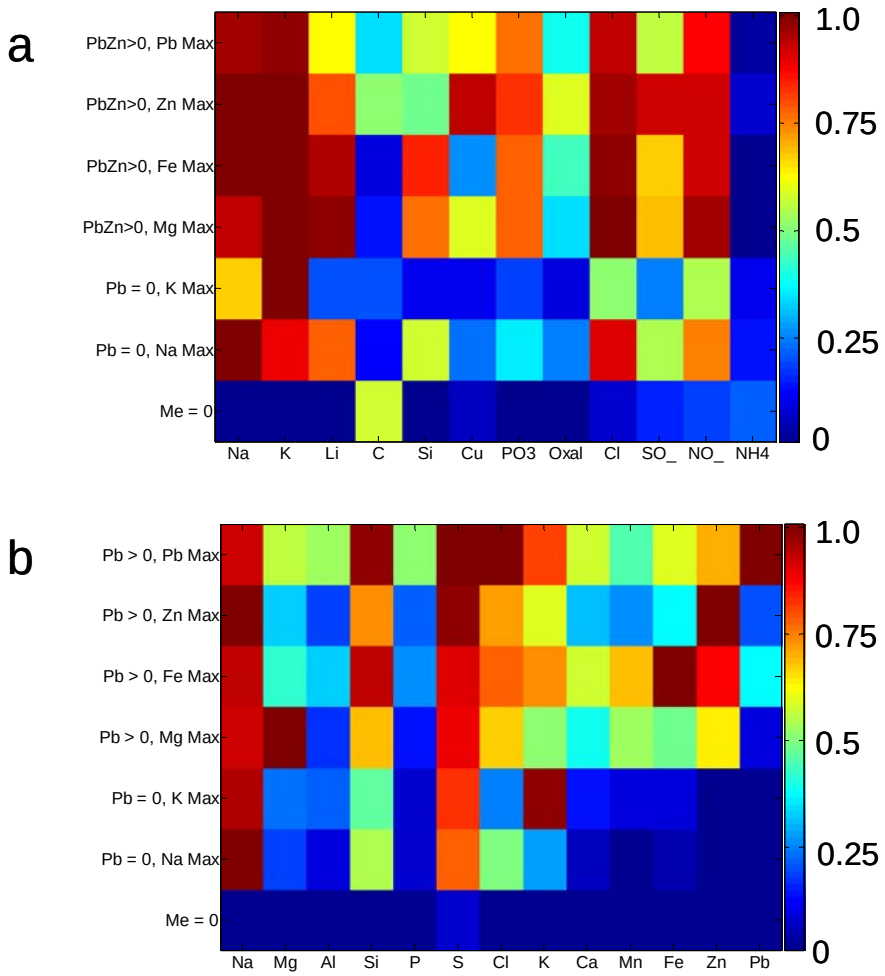

Figure 6.4. Mixing state of metal containing particles analyzed on Mar 24 derived from the ATOFMS (panel (a)) and CCESM/EDX (panel (b)) data sets. The color axis gives the fraction of particles on the y axis that contain the markers shown on the x axis. All classes and markers are defined in Table 6.2.

By Fig 6.4a, it is seen that ~50% of the Pb**»**Zn>0 particles were also mixed with carbon, suggesting combustion as a source. Compared to Me>0, Pb & Zn = 0 classes, the Pb**»**Zn>0 classes contain a higher fraction of particles with a $^{36}C_3^+$ peak. This marker is an important identifier for elemental carbon (EC), and indeed EC was most strongly mixed within the Pb**»**Zn>0 Zn max type. This is further corroborated by the fact that the STXM/NEXAFS also identified soot in Zn containing particles. Using Art2a, a cluster accounting for 6.3% of the total Pb containing particles contained Cu, EC, Oxalate, Zn and Pb. For the current analysis this is reflected in the fact that Zn max particles also contain a higher proportion of Cu and Oxalate ion. For the Zn max particles, ~65% of them contain the oxalate marker (Fig 6.4a). Reasons for this are not currently known, but it is common knowledge that Oxalate can bind strongly to metal ions within fogwater [*Sedlak and Hoigne*, 1993]. The formation of metal-oxalate complexes from the constituent ions has an equilibrium constant of greater than 10^6 M^{-1}, and tends to increase with the oxidation state of the metal. Although we are not measuring fog water, if the metals are emitted with hot water vapor, it is plausible that the particles are in the aqueous phase when first emitted and that the oxalate complexes can form.

Most of the Pb**»**Zn>0 particle classes are strongly associated with traces of alkali metals (Li, Na and K). Most of the particle classes analyzed with the ATOFMS are found to contain K and Li. The CCSEM/EDX provides a different look at K, showing that it is primarily associated with the Pb**»**Zn>0 classes, with the exception of the Pb=0, K max type. Given that the CCSEM/EDX primarily detects K in the Pb**»**Zn>0 particle type while the ATOFMS finds K in nearly all particles means that the concentration of K in

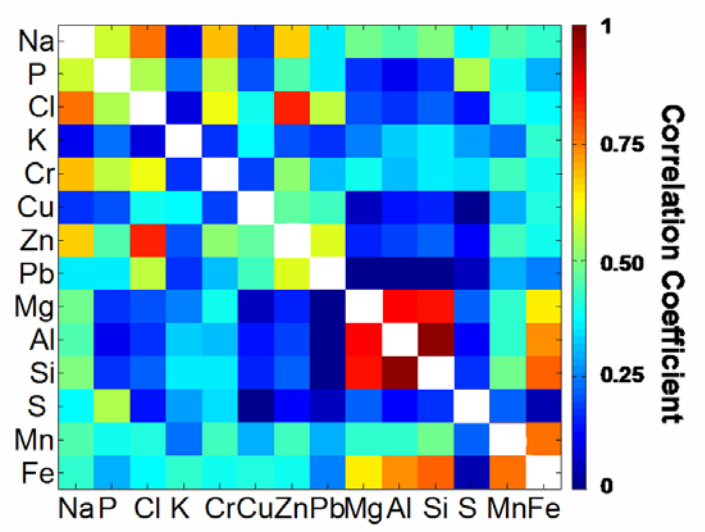

Figure 6.5. Temporal correlation matrix derived from the PIXE data. The data has a 6 hour time resolution. The data were taken from 3/6/06 – 3/31/06

the Pb**»**Zn>0 particle classes is higher than in the other particle classes where CCSEM/EDX does not detect it.

The mixing state relations observed above are also indicated by PIXE temporal correlations. The temporal correlation matrix derived from the PIXE data is shown in Figure 6.5. Zn exhibits a stronger correlation (r^2=0.7) with Cl than any other element, including Na. Therefore, it is expected that the Zn max particles are internally mixed with Cl. In addition, Zn and Cl are moderately correlated with Na, Pb, P, Cr and Cu – all of which were seen to be internally mixed by the ATOFMS and CCSEMEDX. Furthermore, the PIXE correlation matrix suggests strong associations between Al, Si and Mg as was shown by CCSEM/EDX and ATOFMS (Figs 6.3-6.4).

6.4.2.2 Mixing State of the Pb & Zn=0, Me>0 Class

Particles that were emitted after the heavy rain event often did not contain Zn or Pb, but were frequently associated with similar plumes, therefore their characterization is also warranted. Figure 6.6 graphically presents ~1500 (CCSEM/EDX) and ~360 (ATOFMS) particles from the Me>0, Pb & Zn = 0 class. The most dominant subclass of the Me>0, Pb & Zn = 0 class was identified as Na max in both CCSEM/EDX and ATOFMS data. As seen in Fig 6.4a, this particle class a significant contribution from Cl, suggesting NaCl is the primary species. From the CCSEM/EDX data, an average composition of $Na_{1.00}Cl_{0.74}S_{0.24}Si_{0.06}OE_{<0.05}$ (*OE*-other elements) was determined, suggestive of mixed sodium chloride and sodium sulfate particles. Sodium nitrate may also be present as the ATOFMS data showed that ~70% of the Na max particles contain

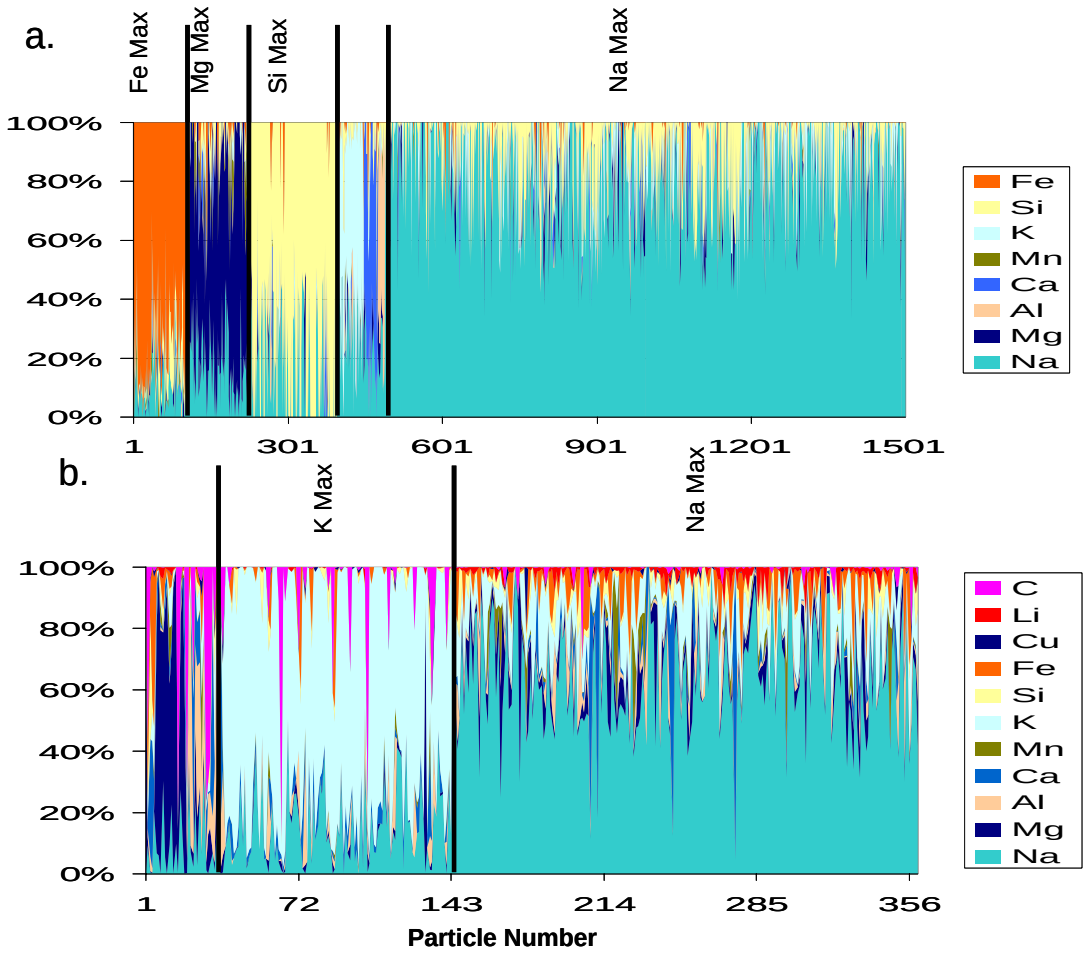

Figure 6.6. Chemical associations (mixing state) for single particles that do not contain Zn and Pb sampled on Mar, 24 5:15-5:30 UTC derived from the CCSEM/EDX (panel (a)) and the ATOFMS (panel(b)).

NO species. The occasional presence of Mg at low concentrations indicates that a sea salt origin is unlikely.

As noted above, the primary difference between the CCSEM/EDX and ATOFMS data is the higher abundance of K max particles in the ATOFMS data set. Additionally, fewer Fe max particles were identified with ATOFMS than with CCSEM/EDX data. Li is more abundant in the Na max class while K max particles lack Li. It may be that there is simply less Li in the K max particles, or alternatively, that a matrix effect in the K max particles suppresses the formation of Li^+ ions. Further differences in the K max and Na max particle classes are observed in Figure 6.6. For example, Na max is more abundant in $^{35}Cl^-$, $^{79}PO_3^-$, and Si markers while K max has more $^{12}C^+$. This indicates that the Na max particle type is more strongly associated with common inorganic markers (Cl, Si, and P) whereas the K max type is more commonly associated with carbon and secondary nitrate and sulfate markers.

6.4.3 Particle Morphology

Particle morphology is an important microphysical trait that helps determine aerodynamic behavior, health effects, speciation, phase, formation mechanisms, and sources. Detailed morphologies from SEM images of metal rich particles are shown in Figure 6.7. The non-spherical nature of Zn and Pb containing particles (panels a,b,d and e) is clearly seen. The Zn containing crystal in Fig. 6.7a is internally mixed with soot. This is consistent with ATOFMS results from Fig 6.4a, where > 50% of the Zn max particles are mixed with carbon. Zn particles containing Fe and Mn are near-perfect spheres (Fig 6.7c). The majority of Pb rich particles are small compact and nearly

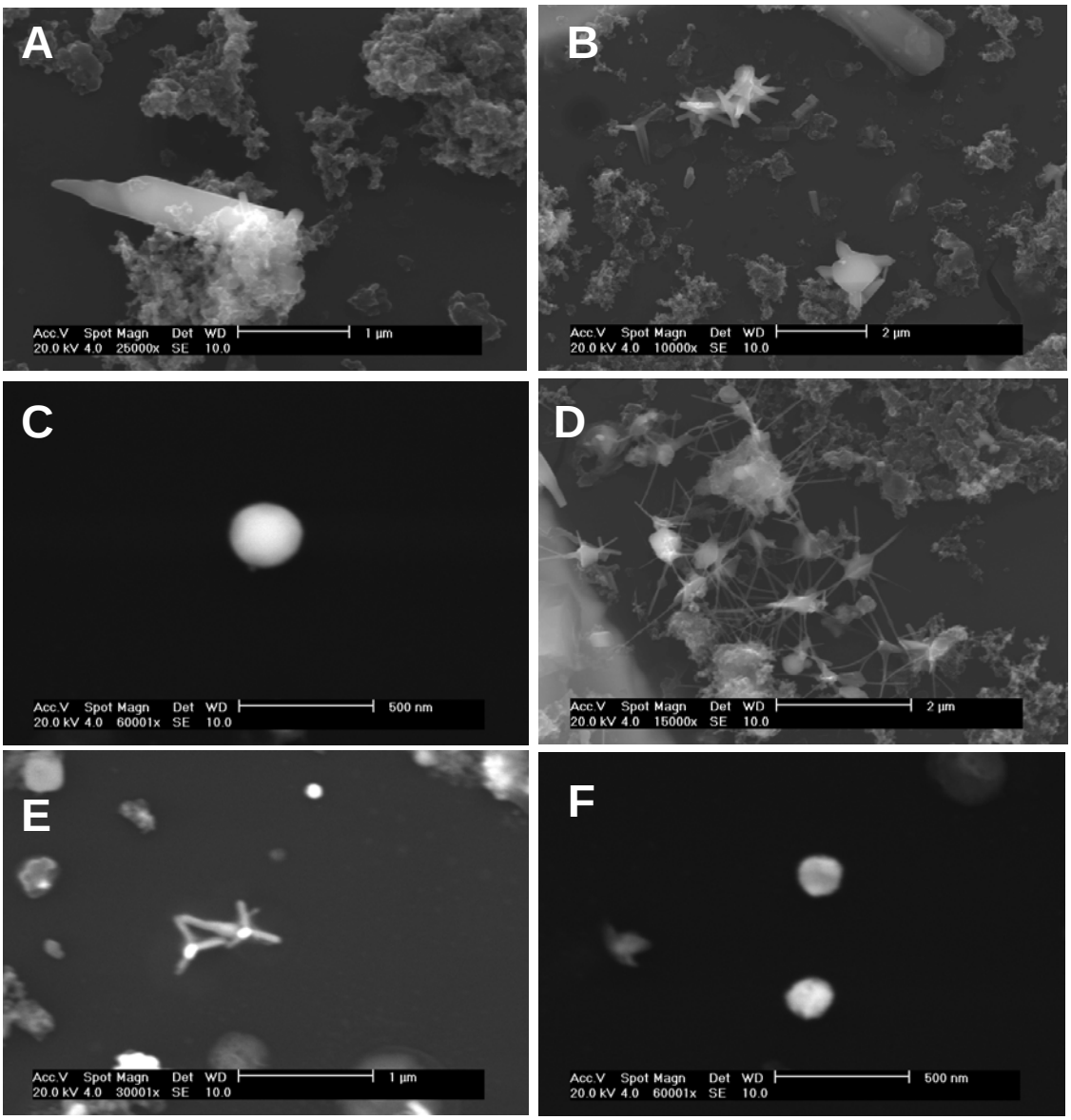

Figure 6.7. SEM images illustrating the morphology of metallic particles observed in Northern Mexico City. A) Zn containing crystal attached to what is presumably elemental carbon B) Needle – like Zn containing particles C) Spherical particle containing Fe, Zn and Mn D) Needle – like particles containing Pb, Zn and Cl E) Tetrahedral Zn particles F) compact, nearly spherical Pb rich particles.

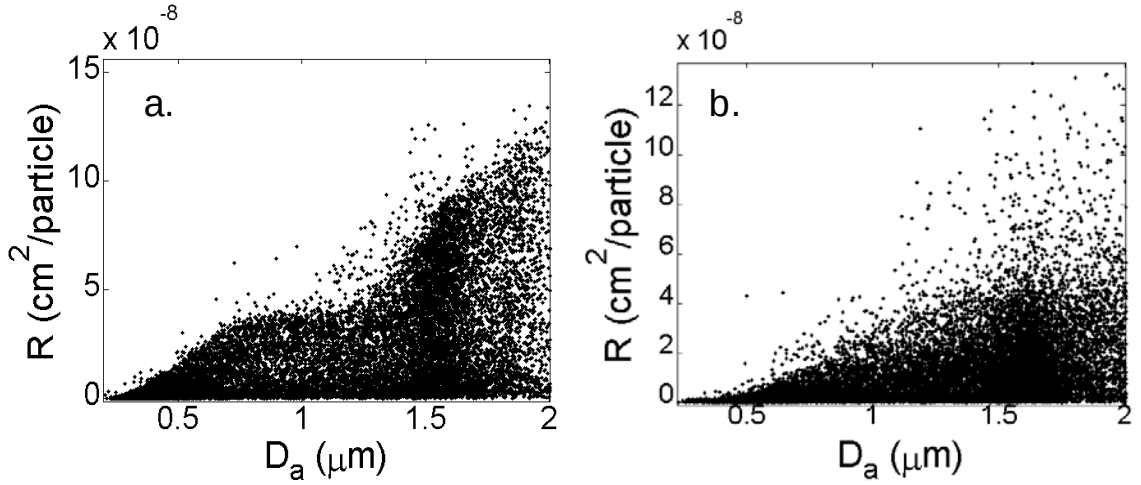

Figure 6.8. Partial scattering cross section vs aerodynamic diameter for A) spherical Ca rich particles sampled during MILAGRO and B) PbZn rich particles sampled during MILAGRO. The spherical particles have a well defined curve at the upper limit of data points. The PbZn do not have this feature and therefore are likely nonspherical in the ambient atmosphere.

spherical (Fig 6.7f). In Figs 6.7b, d, and e, needle like Zn and Pb particles are shown. Detailed SEM/EDX analysis confirmed that most needle like structures were composed of mostly Zn and O, with only minor amounts of other elements, suggesting these may be similar to tetrahedral ZnO particles previously observed [*Bradley, et al.*, 1981].

Particle morphology may also be inferred by plotting the amount of scattered light vs. aerodynamic diameter for particles separated by chemical composition using ATOFMS. Such a plot is shown in Fig 6.8 for organic particles and Pb and Zn rich particles. Qualitatively, the resulting curve indicates whether or not particles are homogenous spheres. Homogenous, spherical particles scatter light with a pattern similar to that for organic carbon particles in Fig. 6.8a, and nonspherical or inhomogeneous particles scatter light with a pattern similar to the Zn and Pb containing particles in Fig. 6.8b [*Bohren and Huffman*, 1981; *Moffet and Prather*, 2005]. Using a method presented elsewhere [*Moffet and Prather*, 2005; *Cross, et al.*, 2007] we determined that the effective densities of 0.1-0.6 μm metallic particles are between 2.4-3.4 g/cm^3, assuming a refractive index between 1.4 to 1.7.

6.4.4 Phase, Speciation and Possible Sources

The phase and speciation of Pb particles are of critical interest because they influence the particle toxicity. The speciation of the chemical constituents often regulates particle solubility. The metal solubility, in turn, affects particle mobility in the human body while the oxidation state often determines the metal's toxicity [*Dreher, et al.*, 1997; *Hodgson, et al.*, 2001]. For the Zn rich particles, we determined the chemical speciation directly using STXM/NEXAFS (Sec 6.4.4.1). Then, results from all methods are used

here provide further insight into the chemical speciation for all of the particles observed in this study (Sec 6.4.4.2). Since the source of the particles will influence the phase and speciation, a discussion of possible sources is presented in Sec 6.4.4.3.

6.4.4.1 Zn Speciation Using STXM/NEXAFS

The STXM/NEXAFS technique was used to give the speciation of the Zn containing particles. Two different major Zn-containing particle classes were distinguished based on morphology and NEXAFS spectra. Representative STXM images collected at 1024 eV are shown in Fig 6.9. Particles shown in Fig 6.9a (type A) were found to be internal mixtures with a Zn containing crystal, EC and K while particles in Fig 6.9b (type B) were found to be needle-like Zn particles. The presence of EC and K in type A were confirmed with the corresponding carbon K-edge NEXAFS spectra - a result consistent with ATOFMS and CCSEM/EDX observations.

To elucidate the chemical speciation of atmospheric Zn-containing particles, the Zn L-edge NEXAFS spectra of ZnO, ZnS, $Zn(NO_3)_2 \bullet 6H_2O$, $ZnCl_2$, $ZnSO_4$ standard reference materials and atmospheric particle types A and B were measured. Representative normalized Zn L-edge NEXAFS spectra for both particle classes and two Zn-containing standards, $Zn(NO_3)_2 \bullet 6H_2O$ and ZnO, are shown in Fig 6.9 c and d. The constant linear pre-edge background (1010-1020 eV) was subtracted from the spectra and the resulting spectra were then normalized to the same total Zn, which is defined as the difference between the post-edge (1060 eV) and pre-edge (1010 eV) absorbencies. Therefore, spectral differences correspond to differences in chemical structure and not

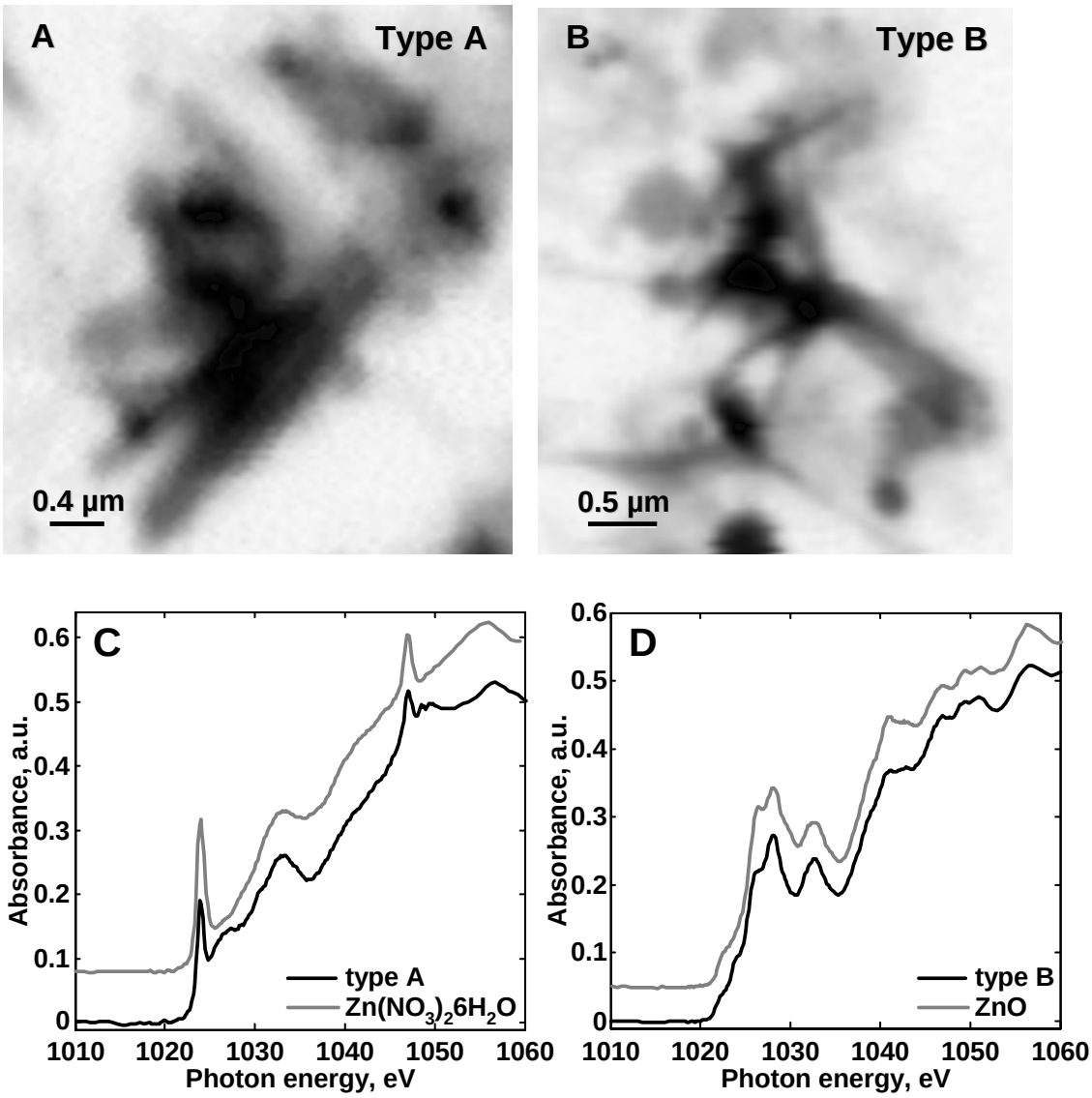

Figure 6.9. Upper panel: single energy (1024eV) STXM images of two major classes of Zn particles observed in Northern Mexico City. A) particle type A: Zn crystals internally mixed with elemental carbon B) type B: Needle-like Zn particles. Lower panel: representative Zn L-edge normalized NEXAFS spectra for C) particle type A and $Zn(NO_3)_26H_2O$ standard and D) particle type B and ZnO standard.

particle thickness. The representative spectra in Fig 6.9 c and d for particle types A and B correspond to the average spectrum collected over six single particles located at different sample regions. Spectra of ZnS, $ZnSO_4$ and $ZnCl_2$ standards did not match the spectra of the Zn-containing particles. The striking similarities in the spectral contours and intensities of the $Zn(NO_3)_2 \cdot 6H_2O$ and ZnO spectra in Fig 6.9 c and d with those of particle classes, A and B, respectively, provide clear chemical identification. While the spectra of particle type B exactly matches that of ZnO, small deviations between the spectra of particle type A and $Zn(NO_3)_2 \cdot 6H_2O$ are observed at ~1025 eV and ~1050 eV. These small deviations may arise due to the presence of minor amounts of other Zn compounds.

6.4.4.2 On the Speciation and Phase of Pb«Zn >0 Particles

The source of Pb»Zn>0 particles influences both the chemical speciation/oxidation and phase of metallic constituents. If the source is garbage incineration, the Pb»Zn particles may be metal chlorides [*Linak and Wendt*, 1993; *Wu and Biswas*, 1993; *Eighmy, et al.*, 1995]. The chloride may be substituted with a conjugate base (e.g. NO_3) upon reaction with acidic gases:

$MCl_{n\,(s)} + nHNO_{3\,(g)} \rightarrow M(NO_3)_{n\,(s)} + nHCl_{(g)}$

where M can represent Zn or Pb. The STXM/NEXAFS and ATOFMS data suggests that $Zn(NO_3)_2$ is a major component of some particle classes. Particles originating from smelting could contain several complex inorganic phases that would depend on the specific starting material used.

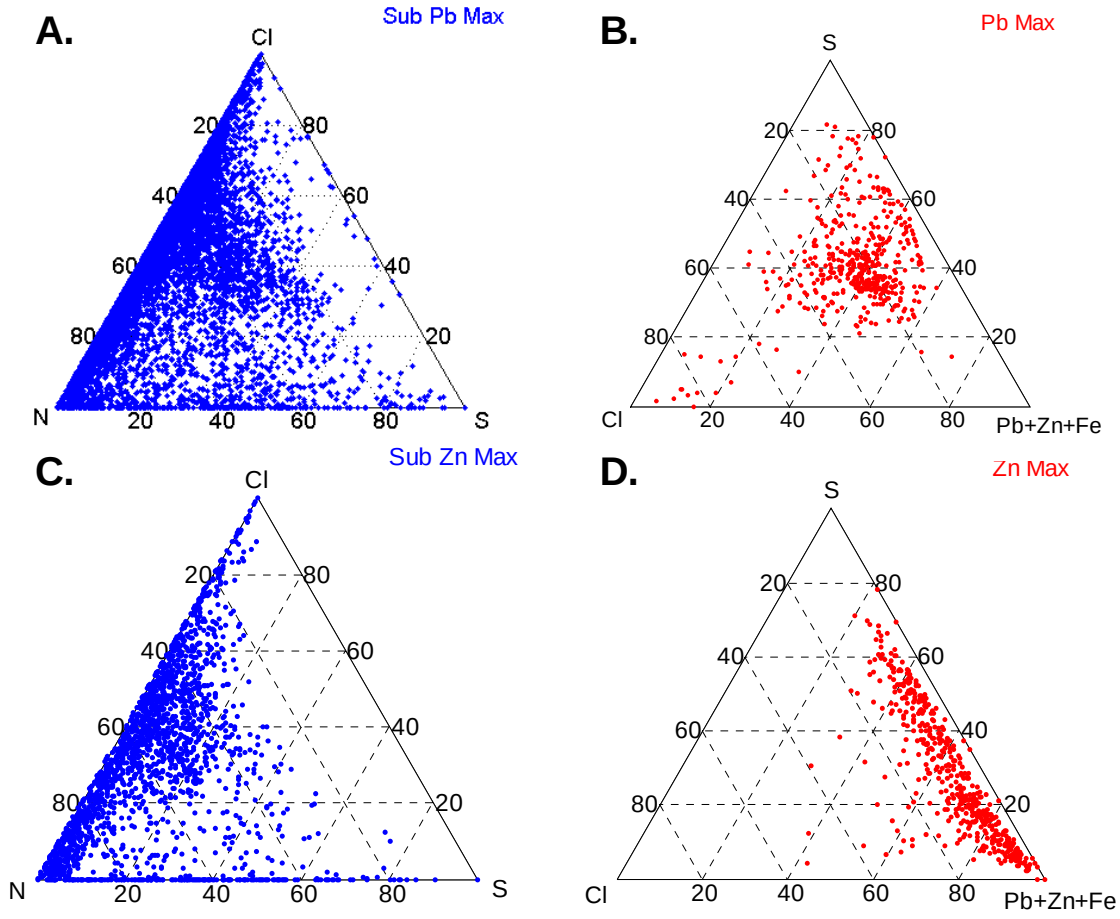

Figure 6.10. Ternary plots illustrating the chemical composition of secondary/primary species N, Cl, and S. A) N-S-Cl ternary diagram for submicron Pb Max particles. B) **(**FeZnPb)-S-Cl ternary diagram showing CCSEM/EDX-measured compositions of "Me>0, Pb >0, Pb max**"** individual particles (yellow dots). Red dots correspond to nominal values of various PbCl2/PbSO4 mixtures C) N-S-Cl ternary diagram for submicron Zn Max particles D) **(**FeZnPb)-S-C ternary diagram showing CCSEM/EDX-measured compositions of "Me>0, Pb >0, Zn max" individual particles

Many of the metal species within the Pb**»**Zn>0 class are needle like crystals. The STXM/NEXAFS spectra confirm that some needle like particles are ZnO. ZnO particles have been observed in other studies [*Bradley, et al.*, 1981]. In ZnO particles, nitrogen, chloride and sulfate may be present as secondary compounds on the particle surface. This is supported by both ATOFMS and CCSEM/EDX data which indicate sulfur, chloride and nitrogen internally mixed in Zn rich particles.

Pb Max particles are shown to be enriched in Cl by both the ATOFMS and CCSEM/EDX techniques. Ternary plots showing the distribution of Pb, S, N, and Cl for Pb Max particles are shown in Fig. 6.10. In Fig 6.10 a and c, ATOFMS shows the distribution of S, N and Cl, where S represents the sum of $^{80}SO_3^-$ and $^{97}HSO_4^-$, and N represents the sum of $^{46}NO_2^-$ and $^{62}NO_3^-$. For both the Pb max and Zn max particles it is seen that N and Cl dominate the ATOFMS peak areas. For the CCSEM/EDX, Cl is present in both Pb max and Zn max, but Cl is much more prevalent in the Pb max particle type. This could be because of contributions from the ZnO class and/or reaction with acidic gasses. The apparent discrepancy of the S in the Zn Max particle type may be due to several factors. It is possible that the majority of Cl is on the surface and that the ATOFMS is not analyzing the particle core which is enriched in S, or that the ATOFMS has a lower ionization efficiency for S compounds. This is supported by the fact that the ATOFMS saw the highest number of S containing particles in the Zn max particle type.

6.4.4.3 Possible Sources of Metal Rich Particles in Mexico City

There are numerous industrial sources of particles in northern Mexico City. The emissions inventory for the area (within 5km of the sampling site) indicates that smelting

releases a substantial fraction of the $PM_{2.5}$ compared to other industries. The findings of this paper are consistent with smelting as a source of metal rich particles. Specifically, (1) tetrahedral ZnO particles were observed, which have been attributed to copper smelting in other studies [*Bradley, et al.*, 1981]; (2) Fe, Si, Al and Cu containing particles have been reported in smelting emissions and were observed in particles detected here [*Pina, et al.*, 2000; *Ohmsen*, 2001; *Pina, et al.*, 2002; *Tan, et al.*, 2002; *Batonneau, et al.*, 2004; *Beavington, et al.*, 2004]. However, in contrast with our observations, previous studies did not report large amounts of Cl associated with smelter emissions. Previous source studies on smelters also noted high SO_2 concentrations within smelter plumes, which were not observed in this study. In this study, weak correlations were seen between SO_2, Zn and Pb. Johnson et al (2006) noted that Na and Zn plumes from the northeast region of Mexico City were not strongly associated with SO_2 whereas V and SO_2 were reported from the northwest Tula region. Zn and Pb containing particles identified by ATOFMS in this study also came from the northeast [*Moffet, et al.*, 2007], in agreement with the observations of Johnson (2006).

On the other hand, municipal and hazardous waste incineration is a source that does emit high concentrations of Pb, Zn and Cl containing particles [*Ondov and Wexler*, 1998; *Chang, et al.*, 2000; *Walsh, et al.*, 2001; *Tan, et al.*, 2002; *Hu, et al.*, 2003]. The PIXE, ATOFMS and CCSEM/EDX analysis presented here indicates that these elements are internal mixtures, and their mass concentrations are positively correlated. Metal particles internally mixed with carbonaceous material (including EC) suggest that these particles result from high temperature combustion of both metal and carbon containing material. The study of [*Tan, et al.*, 2002] compared single particle mass spectra from

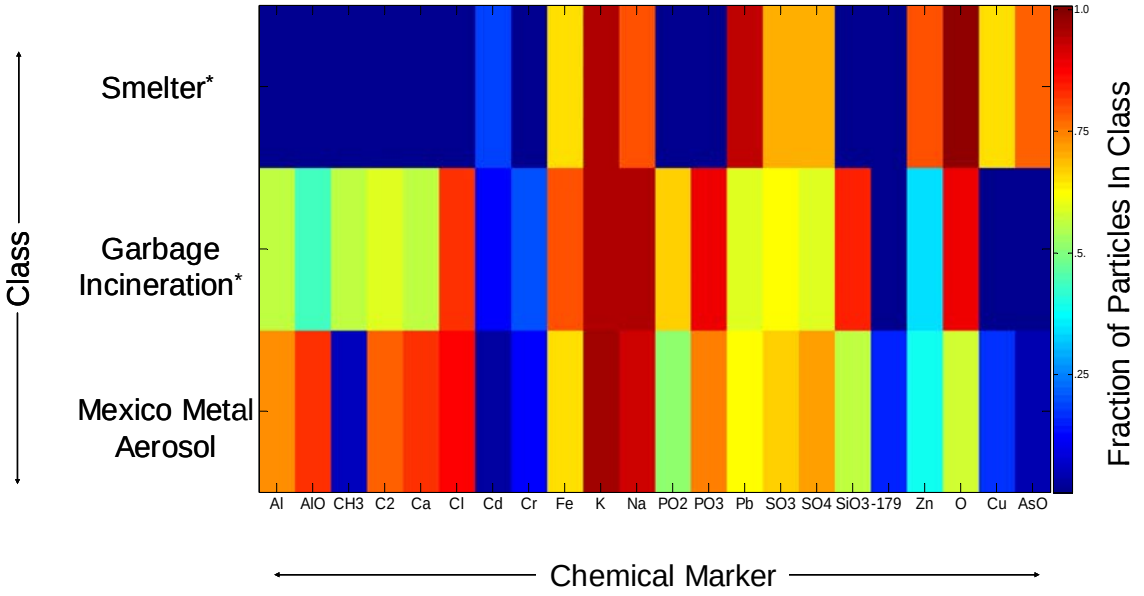

Figure 6.11. A comparison of Mexico City aerosol with two likely industrial sources located in Mexico City. This figure shows that the Mexico City Metal aerosol most closely matches garbage incineration rather than smelting. Key elemental tracers include Cl, P, Al and C_2^+. The ATOFMS data used for this figure is the "Total" particle set defined in Table 6.1.

* The source data was obtained from Tan, 2002.

nonferrous smelters and municipal waste incinerators and determined that they have similar source signatures with the exception of P and Cl. In Fig 6.4, both P and Cl are abundant in the Pb**»**Zn>0 particles, consistent with the results of Tan et al, 2002. Figure 6.11 compares all of the particles reported here with the source samples of Tan, 2002. The elements common to incineration and the Mexico City metal containing particles have similar markers, namely Cl, P, Ca and carbonaceous markers. From Fig. 6.11 it is apparent that the Mexico City metal particles contain more Al and carbonaceous markers. This may be due to influence from other aerosol contributors such as secondary organic carbon and fugitive dust not present in the fly ash samples in Tan, 2002.

The fact that incineration is not listed in the emissions inventory for Mexico City does not mean that this activity does not occur. The authors noted (using satellite imagery) a garbage incinerator in the northern part of Mexico City where Pb/Zn/Cl containing particles were shown to be coming from [*Moffet*, 2007]. This incinerator was near a large landfill in the northwestern of the MCMA. Particles of this type could also arise from industrial heat sources, such as kilns, using tires, hazardous waste and municipal waste for fuel.

6.5. Conclusions

In this paper, a variety of techniques were used to analyze Zn and Pb containing particles originating from industrial sources in Northern Mexico City. Peak PM_{10} concentrations of Zn and Pb were 1.4 and 1.14 $\mu g/m^3$ respectively. By analyzing the time series, we determined that the metal rich particles peaked at the sampling site during the early morning hours. This observation is consistent with previous studies which showed

that high Zn and Pb are correlated with air masses from the northeastern part of the city, which typically occur in the early morning. Further evidence pointing to an industrial source of the metal rich particles was obtained by data indicating that the lowest metal particle concentrations were observed during a holiday weekend.

ATOFMS and PIXE results show that the particles containing Zn and/or Pb are mixed with Cl. Although CCSEM/EDX did not find as much Cl mixed with Zn in the particles, PIXE results indicate that Zn correlates strongly with Cl. This may be due to heterogeneous reaction with nitric acid. This assertion is supported by STXM/NEXAFS results that show Zn rich particles composed of $Zn(NO_3)_2 \bullet 6H_2O$. Also, CCSEM/EDX images indicated that many Zn rich particles had a needle like morphology suggestive of ZnO that was identified in previous studies. STXM/NEXAFS confirmed the speciation of the needle-like Zn particles to be ZnO. These particles were also found to be enriched in Na, Fe and Si as well as other metals, indicating other complex phases are present in these particles.

Although several of the elements observed in the particles studied here are also in smelter emissions, as well as other sources, the specific combination of Pb, Zn and Cl in individual particles has not been reported to be characteristic of smelting sources. This suggests that other sources, such as refuse combustion, may be responsible for the metal rich particles observed here. This hypothesis was strengthened through a direct comparison of the Mexico City data with source samples from non-ferrous smelters and garbage incineration. Moreover, three different single particle techniques confirmed that many of the Zn rich particles are mixed with elemental carbon. The presence of elemental carbon indicates a combustion source for these metal rich particles. Of the possible

combustion sources for Zn particles, combustion of waste is most consistent with the Zn-Pb-Cl mixing state.

The frequent observation of these metal rich particles in an area with a high population density has implications for health effects. The largest fraction of the Pb particles is below 2.5μm and therefore these particles are efficiently deposited in the human lung. Also, because it was found that $Zn(NO_3)_2$ particles were present in these samples, $Pb(NO_3)_2$ may be present as well. Lead nitrate is soluble, and therefore is more mobile within the human body than an insoluble Pb species. Because we suspect that the metals observed in this study are also present as metal chlorides, they may undergo ageing reactions that transform the metals into their corresponding nitrate compounds. This implies that their solubility evolves over time a result of this reaction.

6.6 Acknowledgements

Chapter 6, in full, is a manuscript to be submitted:

Ryan C. Moffet, Yury Desyaterik, Rebecca J. Hopkins, Alexei V Tivanski1, Mary K. Gilles, V. Shutthanandan, Luisa T. Molina, Rodrigo A. Gonzalez, Kirsten S. Johnson, Violeta Mugica, Mario J. Molina, Alexander Laskin and Kimberly A. Prather: Characterization of Aerosols Containing Zn, Pb, and Cl from an Industrial Region of Mexico City, *In Preparation,*. The dissertation author was the primary author of this paper.

The authors would like to thank Gustavo Sosa, Philip Sheehy, Rainer Volkamer, Jose Jimenez, and Ken Docherty for their help and guidance during the MCMA-2006 field study. Rene Sanchez overcame the location problems of our digitizers. Robert

Osborne and Don Collins helped organize and consolidate the shipment of equipment into Mexico as well as providing APS data. Tania Perez and Ricardo Cepeda provided timely logistical support. Rafael Ramos graciously provided gas phase and PM data from the RAMA monitoring network. Financial support for this study was provided by the National Science Foundation under grants ATM-0511803 and ATM-0528227 (UCSD research group) and Atmospheric Science Program of the Department of Energy's office of Biological and Environmental Research (PNNL, LBNL and MIT research groups). The CCSEM/EDX particle analysis was performed in the Environmental Molecular Sciences Laboratory, a national scientific user facility sponsored by the Department of Energy's Office of Biological and Environmental Research at Pacific Northwest National Laboratory. PNNL is operated by the U.S. Department of Energy by Battelle Memorial Institute under contract DE-AC06-76RL0. STXM/NEXAFS experiments at the ALS were partially supported by the Director, Office of Science, Office of Basic Energy Sciences, Division of Chemical Sciences, Geosciences, and Biosciences of the U.S. Department of Energy at Lawrence Berkeley National Laboratory under Contract No. DE-AC02-05CH11231.

6.7 References

Batonneau, Y., et al. (2004), Speciation of PM10 sources of airborne nonferrous metals within the 3-km zone of lead/zinc smelters, *Environmental Science & Technology*, *38*, 5281-5289.

Beavington, F., et al. (2004), Comparative studies of atmospheric trace elements: improvements in air quality near a copper smelter, *Science of the Total Environment*, *332*, 39-49.

Bohren, C. F., and D. R. Huffman (1981), *Absorption and Scattering of Light by Small Particles*, John Wiley and Sons, INC., New York.

Bradley, J. P., et al. (1981), Structure and Evolution of Fugitive Particles from a Copper Smelter, *Environmental Science & Technology*, *15*, 1208-1212.

Broday, D. M., and P. G. Georgopoulos (2001), Growth and deposition of hygroscopic particulate matter in the human lungs, *Aerosol Science and Technology*, *34*, 144-159.

Cahill, T. A., and P. Wayakabashi (1993), Compositional analysis of size segregated aerosol samples, *ACS Adv. Chem. Ser.*, *232*, 211-228.

Chang, M. B., et al. (2000), Characteristics of heavy metals on particles with different sizes from municipal solid waste incineration, *Journal of Hazardous Materials*, *79*, 229-239.

Cross, E. S., et al. (2007), Laboratory and ambient particle density determinations using light scattering in conjunction with aerosol mass spectrometry, *Aerosol Sci. Technol.*, *41*, 343-359.

Dockery, D. W., et al. (1993), An Association between Air-Pollution and Mortality in 6 United-States Cities, *New England Journal of Medicine*, *329*, 1753-1759.

Dreher, K. L., et al. (1997), Soluble transition metals mediate residual oil fly ash induced acute lung injury, *Journal of Toxicology and Environmental Health*, *50*, 285-305.

Eighmy, T. T., et al. (1995), Comprehensive Approach toward Understanding Element Speciation and Leaching Behavior in Municipal Solid-Waste Incineration Electrostatic Precipitator Ash, *Environmental Science & Technology*, *29*, 629-646.

Florea, A. M., and D. Busselberg (2006), Occurrence, use and potential toxic effects of metals and metal compounds, *Biometals*, *19*, 419-427.

Flores, J., et al. (1999), PIXE analysis of airborne particulate matter from Xalostoc, Mexico: winter to summer comparison, *Nuclear Instruments & Methods in Physics Research Section B-Beam Interactions with Materials and Atoms*, *150*, 445-449.

Gard, E., et al. (1997), Real-time analysis of individual atmospheric aerosol particles: Design and performance of a portable ATOFMS, *Analytical Chemistry*, *69*, 4083-4091.

Hodgson, M. J., et al. (2001), Hypersensitivity pneumonitis in a metal-working environment, *American Journal of Industrial Medicine*, *39*, 616-628.

Hopkins, R. J., et al. (2007), Chemical Bonding and Structure of Black Carbon Reference Materials and Individual Carbonaceous Atmospheric Aerosols, *J. Aerosol Sci.*, *In Press*.

Hu, C. W., et al. (2003), Characterization of multiple airborne particulate metals in the surroundings of a municipal waste incinerator in Taiwan, *Atmospheric Environment*, *37*, 2845-2852.

Johnson, K. S., et al. (2006), Aerosol composition and source apportionment in the Mexico City Metropolitan Area with PIXE/PESA/STIM and multivariate analysis, *Atmospheric Chemistry and Physics*, *6*, 4591-4600.

Laskin, A., et al. (2006), Analysis of individual environmental particles using modern methods of electron microscopy and X-ray microanalysis, *Journal of Electron Spectroscopy and Related Phenomena*, *150*, 260-274.

Linak, W. P., and J. O. L. Wendt (1993), Toxic Metal Emissions from Incineration - Mechanisms and Control, *Progress in Energy and Combustion Science*, *19*, 145-185.

Londahl, J., et al. (2007), Size-resolved respiratory-tract deposition of fine and ultrafine hydrophobic and hygroscopic aerosol particles during rest and exercise, *Inhalation Toxicology*, *19*, 109-116.

Ma, Y., et al. (1991), High-Resolution K-Shell Photoabsorption Measurements of Simple Molecules, *Physical Review A*, *44*, 1848-1858.

Maxwell, J. A., et al. (1989), The Guelph Pixe Software Package, *Nuclear Instruments & Methods in Physics Research Section B-Beam Interactions with Materials and Atoms*, *43*, 218-230.

Michelsen, H. A., et al. (2007), Particle formation from pulsed laser irradiation of soot aggregates studied with a scanning mobility particle sizer, a transmission electron microscope, and a scanning transmission X-ray microscope, *Applied Optics*, *46*, 959-977.

Moffet, R. C., et al. (2007), Measurement of ambient aerosols in northern Mexico City by single particle mass spectrometry, *Atmos. Chem. Phys. Discuss.*, Accepted.

Moffet, R. C., de Foy, B., Molina, L. T., Molina, M. J., Prather, K. A. (2007), Characterization of Ambient Aerosols in Northern Mexico City with Single Particle Mass Spectrometry, *Atmospheric Chemsitry and Physics Discussions*, *In Preparation*.

Moffet, R. C., and K. A. Prather (2005), Extending ATOFMS measurements to include refractive index and density, *Analytical Chemistry*, *77*, 6535-6541.

Molina, L. T., et al. (2007), Air quality in North Americas most populous city - overview of MCMA-2003 Campaign, *Atmos. Chem. Phys. Discuss.*, *7*, 3133-3177.

Molina, M. J., and L. T. Molina (2002), *Air Quality in the Mexico Megacity: An integrated assessment*, Kluwer Academic.

Mugica, V., et al. (2002), Temporal and spatial variations of metal content in TSP and PM10 in Mexico City during 1996-1998, *Journal of Aerosol Science*, *33*, 91-102.

Murphy, D. M., et al. (2007), Distribution of lead in single atmospheric particles, *Atmos. Chem. Phys. Discuss.*, *7*, 3763-3804.

Ohmsen, G. S. (2001), Characterization of fugitive material within a primary lead smelter, *Journal of the Air & Waste Management Association*, *51*, 1443-1451.

Ondov, J. M., and A. S. Wexler (1998), Where do particulate toxins reside? An improved paradigm for the structure and dynamics of the urban mid-Atlantic aerosol, *Environmental Science & Technology*, *32*, 2547-2555.

Pina, A. A., et al. (2000), Scanning electron microscope and statistical analysis of suspended heavy metal particles in San Luis Potosi, Mexico, *Atmospheric Environment*, *34*, 4103-4112.

Pina, A. A., et al. (2002), Scanning and transmission electron microscope of suspended lead-rich particles in the air of San Luis Potosi, Mexico, *Atmospheric Environment*, *36*, 5235-5243.

Prather, K. A., et al. (1996), Ambient aerosol analysis using aerosol-time-of-flight mass spectrometry, *Abstracts of Papers of the American Chemical Society*, *211*, 159-ANYL.

Schwartz, J., et al. (1996), Is daily mortality associated specifically with fine particles? *Journal of the Air & Waste Management Association*, *46*, 927-939.

Sedlak, D. L., and J. Hoigne (1993), The Role of Copper and Oxalate in the Redox Cycling of Iron in Atmospheric Waters, *Atmospheric Environment Part a-General Topics*, *27*, 2173-2185.

Shutthanandan, V., et al. (2002), Development of PIXE, PESA and transmission ion microscopy capability to measure aerosols by size and time, *Nuclear Instruments & Methods in Physics Research Section B-Beam Interactions with Materials and Atoms*, *189*, 284-288.

Suarez, A. E., and J. M. Ondov (2002), Ambient aerosol concentrations of elements resolved by size and by source: Contributions of some cytokine-active metals from coal- and oil-fired power plants, *Energy & Fuels*, *16*, 562-568.

Tan, P. V., et al. (2002), Aerosol laser ablation mass spectrometry of suspended powders from PM sources and its implications to receptor modeling, *Journal of the Air & Waste Management Association*, *52*, 27-40.

Tivanski, A. V., et al. (2007), Oxygenated Interface on Biomass Burn Tar Balls Determined by Single Particle Scanning Transmission X-ray Microscopy, *J. Phys. Chem. A*, *In Press*.

Vega, E., et al. (2001), Chemical composition of fugitive dust emitters in Mexico City, *Atmospheric Environment*, *35*, 4033-4039.

Walsh, D. C., et al. (2001), Refuse incinerator particulate emissions and combustion residues for New York City during the 20th century, *Environmental Science & Technology*, *35*, 2441-2447.

Wu, C. Y., and P. Biswas (1993), An Equilibrium-Analysis to Determine the Speciation of Metals in an Incinerator, *Combustion and Flame*, *93*, 31-40.

7

Characterization of an Ambient Coarse Particle Concentrator Used for Human Exposure Studies: Aerosol Size Distributions, Chemical Composition, and Concentration Enrichment

7.1 Synopsis

The goal of this experiment involved determining in real time the size, concentration enrichment, and chemical composition of coarse (> 2.5 μm) and fine (< 2.5 μm) mode particles within the non-concentrated and concentrated flows of a coarse particle concentrator used for human exposure studies. The coarse particle concentrator in this study was intended to concentrate ambient particles in the $PM_{10-2.5}$ size range before sending them into a human exposure chamber. The chemical compositions of particles in the upstream and downstream flows of the concentrator were monitored with an aerosol time-of-flight mass spectrometer (ATOFMS) in set time intervals over the course of three days. From the ATOFMS analysis, it was found that there was no change in the composition of the ten major particle types observed between the upstream and downstream flows of the concentrator under normal operating conditions. A characterization of the aerosol chemical composition and its dependence on sampling conditions is also discussed. Aerosol size distributions were measured with three aerodynamic particle-sizing (APS) instruments that were sampling simultaneously from different regions of the concentrator. The APS size distributions were used to scale

ATOFMS data and measure the ambient concentration factor for the coarse particle concentrator and the exposure chamber. The average concentration factor (ratio of inlet number concentration to the outlet number concentration) for the particle concentrator was 60±17 for the 2.5-7.2 µm size range before dilution and transport to the exposure chamber. It was observed that not only were the coarse particles being concentrated, but the fine particles as well with the concentration factor ranging from 2 to 46 between 0.54 and 2.5 µm.

7.2 Introduction

A large number of epidemiology studies indicate that particulate matter (PM) less than 10 µm in diameter (PM_{10}) is associated with adverse health effects including mortality [*Dockery and Pope*, 1994; *Dockery et al.*, 1993; *Dockery et al.*, 1992; *Gamble*, 1998; *Peters et al.*, 1997]. However, mortality is not the only effect of concern - other indicators, such as increased emergency room visits due to asthma and respiratory problems, are also considered important [*Gavett and Koren*, 2001; *Leikauf*, 2002]. Recent toxicology studies have shown that coarse PM may stimulate the release of inflammatory mediators in the lung and thus may be linked with respiratory problems [*Monn and Becker*, 1999]. Determining whether or not coarse mode particles cause adverse health effects, and if so, to what extent, is extremely important for the health community and policy makers.

In order to study the health effects of coarse particles, a system was developed to expose humans to concentrated ambient aerosols. This exposure system was built using a coarse particle concentrator implementing virtual impaction [*Demokritou et al.*, 2003]

and an exposure chamber. The coarse particle concentrator was designed to concentrate particulate matter in the $PM_{2.5-10}$ range while at the same time, providing a large enough flow of concentrated aerosol to fulfill human breathing requirements. The coarse concentrator has a low pressure drop between impaction stages to reduce the loss of semivolatile compounds that may be on the PM. For this reason, the change in chemical composition between the upstream aerosol flow and the concentrated downstream aerosol flow should be minimized. However, since the vapor phase semivolatile species are not concentrated along with the PM, the equilibrium may be disturbed leading to a possible chemical change in the aerosol. In this manuscript, we describe an experiment in which particles in the upstream and downstream flows were analyzed with aerosol time-of-flight mass spectrometry (ATOFMS), to determine if there are any chemical differences induced by the concentration process.

The opportunity was also taken to monitor the chemical composition of particles during human exposure studies to determine the chemical variability of coarse particles over short time periods. Determining the size segregated chemical composition of an aerosol is an essential part of any human exposure study in order to correlate particle types with any deleterious health effects that may occur. An advantage of using a real time, single particle instrument such as the ATOFMS in exposure studies is the ability to measure chemical changes with short temporal resolution. This information can be used to establish correlations between particle composition and other real time measurements taken during human exposure studies such as human heart rate variability. Traditionally chemical analysis is accomplished by collecting a predetermined particle size range on a variety of filter media. However, when particulate matter is collected in such a manner,

there is potential for loss of semivolatile compounds (compounds that partition appreciably to both the particle and gas phases under normal ambient conditions) that may contribute significantly to the toxicological properties of the aerosol [*Eatough et al.*, 2003; *Seagrave et al.*, 2003]. Since the particles are under vacuum for less than 1 ms in the ATOFMS, loss of semivolatile compounds is minimal, making the analysis of these species more feasible [*Tobias et al.*, 2000]. Further problems are associated with bulk measurements because chemical reactions may occur on the filter substrate between sample collection and analysis which may change the toxicological properties of the particulate matter. It can also be difficult to collect enough particulate matter for mass measurements during a typical human exposure studies (which only last for two hours). ATOFMS can provide a relative measure of the amount of species on certain particle types, but the use of laser desorption/ionization can introduce detection biases and challenges for chemical quantitation. Additionally, the size distribution obtained from the ATOFMS is not representative of the actual aerosol size distribution due to the decreasing detection efficiencies of smaller sizes. The latter point is overcome in this paper by a method of scaling the ATOFMS measurement to another real-time size distribution measurement – the aerodynamic particle sizer.

This paper reports results from a study performed to monitor the size and chemical composition of aerosol particles in real time during human exposure studies carried out at the EPA Human Studies Facility in Chapel Hill, NC. During three characterization studies, the chemical composition of the inlet and outlet of the concentrator were monitored to look for any changes induced by the concentrator. Additionally, using several APS instruments, concentration factors at the outlet of the

concentrator are presented to provide information on the levels of coarse and fine particles to which the human subjects are exposed.

7.3 Experimental Methods

The experimental setup used in this study is shown in Figure 7.1. Ambient air was drawn in at 5000 LPM from the roof top of the EPA Human Studies Facility in Chapel Hill, NC and transferred downward into the building (T = 21ºC) to the PM_{10} inlet of the concentrator via a 16 ft long duct with a 1 ft outer diameter. The size selective inlet and the virtual impactors are the same as those used in Demokritou et. al. (2003). The major outward flow was 4500 LPM for the first impaction stage while the major outward flow out was 450 LPM for the second impaction stage, giving a 50 LPM concentrated aerosol flow. The concentrated aerosol flow had a theoretical concentration factor (CF) of 100 (obtained from the ratio of the inlet flow to the outlet flow), assuming coarse particles have 100% transmission. After flowing out of the virtual impaction stages, the concentrated aerosol was diluted with a sheath of conditioning air (150 LPM, RH ~ 5 %), which was introduced around the concentrated aerosol flow. This conditioning air was added to provide enough airflow for the human subjects' breathing requirements and to condition the air to moderate the outside temperature and relative humidity changes. The flow velocities of the conditioning air and the concentrated air were matched to ensure laminar flow. After the 150 LPM conditioning air was added, the overall theoretical concentration factor of the aerosol was 25.

Particle size distributions were measured with two model 3321 APS instruments and one model 3310 APS instrument (TSI Inc., St Paul, MN). The APS instrument

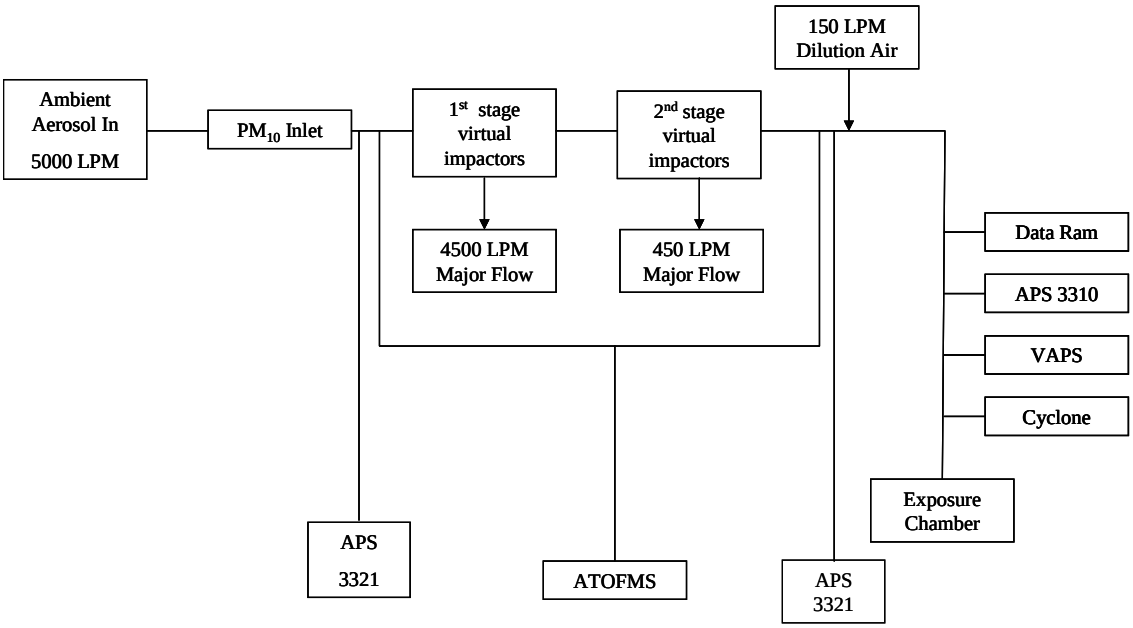

Figure 7.1. Experimental layout for the coarse concentrator/exposure chamber studies.

measures aerodynamic particle size by measuring the particle time-of-flight between two laser beams and relating this time to aerodynamic diameter. The APS 3321 instruments were redesigned to eliminate coincidence errors and errors associated with the recirculation of particles inside the scattering region of the instrument. As shown in Figure 7.1, the two 3321 APS instruments were located between the PM_{10} inlet and the first virtual impaction stage while the second 3321 APS instrument was located between the second virtual impaction stage and the dilution air. The 3310 APS instrument was located between the Data RAM (Thermo) and versatile air pollutant sampler (VAPS) (University Research Glass). The VAPS was used to collect samples on filters to compare both mass and chemical composition. The APS 3310 measured the aerosol concentration just after mixing with the dilution air and before the exposure chamber. The 3321 APS instruments were factory calibrated prior to this experiment to ensure both the particle size and number concentration were accurate and consistent. All sampling lines to the APS and ATOFMS were fabricated with 1/2" and 3/8'' stainless steel tubing respectively. All sampling probes were aligned parallel to the direction of flow, having diameters and flow rates such that anisokinetic losses were negligible. The two APS 3321 instruments typically differed by 2-22% in the individual size bins on the same aerosol sample. Since the two instruments were running simultaneously in different positions to calculate concentration factors in various regions of the concentrator/exposure chamber system, their readings needed to be made comparable with one another. To accomplish this, scaling factors between the two instruments were experimentally determined for each APS size bin as follows. Let the scaling factor be defined as

$$\gamma_i = N_{av}/N_i \qquad \text{(Eq. 7.1)}$$

where N_{av} is the average number concentration reading between the two APS instruments on the same aerosol sample, and N_i is the raw number concentration given by the *i*th APS on that same sample. The value of γ_I was determined during a separate 25 minute study in which the two APS instruments sampled the same aerosol flow through identical sampling lines. A scaled number concentration that is consistent between the two instruments is then given by Equation 2:

$$N_{sc} = \gamma_i N_{s,i} \qquad \text{(Eq. 7.2)}$$

where $N_{s,i}$ is the raw experimental number concentration to be scaled (for a different aerosol sample than N_i). All of APS number concentrations ($N_{s,i}$) collected during the characterization and exposure studies were adjusted according to Eq. 2. Since the scaling factors changed between the concentrated and non concentrated aerosol streams, different scaling factors for the different streams were determined.

A transportable ATOFMS instrument [*Gard et al.*, 1997] was used for the characterization of particle size and chemical composition in this study. In Figure 7.1, the ATOFMS sampled particles from the coarse concentrator system 1) directly after the PM_{10} size selective inlet (before passing through the virtual impactors), or 2) after the second stage of impaction, but before the dilution air was supplied to the system. The sampling lines for the APS systems and the ATOFMS were similar in their materials

(stainless steel), probes, bends and lengths as to enable reliable scaling of the ATOFMS data to the APS data. A scaling function (S_{ATOFMS}) was used to scale the ATOFMS number concentration for different particle classes to an APS number concentration. S_{ATOFMS} was determined as a function of aerodynamic diameter (using the 37 logarithmically spaced APS bins between 0.561 and 7.498 μm) according to the relation

$$S_{ATOFMS} = N_{aps}/N_{ATOFMS} \quad \text{(Eq. 7.3)}$$

where N_{aps} is the APS number concentration and N_{ATOFMS} is the ATOFMS number concentration on the same sample. Scaling in this manner is a semiquantitative way to correct for the size bias and low transmission efficiency of the ATOFMS inlet [*Allen et al.*, 2000]. APS and ATOFMS data for the entirety of each exposure or characterization study were used to calculate S_{ATOFMS}.

Two different types of experiments were performed during sampling periods consisting of exposure experiments and a characterization experiment. Exposures refer to sampling periods when a human subject was in the exposure chamber. The two exposure experiments that were monitored with the ATOFMS took place on 8/25/03 from 9:57-11:57 and on 8/27/03 from 9:27-11:27, EDT. The characterization of the concentrator refers to a study in which the inlet and outlet of the concentrator were monitored for eight 1 hour time periods alternating the ATOFMS measurements between the upstream and downstream flows of the concentrator. The characterization sampling period of 12:00 – 21:00 EDT on 8/26/03 was used to determine whether or not the virtual impactors chemically altered the particles.

ATOFMS data from the characterization experiment and the exposure studies were analyzed with ART-2a [*Song et al.*, 1999], using a vigilance factor of 0.7, a learning rate of 0.05 and 20 iterations. ART-2a is an artificial intelligence algorithm that sorts single particle mass spectra into specific particle types or clusters. Using a vigilance factor of 0.7 with ART-2a analysis, 138 clusters were obtained. The 20 most populated clusters represented 88% of the particles. The 138 clusters were placed into 10 general classes and labeled according to the dominant species: elemental carbon (EC)- with no negative spectrum (EC-no neg), Long EC (having EC peaks above m/z = 100), Calcium dust (Ca Dust), Potassium (K) – sulfate - Organic carbon (OC) (K-sulfate-OC), EC-K-sulfate, Dust, K-Phosphate, Sea Salt, OC while the rest were placed in a "No ID" class. 10 classes were settled upon for two reasons: 1) to keep the statistics high enough enable reliable comparisons and 2) the other minor particle classes represented a very small fraction of the particles. Criteria used to distinguish the classes are discussed in the results and discussion section.

For comparing the chemical compositions in the exposure and characterization studies, raw number concentrations (N_r) of the particle classes were scaled to give a scaled number concentration (N_s) according to the relationship:

$$N_s = S_{ATOFMS} N_r \qquad \text{(Eq. 7.4)}$$

where S_{ATOFMS} was introduced in Eq. 3. Again, it should be noted that because the ATOFMS number concentration is not representative of atmospheric particle concentrations, this scaling procedure is used to transform the ATOFMS number

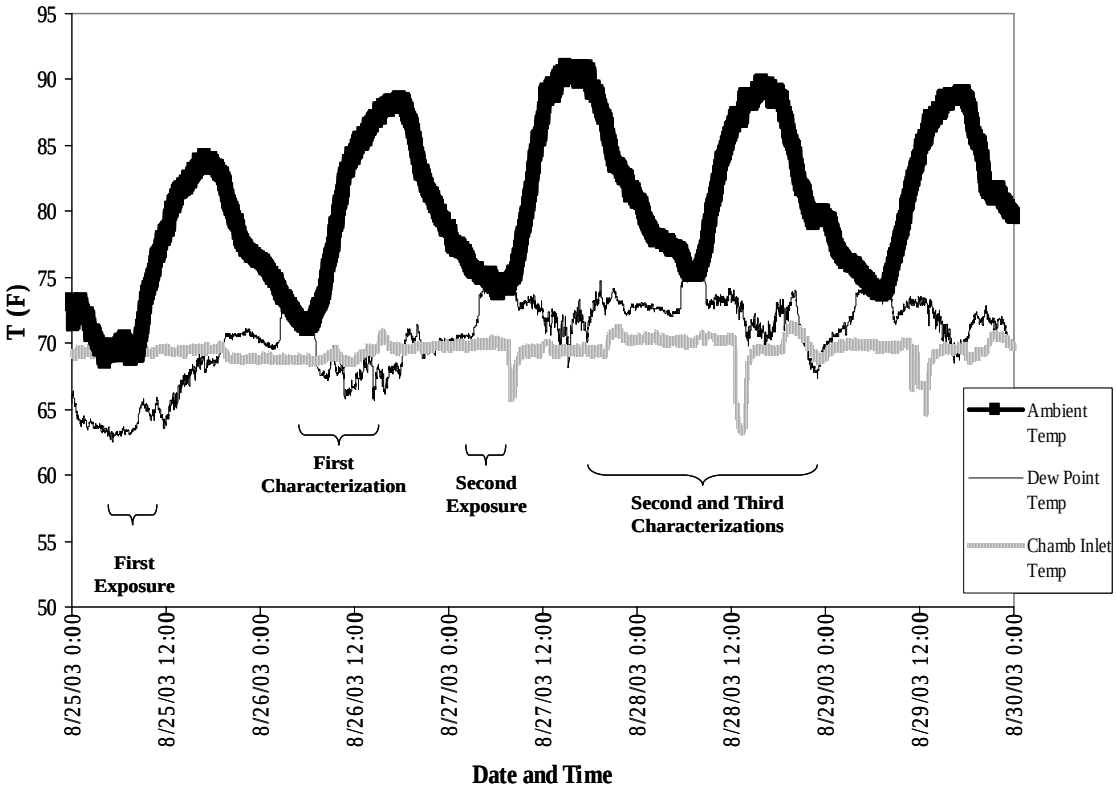

Figure 7.2. Temperature conditions during the time of the coarse concentrator studies.

concentration into a scaled APS number concentration for different particle classes. Scaling to the APS compensates for the strong dependence the transmission efficiency of the ATOFMS inlet has on particle size.

7.3.1 Sampling Conditions

Two important factors when sampling from the coarse concentrator are the temperature and relative humidity (RH) of the ambient air being introduced. When a relatively warm and humid aerosol containing ambient air sample is transferred into the concentrator at room temperature, there is a possibility for condensation to occur. The temperature around which this process occurs and the air parcel becomes saturated is called the dew point temperature (T_d). The Clausius Clayperon relationship can be used to calculate the dew point temperature. The results of this calculation over the entire study are shown in Figure 7.2. Figure 7.2 shows T_D, outside temperature, and the chamber inlet temperature during the characterization and exposure studies. The chamber inlet temperature is the temperature of the aerosol flow going into the chamber. This temperature was close to that of the building. During the first exposure and characterization studies, the dew point temperature was lower than the inlet temperature of the exposure chamber. During the second exposure and the second and third characterization studies, the dew point was above chamber inlet temperature.

7.4 Results and Discussion

7.4.1 Concentration Factors and APS Size distributions

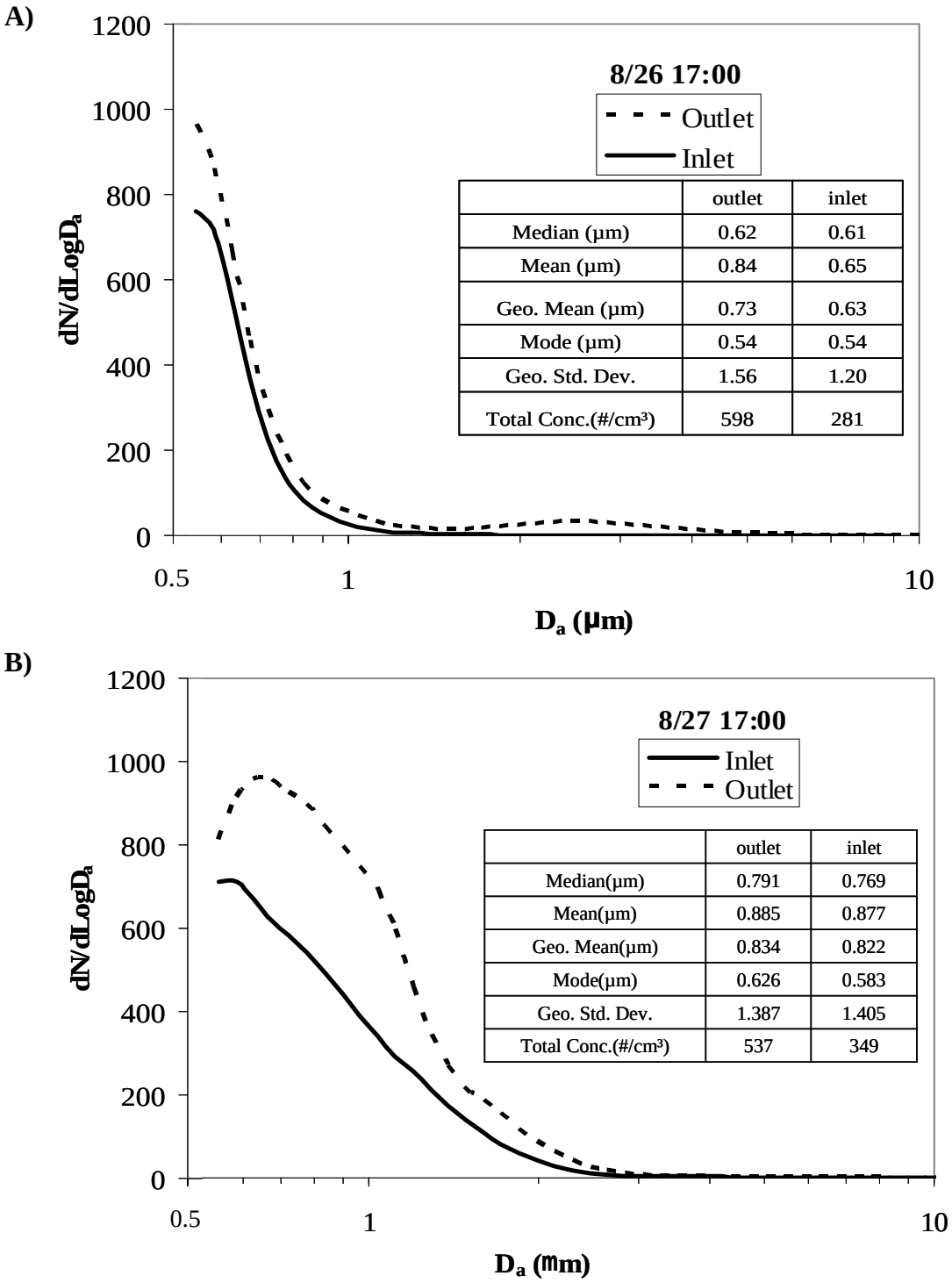

	outlet	inlet
Median (µm)	0.62	0.61
Mean (µm)	0.84	0.65
Geo. Mean (µm)	0.73	0.63
Mode (µm)	0.54	0.54
Geo. Std. Dev.	1.56	1.20
Total Conc.(#/cm³)	598	281

	outlet	inlet
Median(µm)	0.791	0.769
Mean(µm)	0.885	0.877
Geo. Mean(µm)	0.834	0.822
Mode(µm)	0.626	0.583
Geo. Std. Dev.	1.387	1.405
Total Conc.(#/cm³)	537	349

Figure 7.3. A) Size distributions at the inlet and outlet of the concentrator during normal sampling conditions B) Size distributions at the inlet and outlet during a condensation event.

There was strong evidence for condensation events during the second exposure study and the last two characterization studies. Initial evidence of condensation was indicated by the accumulation of liquid water in the PM_{10} inlet. In addition, the aerosol size distributions showed a size shift as shown in Figure 7.3 which shows the distributions measured at the inlet and outlet during two different studies. Figure 7.3Ashows the APS size distributions for the first characterization study where the room temperature was above the dew point temperature, and Figure 7.3B shows the distributions for the second characterization study when room temperature was below the dew point temperature. All times where the dew point temperature went above room temperature and the size distributions widened will be referred to as condensation events. Even when the outlet number concentration during the condensation events was divided by the concentration factor, there was still a difference between the inlet and outlet distributions, suggesting additional condensation occurring as the particles were being sampled into the building.

For some highly hygroscopic particles, condensation occurs at temperatures below T_D, while for hydrophilic particles, condensation occurs above T_D. Thus, particles having different compositions may have different growth characteristics under saturated conditions. To investigate the possible chemical bias for water condensation, we examined the size distribution shifts for several particle classes and found consistent changes for all particle types.

Table 7.1 Concentration factors (CF) before and after dilution

D_a (μm)	CF Before Dilution	CF After Dilution	D_a (μm)	CF Before Dilution	CF After Dilution
0.54	2	0	2.13	23	17
0.58	2	0	2.29	31	14
0.63	2	1	2.46	46	18
0.67	2	1	2.64	59	17
0.72	2	1	2.84	68	17
0.78	2	1	3.05	64	17
0.84	2	2	3.28	63	17
0.90	2	1	3.52	61	13
0.97	2	1	3.79	64	15
1.04	3	1	4.07	63	13
1.11	3	1	4.37	58	14
1.20	4	2	4.70	72	15
1.29	4	3	5.05	83	18
1.38	5	3	5.43	71	9
1.49	5	3	5.83	63	8
1.60	6	6	6.26	38	6
1.71	8	8	6.73	71	4
1.84	10	11	7.23	11	4
1.98	15	13			

From the size distributions measured in the various regions, the concentration factors were calculated and the results are shown in Table 7.1. The concentration factor (CF) was calculated by dividing the inlet number concentration by the outlet numberconcentration for each size bin. The undiluted concentration factor agrees well with the results obtained from the work of Demokritou et al. (2003). In that work, Demokritou et al. determined a concentration factor of 68 using hollow glass spheres having a mean diameter of 3.68 μm. In this study, the concentration factors were determined using ambient aerosols having a mean diameter of 0.71 μm that gave an average concentration factor of 60±17 for coarse mode particles (2.5-7.2 μm) before dilution. The concentrationfactors in Table 7.1 are seen to fluctuate dramatically at higher sizes due to more factor of 60±17 for coarse mode particles (2.5-7.2 μm) before dilution. The concentration factors in Table 7.1 are seen to fluctuate dramatically at higher sizes due to more uncertainty in counting statistics. There are two possible reasons for the poor counting statistics at the higher sizes: 1) very low particle concentrations at these sizes and/or 2) low the APS transmission efficiency at these higher sizes.

One topic that has not been addressed in previous studies [*Demokritou et al.*, 2003] that may be of interest to the health effects community is the concentration factor for fine particles. The cutpoint of an inertial impactor is defined as the size where 50% of the particles of a given size follow the major flow and 50% follow the minor flow [*Hinds*, 1999]. Therefore, if the ratio of flows is greater than a factor of 2, particles below the cutpoint will still be concentrated. This is clearly demonstrated in the present study since concentration factors ranging from 2 to 46 were obtained for particles with D_a between 0.54 – 2.46 μm. This is an important finding as particles in this size range can have

significantly different compositions and sources than coarse mode particles [*Hughes et al.*, 2000]. Since the cutpoint region is characterized by a fairly sharp cutoff, the concentration factors vary strongly with D_a. The concentration factors after addition of dilution air differed from the undiluted concentration factors by a factor of 4-5 for coarse mode particles, which is consistent with the dilution ratio of the concentrated to diluted streams.

The above concentration factor analysis allows direct comparison with Demokritou et al, but it is also important to estimate the relative contribution both the coarse and fine modes have to particle mass before and after undergoing the concentration process. To estimate the relative contributions to coarse and fine mode mass, we assumed a density of 1 g/cm^3 and calculated the coarse and fine mode mass fractions using the APS data. Although this is a simplistic assumption that neglects the true densities and shape factors, it is sufficient for the comparisons that follow. It was found that before concentration, 77% of the particles contributed to the fine mode mass and 23% of the particles contributed to the coarse mode mass. In the chamber, the trend reversed so that 25% of the particles contributed to the fine mode mass and 75% of the particles contributed to the coarse mode mass. These numbers are consistent with the mass fractions derived from the cyclone for the concentrator outlet just before the chamber; with these measurements showing that 31% of the mass was in the fine mode and 69% of the mass was in the coarse mode. Filter data also show that the concentration during the exposures is fairly high, being 56.12 and 102.83 mg/m^3 during the first (8/25) and second (8/27) exposures, respectively.

When interpreting the results in this section with regards to health effects it is crucial to keep in mind how the size distributions of the particles change when number, surface area, and mass are used. It may be important that the particles in the fine mode are being concentrated when considering the health effects linked with the total surface area and number concentration of the particles. However, if one is mainly concerned with the effects of particle mass on health, then the concentration of particles at or below the cut point of the concentrator becomes less of an issue.

7.4.2 Raw ATOFMS Size Distributions and Scaling Function (S_{ATOFMS})

Under normal ambient conditions, particles are not frequently detected over 3 μm with the ATOFMS. Figure 7.4 shows a size distribution produced using raw ATOFMS counts for concentrated and non concentrated aerosol streams. These raw ATOFMS counts include only particles that were chemically analyzed by the ATOFMS. When sampling the concentrated stream of the coarse particle concentrator, particles above 4 μm were commonly detected with the ATOFMS, an observation which supports their enrichment. Figure 7.4 also shows a peak occurring at ~1.7 μm, corresponding to the most efficiently focused size into the ATOFMS.

As mentioned in the experimental section, S_{ATOFMS} is the factor that we need to multiply the ATOFMS number concentration by to obtain a number concentration that has been standardized to the APS instruments. S_{ATOFMS} was calculated every hour for the duration of the characterization and exposure studies. Figure 7.5A shows the hourly scaling functions calculated for the first characterization study. As shown in the figure,

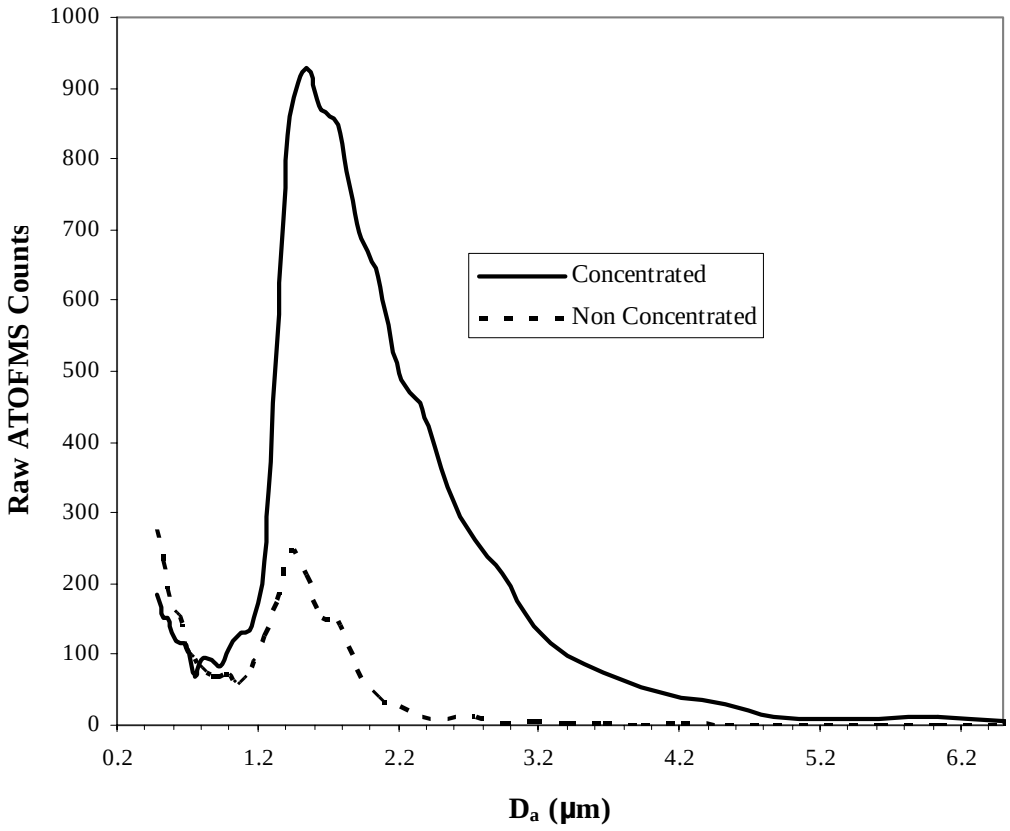

Figure 7.4. Raw size profiles produced by ATOFMS with the coarse concentrator on and off.

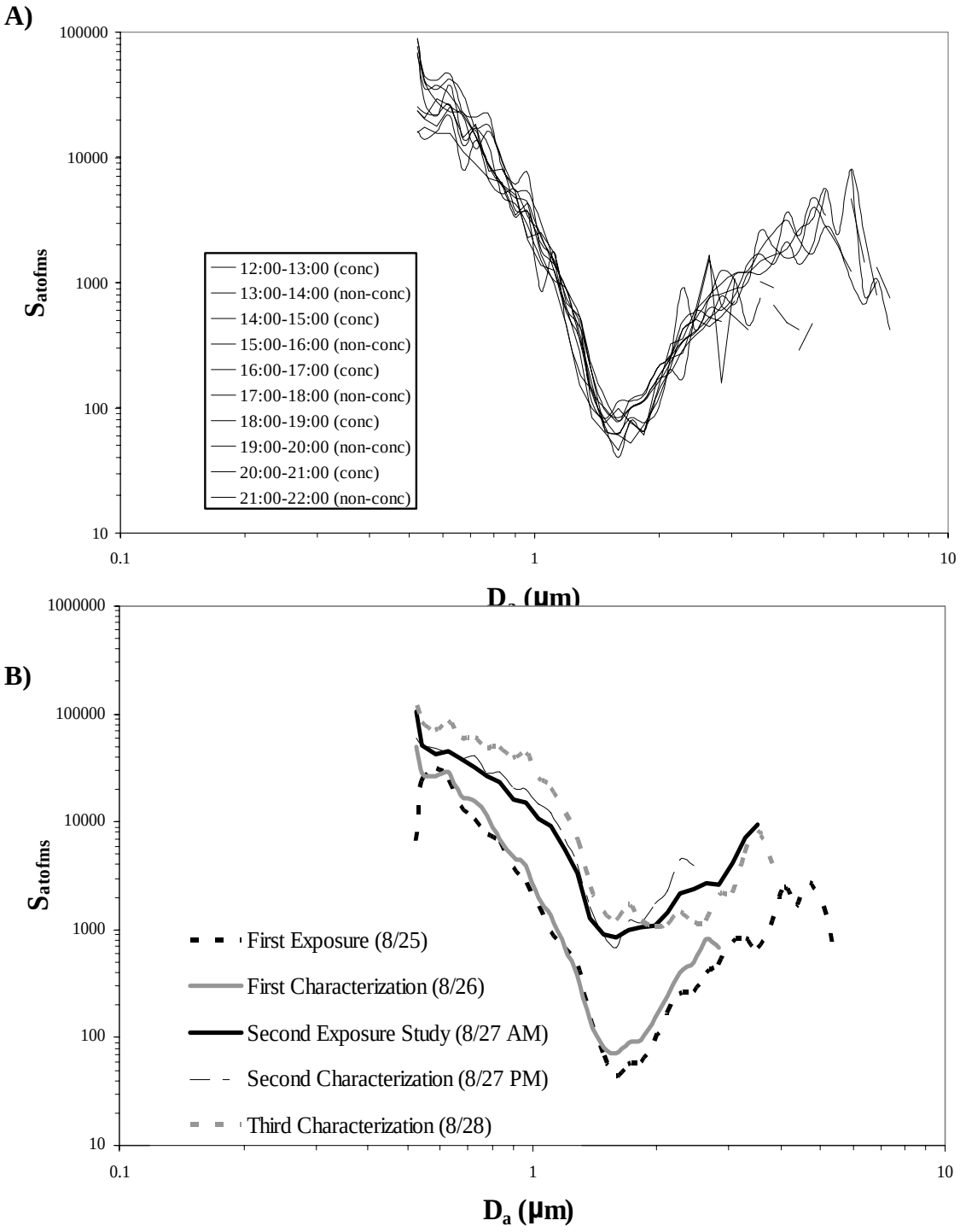

Figure 7.5. A) Hourly scaling functions for the first characterization study. B) Scaling functions derived for important time frames during the coarse concentrator studies. The curves represent averages of one hour samples for the entirety of each study.

the scaling function remained relatively constant throughout the period of one day. Figure 5A also shows that the scaling function is relatively constant between concentrated and non-concentrated aerosol streams. However, at the extremes of the scaling function (i.e. for very large and very small D_a), the function shows larger oscillations due to the smaller sample sizes used for averaging.

Figure 7.5B shows S_{ATOFMS} as a function of aerodynamic diameter for the three characterization and two exposure experiments. The scaling functions can be used for the determination of any detection efficiency changes for a given aerosol concentration or composition. The S_{ATOFMS} did not change much throughout the period of one day, however it changed significantly on a day-to-day basis most likely due to changes inambient temperature and RH. During the first exposure and characterization experiments, the relative humidity was low and there was no condensation occurring on the particle surfaces. All of the other experiments were accompanied by high RH, causing condensation of water on particle surfaces. Condensation events are evident in the ATOFMS data by a decrease in the detection efficiency as illustrated by the overall increase in S_{ATOFMS} for the periods when condensation was occurring. This is most likely due to the fact that inorganic aqueous aerosols typically have higher ionization thresholds and produce lower ion currents [*Neubauer et al.*, 1997], yielding a smaller fraction of mass spectra thereby raising S_{ATOFMS}.

7.4.3 ATOFMS Chemical Analysis

As described in the Experimental Methods section, the ambient particles detected in North Carolina could be divided into 10 major chemical types based on the distinct patterns in their mass spectra and ART-2a analysis. The most prevalent class observed for coarse mode particles was the K-Phosphate class. This class was dominated by negative ion phosphorous (PO_3 and H_2PO_4 at m/z = -79 and -97) and positive ion K (m/z = +39) peaks. Possible contributors to the K-Phosphate class include coal combustion,vegetative detritus, biomass burning, pollen, and road dust [*Guazzotti et al.*, 2003; *Liu et al.*, 2003; *Noble and Prather*, 1997].

Figure 7.6 shows a soil/dust particle that was labeled as the dust class due to its intense aluminosilicate peaks. Silicates and aluminum are the major markers for crustal material [*Guazzotti et al.*, 2001; *Silva and Prather*, 2000]. Silicate ions were observed in the negative spectrum, while aluminum appeared in the positive ion spectrum in theatomic ion form with the oxides of aluminum in the negative spectrum. This particular soil particle contains markers consistent with the fact that the North Carolina Piedmont soils are composed mainly of kaolinite ($Al_2Si_2O_5(OH)_4$), which is an aluminosilicate mineral [*Rice et al.*, 1985; *Robarge*, 2003].

An interesting sub-class of the K-Phosphate class was the amine particle type shown in Figure 7.7. The amine class was labeled as such based on the presence of major ion peaks at m/z = 58, 59, 60, 74, 86, 104 and minor unknown peaks at m/z = 154 and 184. With the exception of the peak at m/z = 104, the other major peaks are all consistent with those detected in previous field studies in Atlanta and in laboratory studies with pure

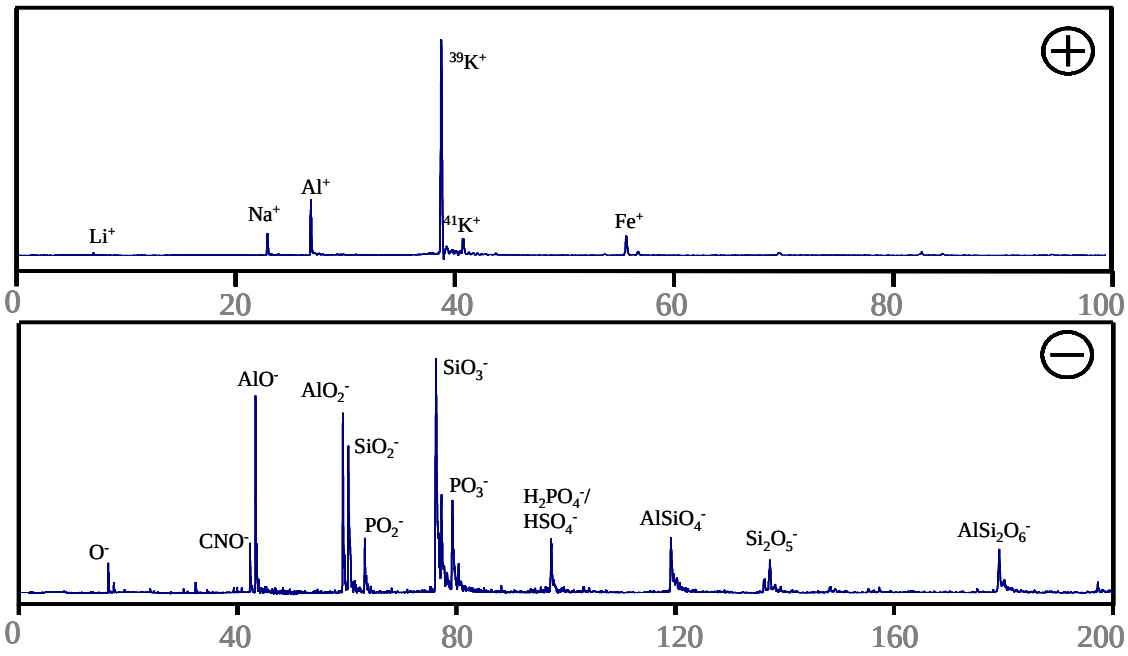

Figure 7.6. A single particle member of the dust class.

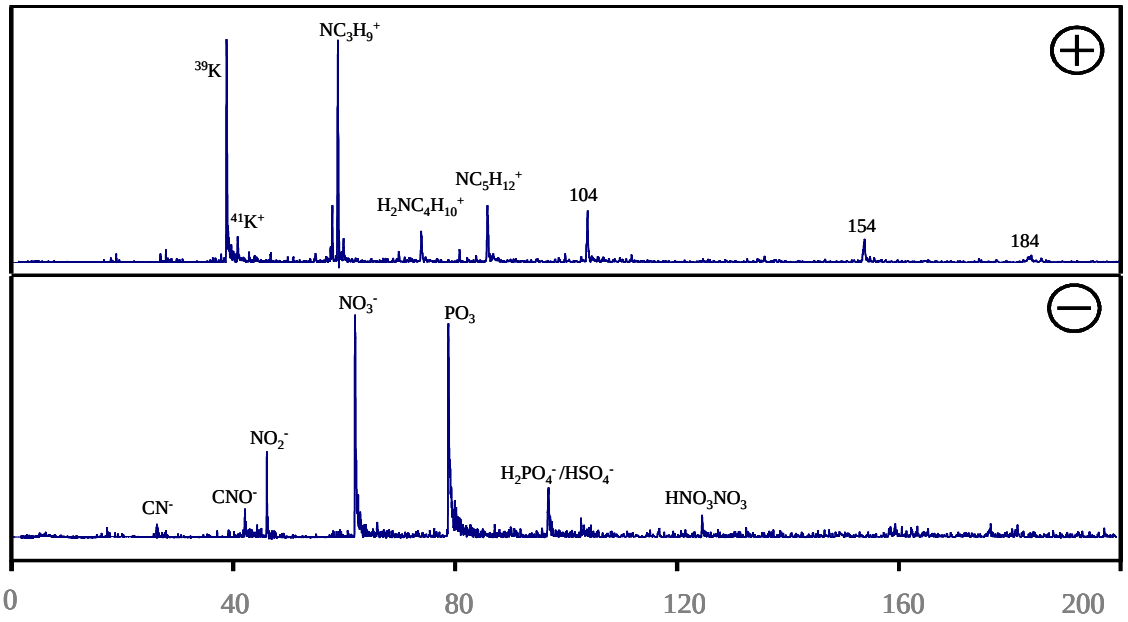

Figure 7.7. A single particle member of the amine sub-class. This class was common only in coarse mode particles and always occurred with a large ^{39}K signal.

alkyl amines [*Angelino et al.*, 2001]. However, the amines in this study appear to be adifferent organic species and from a different origin due to the fact that they are present only in the coarse mode and are coupled with a large potassium ion signal. Furthermore, these peaks did not show any correlation with RH or an anti-correlation with temperature, suggesting that this class is not semivolatile and therefore does not undergo a significant amount of gas-to-particle partitioning. The identity of the peak m/z = 104 is unknown, but may represent the protonated molecular ion (i.e. MH^+) of a nitrogen-containing organic species. The isotopic ratio for 104/106 does not support the identification of the peak at m/z = 104 as K_2CN - a peak observed in previous studies by our group [*Silva and Prather*, 2000]. Possible sources for the amines and nitrogen containing organic species include 1) swine and/or poultry farms 2) combustion activities 3) synthetic or natural fertilizers 4) sea spray or 5) reactions of NO_x with biogenic compounds [*Cornell et al.*, 2003]. It should be noted that North Carolina is known to have high concentrations of ammonia and other nitrogen-containing organic compounds due to large swine and poultry operations [*Robarge et al.*, 2002; *Walker et al.*, 2000].

Although the focus of the coarse concentrator experiments was on the $PM_{2.5-10}$ fraction, the $PM_{2.5}$ fraction still made up the largest portion of the particles sampled (by number) in this study as discussed above (Figures 7.3 and 7.4). The two classes making up the bulk of the $PM_{2.5}$ fraction were the classes containing elemental carbon (EC) and organic carbon (OC). The mass spectrum of a typical particle that was classified as “long EC” is shown in Figure 7.8. This class was dominated by carbon clusters appearing in 12 m/z unit increments extending out to masses beyond m/z = 100. The other EC classes were typified by carbon peaks at lower m/z units such as 12 and 36, and either produced

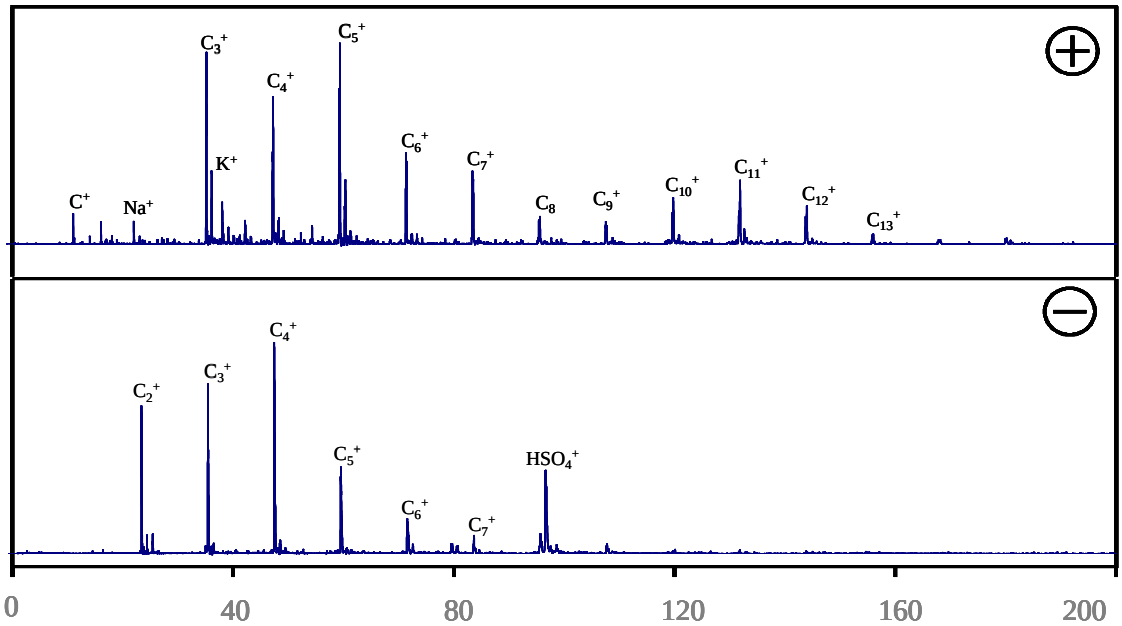

Figure 7.8. A single particle member of the long-EC class.

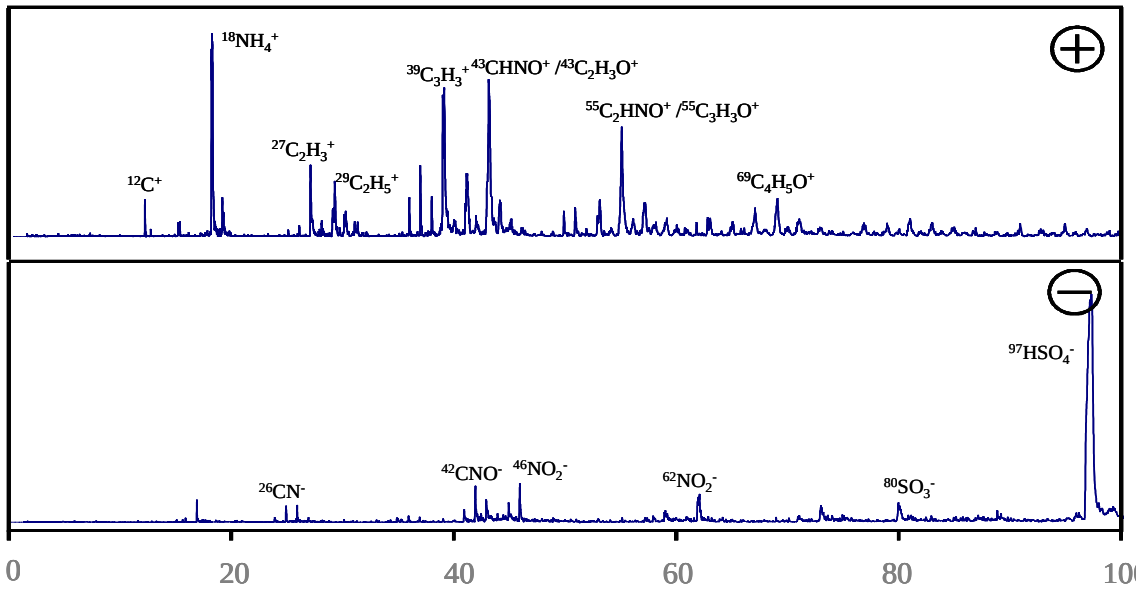

Figure 7.9. A single particle member of the OC class.

no negative spectrum or had sulfates and elemental carbon peaks in the associated negative spectrum. The lack of negative ion peaks was most likely an instrumental issue. A typical OC spectrum is shown in Figure 7.9. The spectra for particles in this class contain the usual organic peaks at m/z = +12 and +27, but additionally have major peaks at m/z = +43 and +55 corresponding to either oxidized carbon compounds ($^{43}C_2H_3O^+$ and $^{55}C_3H_3O^+$) or nitrogen-containing organics ($^{43}CHNO^+$ and $^{55}C_2HNO^+$). The OC class also shows a dominant peak at m/z = +18 most likely due to secondary $^{18}NH_4^+$, but also possibly due to the presence of nitrogen-containing organic species.

Several different types of secondary species were found on all particles in the PM_{10} size range. From Figures 7.6, 7.7 and 7.8, bisulfate $[^{97}HSO_4]^-$ and nitrate $[^{62}NO_3]^-$ were detected on a variety of particle types. Other possibilities for secondary species include oxidized organic carbon and ammonium. Throughout the study, ammonium (m/z = 18) and oxidized organic carbon (m/z = +43 and +55) showed a strong positive correlation with RH over all size ranges. At night the fraction of particles detected having ammonium and organic carbon was as high as 65%. During the daytime, when the exposure studies were carried out, the percentage of detected particles having ammonium and oxidized organic carbon was near the daily minimum of 30-40%. These observations are consistent with previous observations made by our group in the southeastern United States [*Liu et al.*, 2003]. Depending on the availability of HNO_3 or H_2SO_4 in the atmosphere, ammonia may react with these species in the gas phase to produce secondary NH_4NO_3 or NH_4HSO_4 on ambient particles [*Finlayson-Pitts and Pitts*, 2000]. These observations suggest there was a significant amount of gas-to-particle partitioning occurring in this area. Ammonium, sulfates, and nitrates are important from a health

effects perspective due to their reactions with strong acids, which are known to be associated with the inflammation of the throat and lungs [*Lippmann*, 1989].

7.4.4 Chemical Characterization of the Concentrator and Exposure Studies

For the purpose of characterizing the coarse particle concentrator, a sampling protocol was developed where the non-concentrated flow of the concentrator was measured for a set time interval followed by a measurement of the concentrated flow for the same duration of time. For the first and second characterizations, this time interval was 1 hr and for the third characterization study this time interval was ½ hr. Particles from all time intervals were classified with ART-2a and subsequently classified into the ten major particle types discussed above. Results from the first characterization study are shown in Table 7.2.

Table 7.2 shows that the coarse concentrator does not significantly affect the particle composition. The first row in Table 7.2 shows the uncertainty associated with each particular column. The uncertainty is given by Poisson statistics where the variance associated with the measurement is equal to the square root of the number of particles used to calculate the ATOFMS number concentration. The uncertainty is seen to be large where the particle counts are low - particularly above 2.5 µm. Although the measurements for the coarse mode particles are associated with a much higher uncertainty, measurements for fine mode particles also indicate that the concentrator does not change the chemical composition of the particles with a higher degree of confidence.

Table 7.2 Percent of particle types for the upstream (US) and downstream (DS) particles for the first, second and third characterization studies. The uncerntianty refers to the entire column since it is normalized.

Particle Class	First Characterization				Second Characterization				Third Characterization			
	>2.5 µm		<2.5 µm		>2.5 µm		<2.5 µm		>2.5 µm		<2.5 µm	
	% US	% DS	% US	% DS	% US	% DS	% US	% DS	% US	% DS	% US	% DS
Uncertainty	± 36	± 5	± 5	± 3	± 49	± 11	± 4	± 3	± 51	± 13	± 5	± 3
EC – No Neg.	0	0	36	32	3	1	55	47	3	1	73	62
Long EC	0	0	2	2	0	0	2	3	0	0	2	2
Ca Dust	18	17	0	1	30	14	1	2	0	12	1	1
K-Sulfate-OC	0	4	21	19	15	5	8	9	3	3	4	5
EC-K-Sulfate	0	0	17	18	3	1	12	12	3	1	6	8
Dust	25	25	2	4	8	23	2	6	24	27	2	5
K-Phosphate	50	45	13	14	37	39	13	12	56	34	11	12
Sea Salt	7	7	0	1	5	16	1	3	12	20	1	4
OC	0	0	8	9	0	1	7	6	0	0	1	2
No ID	0	1	0	1	0	2	0	1	0	0	0	0

To determine if the concentrator affected the partitioning of the semivolaitle species onto the particles, two analysis steps were conducted. A general comparison was made of the overall particle composition upstream and downstream of the concentrator during periods where we switched the sampling lines between the two locations. No overall increase in ion intensities was observed for particles downstream of the concentrator relative to upstream values. This was determined by comparing separate ART-2a analyses on the upstream and downstream particles and comparing the resulting types. No new particle types were formed within the outlet stream that were missing in the inlet stream. We also examined the digital mass spectra [*Liu et al.*, 2003] of the ten major particle types to determine if there was a fractional (or area) increase or decrease in the most likely semivolatile species (i.e. ammonium, amines, nitrate, and organic carbon species). Again, no change was observed, further supporting the fact that no material was added or lost from the particles during the concentration process.

Table 7.2 also shows that the majority of the particles in the fine mode are classified as either EC or OC, whereas coarse mode particles are mostly dust and inorganic potassium types as observed during the exposure studies. The size-composition relationship reflects the sources and mechanism of formation of the individual particles. For example, EC and OC are expected to be in the fine mode since they are generated by combustion processes and the coarse mode particles consist mainly of dust generated by mechanical or abrasion processes.

The percentages of particle classes during the two hour human exposure studies were also examined and are shown in the pie charts of Figure 7.10. During the first exposure, when no condensation occurred ($T_s > T_d$), there were fewer organics in both the

coarse and fine modes than there were during the second exposure when condensation was occurring ($T_s < T_d$). Large amounts of polar biogenic organic compounds such as the reaction products of terpenes with ozone, have been identified in the Chapel Hill region [*Edney et al.*, 2003; *Hagerman et al.*, 1997], and are known to be hygroscopic due to the polar nature. Because of their hygroscopicity, these particles will attract liquid water and grow larger when conditions of saturation are reached. Correspondingly, organics (m/z = 12, 27, 43) were found to contribute to the coarse mode during the second exposure study when condensation was occurring as shown by the pie charts of figure 10. From the pie charts of Figure 7.10, we see that during the first exposure there are fewer organics in the first exposure than there are in the second exposure when the temperature and humidity were higher. Since the wind direction remained relatively constant during the week when the two exposures were carried out, the change in the amount of organics in the coarse mode was likely due to other conditions such as temperature and RH.

7.4.5 Temporal Evolution of Particle Classes During Exposure Studies

The ability of the ATOFMS to track particle classes in very short time periods can provide important composition information for relatively short exposure studies. Figure 7.10a shows the temporal profile for concentrated particles during the first two hour exposure study conducted on 8/25/03. The raw counts for each particle class are plotted with a temporal resolution of 10 minutes. The most noticeable temporal trend during the first exposure was the decrease of the K-Phosphate class and the increase of the EC class as time progressed from ~10:50 to the end of the exposure. Figure 7.10b shows the

Figure 7.10. Temporal profiles for the major particle classes during a) the first two hour exposure study on 8/25/03 and b) the second two hour exposure study on 8/27/03. The sampling locations were changed from concentrated to non concentrated as illustrated by the vertical lines. The pie charts show fractional abundance during both the exposure studies.

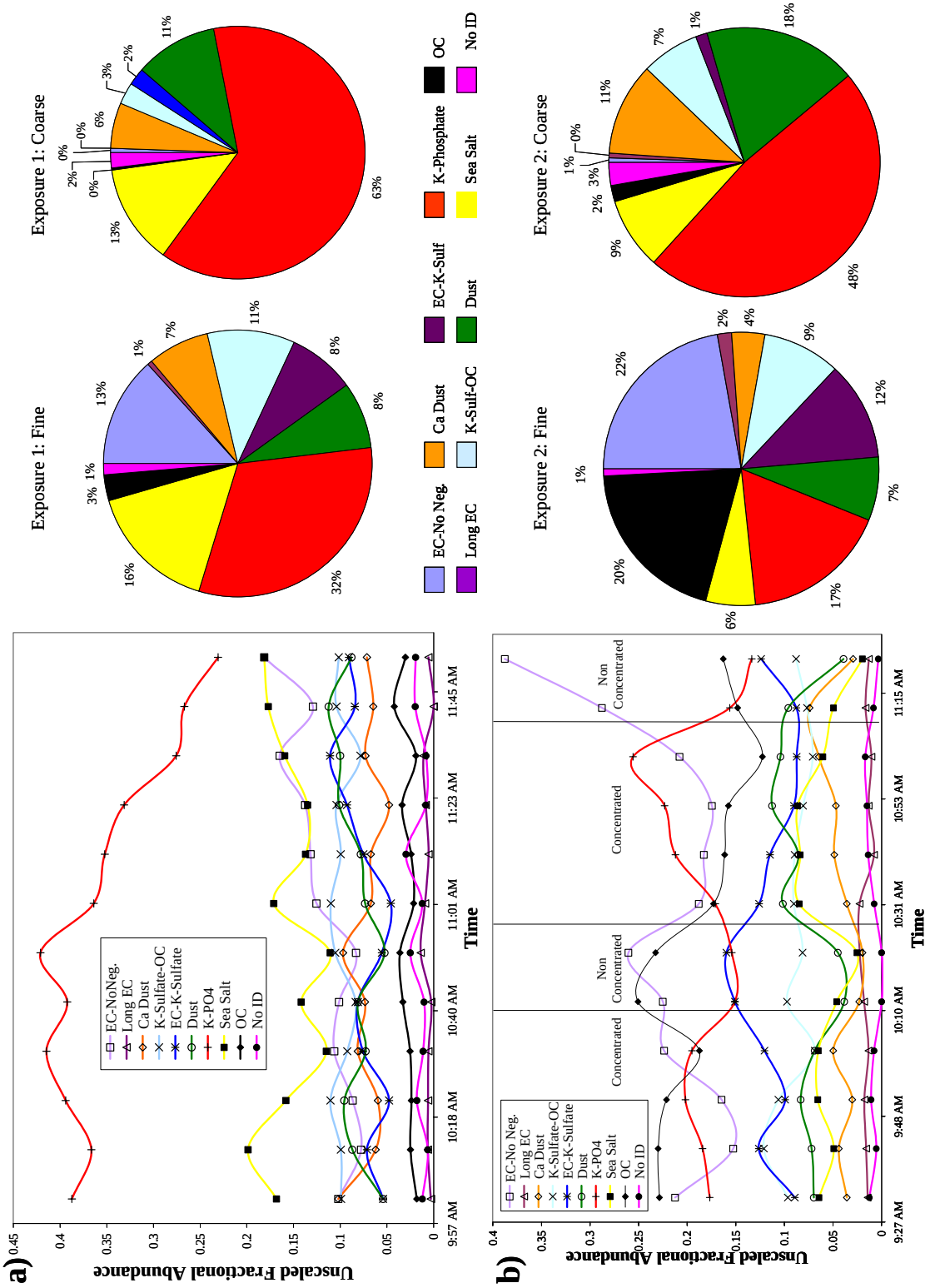
Exposure 1: Coarse
Exposure 1: Fine
Exposure 2: Coarse
Exposure 2: Fine
EC-No Neg.
Long EC
Ca Dust
K-Sulf-OC
EC-K-Sulf
Dust
K-Phosphate
Sea Salt
OC
No ID
a)
Unscaled Fractional Abundance
Time
EC-NoNeg.
Long EC
Ca Dust
K-Sulfate-OC
EC-K-Sulfate
Dust
K-PO4
Sea Salt
OC
No ID
9:57 AM
10:18 AM
10:40 AM
11:01 AM
11:23 AM
11:45 AM
b)
Concentrated
Non Concentrated
9:27 AM
9:48 AM
10:10 AM
10:31 AM
10:53 AM
11:15 AM

temporal evolution of the same classes for the second two hour exposure study conducted on 8/27/03. During this study, the sampling location of the ATOFMS was switched between the concentrated and non-concentrated aerosol streams. The concentrated aerosol stream was sampled for two 45 minute time periods, and the non concentrated stream was sampled for two 15 min time periods. These different time periods are separated by the vertical lines in Figure 7.11. When the sampling location was switched from concentrated to non-concentrated, there was a sharp increase in the EC and OC particle types, while a corresponding decrease occurred in the inorganic particle classes such as dust. This is expected given the fact that the EC and OC classes occur in the fine mode and inorganic particle types predominantly occur in the coarse mode. The less abundant classes shown in Figures 7.11a and 7.11b do not show as much temporal variation, most likely due to their low frequency of detection during the short 10 minute time period used for this analysis. A comparison of the results from these two exposures shows how coarse particle composition (and their associated sources) can vary over very short time periods. Without knowing the composition differences from study-to-study, it would be difficult to draw conclusions on how coarse particles affect human health based on coarse particle mass loadings alone.

Additional measurements run alongside the ATOFMS would greatly compliment the semiquantitative data from the ATOFMS. Past measurements using a Micro Orfice Uniform Deposit Impactor (MOUDI) have been used to produce quantitative results from the ATOFMS data [*Bhave et al.*, 2002]. In this previous study, the time resolution was restrained to 4 hr intervals to collect enough mass with the MOUDI, but with the elevated

mass exiting the concentrator, the time resolution could likely be increased in a similar study. Having this additional information would also be important from a toxicological perspective, allowing the comparison of species concentrations and particle size with human response.

Comparison of the particles sampled during these two exposure studies demonstrates how even for coarse particles, the composition of the particles can vary significantly from day to day. In order to develop a better understanding of the health effects of particles, it is important to be able to go beyond studies just differentiating coarse versus fine particles, because the dominant composition (i.e. inorganic vs. organic) for a given size range can change, making interpretation of the health effects results difficult [*Brunekreef*, 2002]. Having the ability to track the particle mixing state will ultimately allow for linking the observed particle compositions to specific sources upon comparison with source fingerprints obtained in single particle source characterization studies. This may make it possible to reach the ultimate goal of linking health effects with specific PM sources.

7.5 Conclusions

The coarse particle concentrator used for human exposure studies did not cause significant chemical changes of particles between the inlet and the outlet of the concentrator itself. Since hygroscopic species are abundant in this region of the country, the dynamics involving these particles should be kept in mind while interpreting results from human exposure studies. Changes in ambient temperature and RH probably cause a variation in the amount of organic and semivolatile species found in coarse mode

particles from day to day. This was seen in this study as an increase in organics during the exposure when the dew point temperature of the aerosol stream exceeded the sampling temperature. One possible way to avoid changing the chemical composition artificially would be to somehow match the temperature of the concentrator and sampling lines to ambient temperatures, as well as match the RH of the dilution air to the ambient RH.

The size distributions for the inlet and outlet of the concentrator were characterized along with their associated concentration factors with the use of the APS instruments. The concentration factor for ambient particles was found to be around 50 or 60 – a value within good agreement with the laboratory characterization of the concentrator. Concentration factors for fine mode particles which showed an increase from 2-46 for the 0.54-2.5 μm size range.

This study additionally showed the variability of coarse particle composition during short two hour exposures, detecting chemical changes in concentrated ambient aerosol at a time resolution of 10 minutes. Relating the chemical classes to sources and a comparison of the exposure data with bulk measurements is work currently in progress and will be presented in the near future.

7.6. Acknowledgements

Chapter 7, in full, is a reprint of the material as it appears in:

Moffet, R. C.; Shields, L.G.; Berntsen, J.; Devlin, R. B.; Prather, K. A. (2004). Characterization of an Ambient Coarse Particle Concentrator Used for Human Exposure Studies: Aerosol Size Distributions, Chemical Composition and Concentration

Enrichment. *Aerosol Science and Technology*. 38(10), 1123-1137. The dissertation author was the primary author of this paper.

All members of the Prather research group at UCSD were extremely helpful during every stage of this study. David Kosnikowski for TRC Environmental gave assistance in operating the coarse concentrator used in this study. The research presented is supported by the University of Rochester EPA PM Center under grant R827354. This report has been reviewed by the National Health and Environmental Effects Research Laboratory, United States Environmental Protection Agency and approved for publication. Approval does not signify that the contents necessarily reflect the views and policies of the Agency nor does mention of trade names or commercial products constitute endorsement or recommendation for use.

7.7 References

Allen, J.O., D.P. Fergenson, E.E. Gard, L.S. Hughes, B.D. Morrical, M.J. Kleeman, D.S. Gross, M.E. Galli, K.A. Prather, and G.R. Cass: Particle detection efficiencies of aerosol time of flight mass spectrometers under ambient sampling conditions, Environmental Science & Technology, 34 (1), 211-217, 2000.

Angelino, S., D.T. Suess, and K.A. Prather: Formation of aerosol particles from reactions of secondary and tertiary alkylamines: Characterization by aerosol time-of-flight mass spectrometry, Environmental Science & Technology, 35 (15), 3130-3138, 2001.

Bhave, P.V., J.O. Allen, B.D. Morrical, D.P. Fergenson, G.R. Cass, and K.A. Prather: A field-based approach for determining ATOFMS instrument sensitivities to ammonium and nitrate, Environmental Science & Technology, 36 (22), 4868-4879, 2002.

Brunekreef, B.: Exposure assessment in environmental epidemiology: The role of validation sub-studies, Epidemiology, 13 (4), S101-S101, 2002.

Cornell, S.E., T.D. Jickells, J.N. Cape, A.P. Rowland, and R.A. Duce: Organic nitrogen deposition on land and coastal environments: a review of methods and data, Atmospheric Environment, 37 (16), 2173-2191, 2003.

Demokritou, P., T. Gupta, S. Ferguson, and P. Koutrakis: Development of a high-volume concentrated ambient particles system (CAPS) for human and animal inhalation toxicological studies, Inhalation Toxicology, 15 (2), 111-129, 2003.

Dockery, D.W., and C.A. Pope: Acute Respiratory Effects of Particulate Air-Pollution, Annual Review of Public Health, 15, 107-132, 1994.

Dockery, D.W., C.A. Pope, X.P. Xu, J.D. Spengler, J.H. Ware, M.E. Fay, B.G. Ferris, and F.E. Speizer: An Association between Air-Pollution and Mortality in 6 United-States Cities, New England Journal of Medicine, 329 (24), 1753-1759, 1993.

Dockery, D.W., J. Schwartz, and J.D. Spengler: Air-Pollution and Daily Mortality - Associations with Particulates and Acid Aerosols, Environmental Research, 59 (2), 362-373, 1992.

Eatough, D.J., R.W. Long, W.K. Modey, and N.L. Eatough: Semi-volatile secondary organic aerosol in urban atmospheres: meeting a measurement challenge, Atmospheric Environment, 37 (9-10), 1277-1292, 2003.

Edney, E.O., T.E. Kleindienst, T.S. Conver, C.D. McIver, E.W. Corse, and W.S. Weathers: Polar organic oxygenates in PM2.5 at a southeastern site in the United States, Atmospheric Environment, 37 (28), 3947-3965, 2003.

Finlayson-Pitts, B.J., and J.N. Pitts: Chemistry of the Upper and Lower Atmosphere, Academic Press, San Diego, 2000.

Gamble, J.F.: PM2.5 and mortality in long-term prospective cohort studies: Cause-effect or statistical associations? Environmental Health Perspectives, 106 (9), 535-549, 1998.

Gard, E., J.E. Mayer, B.D. Morrical, T. Dienes, D.P. Fergenson, and K.A. Prather: Real-time analysis of individual atmospheric aerosol particles: Design and performance of a portable ATOFMS, Analytical Chemistry, 69 (20), 4083-4091, 1997.

Gavett, S.H., and H.S. Koren: The role of particulate matter in exacerbation of atopic asthma, International Archives of Allergy and Immunology, 124 (1-3), 109-112, 2001.

Guazzotti, S.A., D.T. Suess, K.R. Coffee, P.K. Quinn, T.S. Bates, A. Wisthaler, A. Hansel, W.P. Ball, R.R. Dickerson, C. Neususs, P.J. Crutzen, and K.A. Prather: Characterization of carbonaceous aerosols outflow from India and Arabia:

Biomass/biofuel burning and fossil fuel combustion, Journal of Geophysical Research-Atmospheres, 108 (D15), -, 2003.

Guazzotti, S.A., J.R. Whiteaker, D. Suess, K.R. Coffee, and K.A. Prather: Real-time measurements of the chemical composition of size-resolved particles during a Santa Ana wind episode, California USA, Atmospheric Environment, 35 (19), 3229-3240, 2001.

Hagerman, L.M., V.P. Aneja, and W.A. Lonneman: Characterization of non-methane hydrocarbons in the rural southeast United States, Atmospheric Environment, 31 (23), 4017-4038, 1997.

Hinds, W.C., Aerosol Science and Technology, John Wiley and Sons, New York, 1999.

Hughes, L.S., J.O. Allen, P. Bhave, M.J. Kleeman, G.R. Cass, D.Y. Liu, D.F. Fergenson, B.D. Morrical, and K.A. Prather: Evolution of atmospheric particles along trajectories crossing the Los Angeles basin, Environmental Science & Technology, 34 (15), 3058-3068, 2000.

Leikauf, G.D.: Hazardous air pollutants and asthma, Environmental Health Perspectives, 110, 505-526, 2002.

Lippmann, M.: Background on Health-Effects of Acid Aerosols, Environmental Health Perspectives, 79, 3-6, 1989.

Liu, D.Y., R.J. Wenzel, and K.A. Prather: Aerosol time-of-flight mass spectrometry during the Atlanta Supersite Experiment: 1. Measurements, Journal of Geophysical Research-Atmospheres, 108 (D7), -, 2003.

Monn, C., and S. Becker: Cytotoxicity and induction of proinflammatory cytokines from human monocytes exposed to fine (PM2.5) and coarse particles (PM10-2.5) in outdoor and indoor air, Toxicology and Applied Pharmacology, 155 (3), 245-252, 1999.

Neubauer, K.R., M.V. Johnston, and A.S. Wexler: On-line analysis of aqueous aerosols by laser desorption ionization, International Journal of Mass Spectrometry and Ion Processes, 163 (1-2), 29-37, 1997.

Noble, C.A., and K.A. Prather: Real-time single particle monitoring of a relative increase in marine aerosol concentration during winter rainstorms, Geophysical Research Letters, 24 (22), 2753-2756, 1997.

Peters, A., D.W. Dockery, J. Heinrich, and H.E. Wichmann: Short-term effects of particulate air pollution on respiratory morbidity in asthmatic children, European Respiratory Journal, 10 (4), 872-879, 1997.

Rice, T.J., S.W. Buol, and S.B. Weed: Soil Saprolite Profiles Derived from Mafic Rocks in the North-Carolina Piedmont.1. Chemical, Morphological, and Mineralogical Characteristics and Transformations, Soil Science Society of America Journal, 49 (1), 171-178, 1985.

Robarge, W., 2003. Personal Communication

Robarge, W.P., J.T. Walker, R.B. McCulloch, and G. Murray: Atmospheric concentrations of ammonia and ammonium at an agricultural site in the southeast United States, Atmospheric Environment, 36 (10), 1661-1674, 2002.

Seagrave, J., J.L. Mauderly, and S.K. Seilkop: In vitro relative toxicity screening of combined particulate and semivolatile organic fractions of gasoline and diesel engine emissions, Journal of Toxicology and Environmental Health-Part A, 66 (12), 1113-1132, 2003.

Silva, P.J., and K.A. Prather, Chapter 6: Characterization of individual particles emitted from the charbroiling of meat, University of California, Riverside, Riverside, 2000.

Song, X.H., P.K. Hopke, D.P. Fergenson, and K.A. Prather: Classification of single particles analyzed by ATOFMS using an artificial neural network, ART-2A, Analytical Chemistry, 71 (4), 860-865, 1999.

Tobias, H.J., P.M. Kooiman, K.S. Docherty, and P.J. Ziemann: Real-time chemical analysis of organic aerosols using a thermal desorption particle beam mass spectrometer, Aerosol Science and Technology, 33 (1-2), 170-190, 2000.

Walker, J.T., V.P. Aneja, and D.A. Dickey: Atmospheric transport and wet deposition of ammonium in North Carolina, Atmospheric Environment, 34 (20), 3407-3418, 2000.

8

Conclusions

The work in this dissertation represents an advance of the ATOFMS technique to measure the optical and microphysical properties of aerosol particles in ways that have not been accomplished in the past. Specifically, the development of the ATOFMS to measure the simultaneous optical, aerodynamic and mass chemical properties of single aerosol particles has been used to advance our understanding of aerosol chemical and physical processes in the ambient atmosphere. By calibrating the optical detection and aerodynamic sizing region of the ATOFMS, traditional single particle measurements of size and chemical composition have been extended to include refractive index and density for laboratory generated aerosols. These improved ATOFMS measurements were applied to ambient particles in Riverside, CA and Mexico City. In these studies, the ATOFMS was used to first separate the particles on the basis of chemical composition prior to the determination of optical and microphysical properties. Unique interconnections were resolved between physical, chemical and optical properties of the ambient particles that will prove useful for evaluating how aerosol particles affect climate and visibility. The techniques used here were also applied to the study of aerosols that are harmful to human health. In Mexico City, a comprehensive analysis was done on particles rich in toxic metals such as Pb. Furthermore, the ATOFMS was directly used in a study of human health effects for the purpose of evaluating whether or not a coarse particle concentrator changes the chemical and physical properties of the particles. In sum, the ATOFMS measurements are of high value for climate and health effects measurements.

However, before applying the measurements to ambient data, it was imperative that laboratory characterization of the instrument response characteristics is essential for interpreting real atmospheric aerosol optical and microphysical properties.

Method development and data analysis techniques were first carried out on laboratory generated aerosol with the goal of determining optical and microphysical properties. The photomultiplier tubes used to make the optical measurements in the ATOFMS instrument were calibrated to enable a direct comparison to single particle scattering models. In so doing, the refractive index and density were determined for particle classes containing over 10,000 particles. The emphasis of the laboratory experiments was then shifted to determine if the ATOFMS nozzle inlet would change the physical characteristics of aerosol particles produced in a thermodynamically metastable state. It was found that the ATOFMS did not noticeably change the refractive index of spherical metastable sea salt particles. Based on these results, water uptake experiments for more complex aerosol mixing states may be explored using the traditional inlet; the aerodynamic lens will not be effective for these measurements because the long amount of time spent in vacuum has been shown by others to result in complete dehydration. It was further observed that spherical particle types may be distinguished from nonspherical particles by observing how light scattering depends on the aerodynamic diameter: spherical particles follow the scattering pattern predicted by Mie theory while nonspherical particles do not. These laboratory characterizations may be used to interpret measurements of ambient aerosols as a function chemical composition, size and time.

The optical measurements and data analysis techniques that were developed in the laboratory were applied to field measurements in Riverside and Mexico City, resulting in the

determination of the optical and microphysical properties of particles separated on the basis of chemical composition. A range of particle properties were detected in ambient studies. Some single particle chemical mixing states (primarily OC and Sea Salt) displayed a spherical morphology enabling the refractive index and density to be determined using Mie theory. Some of the spherical particles only had significant numbers below 600 nm and for these particles it was determined that only the effective density could be determined. In Mexico City, a wide range of values for refractive index and/or density was observed. This is believed to be due to the different microphysical characteristics of fresh and aged particles. For EC particles in both Riverside and Mexico morphological properties were seen to depend on particle age: heavily aged EC particles were seen to be coated with a large amount of nonabsorbing material, whereas freshly emitted EC particles were nonspherical but still mixed with presumably less nonabsorbing material. The coating of EC particles was found to have a large impact on how the single scattering albedo for EC particles varies as a function of size. This observation shows that the climate forcing nature of EC is strongly dependent on its mixing state since aged and fresh particles will absorb and scatter light differently. Overall, this new method of measuring ambient aerosols is of great use for research on aerosol radiative effects, and serves a dual benefit for studying aerosols suspected to be harmful to human health.

For particles rich in toxic metals, the first ever ATOFMS study comparison study with data from a computer controlled scanning electron microscopy coupled with energy dispersive X-Ray analysis was carried out in Mexico City. Using ATOFMS temporal profiles together with a backtrajectory analysis, it was observed that not only does the city center act as a source of particles, but it also acts as a receptor site for toxic metal particles early in the

morning. When the ATOFMS measurements were deployed in a northern region of Mexico City, daily plumes of Pb containing particles were observed to be coming from industrial activities in the northeastern part of the city. Using the ATOFMS it was found that the particles contained a unique Pb/Zn/Cl/P mixing state that matched most closely to the source profile of garbage incineration rather than non-ferrous smelting. Several techniques were used to obtain different yet complimentary information on the particles: quantitative measurements of single particles by CCSEM/EDX, speciation was given by STXM/NEXAFS, and quantitative bulk analysis by PIXE and high volume samplers. Because these particles are associated with toxic metals, they may have an impact on human health in Mexico City. The ATOFMS measurements when used with peripheral instrumentation is a powerful method for measuring the microphysical properties of ambient aerosols, which is of use in health effects studies.

In order to study how aerosols affect human health, it is often necessary to conduct exposure studies where both the human subject and aerosol properties are monitored. For short human exposure studies that are most common, the ATOFMS was an ideal method for measuring the physical and chemical properties. For 2 hr exposures, 15 min time resolution was obtained for the major particle classes. In addition, the ATOFMS was used to show that a coarse particle concentrator does not change the chemical composition of the particles; however, sampling conditions were observed to change the characteristics of the aerosols from study to study during the same season. While the ATOFMS is a powerful method for determining the chemical, optical and microphysical properties, more development is needed to improve the data quality for all fields of research.

In order to guide future measurements, it is instructive to first look at the past, present, and future state of the art in optical measurements of single aerosol particles. The optical system of the ATOFMS is what is historically known as an optical particle counter (OPC). To look back at challenges for OPC measurements, consider the quote by [*McMurry*, 2000]:

> For instruments that show the expected dependence of response on size, theory can be used to determine the relationship between response and size for particles having a refractive index different from the calibration aerosol. This approach is sometimes used for atmospheric measurements. The challenge that arises when OPCs are used for atmospheric measurements is that the particle properties (shape, refractive index, and morphology) required to determine size from pulse data are typically unknown.

This much needed information that was previously unknown by classic OPC measurements has now been elucidated through the use of ATOFMS, which provides simultaneous information regarding the aerodynamic size and chemical composition of particles. However, these measurements have only been carried out for large numbers of particles. In order to push the optical measurements to the single particle level several challenges must be met:

1. more independent variables must be measured for the single aerosol particles such as scattering at multiple angles, polarizations and wavelengths
2. the undesirable effects of the divergent particle beam from the nozzle must be overcome by either creating a different chamber for optical measurements or using a different inlet.
3. the time resolution must be increased to ~100 Hz for hit particles to enable time resolved measurements of refractive index and density for a wide range of particle sizes and mixing states.

4. the ion peaks in the mass spectra should be calibrated to achieve more quantitative information on the individual chemical species within collections of similar particles in addition to the current measurements of number concentrations. Although, it should be noted that measurement of particle effective density is a first order measurement of mass. These measurements are being made several ways by our group [*Moffet and Prather,* 2005; *Spencer et al.*, 2007])

To improve on points 1-2, it would be wise to make a third analysis chamber for the ATOFMS where a wide laser beam can be used to make angular light scattering measurements. The long dimension of the scattering laser beam would have to be perpendicular to the particle beam so that even divergent particles would experience the same intensity as a particle traveling through the center of the laser beam. If a wide laser beam was used in the current tracking region, it would cause the ATOFMS to hit fewer particles because divergent particles would be tracked but not hit by the desorption/ionization laser. If a separate chamber was used for the optical measurement, the usual tracking system could be used to maintain the optimal hit percentage. Adding a separate optical chamber to the instrument would also greatly improve the quality of information given by the ATOFMS. If a multi angle scattering measurement was incorporated, the fraction of forward to backward scattered light could be determined and used to validate radiative transfer models and other in-situ optical measurements. If the multi angle measurement was carried out in addition to or with an intensified CCD camera, detailed information on particle morphology and optical size may be obtained such as in [*Aptowicz et al.*, 2004; *Aptowicz et al.*, 2006]. Lastly,

research on points 3-4 has been advancing steadily within the last few years and will undoubtedly help with any optical measurement done using the ATOFMS.

The research presented in this dissertation has advanced the technique of single particle mass spectrometry to measure the optical and microphysical properties of aerosol particles in both the laboratory and in the field. With continual development of this technique, it will prove to be ever more useful for the advancement of the fields of atmospheric chemistry, aerosol science, climate science, medical science and environmental science. Such a wide range of impacts clearly justifies continued research in this area. The next obvious steps to improve on the points listed above are 1) to widen the scattering laser beam perpendicular to the particle beam 2) implement a different wavelength of laser 3) make measurements at different angles; as mentioned above, it would be wise to carry out these improvements below the particle tracking region of the ATOFMS. With these improvements, it should be possible to measure the complex refractive index, effective density and morphology for single aerosol particles as a function of time, size and chemical mixing state. Such a powerful measurement would be unprecedented, and would provide a wealth of information measured in situ to guide remote sensing and modeling efforts.

References

Aptowicz, K.B., Y.L. Pan, R.K. Chang, R.G. Pinnick, S.C. Hill, R.L. Tober, A. Goyal, T. Leys, and B.V. Bronk: Two-dimensional angular optical scattering patterns of microdroplets in the mid infrared with strong and weak absorption, Optics Letters, 29 (17), 1965-1967, 2004.

Aptowicz, K.B., R.G. Pinnick, S.C. Hill, Y.L. Pan, and R.K. Chang: Optical scattering patterns from single urban aerosol particles at Adelphi, Maryland, USA: A classification relating to particle morphologies, Journal of Geophysical Research-Atmospheres, 111 (D12), -, 2006.

McMurry, P.H.: A review of atmospheric aerosol measurements, Atmospheric Environment, 34 (12-14), 1959-1999, 2000.

Moffet, R.C., and K.A. Prather: Extending ATOFMS measurements to include refractive index and density, Analytical Chemistry, 77 (20), 6535-6541, 2005.

Spencer, M.T., L.G. Shields, and K.A. Prather: Simultaneous measurement of the effective density and chemical composition of ambient aerosol particles, Environmental Science & Technology, 41 (4), 1303-1309, 2007.